Author:
Gibbins, David Rhys

Title:
The Design and Simulation of Complex UWB Antennas for the Purpose of Breast Cancer Detection

The Design and Simulation of Complex UWB Antennas for the Purpose of Breast Cancer Detection

David Rhys Gibbins

A thesis submitted to the University of Bristol in accordance with the requirements of the degree of Doctor of Philosophy in the Faculty of Engineering

Department of Electrical and Electronic Engineering

September 2009

Word count : 44,000

Abstract

Breast Cancer is the most prevalent form of cancer in women (excluding skin cancers), however with early detection there is a high chance of successful treatment and long-term survival. Microwave imaging as a means of detection has gained interest recently, due to advances in both hardware and imaging software. The method offers a potential alternative to current imaging techniques that would be inexpensive, provide sensitive 3D imaging data, avoid using ionising radiation and would yield a system that is both quick and comfortable for the patient.

This thesis presents a new UWB wide-slot antenna that has been designed to operate in the multistatic-radar breast imaging system being developed at the University of Bristol. The antenna has been made as compact as possible so as to maximise the number of elements in the imaging array and is around half the size of equivalent existing designs. To further reduce it's overall dimensions a direct coax feed has been developed that eliminates the need for an SMA connector. The simulated and measured performance of this antenna show that it has a -10dB input bandwidth in excess of 6 GHz with a lower cut off frequency of 4GHz. It is capable of radiating high fidelity UWB pulses into a high dielectric medium with properties similar to adipose breast tissue and that it is capable of doing this at angles of up to 60° away from boresight.

The thesis then goes on to present a novel meshing technique that potentially offers a way of efficiently simulating a section of the imaging array, by means of generalised co-ordinate FDTD. This hybrid technique involves descritizing the majority of the problem geometry with meshes based on orthogonal co-ordinate systems. These mesh regions are then linked together using sections of purpose built orthogonal curvilinear mesh that provides a smooth transition. Because the whole mesh is orthogonal there is no need for extra interpolation steps in the FDTD algorithm and the problem can be solved as efficiently as with conventional Cartesian FDTD. Central to this scheme is the orthogonal

curvilinear mesh upon which the rest of the mesh is based. This mesh is produced using a technique that takes advantage of the orthogonality of isopotentials and field lines in a potential field, found using an finite difference Laplace solver.

A simulation of two wide-slot antennas angled at 45° to one another has been used to verify this meshing technique. Numerical experiments have shown that it is able to reproduced the measured coupling between two such antennas. The electric near-field of the antenna compares favourably with equivalent results obtained from a Cartesian FDTD simulation. And with reference to the measured antenna fields it has been shown that the mesh is able to produce a response from a dielectric scatterer that is consistent with the same scenario in a cartesian simulation.

Dedicated to

my parents, Robbie and Irena

Acknowledgements

First and foremost I would like to thank my supervisor Prof. Ian Craddock for his help and encouragement over the duration of my research. I greatly appreciate the fact that he was always there when I needed help or to ask a question. Also I would like thank the EPSRC, The faculty studentship and the Thomas John Jones Memorial fund for providing financial support over the course of my studies.

For his patience and invaluable help with all things UWB I am indebted to Maciek Klemm, similarly to Dr Geoff Hilton for his assistance with the practical side of antenna analysis. I am also grateful to Professor Chris Railton for his help with the in-house FDTD code and orthogonal meshes. A large amount of work that went into developing the "wide-slot" was practically based and for countless discussions on the construction manufacture and all things antenna I would like to thank Ken Stevens. I would also like to express my gratitude to all of my colleagues in the CCR for their friendship and contributions to my work over the past couple of years and make special mention of Siva Kupanna Subramani and Henry Hunt-Grubb.

I am eternally grateful for the love and support of my girlfriend Abi, who put up with and looked after me, my mother and father who helped me believe I could actually finish, my brother, sister, family and friends, without any of whom I could not have completed this work.

Author's Declaration

I declare that the work in this dissertation was carried out in accordance with the regulations of the University of Bristol. The work is original except where indicated by special reference in the text and no part of this dissertation has been submitted for any other degree. Any views expressed in the dissertation are those of the Author and in no way represent those of the University of Bristol. This dissertation has not been presented to any other university for examination either in the United Kingdom or overseas.

SIGNED: 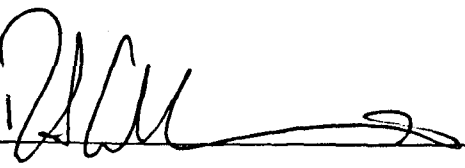

DATE: 7/7/2010

Contents

List of Figures

Publications

Journal Papers

Klemm M., Leendertz J., Gibbins D., Craddock I.J., Preece A., Benjamin R., "Microwave Radar-based Differential Breast Cancer Imaging: Part 1 Imaging in Homogeneous Breast Phantoms and Low Contrast Scenarios", submitted to Antennas and Propagation, IEEE Transactions on

Gibbins D., Klemm M., Craddock I.J., Leendertz J.A., Preece A., Benjamin R., "A comparison of a wide-slot and a stacked patch antenna for the purpose of breast cancer detection", Antennas and Propagation, IEEE Transactions on, Awaiting publication

Klemm M., Leendertz J., Gibbins D., Craddock I.J., Preece A., Benjamin R, "Microwave Radar-based Breast Cancer Detection: Imaging in Inhomogeneous Breast Phantoms", IEEE Antennas and Wireless Propagation Letters, Awaiting publication

Conference papers

Klemm M., Leendertz J., Gibbins D., Craddock I.J., Preece A., Benjamin R. "Towards Contrast Enhanced Breast Imaging using Ultra-Wideband Microwave Radar System", submitted to 2010 IEEE Radio and Wireless Symposium, special session on Biomedical Applications

Gibbins, D.; Klemm, M.; Craddock, I.; Preece, A.; Leendertz, J.; Benjamin, R., "Design of a UWB wide-slot antenna and a hemispherical array for breast imaging," Antennas and Propagation, 2009. EuCAP 2009. 3rd European Conference on , vol., no., pp.2967-2970, 23-27 March 2009.

Klemm M., Leendertz J., Gibbins D., Craddock I.J., Preece A., Benjamin R. "Experimental and clinical results of breast cancer detection using UWB microwave radar", 2008 IEEE Antennas and Propagation Society International Symposium, 5-11 July 2008

Craddock I.J., Klemm M., Leendertz J., Gibbins D., Preece A., Benjamin R. "Development and application of a UWB radar system for breast imaging", 2008. LAPC Loughborough Antennas and Propagation Conference, 17-18 March 2008 Page(s):24 – 27

Gibbins D.R., Klemm M., Craddock I.J., Hilton, G.S., Paul, D.L., "The Design of a Wide Slot Antenna for the Transmission of UWB Signals into the Human Body using FDTD Simulation," Antennas and Propagation, 2007. EuCAP 2007. The Second European Conference on , vol., no., pp.1-5, 11-16 Nov. 2007.

Gibbins D. R., Yamsiri A., Craddock I. J., Hilton G. S., Paul, D. L., "An investigation of a compact UWB antenna by measurement and FDTD simulation," Antennas and Propagation, 2006. EuCAP 2006. First European Conference on , vol., no., pp.1-4, 6-10 Nov. 2006.

Hunt-Grubbe H., Gibbins D., Hilton G., "Radiation Pattern Performances of Single Feed and Differentially Driven Dual Feed Cavity Backed Linear Slot Antennas", Loughborough Antennas and Propagation conference 2006, April 2006.

List of Abbreviations

AUT	Antenna Under Test
BW	BandWidth
CPFDTD	Contour Path FDTD
CPW	Co-Planar Waveguide
FDTD	Finite Difference Time Domain
GPR	Ground Penetrating Radar
HPBW	Half Power Beam Width
LOS	Line Of Sight
NO	Non-Orthogonal
OC	Orthogonal-Curvilinear
PAN	Personal Area Networks
PCB	Printed Circuit Board
PEC	Perfect Electrical Conductor
PICA	Planar Inverted Cone Antenna
RCS	Radar Cross Section
RFID	Radio Frequency ID
UWB	Ultra Wide Bandwidth
VNA	Vector Network Analyser
VSWR	Voltage Standing Wave Ratio
WLAN	Wireless Local Area Network

List of Symbols

$\mathbf{A}_i$	Covariant field component
$\mathbf{A}^i$	Contravariant field component
$\mathbf{B}$	Magnetic flux
c_0	Speed of light in free space
$\mathbf{D}$	Electric Flux
$\mathbf{E}$	Electric field
F	Fidelity
f_H, f_L, f_c	Higher, Lower and centre frequency
G	Gain
g	Metric tensor
$\mathbf{H}$	Magnetic field
L	Antenna element dimension
R	Resistance
S_{11}	Input return loss
S_{21}	Forward transmission coefficient
t	Time
Δt	FDTD time step
Z_{in}, Z_L, Z_0	Input, Load and characteristic impedance

ε_r, ε_0	Relative and free space permittivity
θ_{HP1}, θ_{HP2}	Half power beam width in two orthogonal planes
λ	Wavelength
Ω_A	Solid beam angle

Chapter 1 Introduction

1.1 History: The Genesis of Radio

Wide-bandwidth radio systems or in other words; radio systems that have a large operational frequency bandwidth, have been around since the genesis of radio at the end of the 19th century. The first ever radio system was the "spark gap" transmitter/receiver developed by Hienrich Hertz in 1886, built to carry out his first investigations into radio waves. Hertz apparatus, which can be seen in Figure 1.1, consisted of an induction coil connected across an air-gap that produced a spark at the feed point of a dipole antenna. The electromagnetic pulse produced was received by a single turn loop antenna that also had a spark gap across which the intensity of the received signal could be judged [1]. By altering the size of the receiving loop he found that a certain loop size would produce the longest and consequently highest voltage spark demonstrating the idea of tuning or resonance.

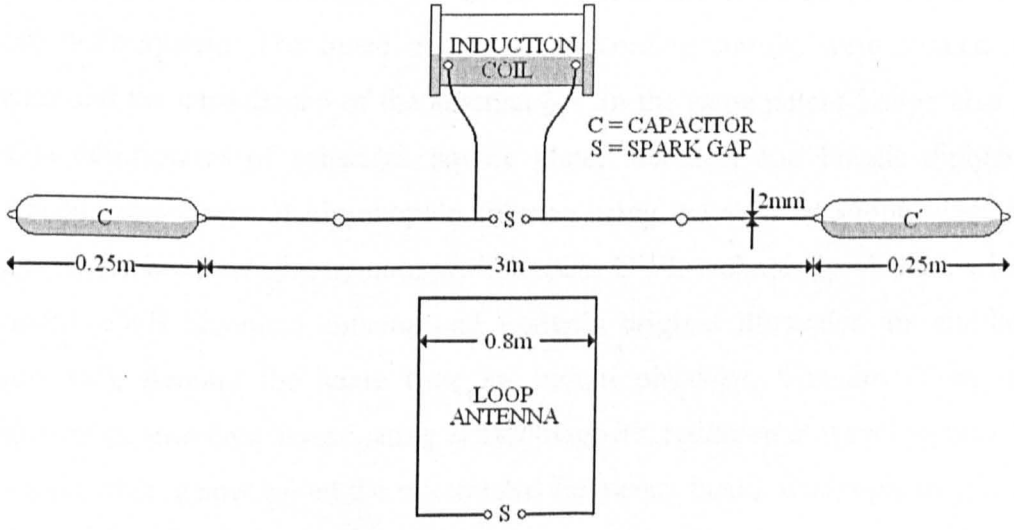

Figure 1.1 Hertz's dipole/loop – the first radio transmitter/receiver system

The system used a spark gap to create an impulse with a wide bandwidth of frequencies, much like the pulses seen in modern Ultra-wideband (UWB) impulse-radio. The narrow-band "thin wire" Hertzian dipole and loop antennas used could

only transmit radiation in a narrow band of frequencies and so the system as a whole cannot be thought of as wide-band. It was not long after this that the first wideband antennas were developed, the majority of which are still easily recognisable to a modern day UWB engineer and used in one form or another in today's UWB systems.

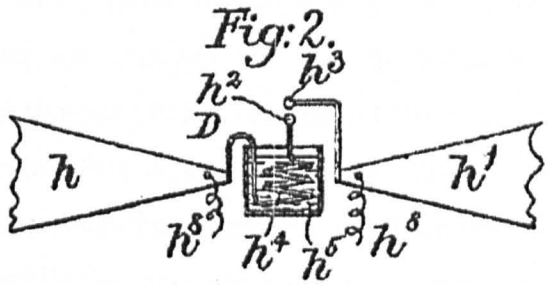

a)

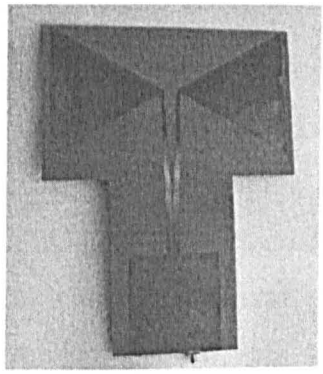

b)

Figure 1.2 (a) Lodge's 1898 precursor to the bowtie antenna [3] (b) a modern UWB bowtie antenna designed for use in a ground penetrating radar system [2].

Some of the early pioneers of antenna and radio technology were amongst others; the British physicist Oliver Lodge, who in 1898 submitted a patent [3] for a syntotic (tuned) radio system. The tuned transmitting/receiving circuits were formed by an inductor and the capacitance of the antenna [4]. In the same patent Lodge also gives the first descriptions of spherical, square plate, biconical and bowtie dipoles and introduced the concept of a monopole antenna using the earth as ground [3]. All of these antennas are now synonymous with modern UWB technology. A comparison of a modern UWB biconical antenna and Lodge's original illustrates the similarities (Figure 1.2). Around the same time an Indian physicist, Chandra Bose, began conducting experiments investigating electromagnetic radiation at wavelengths of 25–50 mm (in what is now called the microwave frequency band). One topic of this work was Bose's investigations of "transitions" between free space and transmission lines from which he developed what he referred to as "collecting funnels". This type of antenna is now known as a horn antenna and is commonly used in modern wideband applications [5] [6].

1.1.1 Commercialisation

It was a physicist and businessman named Guglielmo Marconi who first realised the commercial potential of radio as a long range communication system. It was in the spring of 1895 at his home of Villa Griffone, Italy that he first demonstrated the feasibility of a practical radio link. This was made possible by virtue of the fact that Marconi had realised the importance of having a good ground connections for his transmitter and receiver [7]. The apparatus he used in his early experiments was similar to that seen in his 1897 patent "transmitting electrical signals" [8] (Figure 1.3). As in Hertz's first system the signals were generated by an inductor connected across a spark gap. Marconi connected one terminal of the gap to a wideband square plate antenna while the other, crucially, was connected to earth. Receiving the signals was a detector, again connected to a square plate antenna and earth. This was the first practical wideband communications link, the combination of the high mounted capacitive plate antenna and earth connection proving more effective than any radiator/receiving antenna that had been produced before [9].

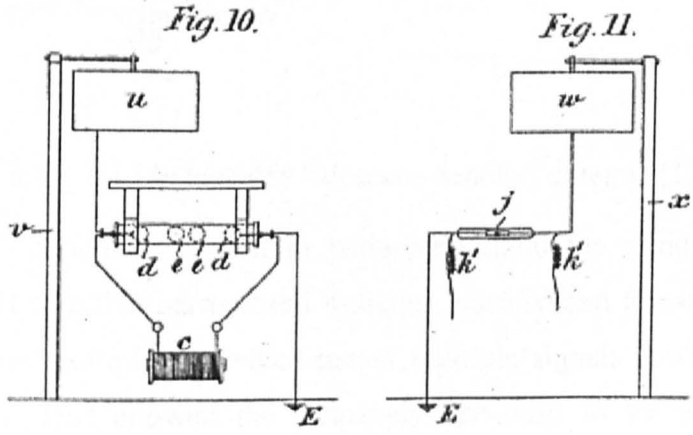

Figure 1.3 Marconi's 1897 patent radio system [8]

With his new arrangement he initially made transmissions over short distances but steadily increased the range. In 1896 Marconi moved to Great Britain and successfully demonstrated his radio system on Salisbury plain. He continued development until

1900 when he finally accomplished multiple transmissions on a single apparatus practically implementing the idea of tuning put forward by Lodge in 1898.

It is perhaps, the events on December 12th, 1901 for which Marconi is best remembered. At about 12.30pm on top of Signal Hill, Newfoundland, Marconi heard three weak but audible signals (Morse code for the letter 's') transmitted by a 45.7m high, wideband, fan monopole located at Poldhu, Cornwall over 3400 km away [10],[7],[11]. The age of wireless communications had begun.

1.1.2 The Shortwave Era

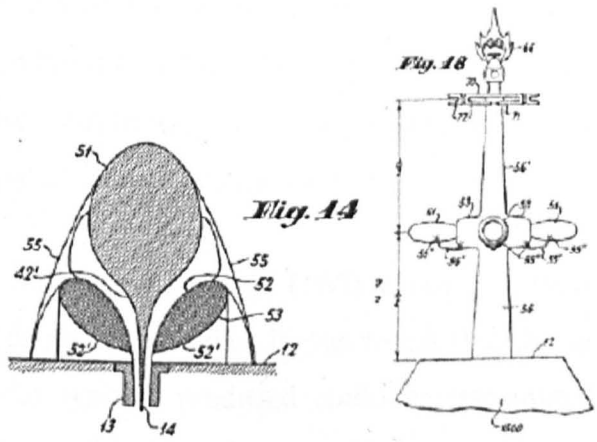

Figure 1.4 Lindenbalds "Volcano Smoke" antenna [13]

After this initial period of interest in wide-band radio the trend turned to more compact and cost effective narrowband systems. Narrowband transmissions allowed frequency division multiplexing which meant multiple signals could be sent over a finite bandwidth. This allowed the frequency spectrum to be used much more efficiently, as a result research in wide-band radio dwindled [12]. It was not until the 1930s that interest was rekindled due to the need for broader bandwidth systems required for the transmission of FM (Frequency Modulation) radio and then television signals [5]. This period saw the rediscovery of old wideband antenna designs including in 1939 Carter's resurrection of Lodge's biconical dipole and conical monopole antennas. New designs were also developed, typical of which was a coaxial horn element developed by Lindenbald [13], which he called a "Volcano Smoke"

antenna. This antenna was used by the Radio Corporation of America (RCA) as an experimental transmitter for Short Wave (SW) television signals (Figure 1.4) and graced the top of the Empire State building for a number of years, coming to symbolise the entire television research effort [5].

After this point development of wideband antennas was slow but steady. As the television and radio communications industry expanded and the need for inexpensive, easy to manufacture wideband antennas grew, new wideband designs were developed. Notable among these were Mariè's wide band slot antenna (1962) and Stohr's 1968 ellipsoidal monopole and dipole [14]. It was also in this period that the military started to take an interest in UWB applications, in particular radar. The pulses produced by UWB systems can be made very short by virtue of the fact that their frequency bandwidths are so wide. This improved the accuracy with which the time of flight of the pulse from transmitter to target and then back again could be measured, improving the spatial accuracy of the devices [15], [12].

The 1970s saw renewed interest in UWB communications, at that time known as "baseband" or "carrier-free" radio. It was found that the low-power ultra wideband signals these radio systems produced could be transmitted alongside conventional narrow band systems without causing interference in either system. However the same problems encountered by the likes of Marconi and Lodge were still present; that of how to transmit multiple signals simultaneously without interference [12].

1.1.3 The Modern UWB Era

It was in the early 1990s with the introduction of time-hopping impulse radio (TH-IR) by Win and Sholtz [16] that the problem of multiple simultaneous users was solved and UWB communications emerged as a commercially viable option. As a result there was an explosion in research and designs of UWB antennas driven by the need for small antennas to work with the proposed systems [12]. It was around this time (1990) that a definition of UWB systems given by the Defence Advanced Research Projects Agency (DARPA) [17] stated that a UWB system is defined as one having a

fractional bandwidth greater than 25%. More recently (2003) the classification of a UWB system was redefined by the Federal Communications Commission (FCC) [18] as one in which the fractional bandwidth is greater than 20%. At the same time the FCC offered the alternative definition that any system with an absolute bandwidth greater than 500 MHz should also be classed as UWB regardless of fractional bandwidth.

One of the key obstacles to the commercial implementation of UWB technology was political rather than technological. Conventionally, radio operators are assigned a narrow frequency range in which they may transmit. UWB systems violate those assignments as they broadcast across such a large range of frequencies. It was argued that UWB signals could be sent at the same frequencies as other transmissions without interference [12]. The FCC's response to this was, in 2002, to rule that unlicensed UWB emissions may be made between 3.1 and 10.6 GHz within certain limits that are determined by the application [19]. This ruling set the current climate for the development of this technology in which UWB research has flourished.

1.2 Contemporary UWB Applications

UWB technology has many potential applications. While the initial hype surrounding the technology was exaggerated, some claiming that "UWB is the ultimate solution to all problems in wireless", many commercial uses have been identified [12]. Topics of current research include: high data rate communication systems, for which a number of different coding schemes have emerged; impulse radio [16] and Direct Sequence Code Division Multiple Access radio (DS-CDMA) [20] to name two; dielectric medium penetrating radar [21] which has proved to be an effective tool in many applications such as land mine detection [22], non-intrusive archaeological investigations [23] and the early detection of Breast Cancer [24], [25]. UWB technology is also being used to implement geolocation.

1.2.1 Communications

UWB systems are seen as one of the most promising solutions for future short range communication systems due to its potential for high-speed data rate and excellent immunity to multi-path interference [26]. Possible applications include transmission of high definition television signals from a set top box to a television and wireless USB (universal serial bus) which could have data transmission rates of 480 Mbits/sec. UWB technology offers many potential advantages over narrowband systems. These include; low transmit power levels and possibly simpler hardware configurations [12]. Below, the main methods of communication using the UWB channel are discussed along with their implications for antenna design.

1.2.1.1 Impulse radio and DS – CDMA (Direct Sequence Code Division Multiple Access)

Impulse radio or "baseband" radio was first developed in the 1970s and was refined by Win and Sholtz [16] who developed the idea of TH-IR, which allowed multiple users to transmit on the same frequency spectrum without "catastrophic" interference [12]. TH-IR uses signals in which each data bit is represented by a number of very short pulses generated by multiplying a spreading sequence of zeros with ±1's located at pseudo random positions. There are alternative methods of spreading a signal across a wideband of frequencies; DS – CDMA is similar to the implementation of TH-IR except that the spreading signal used is made up of only ±1s [12]. DS – CDMA is intended to operate in the prescribed 3.1-10.6 GHz UWB frequency range either in a sub band e.g. 3.1-5.15GHz or utilising the entire bandwidth. In order that errors in the transmitted signals are kept to a minimum, distortion of the pulses must be avoided. As a result of this the antenna used to transmit these signals must have a number of important performance characteristics [27], [5];

- Wide impedance bandwidth – in order to efficiently transmit the UWB signals, minimise reflection loss and avoid pulse distortion.

- Radiation patterns that maintain reasonably constant amplitude and shape across the operational frequency bandwidth which gives;
  - Relatively constant gain – minimising distortion
  - Fixed phase centre over frequency which will result in linear phase – If the phase centre (the location of the effective centre of the spherical wave produced by the antenna) moves with frequency, pulse dispersion (or ringing) will occur.
- Good efficiency – so as to reduce power consumption.

The above terms will be discussed in more detail in the next chapter.

Due to the Ultra-short nature of the pulses and low spectral power density the likelihood of detection and signal interception is low making this system attractive for military applications [15].

1.2.1.2 OFDM (Orthogonal Frequency Division Multiplexing)

OFDM transmits information in parallel over a large bandwidth using a number of different frequency carriers each of which requires only a small amount of bandwidth. In MB-OFDM a number of OFDM channels are combined in order to make use of the frequency bandwidth available in the 3.1-10.6GHz UWB band [28]. As this system does not transmit pulses it is less susceptible to signal dispersion however the frequency band of operation, gain, impedance bandwidth, efficiency and pattern stability are still important considerations when designing antenna for this type UWB system [29].

1.2.1.3 Frequency Hopping (FH)

FH systems transmit a partial bit or number of bits at one frequency and then switch frequencies before transmitting the next packet of information. FH radio can be implemented as a multiple access system of its own or combined with an OFDM scheme operating over a number of smaller frequency bands, which simplifies signal

processing. As the antenna is transmitting at only one frequency at a time antenna design considerations for a UWB antenna operating in a FH system are similar to that of an MB-OFDM system [12].

All of the above systems are potentially intended for implementation in hand-held devices. If this is the case then the size, ease of manufacture, cost and feed method (balanced or not) of the antenna being used should also be considered [27].

1.2.2 Radar

All radar systems rely on the detection of reflected electromagnetic radiation from the boundary between two materials with different electrical properties. Conventional narrowband radar systems operate with modulated carriers and use a typical band width of 10% [30], whereas UWB radars operate with a bandwidth greater than 25% and transmit short high power pulses [12]. The nature of operation of UWB radar gives it some distinct advantages over narrower band systems including; precision distance measurements due to the very short length of the pulses, good energy efficiency allowing its use in light, mobile battery operated sensors and reliable operation in multipath and cluttered environments [31].

UWB radar has many potential applications. Initially UWB radar was the preserve of the military in the form of long range tracking of missiles *etc.* more recently many other applications have been identified, due to its ability to penetrate walls, ground, ice, mud concrete and the human body. Nowadays the most active area of UWB radar research is that of short range imaging. This includes using Ground Penetrating Radar (GPR) for humanitarian de-mining and non-invasive archaeological investigation, through wall imaging and medical applications [32]. The latter includes the remote monitoring of vital signs; heartbeat, breathing etc. and the imaging of various organs; e.g. brain, heart and chest (Breast cancer detection) [33].

The short pulse type operation and therefore antenna design considerations for UWB radar systems are similar to that of impulse radio and so the same requirements apply.

However there are additional design criteria: Depending on the medium through which the antenna is to transmit, dielectric loading of the antenna may have to be taken into account. If the antenna is to be used in an array the way it reacts to the antennas around it is also an issue as may be the geometrical size of the antenna.

1.2.3 Geolocation and Sensor Networks

For sensor networks and UWB Radio Frequency ID (RFID) knowing the exact location of objects is critical. Unlike ranging, geolocation is the exact pinpointing of an objects location in space. This is accomplished by positioning a number of passive receivers around the space within which objects are to be tracked. These monitor signals from any number of active tags which transmit ID pulses at regular time intervals. Comparing the timings at which each passive sensor receives these pulses allows the position of the tag to be found. As these tags must be as small as possible and battery powered and the propagation pathway will be far from ideal, the low power usage and multipath robust nature of UWB systems makes them an ideal candidate for this application. For the same reasons a UWB radio channel is an ideal method of transferring data between nodes of a sensor network.

1.2.4 A Final Thought on UWB Technology

UWB and wideband systems have had a chequered history with many false starts. Even now political and technological hurdles still have to be overcome before the technology becomes widely accepted and commercially successful. An example of the problem faced being the recently failed attempt by the IEEE work group 802.15.3a to create a standard for Personal Area Networks (PANs). While many applications for UWB technology have been identified herein the list is by no means exhaustive. Many military applications are necessarily classified and as UWB is such a new technology there are surely many applications that are yet to be identified.

1.3 Thesis Overview

Chapter 2 examines the fundamental principles used to analyse the performance of UWB antennas. As well as defining a number of terms and definitions used in the subsequent chapters. Chapter 3 begins with a literature review of existing UWB antenna designs and concludes with the optimisation and analysis of a trident fed monopole via Finite Difference Time Domain (FDTD) simulation and measurement. Chapter 4 details the wide-slot antenna's development using the University of Bristol's in house FDTD code. The designs for a cavity and a compact feed are then presented and the resulting antenna is analysed to access its suitability for use in the imaging system.

Chapter 5 presents a novel method of producing hybrid, orthogonal curvilinear meshes with the aim of simulating a section of the Bristol imaging array. The meshing procedure involves producing a volume of orthogonal curvilinear mesh that allows Cartesian and spherical based meshes to be linked. The resulting orthogonal, hybrid lattice can be simulated using a curvilinear-coordinate based FDTD program, with the same efficiency as a standard cartesian based simulation with the same number of nodes. The chapter goes on to examine a two antenna simulation that is used to test the ability of the method to simulate the imaging array.

The first novel contribution of this work is the design of the wide-slot antenna and the hybrid-meshing technique. Based on an existing design, this antenna was heavily modified and optimised to operate in the imaging system. The cavity and bent feed were also designed specifically for this application. The second major novel contribution is the technique developed to construct the curvilinear, orthogonal mesh in Chapter 5 and the way in which this mesh is then used as a basis to construct the rest of the hybrid mesh.

REFERENCES

[1] Kraus J. D., "Heinrich Hertz – Theorist and Experimenter", IEEE Transactions on Microwave Theory and Techniques, vol. 36, no. 5, May 1988, pages(s) 824-829.

[2] Nilavalan R., Hilton G.S., Benjamin R., "Wideband printed bowtie antenna element development for post reception synthetic focusing surface penetrating radar", Electronics Letters, Volume 35, Issue 20, 30 Sept. 1999 Page(s):1771 - 1772.

[3] Lodge O., "Electric telegraphy", US Patent 609,154, August 16, 1898.

[4] Thrower K.R., "History of tuning" 100 Years of Radio, 1995, International Conference on, 5-7 Sep 1995 Page(s):107 – 113.

[5] Schantz H. "The art and science of ultrawideband antennas", Artech House, Norwood, MA, 2005.

[6] Emerson D.T., "The work of Jagadis Chandra Bose: 100 years of millimeter-wave research", Microwave Theory and Techniques, IEEE Transactions on, Volume 45, Issue 12, Part 2, Dec. 1997 Page(s):2267 – 2273.

[7] Corazza G.C., "Marconi's history [radio communication]" Proceedings of the IEEE, Volume 86, Issue 7, July 1998 Page(s):1307 – 1311.

[8] Marconi G., "Transmitting Electrical Signals", US patent 586,193, July 13, 1897.

[9] Bondyopadhyay P. K., "Guglielmo Marconi - The father of long distance radio communication - An engineer's tribute" European Microwave Conference, 1995, Volume 2, 25th Oct. 1995 Page(s):879 – 885.

[10] Belrose J. S., "Fessenden and Marconi: Their Differing Technologies and Transatlantic Experiments During the First Decade of this Century", IEE International Conference on 100 Years of Radio, 5-7 September 1995, page(s) 32-43.

[11] Belrose J.S., "A radioscientist's reaction to Marconi's first transatlantic wireless experiment-revisited", Antennas and Propagation Society International Symposium, 2001. IEEE, Volume 1, 8-13 July 2001, vol.1., Page(s):22 – 25.

[12] Allen B., Dohler M., et al (Editors), "Ultra-Wideband Antennas and Propagation for Communications, Radar and imaging", Wiley, Chichester, 2007.

[13] Lindenblad N.E., "Wide Band Antenna," U.S. Patent 2,239,724 (April 29, 1941).

[14] Schantz H.G., "A brief history of UWB antennas", Ultra Wideband Systems and Technologies, 2003 IEEE Conference on, 16-19 Nov. 2003, Page(s):209 – 213.

[15] Colson S., Hoff H., "Ultra-wideband technology for defence applications" Ultra-Wideband, 2005 IEEE International Conference on, 5-8 Sept. 2005, On page(s): 615-620.

[16] Win M.Z., Scholtz R. A., "Ultra-wide bandwidth time-hopping spread-spectrum impulse radio for wireless multiple-access communications" Communications, IEEE Transactions on, Volume 48, Issue 4, April 2000, Page(s):679 – 689.

[17] Craddock I.J., Nilavalan R, Leendertz J., Preece A., Benjamin R., "Experimental investigation of real aperture synthetically organised radar for breast cancer detection", Antennas and Propagation Society International Symposium, 2005 IEEE, Volume 1B, 2005, Page(s):179 – 182.

[18] U.S. 47 C.F.R. Part 15 Subpart F § 15.503d Ultra-Wideband Operation (Oct 1, 2003 edition).

[19] Federal Communications Committee, First report and order 02-48, 2002.

[20] Runkl, P., McCorkle J. Miller T., Welborn M., "DS-CDMA: the modulation technology of choice for UWB communications", Ultra Wideband Systems and Technologies, 2003 IEEE Conference on, 16-19 Nov. 2003, Page(s):364 – 368.

[21] Daniels D., "Ground-Penetrating Radar", Institution of Electrical Engineers, 2004.

[22] Benjamin R., Craddock I.J., Hilton G.S., Litobarski S., McCutcheon E., Nilavalan R., Crisp, G.N., "Microwave detection of buried mines using non-contact, synthetic near-field focusing" Radar, Sonar and Navigation, IEE Proceedings on, Volume 148, Issue 4, Aug. 2001, Page(s):233 – 240.

[23] Conyers L.B., "Ground penetrating radar for archaeology", Altamira press, 2004.

[24] Hagness S.C., Taflove A., Bridges, J.E.;Two-dimensional FDTD analysis of a pulsed microwave confocal system for breast cancer detection: fixed-focus and antenna-array sensors, Biomedical Engineering, IEEE Transactions on, Volume 45, Issue 12, Dec. 1998, Page(s):1470 – 1479.

[25] Craddock I.J., Nilavalan R, Leendertz J., Preece A., Benjamin R., "Experimental investigation of real aperture synthetically organised radar for breast cancer detection", Antennas and Propagation Society International Symposium, 2005 IEEE, Volume 1B, 2005, Page(s):179 – 182.

[26] Peyrot-Solis M. A., et al, "State of the Art in Ultra-Wideband Antennas", Electrical and Electronics Engineering, 2005 2nd International Conference on, 7-9 Sept. 2005, Page(s):101 – 105.

[27] Sholtz A., Pozar D. M., Namgoong W., "Ultra-Wideband Radio", EURASIP Journal on Applied Signal Processing, Hindawi Publishing Corporation, 2005.

[28] Popescu D.C., Yaddanapudi P., Kondadasu R., "OFDM versus time-hopping in multiuser ultra wideband communication systems" Vehicular Technology Conference, 2005 IEEE 61st, Volume 2, 30 May-1 June 2005 Page(s):1406 - 1410.

[29] Curto S., John M., Ammann M.J., "Groundplane Dependent Performance of Printed Antenna for MB-OFDM-UWB", Vehicular Technology Conference, 2007. IEEE 65th, 22-25 April, 2007, Page(s):352 – 356.

[30] Immoreev I.I., Fedotov P.G.S.D.V., "Ultra wideband radar systems: advantages and disadvantages", Ultra Wideband Systems and Technologies, 2002. Digest of Papers. 2002 IEEE Conference on21-23 May 2002 Page(s):201 – 205.

[31] Fontana, R.J., Foster L.A., Fair, B., Wu D., "Recent Advances in Ultra Wideband Radar and Ranging Systems", Ultra-Wideband, IEEE International Conference on 24-26 Sept. 2007 Page(s):19 – 25.

[32] Yarovoy A.G., Ligthart L.P., "UWB Radars: Recent Technological Advances and Applications", Radar Conference, 2007 IEEE, 17-20 April 2007, Page(s):43 – 48.

[33] Staderini E., "UWB Radars in medicine", IEEE AESS Systems Magazine, January 2002.

Chapter 2 Basic Antenna Elements

2.1 Introduction

There are a number of ways in which the performance of an antenna can be characterised. This chapter gives an introduction to the basic architecture of a generic half wavelength dipole antenna before going onto give a description of the characterization methods that will be used in this thesis, giving definitions of some of the more technical jargon.

2.2 Antenna Architecture and Operation

An antenna can be thought of as a transitional region between a waveguide and free space allowing guided electromagnetic energy to be radiated or conversely a free space wave to be received (converting electrons into photons and vice versa). The transition between these two regions is achieved by virtue of the fact that an antenna acts as a transformer between the impedance seen at the terminals of the waveguide feeding the antenna and that of free-space [1]. Antennas realize this transformation by guiding charges along specially shaped metallic conductors and it is the acceleration (and deceleration) of these charges that causes the radiation [2]. The basic radiation equation is given by;

$$\dot{I}L = Q\dot{\upsilon} \tag{2.1}$$

Where $\dot{I}$ = time changing current (As^{-1}), L = length of current element (m), Q = charge (C) and $\dot{\upsilon}$ = acceleration of charge. The radiation produced is perpendicular to the direction of the current and the radiated power is proportional to the square of $\dot{I}L$ (or $Q\dot{\upsilon}$). From equation 2.1 it can be seen a time varying current as well as an accelerated charge, radiates. For the short pulses and transient responses seen in UWB systems it is often more relevant to focus on charge [2].

2.2.1 An Example Antenna: The Half Wavelength Dipole

One of the simplest antenna is the half wave, centre fed, dipole. This antenna is constructed from two armatures each a quarter of a wavelength long, arranged in a linear fashion with each connected to one terminal of a transmission line. In a transmitting configuration (Figure 2.1) a time varying, electromagnetic wave propagates from the source along the transmission line to the central feed point of the antenna. As the armatures are connected to different terminals one is driven positively and the other negatively (they are 180° out of phase). The result of this is that the current moves in the same direction along both armatures and as has already been seen (Equation 2.1) a time varying current results in radiation [3].

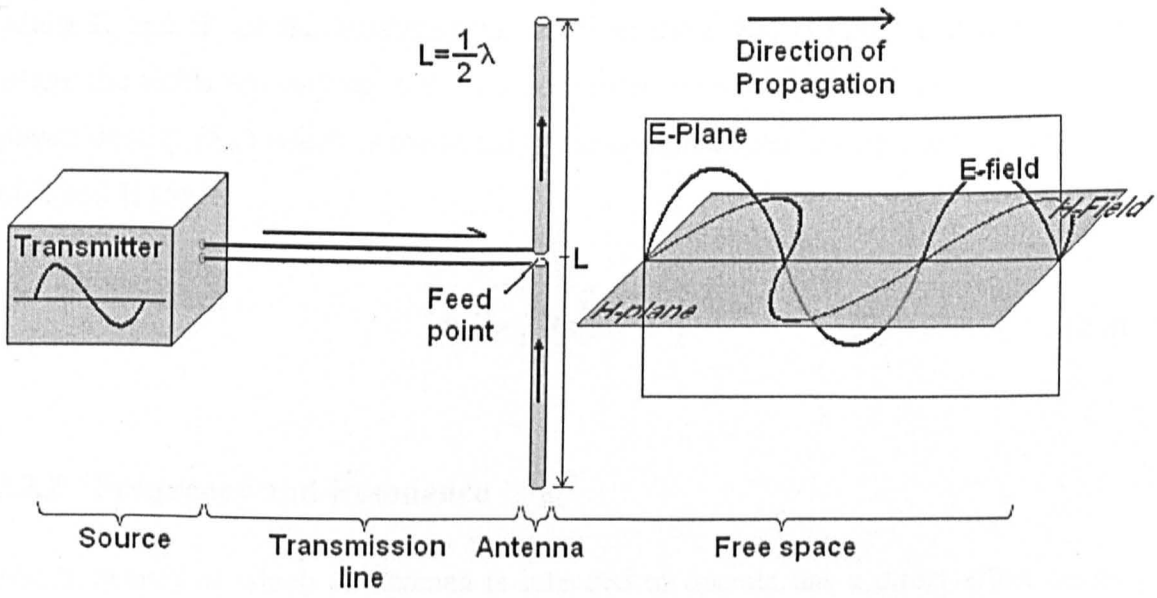

Figure 2.1 A dipole antenna in a transmitting configuration [2].

In receiving mode the process is reversed; the electromagnetic wave inducing a current in the armatures which propagates down the transmission line to be picked up by a receiver.

The electromagnetic wave radiated by the dipole and indeed any radiation source, is made up of two components that are both orthogonal to each other and the direction of

propagation (Figure 2.1). The Electric or E-field acts in the E-plane which is defined by and in the same orientation as the direction of charge acceleration and the direction of propagation. The Magnetic or H-field acts in the H-plane which is orientated at 90° to the E-plane. As both field components act at 90° to the direction of travel they are known collectively as a transverse electromagnetic wave [4].

The power associated with an electromagnetic wave in the far field region (see Section 2.2.3) is given by the quantity known as the "Poynting vector", the instantaneous value of which (S) is given by the equation [5];

$$\mathbf{S} = \mathbf{E}_i \times \mathbf{H}_i \tag{2.1}$$

where $\mathbf{E}_i$ and $\mathbf{H}_i$ are the instantaneous values of the E and H fields. For applications where the fields are varying with time it is often more desirable to find the average power density (S_{av}) which is found using the complex (phasor) representation values of **E** and **H** [5];

$$\mathbf{S}_{av} = \frac{1}{2}\mathrm{Re}\left[\mathbf{E} \times \mathbf{H}^*\right] \tag{2.2}$$

2.2.2 Frequency and Resonance

The frequency at which an antenna is intended to operate has a direct effect on its geometrical size. The dipole above will radiate most effectively when it is operating at frequency where the wavelength is twice that of the antenna's length. This due to the fact that at this frequency a sinusoidal standing wave is set up in the current along the axis of the antenna with a maximum at the feed point and zero current at the armature ends (Figure 2.2) i.e. the antenna is resonant.

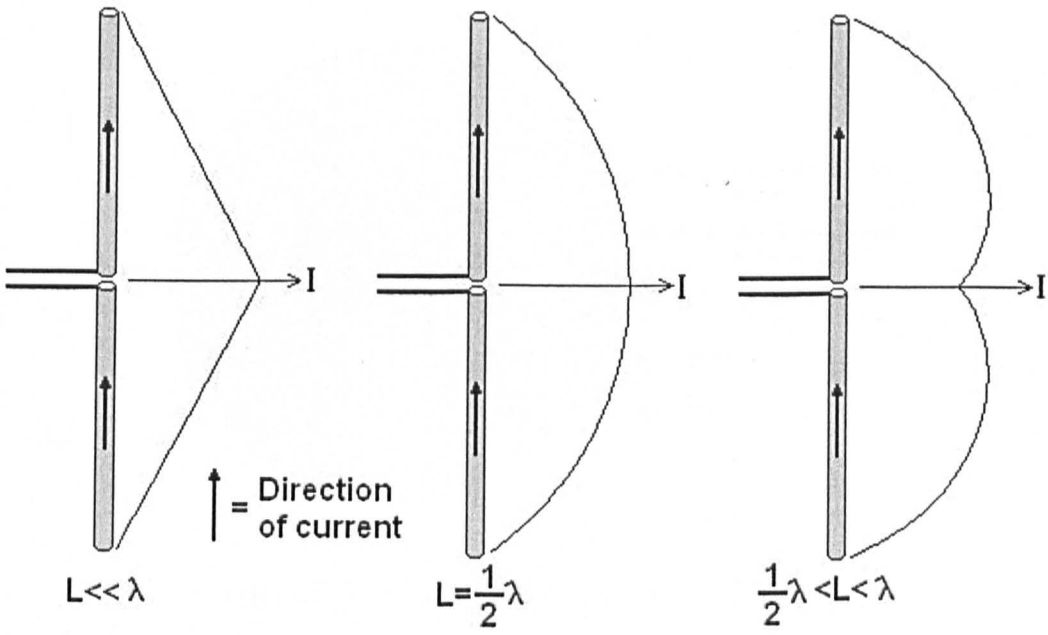

Figure 2.2 The current distribution along dipoles of varying lengths [5]

The input impedance at the terminals of an antenna (Z_{in}), is given by the following expression [5];

$$Z_{in} = (R_L + R_R) + jX_A \tag{2.3}$$

Where R_L is the resistance associated with conduction and dielectric losses in the antenna, R_R is the resistance associated with radiation from the antenna and X_A is the reactance associated with radiation from the antenna. When the antenna is resonant X_A tends to zero. Provided that the feed line has the same impedance as, and so is matched to (see Section 2.4.4), the resonant antenna this will result in all the power from the source being transferred to R_L and R_R resulting in the maximum possible radiation for a given power. Above and below the resonant frequency the antenna is de-tuned and a standing wave cannot form. This is illustrated in the current distribution along dipoles of varying lengths (Figure 2.2). This results in the antenna becoming reactive and energy being stored rather than radiated [5].

2.2.3 Antenna Fields

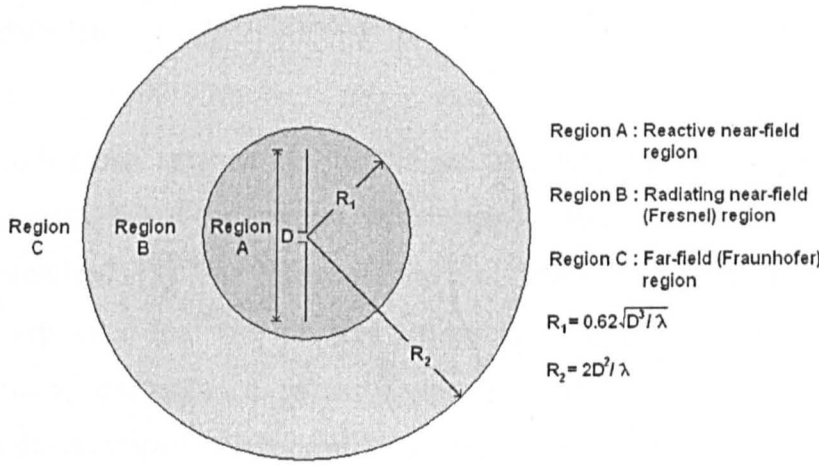

Figure 2.3 Field regions of an antenna [5].

The fields around an antenna are made up of three regions (Figure 2.3). The field region closest to the antenna, known as the reactive near-field, is the region closet to the antenna wherein the reactive field predominates. This region is generally considered to be defined as;

$$R < 0.62\sqrt{D^3/\lambda} \tag{2.4}$$

The second part of the near-field is known as the radiating near-field or Fresnel region and is defined as the region wherein radiating fields are predominant and the angular field distribution is dependent on the radius R. In free space the Fresnel region is generally considered to be defined as;

$$0.62\sqrt{D^3/\lambda} < R < 2D^2/\lambda \tag{2.5}$$

The third region is the far-field or Fraunhofer region wherein the angular field distribution is unaffected by distance from the antenna and as a result it is this region in which radiation patterns are measured (see Section 2.4.2.1). This region is defined as that extending from the boundary of the Fresnel region to infinity [5];

$$R > 2D^2 / \lambda \tag{2.6}$$

2.3 Bandwidth

The bandwidth of an antenna can be defined as "the range of frequencies within which the performance of the antenna, with respect to some characteristic conforms to a specified standard" [5]. The characteristics that define the bandwidth of an antenna are usually separated into two distinct groups namely those which are classed as defining pattern bandwidth i.e. pattern shape, gain and phase and polarization and those which define impedance bandwidth i.e. input impedance and efficiency [2]. For narrow band antennas where pattern characteristics remain unchanged, the impedance bandwidth of an antenna is often sufficient measure. However when it comes to considering UWB antennas a more holistic approach must be taken and ultimately it is the range of frequencies over which the antenna meets a number of desired specifications that determines the bandwidth [1].

In this section the various definitions of bandwidth will be discussed and the various parameters used to define the upper (f_H) and lower (f_L) frequencies of the operational bandwidth will be introduced and their impact and relevance to the definition of bandwidth for a UWB antenna discussed.

2.3.1 Bandwidth Definitions

The simplest way to define the bandwidth (BW) of an antenna is to simply state the width of the frequency band over which the antenna operates:

$$BW = f_H - f_L \tag{2.7}$$

Alternatively it can be defined as a ratio of the upper frequency to lower frequency i.e. $f_H : f_L$ And so an antenna operating from 1 to 2 GHz will have a 2 : 1 bandwidth.

It is sometimes useful to define the bandwidth in terms of the bandwidth centre frequency (f_C). The fractional bandwidth (bw) is given by:

$$bw = \frac{BW}{f_C} \tag{2.8}$$

The result of this calculation can also be expressed as a percentage. The central frequency can also be defined in one of two ways; the first being the arithmetic centre;

$$f_C = \frac{1}{2}(f_H + f_L) \tag{2.9}$$

or alternatively the geometric centre can be found;

$$f_C = \sqrt{f_H \cdot f_L} \tag{2.10}$$

Although sometimes the geometric centre is more applicable to the physics of electromagnetics the arithmetic centre is more widely used [1].

2.4 Defining Bandwidth Frequency Limits

While calculating the bandwidth of a UWB antenna is relatively trivial defining the frequency limits f_L and f_H is not. Below are some of the factors that should be taken into account while defining these limits.

2.4.1 Polarization

The polarization of an antenna is defined as "the polarization (orientation of the E-field component) of the wave transmitted by the antenna at bore-sight" [5]. Observing the time varying E-field vector produced by the dipole (E_I) seen earlier, in a plane orthogonal to the direction of propagation and looking in the direction toward the

antenna, it would be seen that the E-field vector describes a straight line in the orientation of the dipole. This is known as linear polarization (Figure 2.4(a)).

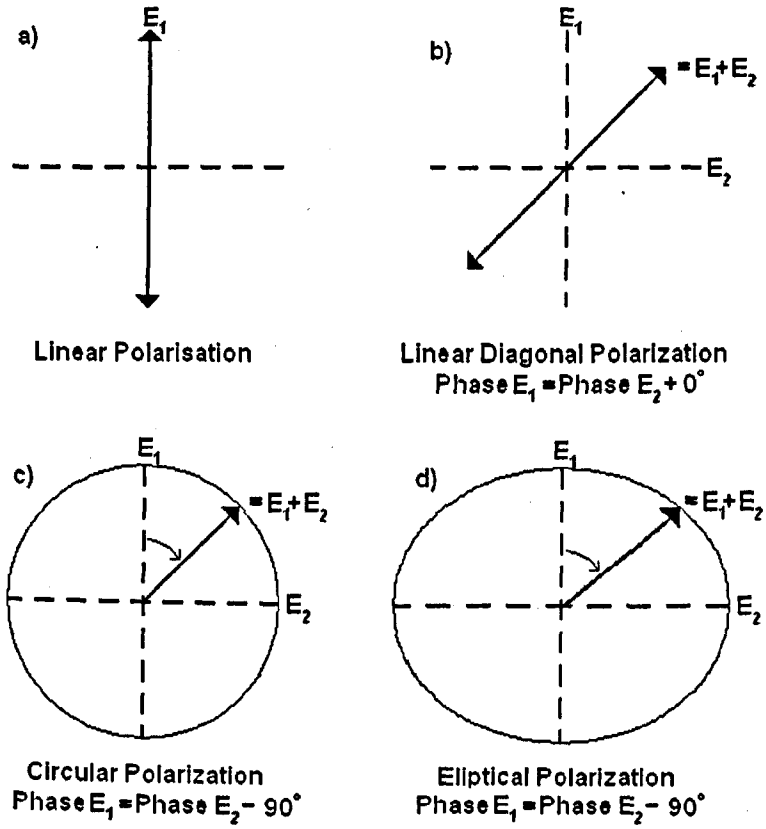

Figure 2.4 (a) Linear, (b) Diagonal, (c) Circular and (d) elliptical polarization states for an electromagnetic wave (direction of travel out of the page) [6]

If two such dipoles were placed orthogonal to one another and fed in phase the E-fields (E_1 and E_2) combine to form a vector would describe a diagonal line. This is known as diagonal or tilted polarisation (Figure 2.4(b)). If the second dipole is fed -90° out of phase with the first then the E-field vector would describe a circle with the vector rotating in a clockwise direction. This is known as right hand or clockwise circular polarisation (Figure 2.4(c)). If the second dipole were fed +90° out of phase with the first the E-field vector would describe an anticlockwise circle, which is known as anti-clockwise or left-hand circular polarisation. The aforementioned examples are special cases of elliptical polarisation (Figure 2.4(d)). In general most

antennas have two E-field components that are not of the same magnitude and so the E-field vector describes an ellipse. This is known as elliptical polarisation and as in the case of circular polarisation it can either be clock-wise or anti-clockwise [6].

As a UWB system usually consists of two identical antennas with a Line Of Sight (LOS) propagation path any variation of polarisation with frequency in one antenna will be matched by the same change in the other. As a result frequency dependent polarisation will have little effect on the system. Of more concern in the instance is misalignment of the antennas resulting in a polarisation mismatch and a loss of power. One scenario when polarisation would be a concern would be when there two different UWB antennas are in the system e.g. a base station transmitting to a remote device. In this case it would be beneficial for both antennas to have a stable polarisation response and f_L and f_H would be dictated by the frequency band where this was the case.

2.4.2 Radiation Patterns

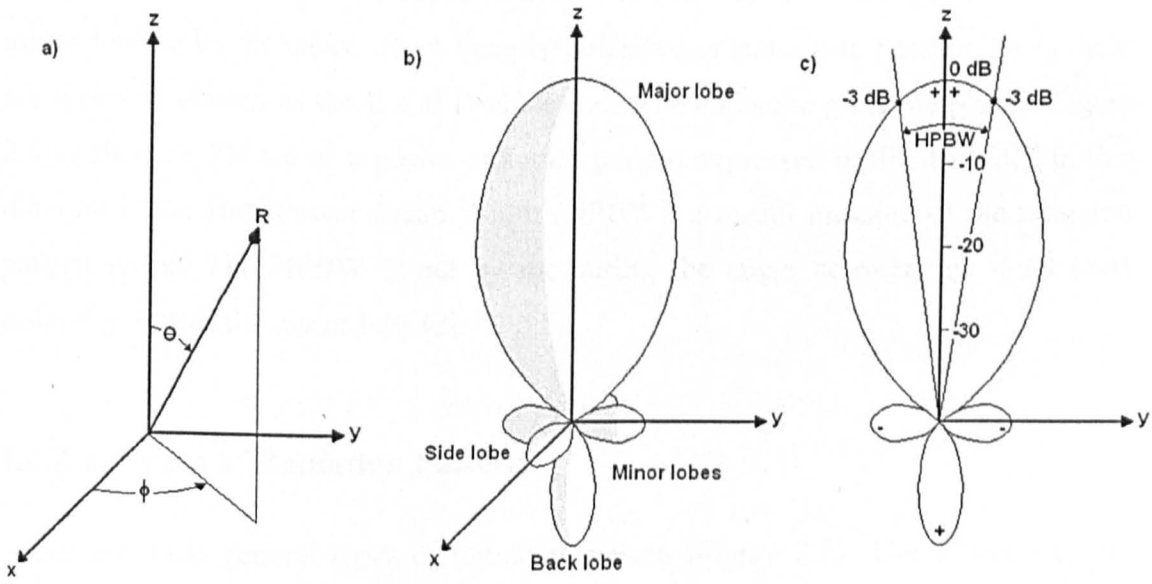

Figure 2.5 (a) The spherical co-ordinate system (b) a 3D power radiation pattern of a directional antenna c) A 2D normalised power radiation pattern expressed in dB, showing the HPBW [2]

A far-field radiation pattern (Figure 2.5(b)) is a measure of the 3D variations of the E-field or power (which is proportional to the field squared) in the far field region. The radiation pattern is given as a function of spherical co-ordinates (Figure 2.5(a)), the value of r being dictated by the field or power [2]. When a pattern is displayed it is usually done in terms of normalised values; for the case of power this is given by:

$$P_n(\theta,\phi) = \frac{S(\theta,\phi)}{S(\theta,\phi)_{max}} \tag{2.11}$$

where $S(\theta,\varphi)_{max}$ is the maximum pointing vector.

A radiation pattern is often made up of a major lobe in which is the direction of maximum radiation. Other lobes are known as minor lobes and are either classed as side lobes which generally have their major axis within 90° of the major lobe or back lobes which are in the opposite direction to the major lobe (Figure 2.5(b)) [5]. Patterns can either be displayed in 3D form or in 2D planes with the major lobe orientated along the z axis (direction of maximum radiation is also known as bore-sight). If a pattern is to be displayed in 2D form then it is usual for two orthogonal cuts of the major lobe to be displayed, for a linearly polarized antenna (see Section 2.4.1) these are typically chosen as the E and H-planes and known as the principle planes. Figure 2.5(c) shows a 2D cut of a power radiation pattern expressed in dB. Included in this diagram is the Half Power Beam Width (HPBW), a useful measure of the radiation pattern shape. The HPBW found by measuring the angle between the -3dB (half power) points of the major lobe [2].

2.4.2.1 Types of Radiation Pattern

There are three general types of radiation pattern (Figure 2.6). The simplest is the hypothetical isotropic pattern which radiates/receives equally in all directions. This pattern is physically impossible because electromagnetic waves are transverse. However this pattern is useful because it serves as a reference point for comparing the patterns of other antenna. The pattern closest to the isotopic that is still physically

possible is the omni-directional pattern that provides coverage at all angles in a particular plane. This is the type of pattern produced by the dipole in Section 2.2.2 and monopoles and is the pattern type chosen for many consumer devices as it offers good all round coverage. The majority of antennas have a directional pattern, that is, they radiate more effectively in one direction than others (the omni-directional pattern is a special type of directional pattern) [1].

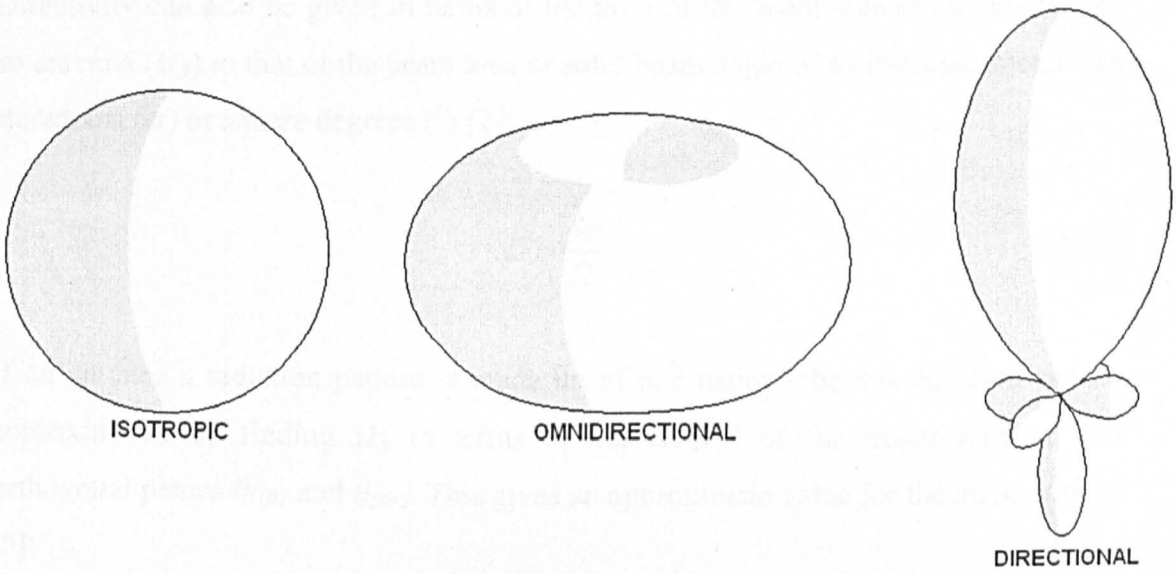

Figure 2.6 Types of radiation pattern

Radiation patterns dictate the bandwidth of UWB systems by virtue of the fact that they are dependent on frequency. Ideally the patterns produced by a UWB antenna will remain constant with frequency in practice some limits must be chosen to dictate when the pattern becomes unacceptable giving the values of f_L and f_H. How these limits are chosen is dependent on the application but could be based on beam width or angle [1].

2.4.3 Directivity and Gain

The directivity (D) of an antenna is a measure of the ability of an antenna to direct energy in a given direction. Antennas with a high directivity have by definition a

highly directive radiation pattern. Directivity is equal to the ratio of the maximum power density $P(\theta,\varphi)_{max}$ (measured at bore-sight) to the average power density $P(\theta,\varphi)_{av}$ radiated by an antenna in it's far field [2];

$$D = \frac{maximum\ power\ density}{average\ power\ density} = \frac{P(\theta,\varphi)_{max}}{P(\theta,\varphi)_{av}} \tag{2.12}$$

Directivity can also be given in terms of the ratio of the beam area in the far-field of an antenna (Ω_A) to that of the beam area or solid beam angle of an isotropic source (4π steradians (sr) or square degrees ($^{\square}$) [2];

$$D = \frac{4\pi}{\Omega_A} \tag{2.13}$$

If an antenna's radiation pattern is made up of one major lobe this equation can be approximated by finding Ω_A in terms of the HPBW of the major lobe in two orthogonal planes θ_{HP1} and θ_{HP2}. This gives an approximate value for the directivity of [5];

$$D = \frac{4\pi}{\theta_{HP1}\theta_{HP2}} \tag{2.14}$$

which, rewritten in terms of degrees and so as to obtain the answer in decibels gives;

$$D = 10\log\left[\frac{41{,}253(\deg^2)}{\theta_{HP1}\theta_{HP2}}\right] \tag{2.15}$$

The Gain of an antenna (G) is an actual realized value and is related to the directivity of an antenna by the efficiency factor (η);

$$G = \eta D \tag{2.16}$$

The efficiency factor takes into account the ohmic losses in the antenna and is given by;

$$\eta = \frac{P_{rad}}{P_{in}} \tag{2.17}$$

where P_{rad} and P_{in} are the radiated power and the input power at the antenna terminals. It should be noted that for very efficient antenna where $\eta \rightarrow 1$ the gain and directivity are approximately equal.

For narrowband antenna efficiency and directivity and therefore gain do not alter significantly across the antenna's operational bandwidth and a single value is given for each parameter. For UWB antennas this is not the case. In most applications it is desirable that the gain remain constant across the required frequency bandwidth as this results in the high and low frequency components of a signal being uniformly transmitted, resulting in minimal distortion of time domain signals [1] (see Section 2.5).

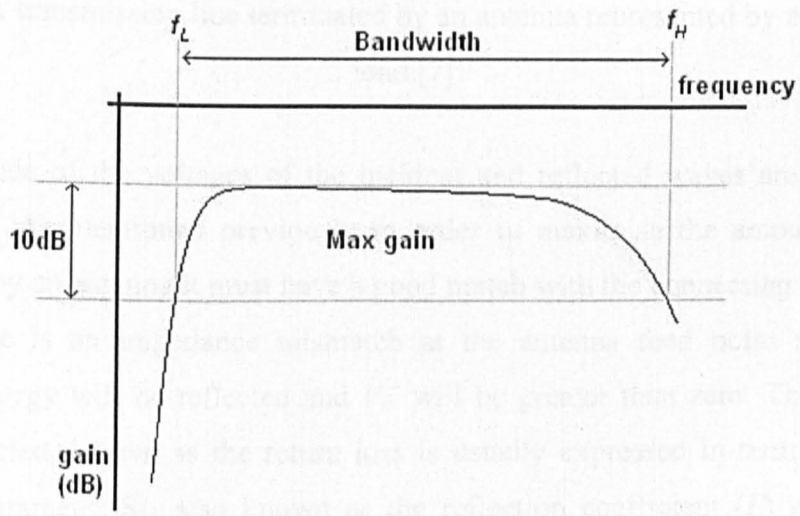

Figure 2.7 Gain versus frequency plot showing -10dB "gain bandwidth" [1]

One method of determining the "gain bandwidth" is to set the frequency limits at the points where the gain falls to a certain level below its maximum. Figure 2.7 shows a gain/frequency plot showing how the frequency limits are found using a typical value of -10dB as the bandwidth limit.

2.4.4 Impedance Bandwidth

An antenna can be thought of as an impedance load (Z_L) on the end of a transmission line with impedance of (Z_0) as in Figure 2.8.

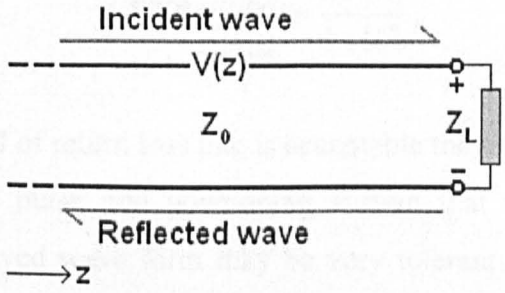

Figure 2.8 A transmission line terminated by an antenna represented by an impedance load [7]

The magnitude of the voltages of the incident and reflected waves are V_0^+ and V_0^- respectively. As mentioned previously in order to maximise the amount of power transmitted by an antenna it must have a good match with the connecting transmission line. If there is an impedance mismatch at the antenna feed point some of the incoming energy will be reflected and V_0^- will be greater than zero. The amount of energy reflected, known as the return loss is usually expressed in terms of either a scattering parameter S_{11} also known as the reflection coefficient (Γ) given by the equation [7];

$$\Gamma = \frac{V_0^-}{V_0^+} = \frac{Z_L - Z_0}{Z_L + Z_0} \tag{2.18}$$

and usually expressed in dB;

$$\Gamma(dB) = 20\log_{10}(\Gamma)$$

Alternatively the return loss can be measured in terms of the Voltage Standing Wave Ratio (VSWR); if there is a mismatch between Z_L and Z_0 the reflected wave will set up a standing wave in the voltage along the transmission line. The ratio of the maximum voltage to the minimum is a measure of the magnitude of the reflected wave and is known as the VSWR [7];

$$SWR = \frac{V_{max}}{V_{min}} = \frac{1+|\Gamma|}{1-|\Gamma|} \tag{2.19}$$

When deciding the level of return loss that is acceptable the value chosen is dependant on application: A low pulse rate positioning system that relies on capturing the leading edge of a received wave form may be very tolerant of mismatch whereas a pulse based radar system, which would interpret the reflected wave as a response from a target and so create a "ghost" image, would not. For most applications a VSWR of less than 2:1 or a return loss of less than -10 dB is chosen. The frequency limits are then dictated by the points at which the return loss of the antenna falls below these values [1] (see Figure 2.9)

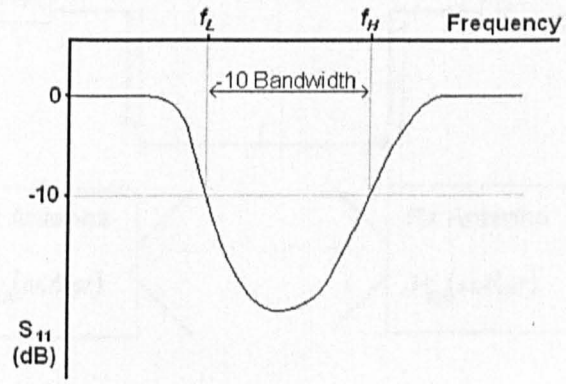

Figure 2.9 The S_{11} of a hypothetical antenna showing the -10 dB bandwidth

Using the impedance bandwidth of an antenna as the sole method for determining bandwidth can be highly deceptive. Energy that is absorbed by the antenna is not necessarily radiated; indeed a 50Ω load on a 50Ω transmission line will have an extremely good return loss but will radiate nothing. As a consequence the impedance bandwidth must be considered in conjunction with the radiation performance of an antenna [1].

2.4.5 Antenna Transfer Function

In order to design an antenna that operates effectively over a large bandwidth all the above factors should be taken into account and a "holistic" approach taken for UWB antenna design. A useful tool in this respect is the system transfer function for a two antenna system. Figure 2.10 shows the typical arrangement for such a UWB measurement which consists of two identical copies of the antenna under test (AUT) orientated such that each antenna has the same face directed toward the other antenna. The transfer responses are found by measuring the S_{21} (transmission loss), usually with a Vector Network Analyser (VNA) [6].

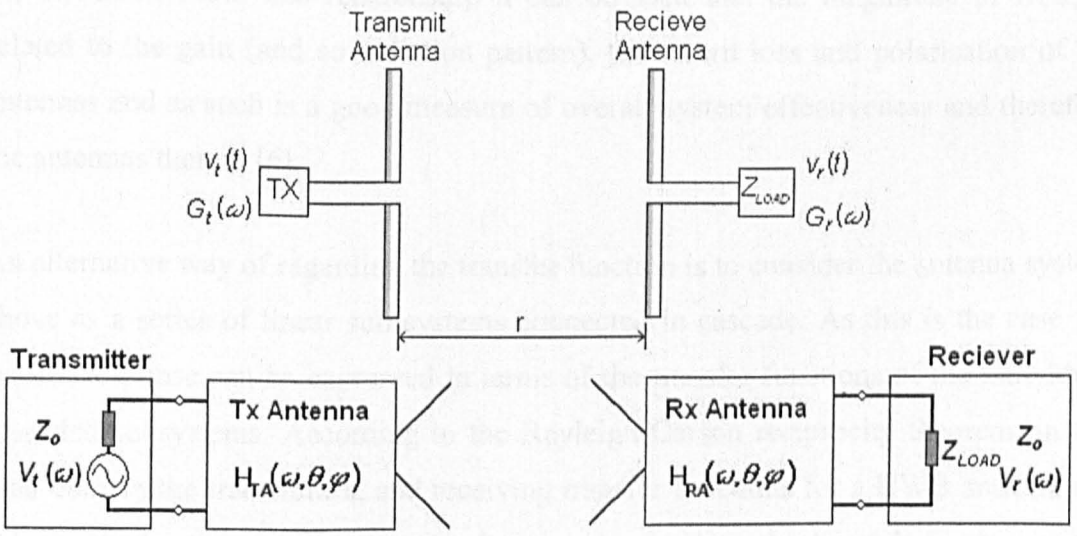

Figure 2.10 Illustration of a transmit/receive antenna system and a block diagram of the system transfer function [6].

The system transfer function ($H(\omega)$) is given by the ratio of the voltage at the receiver ($V_r(\omega)$) to that at the transmitter ($V_t(\omega)$). This can be rewritten in terms of the time average power at the transmitter ($P_t(\omega)$) and receiver ($P_r(\omega)$) ;

$$H(\omega)=\frac{V_r(\omega)}{V_t(\omega)}=\left|\sqrt{\frac{P_r(\omega)}{P_t(\omega)}\frac{Z_{LOAD}}{4Z_0}}\right|e^{-j\varphi(\omega)} \tag{2.20}$$

where Z_{LOAD} is the impedance at the receiver and Z_0 is the transmit antenna impedance. It should be noted that $P_r(\omega)/P_t(\omega)$ can also be given in terms of the frequency dependent Friss equation [6];

$$\frac{P_r(\omega)}{P_t(\omega)}=\left(1-|\Gamma_t(\omega)|^2\right)\left(1-|\Gamma_r(\omega)|^2\right)\,G_t(\omega)\;G_r(\omega)\;\left|\;\rho_t(\omega)\cdot\rho_r(\omega)\right|^2\left(\frac{\lambda}{4\pi r}\right)^2 \tag{2.21}$$

where $\Gamma_r(\omega)$ and $\Gamma_t(\omega)$ are the return losses at the output of the receiving antenna and the input of the transmitting antenna, G_r and G_t are the gains of the receiving and transmitting antenna, $|\,\rho_t(\omega)\bullet\rho_r(\omega)\,|^2$ is the polarisation matching between the transmit antenna and the output of the receiving antenna and r is the distance between the antennas. From this relationship it can be seen that the magnitude of $H(\omega)$ is related to the gain (and so radiation pattern), the return loss and polarisation of the antennas and as such is a good measure of overall system effectiveness and therefore the antennas therein [6].

An alternative way of regarding the transfer function is to consider the antenna system above as a series of linear sub systems connected in cascade. As this is the case the system response can be expressed in terms of the transfer functions of the individual cascaded subsystems. According to the Rayleigh-Carson reciprocity theorem, in the time domain the transmitting and receiving transfer functions for a UWB antenna are not equal; the transmitting transfer function is equal to the time derivative of the receiving transfer function [7];

$$H_{TA}(t,\theta,\varphi)=\frac{\partial H_{RA}(t,\theta,\varphi)}{\partial t} \tag{2.22}$$

or in the frequency domain

$$H_{TA}(\omega,\theta,\varphi)=\frac{j\omega}{c_o}H_{RA}(\omega,\theta,\varphi) \tag{2.23}$$

where $\omega=2\pi f$, f is the operating frequency and c_o is the free-space velocity of light. The system transfer function, in the frequency domain, for two antennas that are separated by distance r is;

$$H(\omega)=H_{TA}(\omega,\theta,\varphi)H_{RA}(\omega,\theta,\varphi)\frac{e^{-jkr}}{4\pi r} \tag{2.24}$$

If these antennas are identical and orientated such that each antenna has the same face directed toward the other antenna this can be rewritten in terms of the receiving transfer function;

$$H(\omega)=H_{RA}(\omega,\theta,\varphi)^2\frac{j\omega e^{-jkr}}{4\pi r c_o} \tag{2.25}$$

The system transfer function has both magnitude and phase components. The requirements for successful transmission of pulses for systems such as UWB radar are that the magnitude be as flat as possible and the phase as linear as possible. If this is not the case then the received pulse will be distorted and dispersed (see next Section). The bandwidth limits can therefore be assigned when either the magnitude of $H(\omega)$ falls a particular level below its maximum or the phase becomes non-linear. Alternatively $H(\omega)$ can be used to synthesise transmitted pulses and the fidelity of the pulse measured (see Section 2.5.3) and the effectiveness of the system gauged in this manner.

2.5 Dispersion and Distortion

In order that a UWB antenna transmit or receive pulses effectively distortion of the pulses must be kept to a minimum. Distortion of the pulses can occur for a number of reasons two of these being a transfer function magnitude that is not constant and nonlinear phase of the antenna transfer function.

2.5.1 Variable Transfer Function Magnitude

If the gain of an antenna and therefore the transfer function varies significantly across the operational frequency range, the different frequency components of a pulse transmitted by the antenna will be radiated at different magnitudes. When this pulse is then received the resulting output will be a distorted version of the original signal. In order to minimise this effect the magnitude of the transfer function should ideally remain constant across the required frequency range [6].

2.5.2 Non-linear Phase and Dispersion

As mentioned previously considering the classic narrowband criteria is often not sufficient to describe the performance of UWB antenna. This is particularly the case for antenna pattern where the gain, which is a scalar property, doesn't take into account variations in phase that can significantly affect the performance of a UWB antenna.

Classical frequency independent antennas such as the log spiral rely on their geometry to maintain their performance over a large band of frequencies. These antennas radiate the high frequency components of a transmit signal from a small portion of their structure while the lower frequency components are transmitted from a larger portion. This results in the effective origin of the transmitted signal or "phase centre" of the antenna, moving with frequency or angle. The consequence of this being a system

transfer function that has non-linear phase behaviour with respect to frequency causing distortion of transmitted pulses. This distortion manifests itself in two ways:

1. Dispersion or stretching of a UWB signal waveform into a longer more distorted waveform. This is typically seen as late time ringing in the transmitted signal (Figure 2.11). Antennas that have this property are known as dispersive antenna.

2. Signal chirp where the high frequency components of the transmitted signal appear at the beginning of the received signal and lower frequency components are prevalent toward the end. [8]

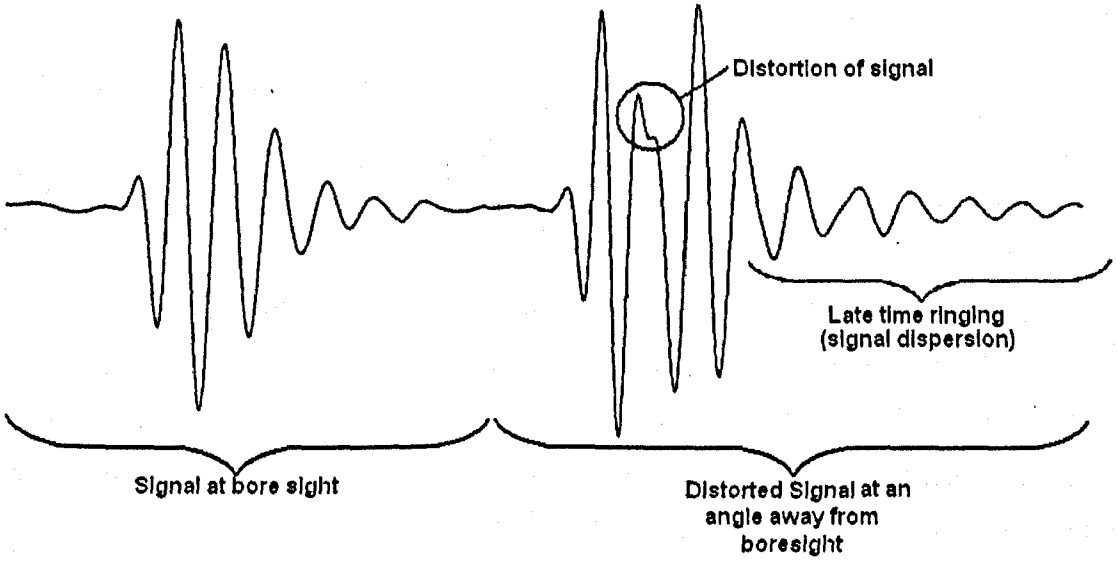

Figure 2.11 Comparison of a non-dispersive, normalised signal transmitted at the bore sight of an antenna pattern with the corresponding normalised signal transmitted away from bore sight which shows significant distortion and dispersion.

2.5.3 Fidelity

The fidelity of a received pulse is a quantity used to evaluate the quality of that pulse. Or in other words the level of distortion in a received signal. It is therefore an

excellent tool for the evaluation of signals synthesised from a measured system transfer function (see Section 2.4.5) in order to gauge the effectiveness of that system and so the antennas contained therein. Quantatively the fidelity F is the maximum magnitude of the cross correlation between the normalized observed response and an ideal response [9].

$$F = \max_{\tau} \int_{-\infty}^{\infty} \hat{e}(t-\tau) \cdot \hat{E}(t) dt \tag{2.26}$$

Where $\hat{e}(t)$ is the observed voltage waveform normalized to unit energy $\hat{E}(t)$ is the normalised reference E-field and τ is the time delay applied to $\hat{e}(t)$. The fidelity of the pulses produced by an antenna or those synthesised from a system transfer function are a good measure of the ability of that system to work effectively. It is generally considered that fidelity greater than 90% is a good result.

2.6 Summary

This chapter has introduced basic antenna concepts and terminology as well as techniques for accessing the performance of UWB antennas. Antenna parameters such as pattern, gain, reflection coefficient (S_{11}) have been introduced and it has been highlighted that unlike the case of narrow band antennas whose performance can be gauged solely on these parameters a more holistic approach must be taken with UWB antenna design. All of the narrow band performance criteria should be taken into account noting how they vary across the operational frequency band but of equal importance is to access the ability of an antenna to effectively radiate and receive UWB signals. This can be accomplished by measuring the signals transmitted by a system directly or measuring system transfer function of two identical AUTs and calculating the fidelity of signals synthesised from that transfer function.

References

[1] Schantz H., "The art and science of ultrawideband antennas", Artech House, Norwood, MA, 2005.

[2] Kraus J. D., "Antennas for all applications", 3rd Edition, McGraw Hill, New York, 2002.

[3] Drabowich S., et al, "Modern Antennas", Chapman and Hall, London, 1998.

[4] Kraus J. D., "Electromagnetics", International Edition, McGraw Hill, New York, 1991.

[5] Balanis C. A., "Antenna Theory", 3rd Edition, Wiley, New Jersey, 2005

[6]Allen B., Dohler M., et al (Editors), "Ultra-Wideband Antennas and Propagation for Communications, Radar and imaging", Wiley, Chichester, 2007

[7] Pozar D. M., "Microwave Engineering", 3rd Edition, Wiley, 2005

[8] Schantz H.G., "Dispersion and UWB antennas", Ultra Wideband Systems, 2004. Joint with Conference on Ultrawideband Systems and Technologies. 2004 International Workshop on, 18-21 May 2004, Page(s):161 – 165.

[9] Lamensdorf D., Susman, L., "Baseband-pulse-antenna techniques", Antennas and Propagation Magazine, IEEE, Volume 36, Issue 1, Feb. 1994 Page(s):20 – 30.

Chapter 3 UWB Antennas for Communications

3.1 Introduction

In general there are two methods of communication that utilise the UWB spectrum; those that split the spectrum up into sub-bands and operate on a multi-band basis or frequency hop e.g. MB-OFDM and fast frequency hopping radio and those that utilise the entire spectrum employing very short pulses e.g. impulse radio and DS – CDMA [1]. Both these methods of operation place considerable demands on an antenna; both techniques demand a wide impedance bandwidth, steady radiation patterns and hence gain in the direction of interest and high radiation efficiency. In addition to this pulsed systems require an antenna with a stationary phase centre and hence linear phase response so as to avoid dispersion and late-time ringing in the received signal. If these antennas are to be used in consumer products they must be cheap to produce. In addition to this if the antenna is intended for use in a fixed device the antenna should be compact and robust, alternatively if the proposed application is that of a mobile device the antenna should have an omni-directional radiation pattern, be of small geometrical size, low profile and be easy to integrate into the device [2]. These requirements make the design of such an antenna one of the most challenging elements of a UWB system

This chapter presents some UWB antennas that have been proposed for use in UWB radio systems. These can be divided up into three main groups; small element electrical antennas, small element magnetic antennas and horn type antennas [3]. This chapter then goes on to give an in depth examination of a square plate, trident fed monopole that has potential for use in UWB radio system.

3.2 Small Element Electrical Antennas

Small element electrical antennas are the physical realisation of the Hertzian ideal dipole and can be thought as being voltage driven with a predominantly electric near-field. These antennas are the largest, most varied group of UWB antennas around today and have their history rooted in the very beginnings of wide-band

communications; Sir Oliver Lodge giving the first descriptions of such antennas in his 1898 patent "Electric telegraphy" [4]. Small element electrical antennas are perhaps some of the most important antennas for communications, their compact size and omni-directional radiation patterns making them ideal candidates for consumer applications. There are a number of families of antennas in this group including; volumetric dipoles and monopoles, discones and their planar, 2D counterparts [3]. Each family will be discussed and a number of examples will be given of antennas that have been proposed for use in UWB communications.

3.2.1 Volumetric Antennas

Volumetric antennas have a three dimensional structure, the very nature of their 3D varying geometry giving this type of antenna a wide impedance bandwidth with stable, omni-directional radiation pattern that provides good gain and phase response across a large frequency range [1].

3.2.1.1 Conical Antennas

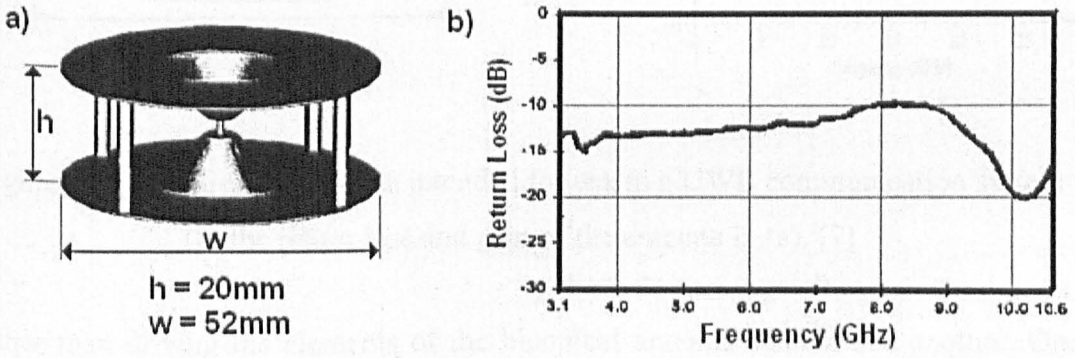

Figure 3.1 (a) a biconical antenna for UWB communications (b) return loss of antenna in (a) [5]

One of the simplest volumetric antennas is the biconical dipole [5]. A biconical antenna is basically made up of two cones with their vertexes placed end to end and

can be thought of as a uniformly tapered transmission line. An example of this type of antenna that has been designed for use in a communication system can be seen in Figure 3.1(a). This particular example is coaxially fed and has plate loading at each end and shorting posts so as to reduce the electrical size of the antenna.

This particular antenna shows a wide impedance bandwidth (Figure 3.1(b)) with a -10dB bandwidth that covers the whole of the UWB spectrum. This antenna also has a relatively stable omni-directional radiation pattern and constant gain across the same frequency range, the gain varying by no more than ±5dB at an angle of 22.5° away from bore sight.

3.2.1.2 The Discone

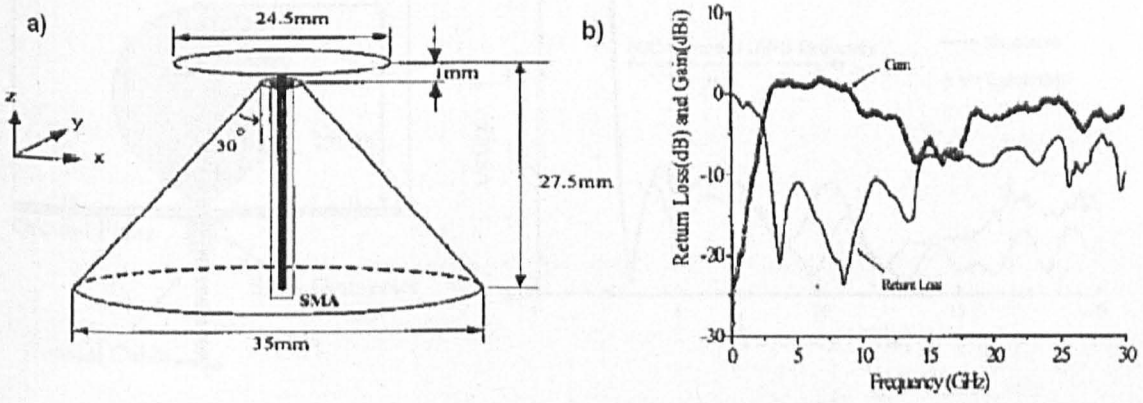

Figure 3.2 (a) A discone antenna intended for use in a UWB communication system (b) the return loss and gain of the antenna in (a). [7]

Rather than driving the elements of the biconical antenna against one another. One element can be driven against a ground plane to give a conical monopole or monocone antenna. This can be done with any dipole antenna to produce an equivalent monopole. Taking this one step further and reducing the size of the ground plane until it becomes electrically small, results in a discone antenna (Figure 3.2 (a)). Discone antennas have previously found use in the UHF band [6] but are now being

investigated for use in UWB applications, including communications and show promising results being compact and relatively easy to manufacture [2], [7], [8], [9].

A discone antenna intended for use in a UWB Communication system can be seen in Figure 3.2(a) [7], [9]. This antenna has relatively stable gain characteristics and a wide impedance bandwidth (Figure 3.2(b)). The antenna has a relatively stable, radiation pattern that remains omni-directional in the x-y plane from 3-11 GHz. In the z-y plane the antenna pattern maintains an approximation to a 1/2 λ dipole pattern across the frequency range but starts to degrade to a multi-lobe pattern by 11 GHz.

3.2.1.3 Bulbous Antenna

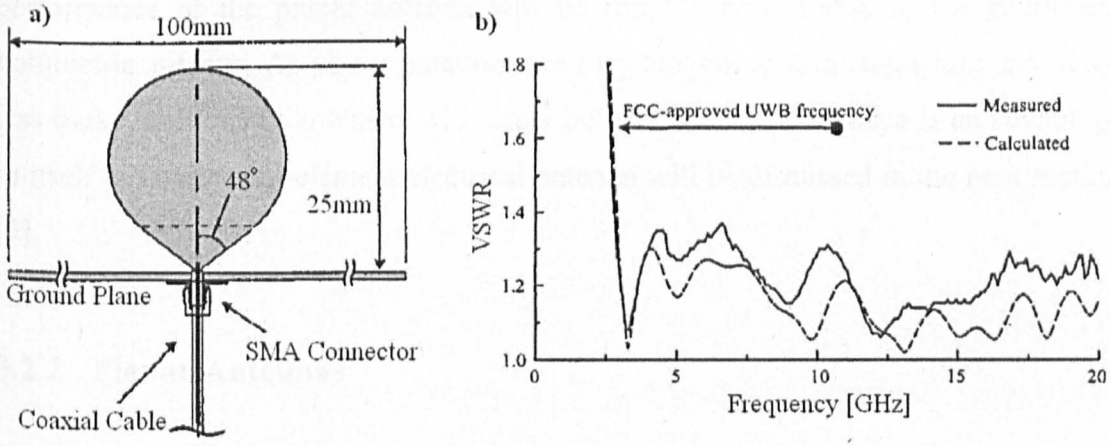

Figure 3.3 (a) A UWB teardrop antenna (b) measured and calculated VSWR for the antenna in (a) [10]

Bulbous antennas have, as their name suggests, a curved 3D structure. Usually this type of antenna is made as a surface-of-revolution i.e. they are made by taking a curve or taper and rotating it about an axis to form a solid surface. The centre frequency of this antenna type is not so much dependent on the element height but more on the circumferential path from the feed to the far side of the antenna. Lindenblad's "Volcano Smoke" antenna intended for use in Short Wave (SW) television transmissions was an early example of such an antenna (Figure 1.5). The very nature

of this type of antenna means that there are many possible element shapes however for ease of manufacture more simple shapes are preferred. Modern bulbous antennas include cylindrical elements [11] and simplified versions of the volcano smoke antenna (teardrop) antenna [10], [12]. An example of a teardrop monopole can be seen in Figure 3.3 (a).

As can be seen from Figure 3.3(b) this antenna has a wide impedance bandwidth and in addition to this it also has very stable, monopole-type, frequency independent radiation patterns which make it a good candidate for UWB applications. The problem with this antenna and indeed all volumetric antennas is that they are difficult to manufacture. In addition to this if a cross section is taken through a volumetric antenna and this is used as a template for a planar, two dimensional antenna then the performance of the planar antenna will be roughly comparable to the equivalent volumetric antenna. As planar antennas are easy and cheap to manufacture and much less bulky, volumetric antennas will rarely be used unless their shape is an advantage in itself. Planar small-element electrical antenna will be discussed in the next section [3].

3.2.2 Planar Antennas

Planar antenna elements are a direct evolution of three dimensional volumetric designs. As mentioned in the previous section this type of antenna offers many advantages over volumetric antennas while offering comparable performance. The majority of antennas of this type are either metal plate antenna or manufactured on Printed Circuit Board (PCB), this means that they are cheap and can be easily integrated into devices. This combined with their omni-directional radiation pattern and good UWB characteristics make them ideal candidates for mobile consumer products [2].

3.2.2.1 Printed Dipoles

Printed dipole antennas consist of two planar 2D elements, printed on a substrate, whose wide bandwidth is a result of their 2D nature. As with the volumetric antenna the performance of printed dipole antennas is dictated by the shape and size of the antenna elements. PCB manufacture allows these antennas to be made precisely, easily and cheaply. The fact that they are printed on a substrate with relative permittivity greater than free space means that they can be made more compact than an equivalent metal plate antenna while operating over the same frequency range. Printed Dipoles [13], [14], [15], [16], [17], [18], [19] were one of the first types of PCB UWB antenna to be proposed and offer frequency stable radiation properties and impedance bandwidth required for UWB operation [3].

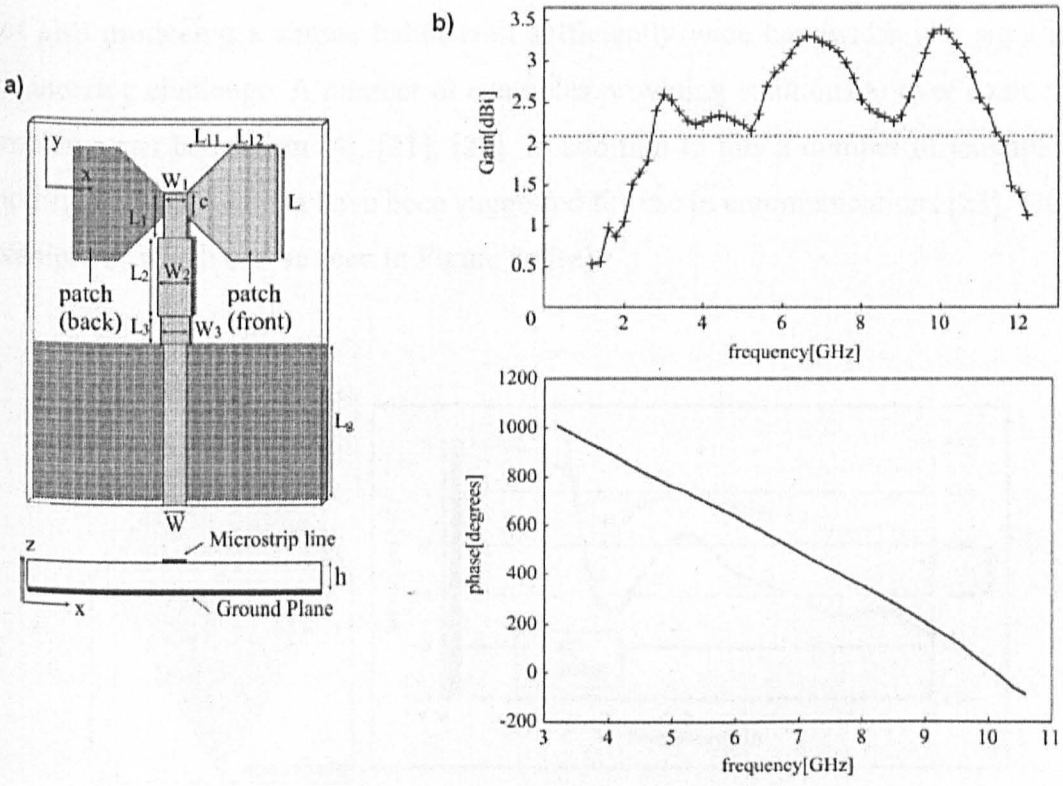

Figure 3.4 (a) a printed bowtie antenna and (b) the antennas peak gain and phase. [20]

Bowtie Antenna

Bow tie antennas are the planar analogues of biconical antennas and consist of two planar isosceles triangle elements placed apex to apex and fed at their centre. This type of antenna was first presented by Lodge in 1898 [4] in the same patent as the biconical antenna. Bow tie antennas of this type show promise in their UWB radiation characteristics but unfortunately they are difficult to match due to their impedance response, which shows significant variations across the UWB band, [3].

Another major drawback of using this antenna type, and indeed all dipoles, is that a dipole is a balanced system whereas most common transmission line types capable of feeding a printed dipole i.e. coax and microstrip are unbalanced. To combat this problem a balun must be used, this not only increases the complexity of the antenna but also producing a simple balun with sufficiently wide bandwidth is a significant engineering challenge. A number of examples providing solutions to over come these problems can be seen in [4], [21], [22]. In addition to this a number of examples of modified bowtie antenna have been suggested for use in communications [23], [20] an example of which can be seen in Figure 3.4 (a).

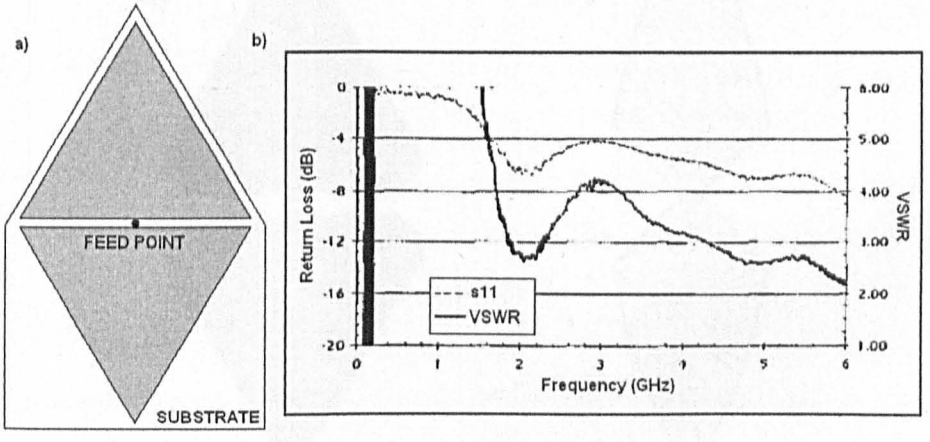

Figure 3.5 (a) schematic of a diamond dipole (b) Return loss and VSWR of the dipole presented in [24]

Figure 3.5 (b) illustrates the bow tie antenna in (a) shows promising UWB characteristics; the gain remaining relatively constant, varying by a maximum of 1.5 dBi, and the phase remaining linear across the 3.1-10.6 GHz UWB frequency band. This is also borne out in the radiation patterns which are relatively stable and of a quasi-omnidirectional nature. The -10dB impedance bandwidth of this antenna is approximately from 3.3GHz -10.5GHz with a few discrepancies at high frequency.

The Diamond Dipole

The diamond dipole design arose from a search for an antenna with good non-dispersive UWB characteristics combined with a good impedance match. A diamond is made up of two isosceles triangles, whose height and base are scaled to be ¼ λ at the centre frequency of interest. Schantz and Fullerton examined a diamond dipole in [20] (Figure 3.5). It was highlighted that while the antenna is non-dispersive and the gain of two such antenna have a quasi-Gaussian response that could prove useful in some applications.

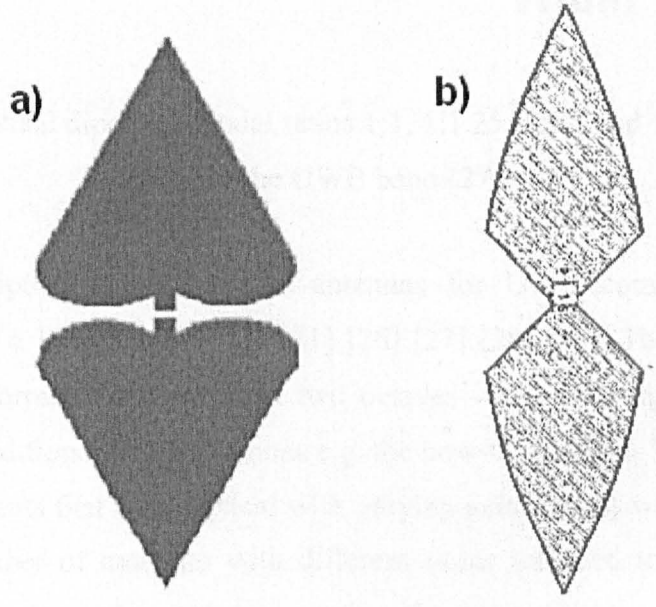

Figure 3.6 Attempts to improve the impedance bandwidth of diamond dipoles; (a) the rounded diamond [25] and (b) the bishops hat antenna [26]

The negative aspect of this antenna's performance is poor impedance matching (Figure 3.5(b)) which never falls below -8dB across the frequency range examined. Various attempts have been made to improve the matching including rounding edges of the antenna next to the feed [25] (Figure 3.6(a)) and the development of the bishops hat antenna [26] (Figure 3.6(b)). The rounded dipole has a -10dB impedance bandwidth of 3GHz from 2.5-5.5GHz and stable radiation patterns from 3-6GHz allowing it to operate in the lower half of the UWB band. The bishop's hat antenna has good matching from +3.5GHz and has a stable dipole type radiation pattern.

Circular and Elliptical Dipoles

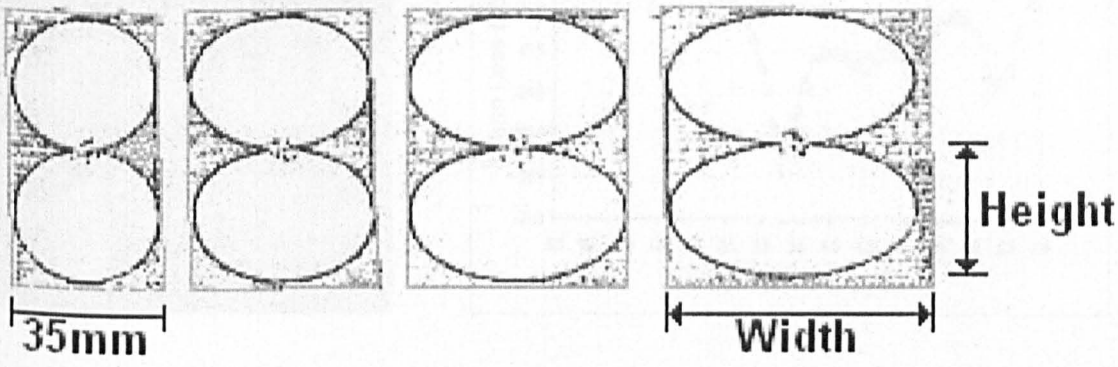

Figure 3.7 Elliptical dipoles, of axial ratios 1:1, 1:1.25, 1:1.5 and 1.75 intended for use in the UWB band [27].

Circular and elliptical printed dipole antennas for UWB communications have recently attracted a lot of interest [4] [21] [26] [27] [28] [29]. These antennas offer good dipole performance over almost two octaves while offering a more compact geometry than traditional UWB antennas e.g. the bow-tie antenna. These antennas are made up of elements that are elliptical with varying axial ratios; width:height. Figure 3.7 shows a number of antennas with different ratios intended to operate at UWB frequencies. It has been found that increasing the axial ratio improves the antenna matching but has a detrimental effect on the uniformity of the radiation pattern. The choice of antenna is therefore dictated by application; lower axial ratios when pattern

is important, higher ratios where matching is critical. For most applications an axial ratio 1.25-1.5 is optimum [27].

Figure 3.8(a) shows an elliptical element dipole that is microstrip fed using a balun transformer (see thining section of microstrip in Figure 3.8(a)). This antenna has a large -10dB impedance bandwidth from 2.5-7+ GHz (Figure 3.8(b)) and maintains a very flat gain between 2-6 GHz (gain and impedance bandwidths extend well beyond these limits with slightly degraded performance.

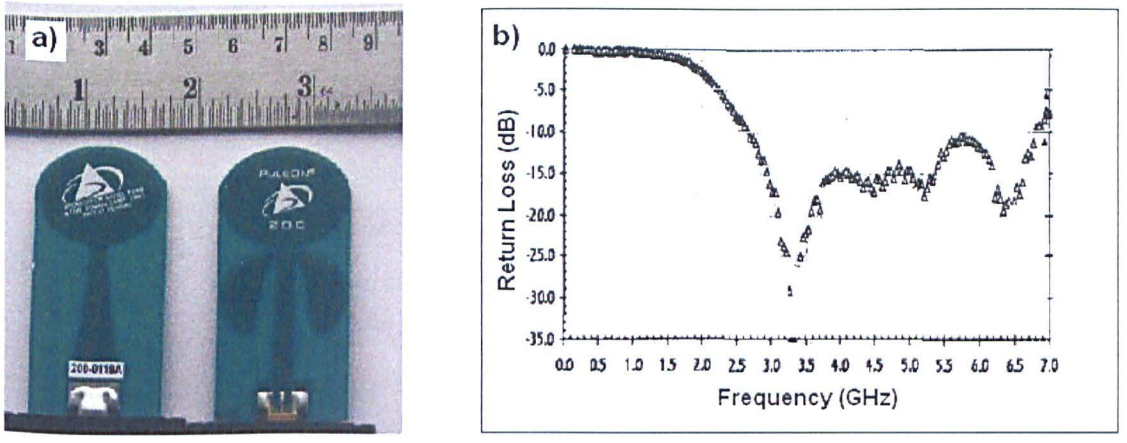

Figure 3.8 (a) A bottom fed planar elliptical dipole and (b) the return loss [21]

As the gain would suggest this antenna has a stable radiation pattern over the UWB band with a typical omni-directional dipole "doughnut". This antenna is intended for use with pulsed systems and transmits pulses well with little distortion [21].

Other Dipole Shapes

The number of designs possible in this class of antenna is almost limitless as virtually any shape imaginable may be used as a planar element [3]. In addition to those antennas discussed above other element shapes that have been suggested for use in UWB communications include; "bell" shaped dipole antenna [30], [31], [32], [33] (Figure 3.9(a)) which consist of two rectangular elements rounded at the feed, "PICA"

(Planar Inverted Cone Antenna) type antennas [34], [35] that have a "tear drop" shape (Figure 3.9(b)) and modified bowtie antennas such as the lotus antenna suggested in [22].

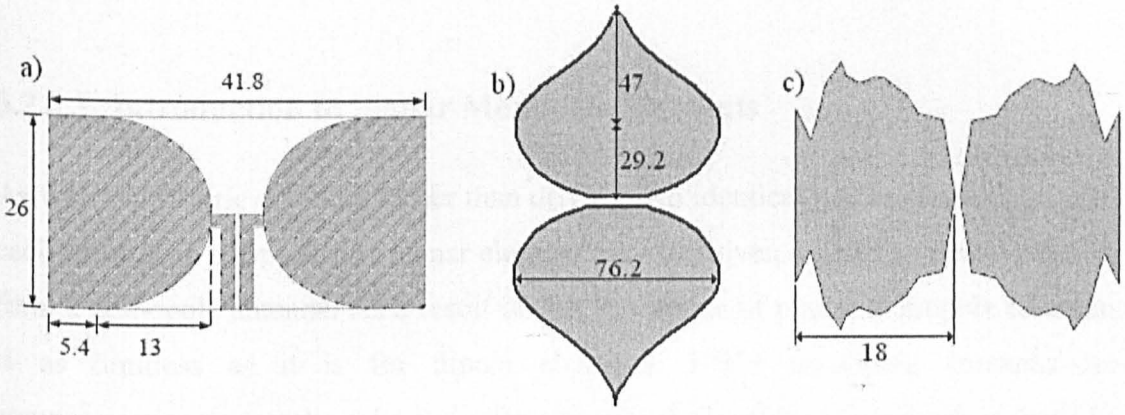

Figure 3.9 (a) A bell dipole [30], (b) a "PICA" Dipole [35] and (c) a dipole whose elements were designed using a genetic algorithm [36].

In addition to this attempts have been made to create an optimised element using genetic algorithms in which a set or population of potential solutions is caused to "evolve" in a Darwinian manner towards a "global optimal solution" [36], [12]. This approach has met with some success; an example of an antenna with elements designed in this way can be seen in figure (Figure 3.9(c)) [36]. The Simulated gain of this antenna remains between 2 and 4.5 dB from 3-12 GHz while the antenna has a measured -10dB impedance match between 3 and 10.5 GHz.

3.2.2.2 Summary of PCB Dipoles.

UWB dipole antennas show some promise in terms of their UWB performance and are cheap and easy to manufacture, however there are a number problems associated with this type of antenna. Firstly there is the fact that these antennas are balanced while the majority of potential feeds in consumer products are unbalanced (coax or microstrip). In order to overcome this a balun must be used [1] increasing the antenna size and complexity. In addition to this dipole antennas must be mounted away from

any metal object or ground plane which may affect their radiation characteristics. These problems mean that this type of antenna is difficult to integrate into consumer devices without making the devices larger and potentially less robust and aesthetically appealing.

3.2.2.3 Introduction to Planar Monopole Elements

As with volumetric antennas rather than driving two identical planar elements against each other as in a dipole, one planar element may be driven against a ground plane to form a monopole antenna. As a result of this the choice of planar monopole elements is as limitless as it is for dipole elements. UWB monopole antennas for communications generally take one of two forms; the traditional approach is that of a metal plate mounted above an orthogonal ground plane and fed from beneath with a coax SMA. Alternatively UWB monopoles are manufactured using PCB technology. The ground plane of antennas constructed in this manner is coplanar with the monopole element. The side of substrate on which the ground plane is printed depends on whether the antenna is microstrip or CPW fed [3].

The next two sections present a number of metal plate and then PCB planar monopoles. A number of examples of simple element shapes will be given for both metal plate and PCB antenna types. This will be followed by some antennas in which the geometry or other aspect of the antenna has been altered in an effort to improve the antenna performance.

3.2.2.4 Planar Metal Plate Monopoles

Planar metal plate monopoles [37], [10], [38], [39], [40], [41], [42], [43] are a direct development of earlier 3D UWB antennas and have radiating elements that are similar to those of PCB planar dipoles. Unlike PCB planar antennas the radiating element is not mounted on a dielectric substrate and as a result dielectric losses are eliminated [13]. Reducing the geometry from three dimensions to two significantly decreases the

manufacturing complexity and size of the antenna compared to their volumetric counterparts while maintaining similar UWB performance [14]. The 3D nature of the monopole and ground and coax feed makes this antenna type impractical for use in mobile applications and integration into PCBs. However for applications where these factors are non-critical such as in a laptop computer or communication base station these antennas are ideal.

Circular Disk Monopoles

As mentioned previously planar monopoles have radiating elements that are similar to those of PCB planar dipoles. One of the simplest examples of this type of antenna is the metal plate circular disc monopole. This type of antenna was first introduced by Honda et al [15] in 1992. More recently this antenna has been investigated by Liang et al [16] for use in UWB communications. Figure 3.10(a) shows the antenna investigated by Liang; The antenna is mounted on a ground plane where L=W=100mm, the gap between the bottom of the antenna element and the ground plane, the feed gap "h" has been set at 0.7mm an optimum value in terms of impedance matching with the antenna.

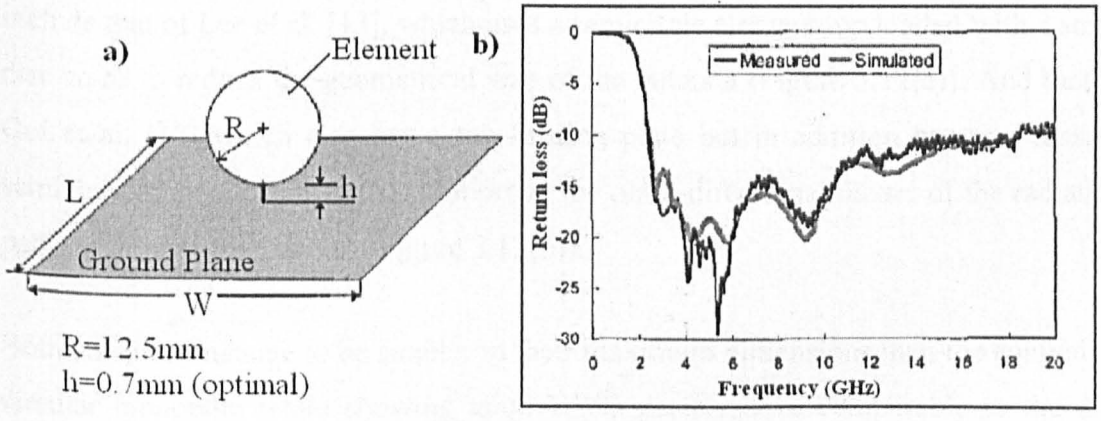

Figure 3.10 (a) the circular plate monopole investigated in [16] and (b) the simulated and measured return loss for this antenna.

The return loss of the disc monopole can be seen in Figure 3.10(b), this figure shows that the antenna has a very large -10dB impedance bandwidth from 2.5 to around 18GHz easily covering the UWB band. The radiation patterns of this antenna remain omni directional between 2 and 10GHz (variations < 5dB) in the plane of the ground with a relatively stable monopole shape (Figure 3.11).

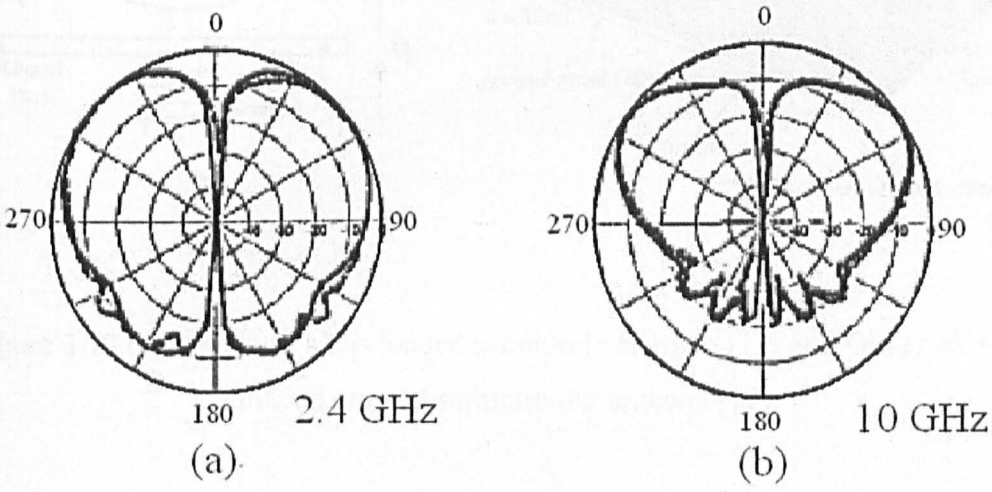

Figure 3.11 Radiation patterns of the disc monopole in [16] at (a) 2.4 and (b) 10 GHz

A number of antenna designs have been proposed based on the above antenna; these include that of Lee et al. [13], which uses a semicircle element top loaded with a small disc so as to reduce the geometrical size of the antenna (Figure 3.12(a)). And that of Ooi et al. [17] which also has a top loading plate but in addition has two crossed semicircular elements in order to improve the omni-directional nature of the radiation patterns at high frequencies (Figure 3.12(b)).

Both antennas manage to be smaller in their maximum dimensions than the equivalent circular monopole while showing good UWB performance comparable to the disc monopole. In addition to this the top loaded crossed semicircular antenna shows an excellent omni-directional pattern showing almost no variation at 3 GHz and varying by 2dB at 6GHz and transmits UWB pulses with minimal distortion and ringing.

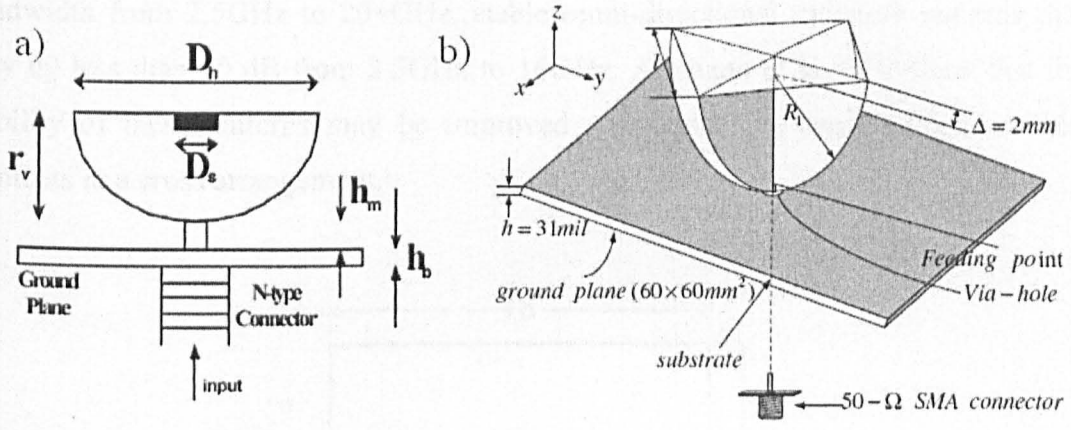

Figure 3.12 (a) Lee *et al.*'s top-loaded semicircle element [13] and Ooi *et al.*'s top loaded crossed semicircular antenna [17]

A number other simple shapes have been investigated for use as metal plate elements; including the monopole equivalent of the bishop hat seen in Figure 3.6 [43] which has an -10dB impedance bandwidth of 3-20+ GHz while the s_{21} of two such antennas transmitting to one another has a magnitude of -20dB at 2.5 GHz which drops to -40dB at 10GHz while the phase is relatively linear across the same frequency range.

Square and Rectangular Elements

One of the element shapes that have seen most research in this class of antennas is variations on the square/rectangle. The simple square monopole shows good UWB omni-directional radiation characteristics while being one of the simplest shapes to construct however it's impedance matching is inadequate for full UWB operation; the -10dB bandwidth of a simple optimised 30mm square element was found to be 2.5-5GHz [18], [19].

A number different ways have been proposed to increase the bandwidth of the square/rectangular monopole. One such method is simply bevelling the bottom

surface of the plate [19], [44]. The antenna proposed by Peyrot-Solis et al. [19] (Figure 3.13) uses this technique to produce an antenna with a -10dB impedance bandwidth from 2.5GHz to 20+GHz, stable omni-directional radiation patterns that vary by less than 10 dB from 2.5GHz to 16GHz. Ammann et al. [19] show that the stability of these patterns may be improved still further by employing two such elements in a cross arrangement.

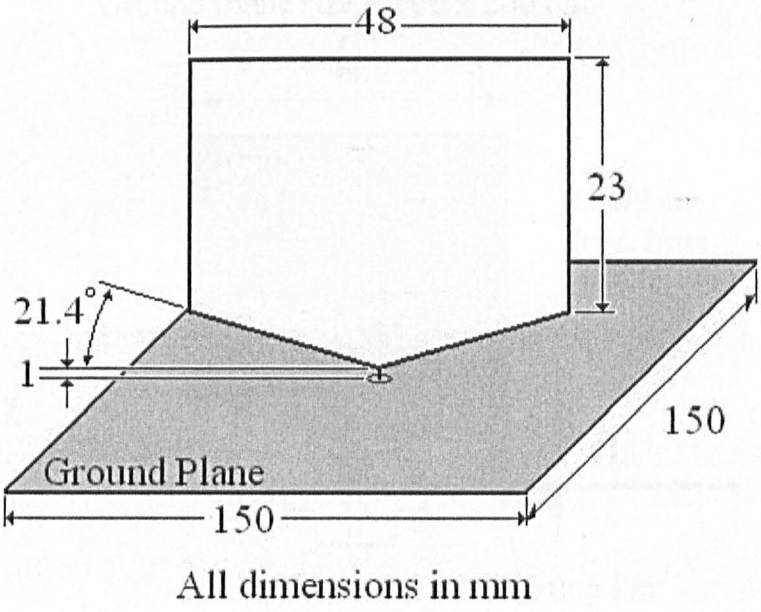

Figure 3.13 A bevelled rectangular plate antenna

Other simple geometric changes have been employed to increase bandwidth include that used by Saou-Wen Su et al. [18], of removing rectangular notches from either the bottom two corners of a rectangular plate, this gives an antenna with a 2-13GHz -10dB impedance bandwidth and a gain that varies from 3dBi at 2GHz to 8dBi at 13 GHz. Removing rectangular notches from and rounding all four corners the plate have also been suggested [45] both methods producing antennas with good UWB performance.

Another method that has been suggested and tested by Ammann and Chen [38], [39] is the use of a shorting pin from one of the corners of a square plate monopole to the

ground. On its own the short improves matching across the entire frequency range while reducing the lower-edge frequency. With an addition of a bevel on the opposite corner (Figure 3.14) the upper-edge frequency is improved dramatically giving an impedance response that remains below -8dB from 790MHz to 10+GHz [39]. The radiation patterns of this antenna are omni-directional at 900MHz, however at 2.4GHz and 5.8GHz there are variations in the pattern greater than 10dB.

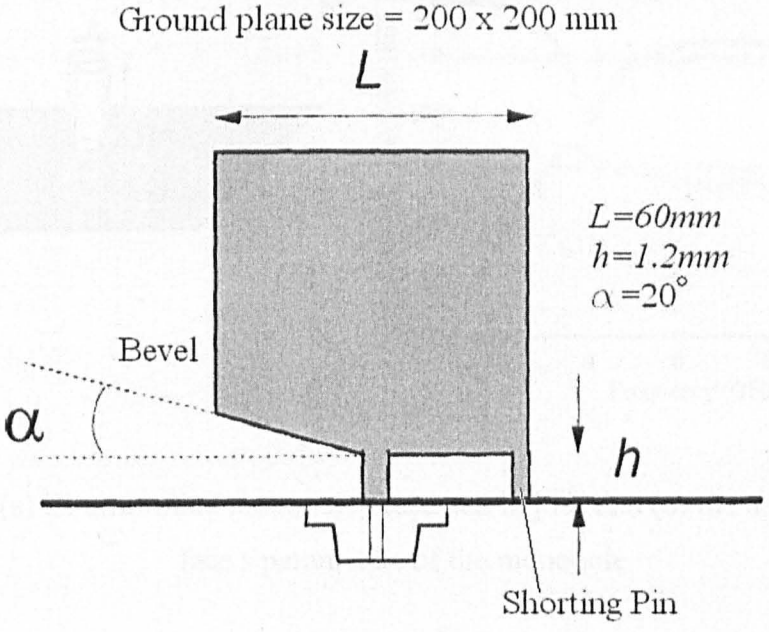

Figure 3.14 The Square plate antenna with shorting pin and bevel presented by Amman and Chen [42]

Certain configurations of multiple feed points along the antennas bottom edge have also been shown to significantly improve this type of antenna's performance [46], [47]. One of the most successful of these designs is that of a trident fed monopole [46] an example of which will be investigated in detail in Section 3.4 of this chapter.

Rolled Antenna Elements

If the size of the square/rectangular monopole antenna is critical then one method of reducing the dimensions, while maintaining performance is to "roll" or fold the

antenna to create a tubular structure this can also lead to improved bandwidths [40]-[42]. An example of this type of antenna has been presented by Chen in [40] (Figure 3.15 (a)). This antenna consists of a rectangular metal plate antenna which has been divided vertically into three sections the outer two of which have been curved back around the centre section.

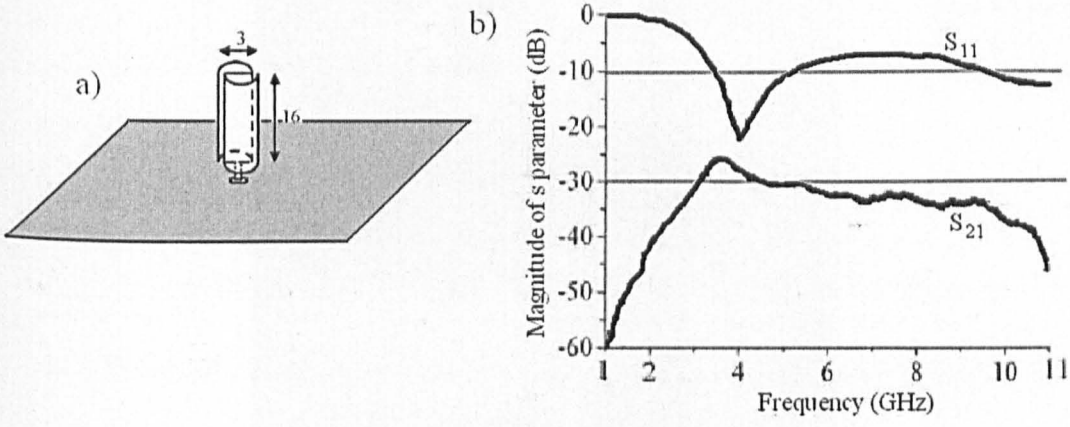

Figure 3.15 (a) Bi-arm rolled monopole presented in [40] and (b) the measured face to face s parameters of the monopole

The impedance matching of this element (Figure 3.15(b)) is below -6dB for the entire UWB bandwidth but there is potential to improve it by optimisation of the radius of the rolled arms. The S_{21} of transmission using two identical elements shows good UWB performance remaining relatively flat from 4-10 GHz when the elements are face to face (Figure 3.15(b)) and showing similar performance when side to side and face to side. This is borne out in the low level of distortion seen in transmitted test pulses [40].

Another interesting example of a folded antenna element can be seen in Figure 3.16 [42]. This antenna consists of a rectangular monopole with a bevelled lower edge mounted above a co-planar counterpoise. The antenna element and counterpoise have been folded such that it could potentially conform to a device the size of a USB memory stick. The impedance matching of this antenna provides a measured VSWR

of below 1:2 from 3 GHz to 11GHz however the radiation patterns lose their omni-directional nature between 6.86 GHz and 10.6 GHz with variations in the pattern of 20 dB at 10.6 GHz.

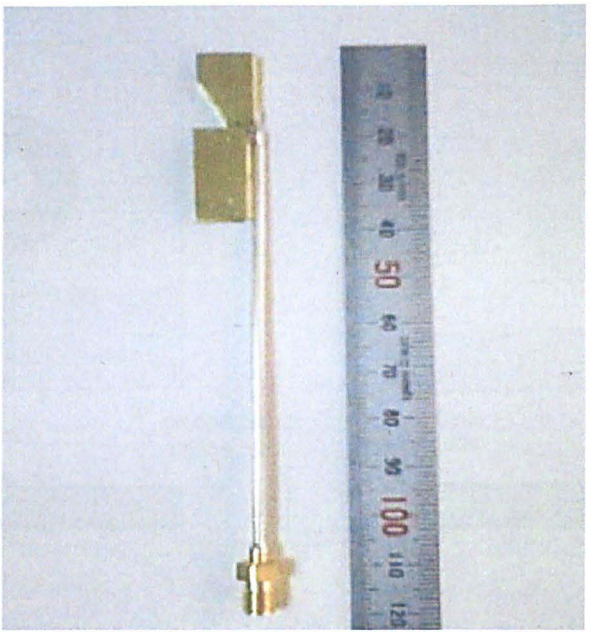

Figure 3.16 The memory size broadband monopole antenna [42]

3.2.2.5 PCB Planar Monopoles

For any monopole the orthogonal ground plane may be may be replaced with a co-planar counterpoise and fed with either a co-planar waveguide or microstrip [2]. If the counterpoise is printed on the opposite side of the substrate to the antenna element then a microstrip feed is convenient (Figure 3.17(a)). If the counterpoise is on the same side as the element a coplanar feed is used [48] (Figure 3.17(b)). This type of wave-guide is often preferred as it is less dispersive than microstrip line.

This type of antenna lends itself to use in mobile handheld devices. The unbalanced feed means that no balun is required, their compact nature and omni-directional UWB characteristics are ideal for the application while their PCB construction means that

they can easily be manufactured in large quantities. The only caveat with PCB planar monopoles is that the antenna element must extend some way beyond the ground plane on which they are mounted [3].

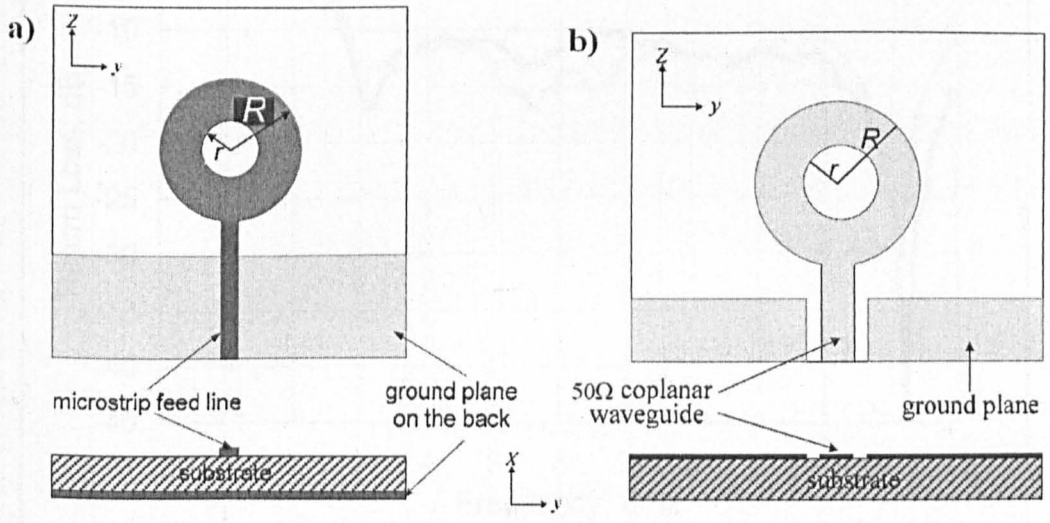

Figure 3.17 A PCB ring monopole element fed by (a) a microstrip and (b) a co-planar waveguide [49] (R = 12.5mm and r = 5mm).

Taeyoung Yang and William Davis introduced an example of a PCB monopole with a semicircular element in 2004 [48] and since then this type of antenna has attracted a lot of interest. The ring monopole antenna in Figure 3.17 is a variation on the standard disc monopole, possible because at these frequencies the currents tend to concentrate themselves at the edges of the element. The impedance characteristics of this antenna and an equivalent disc monopole can be seen in figure Figure 3.18. The impedance bandwidth of both these antennas extends from 3 to above 12 GHz the ring showing slightly better matching in the UWB band.

The radiation characteristics of the PCB ring monopole also show reasonable UWB performance. The radiation pattern is omni-directional at low frequencies but degrades at higher frequencies; a variation in the pattern of approximately 11 dB at 9 GHz. Transmission of a first order Rayleigh pulse with two antennas face to face and

side by side produced a waveform similar to higher order differentiated Rayleigh pulses but in both cases there were some distortions and ringing effects.

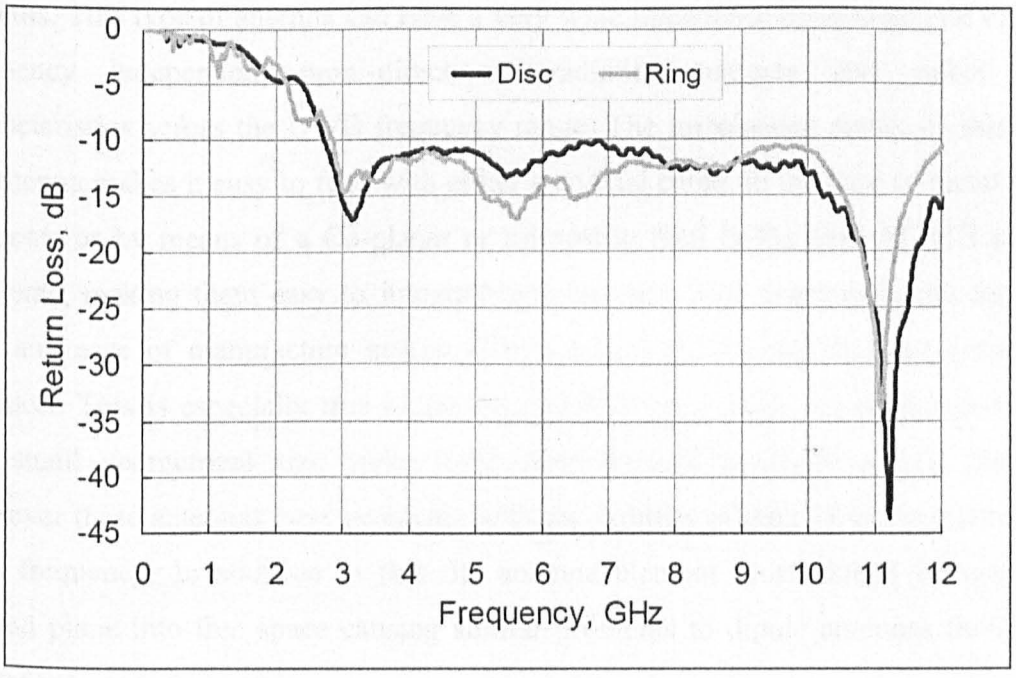

Figure 3.18 The return loss for the CPW fed ring monopole and equivalent disc monopole in [49]

Other element shapes suggested in the literature include elliptical elements [50], [51], those based on rectangular elements with similar alterations as seen in the metal plate monopoles [52], [53], [54] and the PICA [14]. There have also been some elements presented that are based upon a triangular geometry [55], [56]. All these antenna show promising UWB characteristics but all suffer, to one degree or another, with non-omni-directional performance, at higher frequencies.

Frequency notching has also been investigated with this type of antenna. This involves altering the structure of the element resulting in poor matching across a band of frequencies. This can be used to reduce interference with existing systems, such as wireless local area networks (WLAN) [54], [55], [57]. The frequency notching effect is usually achieved by cutting an appropriately shaped slot(s) into the monopole element.

3.2.2.6 Summary of Monopole Antenna

Planar monopole antenna show considerable promise for use in UWB communication systems. This type of antenna can have a very wide impedance bandwidth and exhibit frequency independent omni-directional radiation patterns and stable gain characteristics across the UWB frequency range. The imbalanced nature of this type of antenna makes it easy to feed with either a coaxial cable, in the case of metal plate elements or by means of a Co-planar or microstrip feed in the case of PCB planar elements, making them easy to integrate into devices. This combined with the low cost and ease of manufacture makes these antenna good candidates for consumer products. This is especially true in the case of PCB monopoles whose planar nature and small geometrical size make them ideal for use handheld mobile devices. However these antennas have problems with the stability of their radiation patterns at high frequency. In addition to this the antenna element must extend beyond any ground plane into free space causing similar problems to dipole antennas though to less of an extent.

3.3 Small-Element Magnetic Antennas

Small-element magnetic antennas are physical realisations of the ideal Hertzian magnetic dipole. They are made up of structures that cause the formation of one of more current loops. This type of antenna may be thought of as current driven and having a mainly magnetic near field. This can prove to be an advantage in some situations where the antenna is to be embedded, as magnetic fields couple less readily into nearby objects than electrical fields [3]. Wideband antenna types included in this family are Large Current Radiators (LCRs), loops and slot antennas. In terms of UWB communications by far the most significant group of antennas in this family is that of UWB wide-slot antennas.

3.3.1 LCRs

LCRs are formed from a curved metallic conductor that carries a "sheet" of current along its surface and whose return currents are isolated by a ground plane. LCRs are, by their nature, lossy as any energy radiated by the sheet in the direction of the ground plane is trapped. In terms of loop antennas Shantz has proposed a monoloop [58] for use as a UWB antenna but little performance data has been presented. Possibly the most promising loop antenna is the "clover leaf" antenna which shows non dispersive, broadband characteristics from 3-6 GHz [3].

3.3.2 Wide Slot Antennas

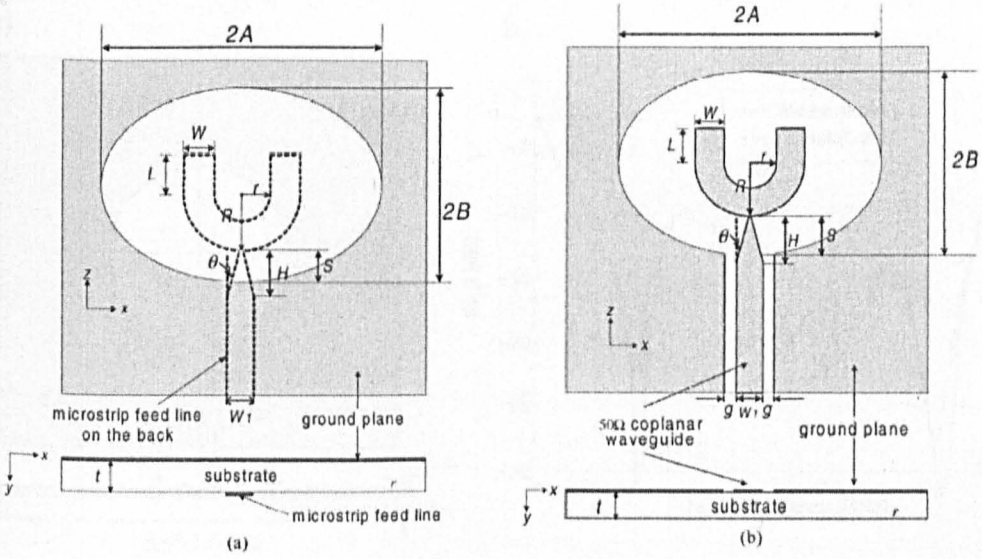

Figure 3.19 An elliptical slot-fed with (a) microstrip and (b) coplanar wave guide [59]

Wide Slot UWB antennas consist of an aperture, whose width and height are of similar size, cut into a ground plane. This type of antenna is constructed using PCB technology, consequently they are usually fed by either a microstrip [60], [61] (Figure 3.19 (a)) or coplanar wave guide (CPW) [62], [63] (Figure 3.19(b)). Although Marchais et al. [64] has also presented an antenna that is fed by a stripline that couples

into wide rectangular slots above and below the stripline. Generally, the preferred choice of feed-line is CPW because of its superior dispersion performance[63].

A number of slot shapes have been proposed for use in such antennas. The most common are elliptical/circular [63], [59], [65], [66] (Figure 3.19 and Figure 3.20(a)) and rectangular/square slot antennas [63], [67], [68], [69] (see the antenna presented in Section 4). Other shapes include a "volcano smoke" shaped slot proposed by Yeo et al [70] and a "tapered-slot-fed annular slot antenna" proposed by Tzyh-Ghuang Ma et al. [71]. An example of a coplanar-fed round slot antenna can be seen in Figure 3.20 (a). The impedance response of this antenna can be seen in Figure 3.20(b) the measured -10dB bandwidth covering from 3-11GHz.

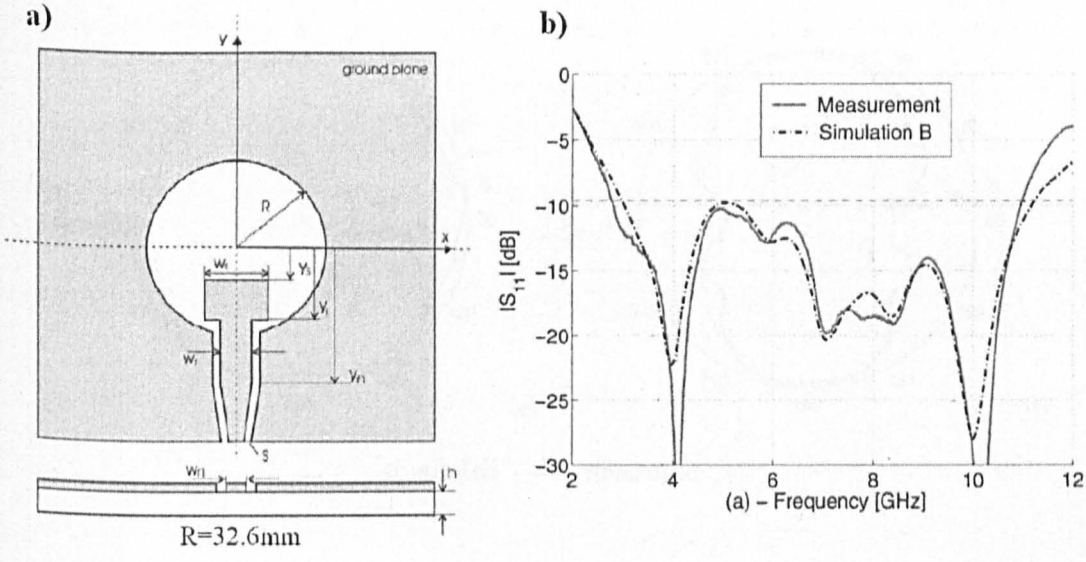

Figure 3.20 (a) a circular CPW fed wide-slot antenna and (b) the simulated and measured s_{11} of the antenna [62].

In the E-plane the radiation patterns of this antenna are bi-directional and symmetrical at low frequencies (Figure 3.21(a)) although this symmetry is lost at higher frequencies (Figure 3.21(b)). In the H-plane the pattern is omni-directional at low frequencies (Figure 3.21(c)) but becomes less so at high frequencies; the pattern varying by 15dB (Figure 3.21(d)). The transmitting transfer function of this antenna at

bore sight is relatively stable, varying by around 10dB in the frequency range 3-11 GHz. The bore sight phase response is linear across the same frequency band, however the position of maximum gain of the antenna is not frequency stable.

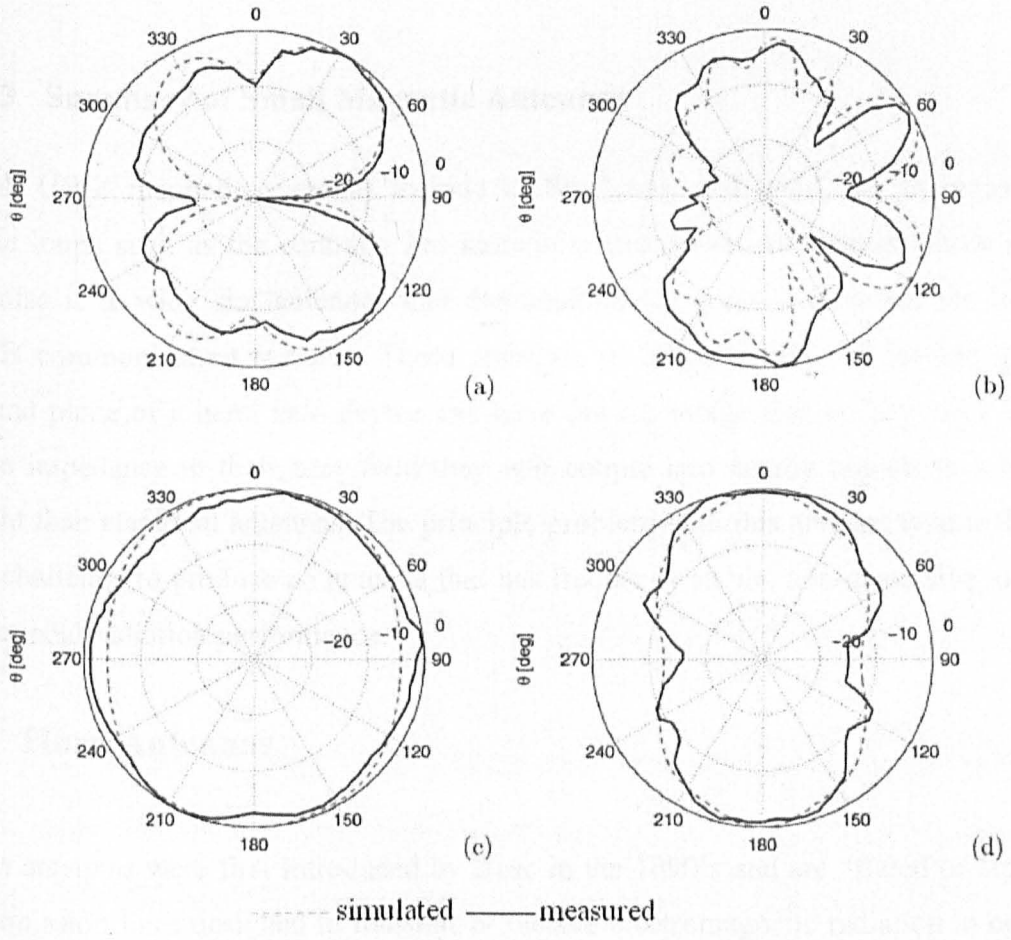

Figure 3.21 The measured and simulated far field radiation patterns of the circular CPW fed wide-slot antenna in [62] with the E-plane pattern at (a) 4GHz and (b) 9GHz and the H-plane at (c) 4GHz and (d) 9GHz.

One of the most critical aspects of feeding a slot antenna is the tuning stub at the end of the CPW or microstrip that allows the wave guide to effectively couple into the slot by giving the correct impedance match. The tuning stubs tend to either mirror the shape of the slot [65], [66] or are forked shaped as in Figure 3.19(a) [63], [64], [59]. As with small electrical antenna attempts have been made to add a frequency notch

feature in an attempt to avoid interference from existing WLAN communication systems at around 5GHz [66]. In wide slot antennas this has been done by using either a fractal tuning stub [60] or by cutting a resonant slot into a circular tuning stub [66], both methods achieving the desired results.

3.3.3 Summary of Small Magnetic Antennas

Small UWB magnetic antennas include LCRs, loops, and wide slot antennas and while loops such as the centrally fed monoloop and cloverleaf antenna show some promise it is wide slot antennas that demonstrate the greatest potential for use in UWB communication systems. These antennas could potentially be located in the ground plane of a hand held device and have the advantage that as they have a low wave impedance in their near field they will couple into nearby objects to a lesser extent than electrical antennas. The principle problem with this antenna type is that it is a challenge to produce an antenna that has frequency stable, non-dispersive, omni-directional radiation performance.

3.4 Horn Antennas

Horn antennas were first introduced by Bose in the 1890's and are "flared or tapered transmission lines designed to transmit or receive electromagnetic radiation in one or more directions. Horn antenna are generally too large, complicated and therefore expensive to be used in consumer products. However just as a three dimensional volumetric antenna may be simplified by using a planar equivalent the same principle maybe applied to horn antennas to produce a planar horn, more commonly referred too as a "Vivaldi" antenna [3].

3.4.1 Vivaldi Antennas

A Vivaldi antenna is made up of a gradually tapered slotline flaring out in a linear or exponential form and was first proposed by Gibson in 1979 [72] and is in a class of

slow leaky, end-fire travelling wave antennas. An example of this type of antenna was investigated by Sorgel et al. [73] can be seen in Figure 3.22.

At different frequencies different parts of the antenna radiate while the size of the radiating part is constant with respect to wavelength. As such the Vivaldi antenna has a theoretically unlimited bandwidth with constant beam width. In practice the radiation pattern of this antenna is dictated by the geometry of the slot which must be carefully designed in order to achieve the desired performance characteristics. If excited conventionally (with a microstrip as in Figure 3.22), the impedance bandwidth of such antennas antenna is dictated by the geometry of the feed region (although more recently (2007) Cerny et al [74] have presented a slot Vivaldi antenna for UWB communications with much more promising impedance characteristics).

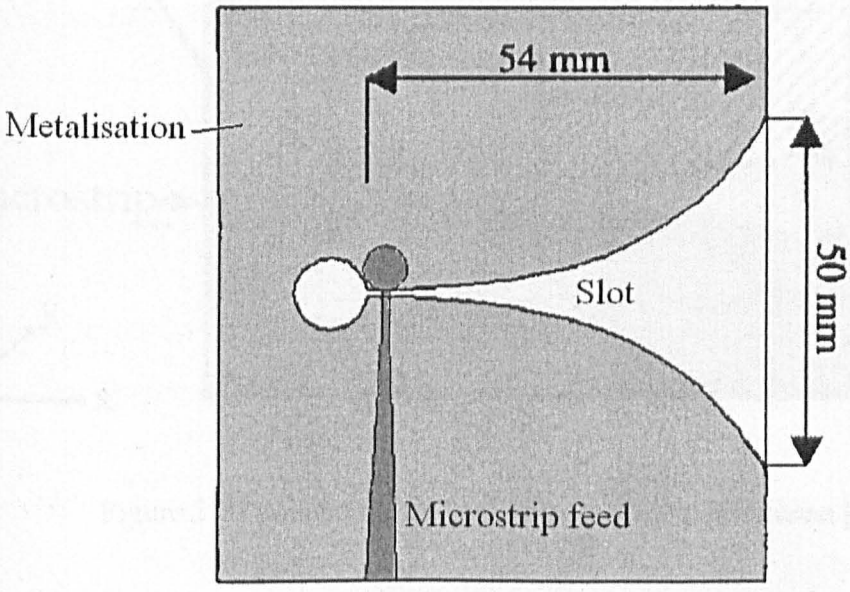

Figure 3.22 An example of a Vivaldi antenna [73]

In an attempt to improve impedance performance over the standard orthogonally microstrip fed antenna the antipodal Vivaldi antenna was introduced by Gazit in 1988 [75]. The antipodal Vivaldi, as seen in Figure 3.23, is made up of two symmetric exponentially tapered patches printed on opposite sides of a dielectric substrate. The

patches are fed, from behind the slot by a micro-stripline in which the ground tapers inwards to form a symmetric twin line, each line feeding one of the patches [75], [76].

In this configuration the antenna has an impedance bandwidth that covers the entire UWB bandwidth [76], the response can be further improved by rounding the ends of the patches which reduces reflections and lowers the lower edge frequency [5], [77]. The Vivaldi antenna is one of the few UWB antennas that maintain a stable directional radiation pattern with frequency, the maximum gain directed along the direction of the slot and typically having a value of 2 dBi at around 3 GHz and rising to and staying at around 8 dBi from 6-10.6 GHz [3], [77], [78].

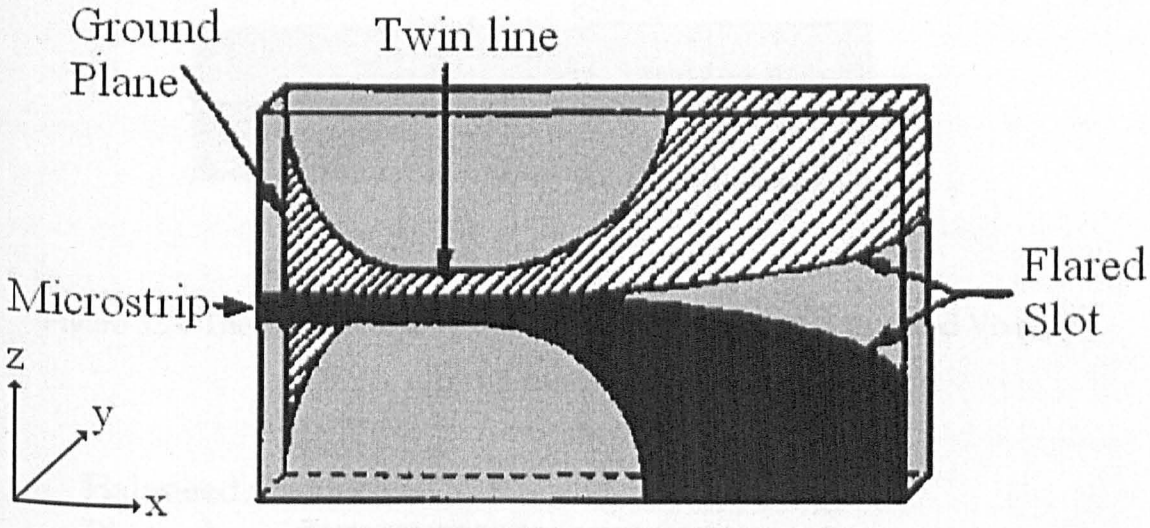

Figure 3.23 An example of an antipodal Vivaldi antenna [76]

The antipodal Vivaldi antenna has been proposed for use in modern UWB applications [78], however it has been noted that as the patches are separated in the *y* direction as well as well as the x direction the electric field between the two patches is slanted (Figure 3.24) which leads to the antenna having unacceptably high levels of cross polarisation, especially at high frequencies [76]. A solution to this problem is the balanced antipodal Vivaldi antenna or BAVA. This antenna is made up of three patches; two identical exponentially tapering patches sandwiching a symmetrical

counterpoise. The Two outer patches taper into a ground either side of the middle patch which tapers into a stripline. This arrangement means that the two components in the *y* direction cancel (Figure 3.24) leaving the resulting E-field vector purely in the *y* direction, significantly reducing the cross polar levels.

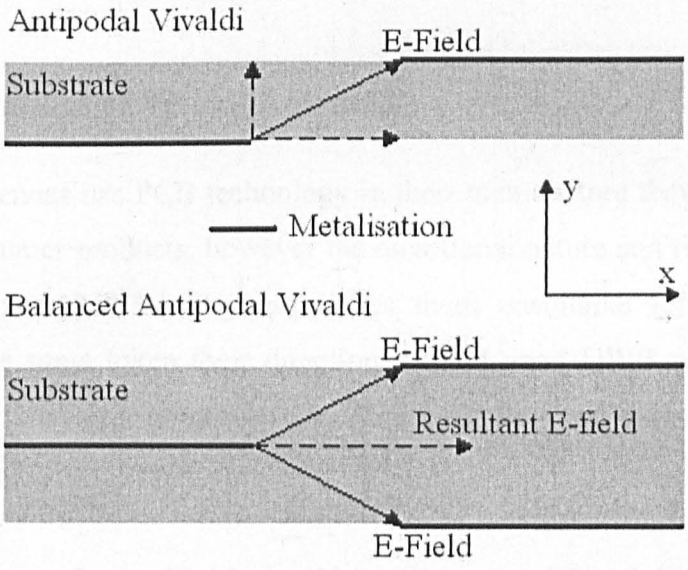

Figure 3.24 The E-field for an antipodal Vivaldi antenna and balanced Vivaldi antenna.

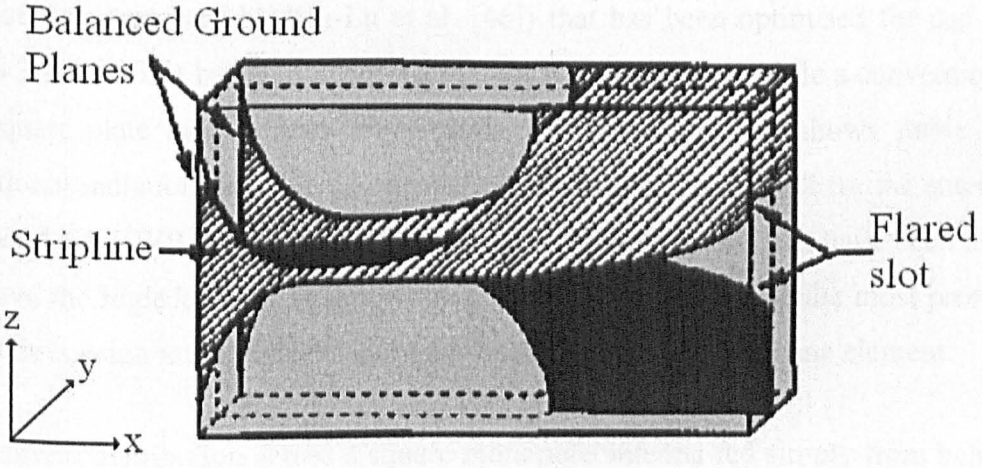

Figure 3.25 An example of a BAVA antenna [76].

The BAVA antenna in Figure 3.25 has an impedance bandwidth in excess of 40:1 with a lower bound of 3GHz. The radiation patterns of this antenna are relatively stable with frequency with the maximum gain in the direction of the slot with a null-beam width of between 40° and 60°. The maximum gain of this antenna reflects this pattern performance varying between 8 and 12 dB from 1-18GHz.

3.4.2 Applications of Vivaldi Antennas

As Vivaldi antennas use PCB technology in their manufacture they are ideally suited for use in consumer products, however the directional nature and relatively large size compared to other UWB antennas, makes them unsuitable for use in handheld devices. By the same token their directionally and good UWB performance makes them ideal candidates for point to point communications and base stations with fixed coverage [3], [5].

3.5 Analysis of a Trident-Fed Square Metal-Plate Monopole Antenna

This section presents the results of an investigation of a square plate monopole (based on that first presented by Kin-Lu et al. [46]) that has been optimised for use in the UWB 3.1-10.6GHz band. In Section 2.1.2.4 it was shown that while a conventionally-fed square plate monopole is very simple to manufacture and shows stable omni-directional radiation patterns, its impedance bandwidth is too small for the antenna to be useful for UWB applications. A number of different techniques have been used to improve the impedance of square/rectangular monopoles. One of the most promising methods is using multiple feeds along the bottom edge of the antenna element.

The current distribution across a square monopole antenna fed simply from below, at one central point, has components both in the lateral and vertical directions. The lateral components not only produce a high level of cross polarization in radiated fields but also degrade the impedance bandwidth of the antenna. By using multiple

feeds a more intense and uniform vertical current distribution can be achieved, reducing the horizontal current components and so improving the UWB performance of the antenna. The number of feeds affects the uniformity of the current distribution and it has been shown that a trident feed will force a more uniform current distribution when compared with single or dual fed designs [46], [47].

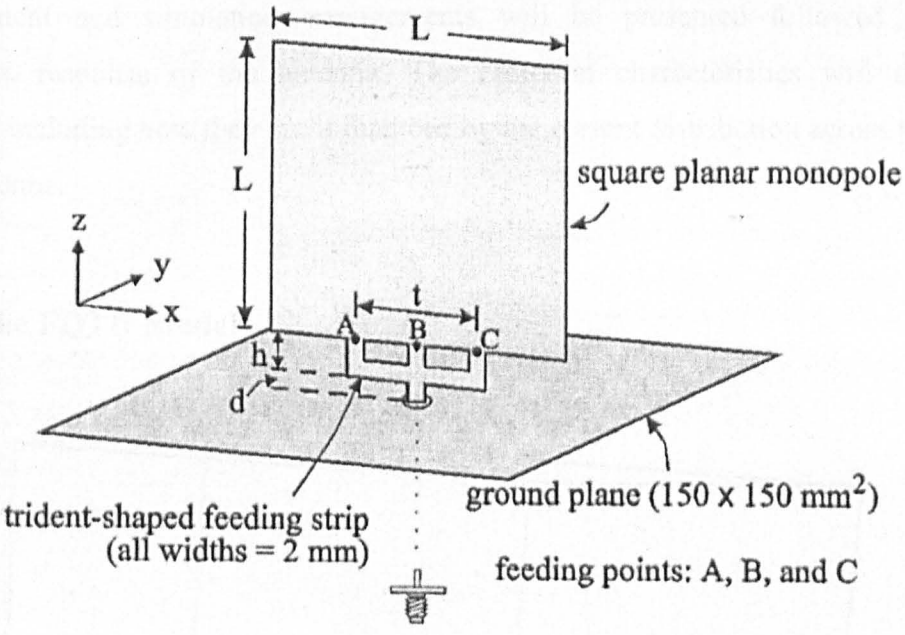

Figure 3.26 The trident fed monopole presented in [46] (L = 40mm).

The approach taken in [78] to implement a three feed point design is a trident shaped feed arrangement that is in the same plane as the antenna element. The element is mounted over an orthogonal ground plane and is fed from beneath using a 50Ω SMA jack. A schematic of this antenna can be seen in Figure 3.26. The trident shaped feed strip simplifies the construction of antenna and makes it more compact compared to previous multiple feed point designs; the design presented in [47] uses two separate feeding strips and a feed network to drive the antenna.

The size of the square element in [2] is 40 mm by 40mm. This original design did not target operation across the specified (3-10GHz) UWB band; the -10dB impedance of

this antenna being 1.4-11.4GHz. As the lower frequency limit of this type of antenna's impedance bandwidth is dictated by the geometrical size of the antenna element there is scope to make the element smaller while achieving satisfactory UWB performance.

This section presents a more compact version of the trident-fed design with an element size of L = 30mm that performs well across the 3.1-10.6GHz band. Measurement and simulation arrangements will be presented followed by the impedance response of the antenna. The radiation characteristics will then be discussed including how they are influenced by the current distribution across the face of the antenna.

3.5.1 The FDTD Model

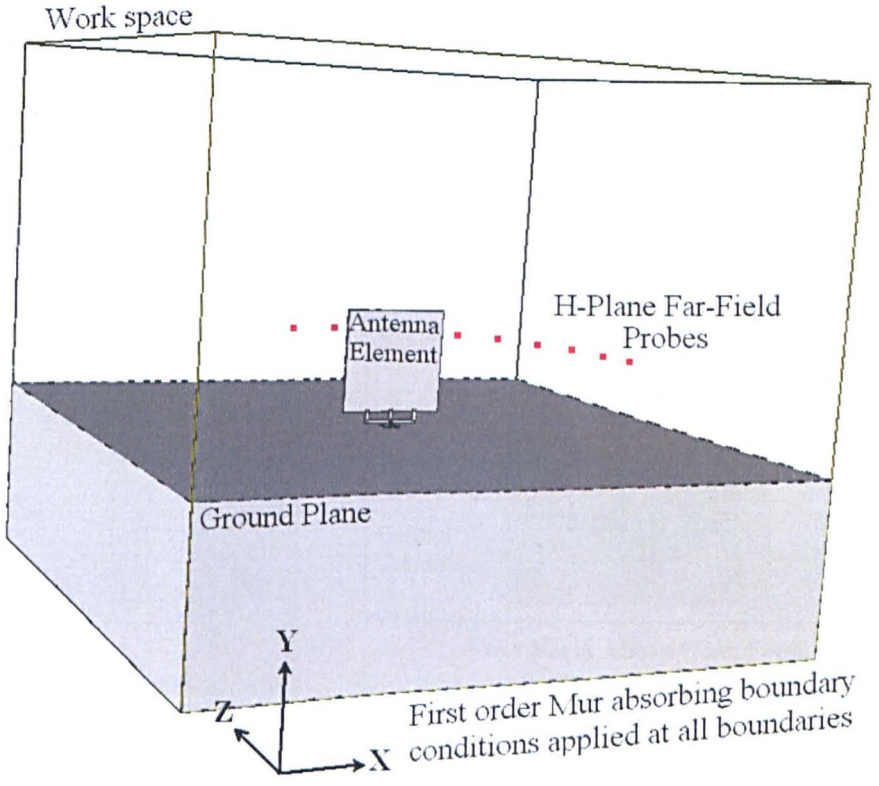

Figure 3.27 The FDTD model used to simulate the trident fed monopole

To investigate the radiation properties and examine the current distribution across the surface of the square monopole it was simulated using the in-house FDTD software developed at the University of Bristol (for a detailed explanation of the theory behind FDTD see Chapter 5). A diagram showing a 3D graphical representation of the FDTD model can be seen in Figure 3.27. The model consists of a metal block which acts as a ground plane. The antenna element (Figure 3.28) is mounted perpendicular to the ground plane and is fed by a 50mm length of 50 Ω coaxial transmission line that passes through the metal block ground. The transmission line excitation is made up of four elements in a cross formation, each extending from the interior conductor of the coaxial line to the outer. The transmission line is terminated at an absorbing boundary condition at the work space boundary. The feed arrangement is illustrated in Figure 3.28.

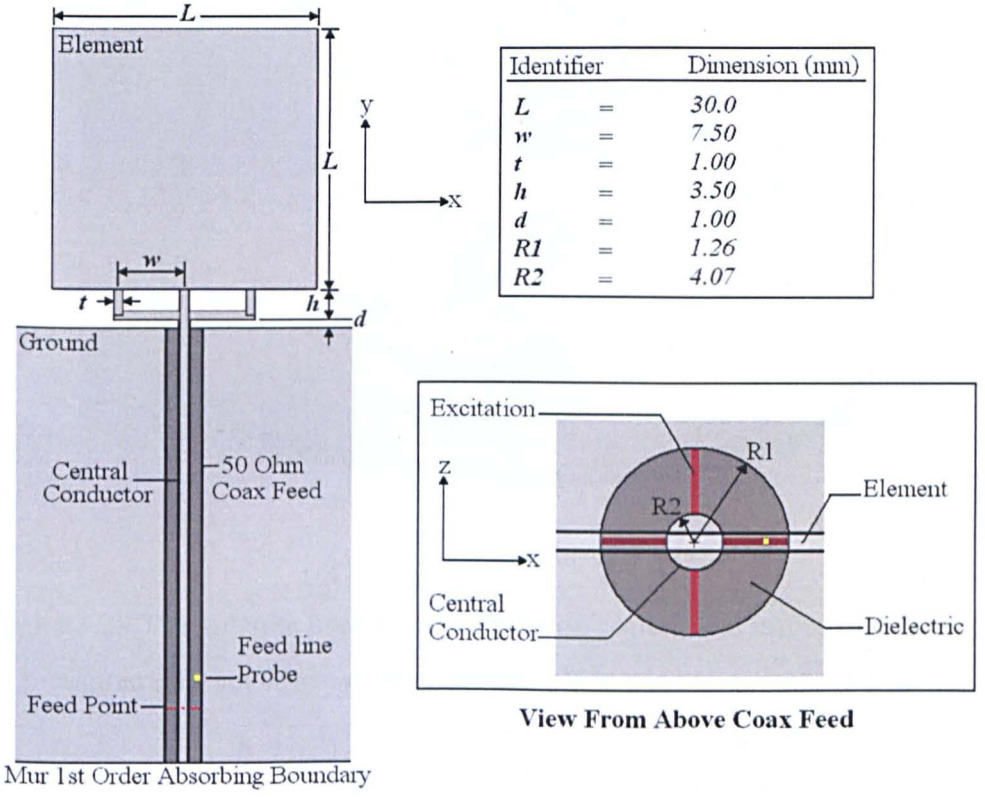

Figure 3.28 The feed arrangement and the dimensions of the antenna element

In order to measure the impedance response of the antenna a field probe was placed in the coaxial transmission line (Figure 3.28). Far field probes were also placed in an arc in the H planes, only a quarter-circle was needed due to the symmetry of the antenna. In addition, a number of "frequency snapshots" were taken of the fields one cell from the surface of the element. With a degree of processing these allow the current distribution current across the face of the antenna to be examined (see Section 3.5.4.2).

3.5.2 Measurement Arrangement

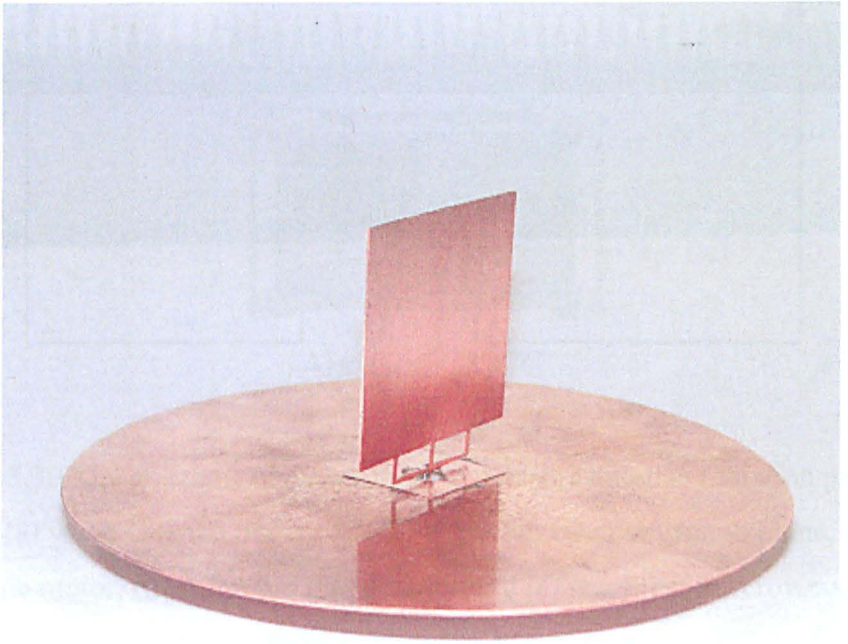

Figure 3.29 The antenna used in both radiation pattern and impedance response measurements set above a small ground plane used to mount the antenna.

To find the measured input response and radiation patterns the antenna element was constructed (Figure 3.29). The element itself was made from 0.25mm thick copper sheet, mounted above a 90mm diameter copper ground plane and fed from beneath by a 50Ω SMA coaxial jack.

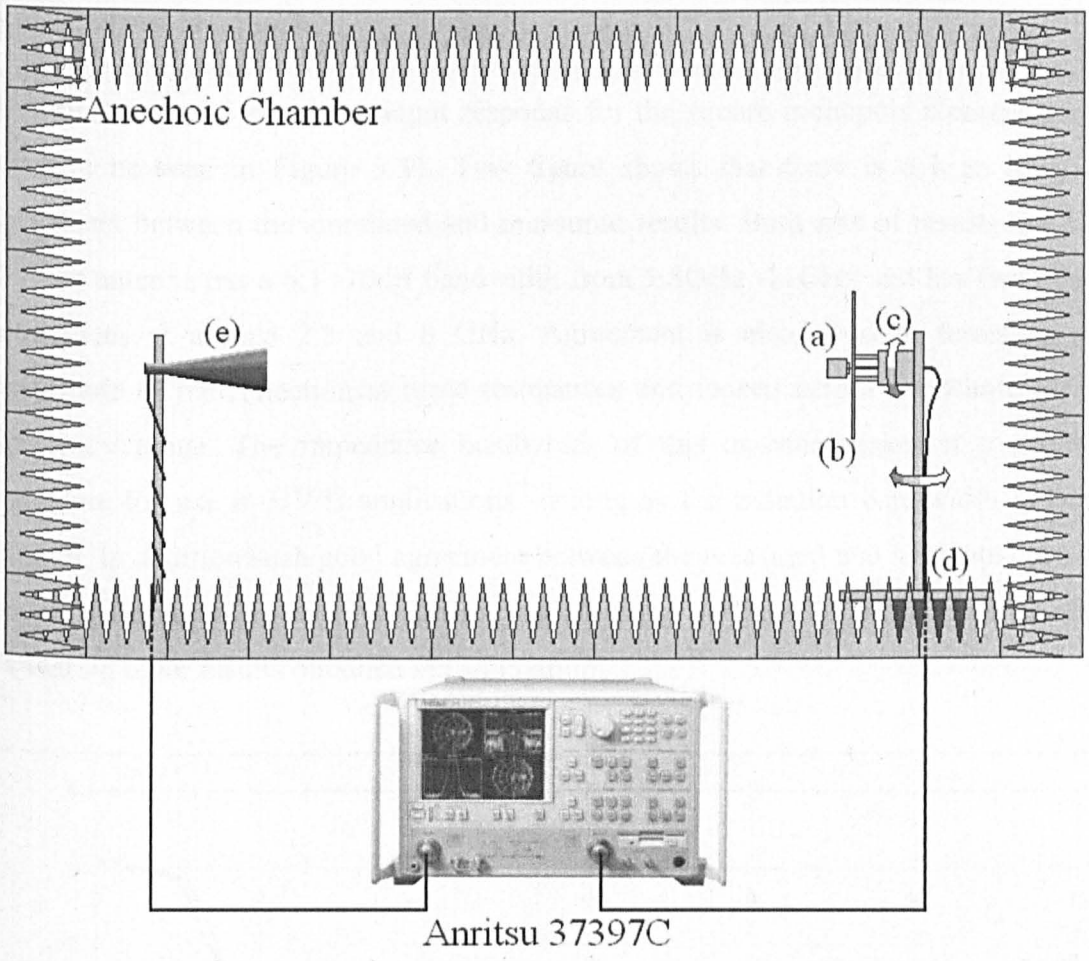

Figure 3.30 The anechoic chamber used to measure antenna radiation patterns wherein; (a) is the antenna under test, (b) is a 0.5m circular ground plane, (c) is the theta plane motor, (d) is the phi plane motor and (e) is a Flann Microwave DP240 dual polarized reference horn antenna.

The input response of the antenna was measured using an Anritsu 37397c Vector Network Analyser (VNA) while mounted on the 90mm ground. The radiation patterns of the antenna were measured in the University of Bristol's anechoic chamber using the same VNA. In the chamber the antenna was mounted on a 0.5m circular ground plane attached to a computer controlled measurement rig with two degrees of freedom allowing three dimensional radiation patterns to be recorded. The reference antenna used for these measurements was a Flann Microwave DP240 dual polarized horn antenna. A schematic of this measurement setup can be seen in Figure 3.30.

3.5.3 Input Response

The measured and simulated input response for the square monopole element under test can be seen in Figure 3.31. This figure shows that there is a high level of agreement between the simulated and measured results. Both sets of results indicate that the antenna has a 6:1 -10dB bandwidth from 1.8GHz -11GHz and has two major resonances at around 2.5 and 8 GHz. Agreement is also good in terms of the magnitude of the reflection at these resonances and indeed across the whole of the frequency range. The impedance bandwidth of this antenna makes it a suitable candidate for use in UWB applications so long as the radiation bandwidth is large enough. In addition such good agreement between the measured and simulated results goes a considerable way to verifying the accuracy of the FDTD computer model, validating other results obtained via simulation.

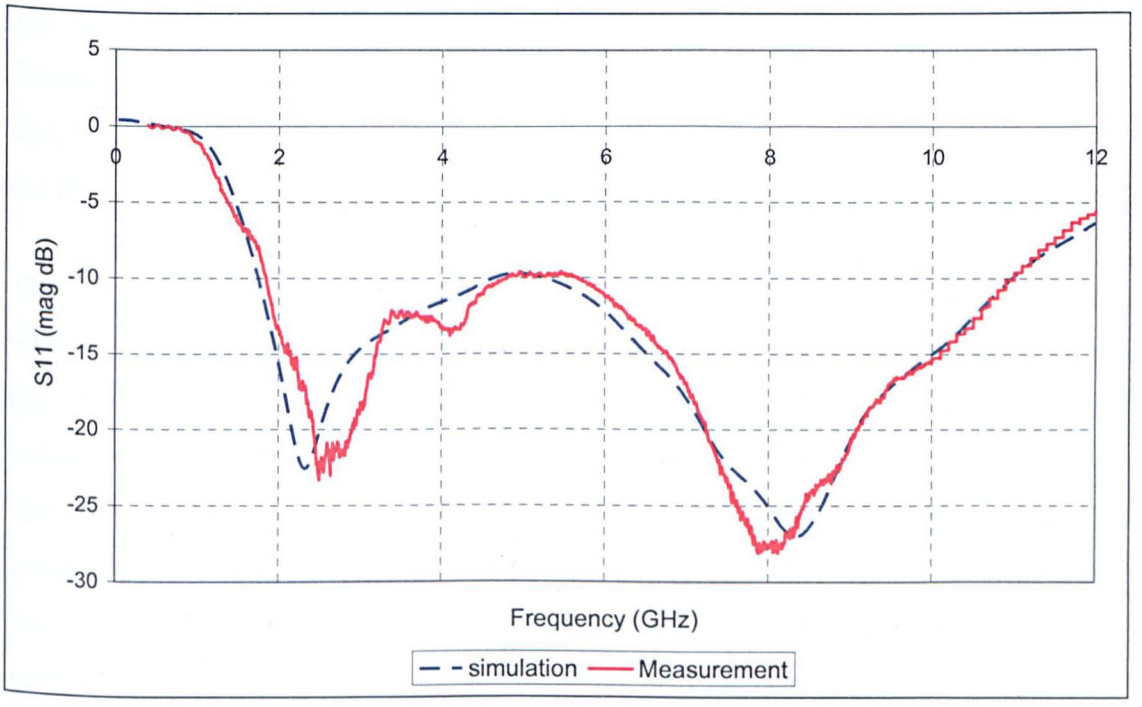

Figure 3.31 The measured and simulated S_{11} for the square plate monopole antenna

3.5.4 Radiation Properties

The two dimensional radiation patterns for the square monopole at various frequencies can be seen in Figure 3.32. These patterns have been normalised such that their maximum values have been set to zero in each case. These patterns show that across the frequency range the antenna has an omni-directional radiation pattern in the H-plane that varies by less that 10 dB at all angles. Figure 3.32 shows that there are low levels of cross polarisation in this plane at all three frequencies; the maximum cross polar levels are least 15 dB below the maximum co-polar levels in each case.

The E-plane patterns which can also be seen in Figure 3.32show that at all frequencies the antenna produces a radiation pattern typical of a monopole antenna similar to those produced by the other metal plate antennas discussed in Section 3.2.2.4..

The cross-polarisation is low at all angles when compared to co-polar levels, the difference between maximum co and cross polar patterns being 30dB at 3 and 6 GHz and 25 dB at 9GHz. The exception to this is at the null of the co-polar patterns where the levels between the two polarisations are comparable.

The 2D radiation patterns provide useful information about the radiation characteristics of the antenna in the planes examined e.g. cross-polar levels but do not give the whole picture and in some cases can be misleading. By examining the 3D radiation patterns in conjunction with the 2D patterns, a better understanding of the antennas performance can be established. The 3D co and cross-polar radiation patterns for the square monopole can be seen in Figure 3.33. These show that as for the 2D patterns the monopole type shape is present at each frequency however away from the E and H planes examined in the 2D patterns the cross polar levels for 6 and 9 GHz are in fact a lot higher. At 3GHz the cross polar-level is 25 dB below the co-polar maximum, the exception is a thin lobe at the y-directed null that has a maximum 15 dB below that of the co-polar maximum. At 6 GHz the maximum cross polar level rises to 14 dB while at 9 GHz this rises to only 3 dB.

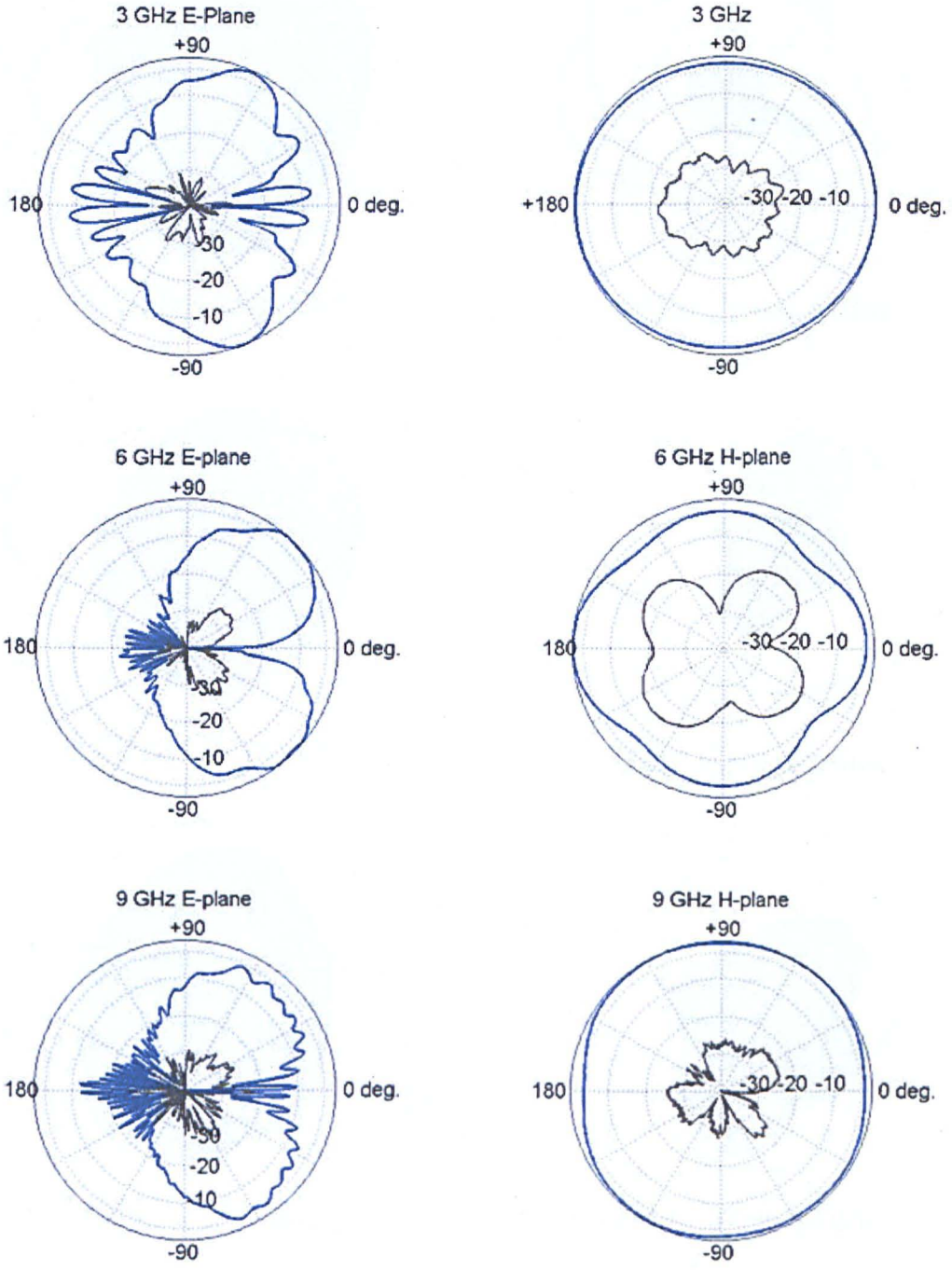

Figure 3.32 Two dimensional, normalised, co-polar and cross-polar radiation patterns for the E and H – planes at 3, 6 and 9 GHz. The radial scale in each case is in decibels (co-polar — cross-polar —).

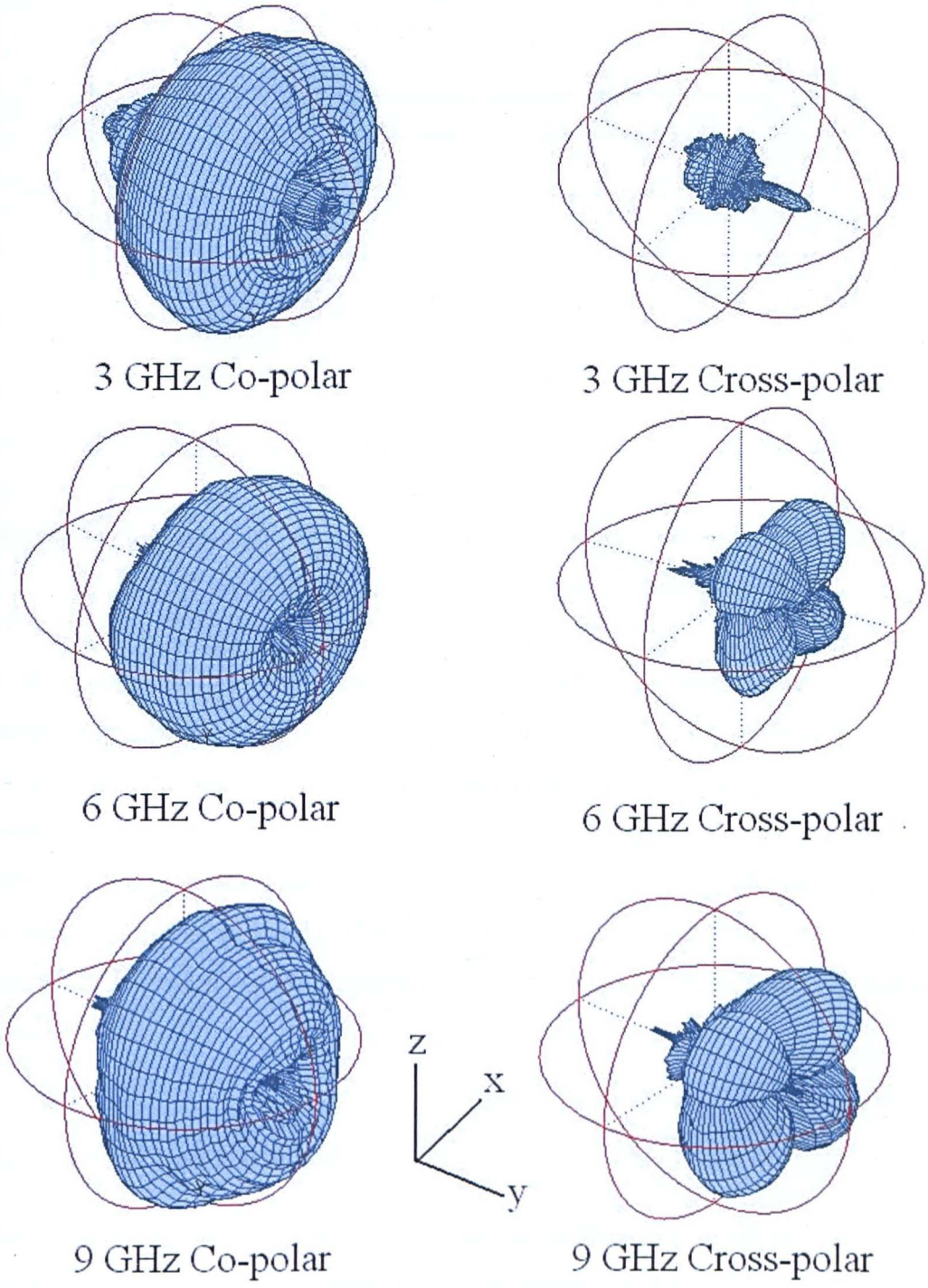

Figure 3.33 The 3D co-polar and cross polar radiation patterns for the square monopole antenna at 3, 6 and 9 GHz

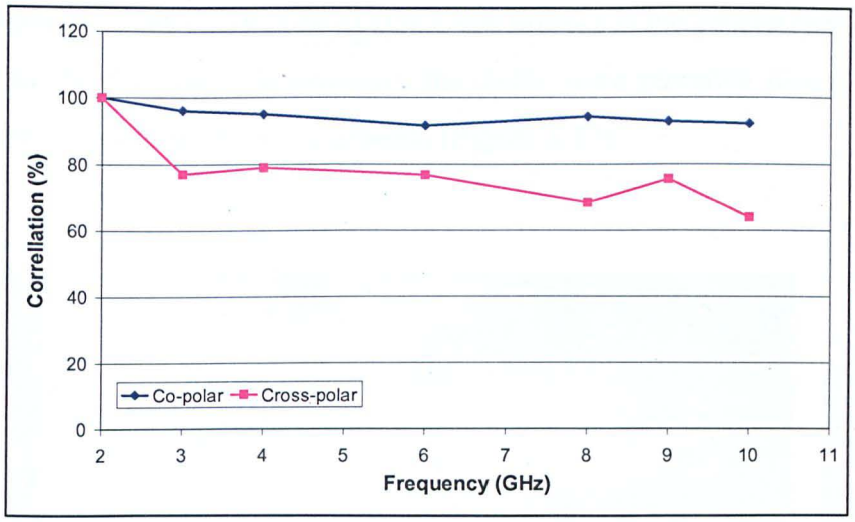

Figure 3.34 Correlation of co and cross polar 3D patterns across the UWB bandwidth using the pattern at 2GHz as the comparison.

An alternative method of examining the radiation patterns is to measure the mathematical correlation between the patterns using a desirable low frequency pattern as a reference. In this case the co and cross polar radiation patterns at 2 GHz were chosen as a reference. The result of this analysis can be seen in Figure 3.34. This shows that the co-polar pattern is stable across the UWB never deviating more than 8% from the original at 2 GHz. The cross polar results show that as expected the level of correlation decreases with frequency falling to just above 60% at the top end of the frequency band.

3.5.4.1 Simulated Far-Field

While the radiation patterns examined in the last section give an impression of what is happening to the radiation patterns across the frequency range the FDTD simulation offers an opportunity to examine what is happening in a certain plane in much more detail. By recording the *y*-directed E-field (the co-polar field) using a horizontal ring of field probes placed in the antenna far-field and then performing a Fourier transform on the time domain data obtained by these probes the H-plane field can be found. Only one quartile of data was required to find the behaviour of the antenna over the

full 360° because of the two planes of symmetry present in the geometry of the square monopole in the *x-z* plane. Accordingly the fields were recorded using 10 probes, covering a 90° arc, 80mm from the antenna (Figure 3.27).

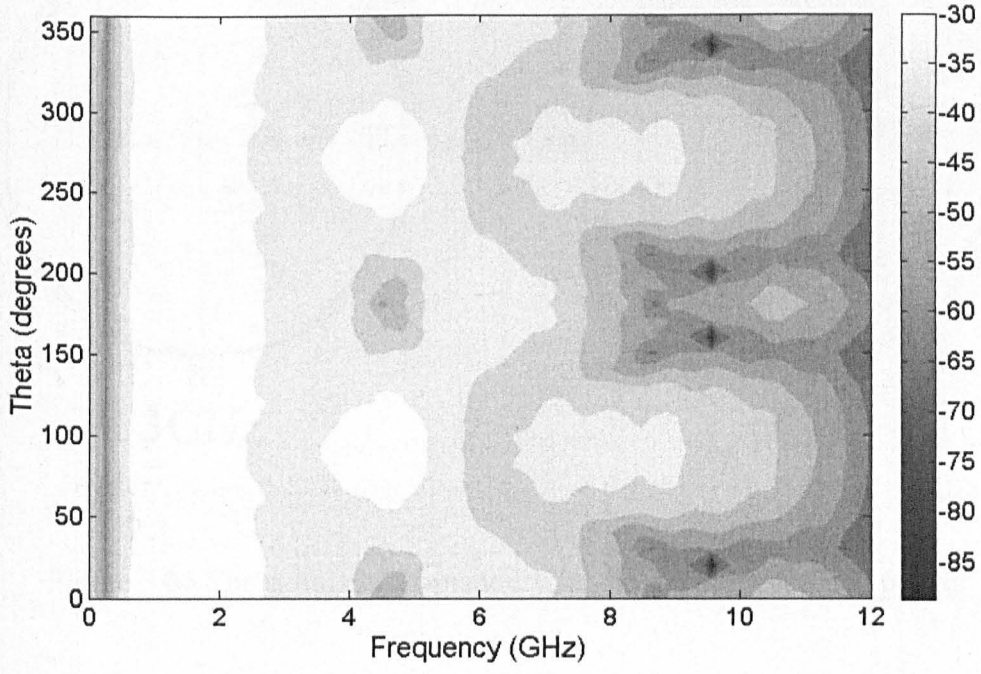

Figure 3.35 The *y*-component of the E-field theta angles 0° to 360° (H-plane) for the frequency range 0-12 GHz (the set between levels = 6dB).

The results from the far field probes can be seen in Figure 3.35. This figure shows that the antenna produces an omni-directional radiation pattern (that doesn't vary by more than 10dB) up to around 8 GHz. The exception to this is a null at bore-sight that is present from 4-5 GHz, which corresponds to an area of relatively large reflection in the input response. Examining the data from Figure 3.36 at 3 and 6GHz in the form of polar plots it can be seen that the antenna has an almost completely omni-directional pattern at 3GHz. At 6 GHz the antenna is radiating more effectively at bore-sight, which is in agreement with the measured H-plane pattern, however the pattern doesn't have the same multi-lobed shape. This difference maybe present because the plane used for the measurements may be slightly different to that used in the FDTD

simulation. In addition to this the ground plane in the FDTD simulation was infinite whereas the one used for measurement was not.

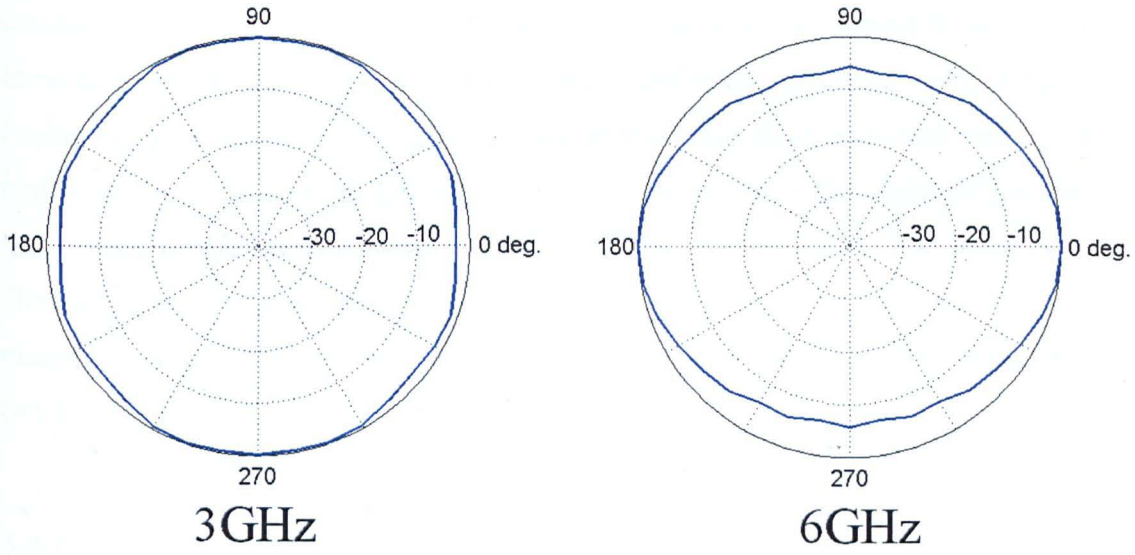

Figure 3.36 The simulated H-plane Ey far-field pattern at 3 and 6 GHz

Beyond 8GHz the simulated results show that the omni-directional nature of the radiation pattern degrades and a multi-lobed pattern starts to form. This occurs at the same frequency as a null in the input response (Figure 3.31). The same behaviour is not present in the measured patterns which remain omni-directional in the H-plane.

3.5.4.2 Current Distributions

Using experimental techniques it is extremely difficult to examine the current distribution across the face of the antenna. The FDTD simulation of the antenna allows these to be examined in detail (Figure 3.37). The current density is derived from the magnetic field tangential to the antenna and hence includes a contribution from the displacement current in the locations where there is no metal. The good agreement already seen between measured and simulated results suggests that these distributions will have a good degree of accuracy. First it should be noted that, as has

been previously found in planar elements [25], [26], [79], the current is concentrated around the edges of the element and at the feed point while the centre of the antenna is relatively "cold". As was intended, the trident feed arrangement used preferentially excites current in the vertical *y*-direction while suppressing current flowing in the horizontal *x*-direction. The y-directed current dominance decreases with frequency explaining the increase in the relative size of the cross-polar radiation pattern. The higher order mode seen in the 9MHz distribution explains the slight difference in shape seen in the corresponding radiation pattern (Figure 3.35). The lobed, omni-directional pattern produced is the same as that seen in the radiation pattern of a monopole antenna when it resonates at frequencies that produce higher order modes (>1/4 λ) [6].

3.5.5 Summary of Results for the Square Monopole

The impedance and radiation performance of a trident-fed, square, metal-plate monopole has been investigated by means of measurement and FDTD simulation and the results presented. The -10dB impedance bandwidth of the antenna in both the simulated and measured results was found to be 6:1 from 1.8-11. Measured radiation patterns show that the antenna has a typical monopole type pattern which is maintained across the operating frequency with rising levels of cross-polarisation. Simulated far-field measurements showed reasonable agreement with the measured results until 8 GHz where after the omni-directional nature of the pattern broke down , which is in contrast to the omni-directional patterned measured. The current distributions found using an FDTD simulation highlight the prevalence of the *y*-directed current that is excited by the trident feed. The increase in the comparative magnitude of the x-directed current with increased frequency explains the corresponding increase in the cross polar radiation pattern. In conclusion the radiation and impedance characteristics of this antenna make it a promising candidate for UWB communication applications.

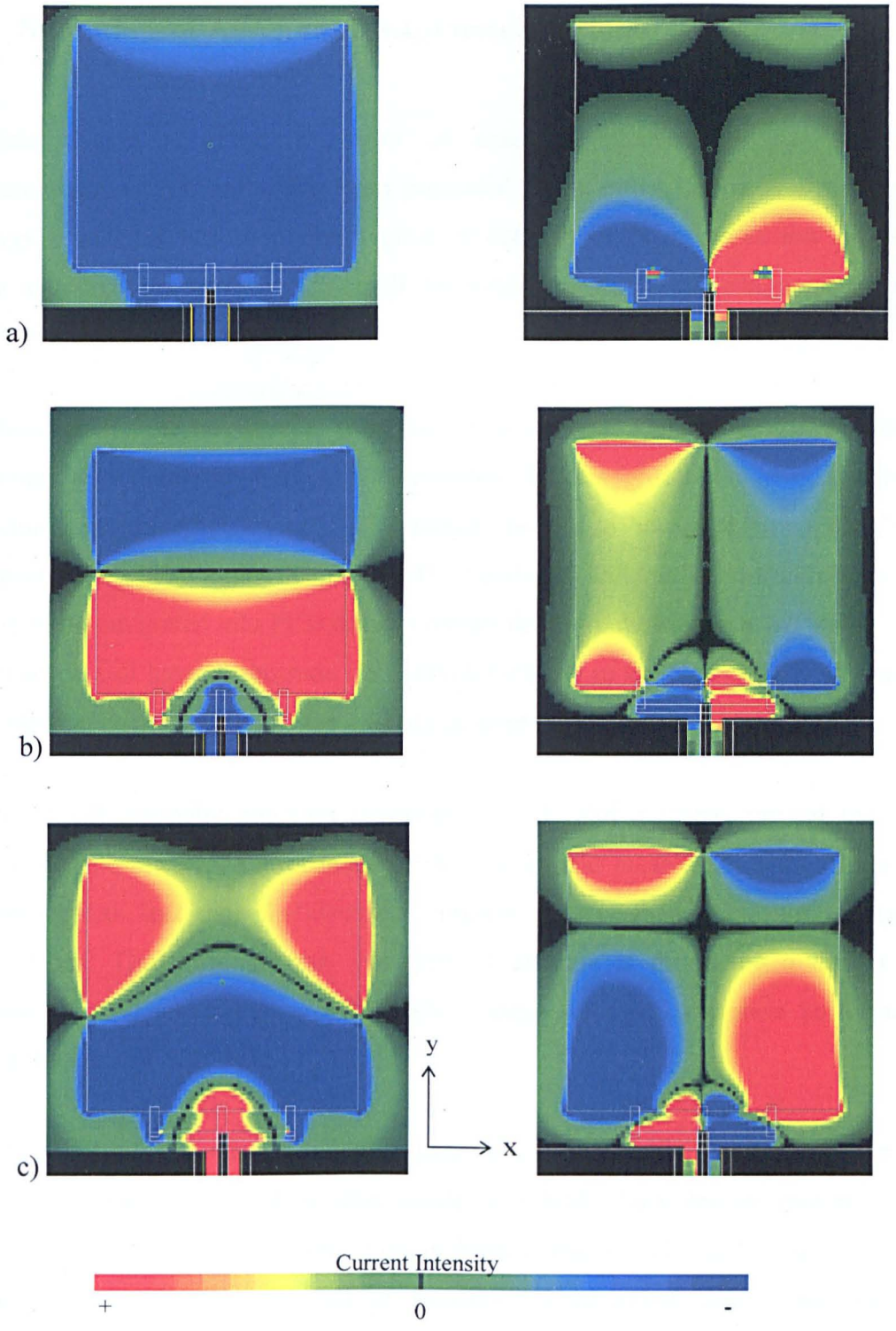

Figure 3.37 *Y* and *X* components of the current distribution across the surface of the antenna at a) 2.2GHz, b) 6GHz and c) 9GHz

3.6 Summary of Antennas for Communications

In this chapter a literature review of antennas intended for use in UWB communication applications has been presented and a trident-fed square metal plate monopole antenna has been investigated in detail. The literature review presented three major groups of antennas; small electrical antennas, small magnetic antennas and horn antennas.

Of these groups the largest was small electrical antennas which included volumetric antennas, and planar dipoles and monopoles. In this group the most promising antennas for mobile consumer UWB products proved to be planar monopoles; their compact size, cheap construction, UWB impedance and radiation bandwidths and ability to be integrated into PCB devices makes them good candidates. However these antennas do still have to protrude from any device and in the case of PCB monopoles the radiation characteristics of the antenna do degrade at high frequencies.

Of the small magnetic antennas investigated wide slot antennas proved the most promising, the low wave impedance of their near field means they will couple into nearby objects less than an electrical antenna making them ideal for embedded applications. The problem with this type of antenna is producing a design that maintains frequency stable, non-dispersive, omni-directional radiation performance across the entire UWB band.

Vivaldi planar horns were also presented; their compact planar nature and cheap construction costs compared to other much more bulky horn designs makes them a candidate for consumer products. Vivaldi horn antennas are one of the few UWB antennas that offer the potential of frequency independent directional radiation patterns and so could be used in fixed point to point applications.

In the final section of this chapter a trident fed square monopole that had been optimised for use in the UWB band was presented and its impedance and radiation

performance was examined using FDTD computer simulation and measurements. These showed that the antenna had sufficient impedance band-width and frequency stable radiation patterns making it a promising candidate for UWB communication applications.

References

[1] Allen B., Dohler M., et al (Editors), "Ultra-Wideband Antennas and Propagation for Communications, Radar and imaging", Wiley, Chichester, 2007.

[2] Zhi Ning Chen, "UWB antennas: Design and application", Information, Communications & Signal Processing, 2007 6th International Conference on 10-13 Dec. 2007 Page(s):1 – 5.

[3] Schantz H. "The art and science of ultrawideband antennas", Artech House, Norwood, MA, 2005.

[4] Chun-Chi Lee, Chia-Wei Wang, Yen R.Y., Hsin-Sheng Huang, "Broadband printed-circuit elliptical dipole antenna covering 750 MHz–6.0 GHz", Microwave and Millimeter Wave Technology, 2008. ICMMT 2008. International Conference on, Volume 3, 21-24 April 2008 Page(s):1207 – 1209.

[5] Morrow J.D., "Shorted biconical antenna for ultra-wideband applications", Radio and Wireless Conference, 2003. RAWCON '03. Proceedings, 10-13 Aug. 2003, Page(s):143 – 146.

[6] Balanis C. A., "Antenna Theory", 3rd Edition, Wiley, New Jersey, 2005.

[7] Xianming Qing, Zhi Ning Chen, Chia M.Y.W, "UWB characteristics of disc cone antenna", Antenna Technology: Small Antennas and Novel Metamaterials, 2005. IWAT 2005. IEEE International Workshop on, 7-9 March 2005, Page(s):97 – 100.

[8] Ando A., Yamada W., Kita N., Mori D., Takao, T., "Novel wide-band antennas for 2.4/5 GHz dual-band MIMO-OFDM WLAN systems", Antennas and Propagation Society International Symposium, 2005 IEEEVolume 3A, 3-8 July 2005, Page(s):553 - 556 vol. 3A.

[9] Yongwei Zhang, Brown A.K., "The discone antenna in a BPSK direct-sequence indoor UWB communication system", Microwave Theory and Techniques, IEEE Transactions on, Volume 54, Issue 4, Part 2, June 2006, Page(s):1675 – 1680.

[10] Taniguchi T., Kobayashi T., "An omnidirectional and low-VSWR antenna for the FCC-approved UWB frequency band", Antennas and Propagation Society International Symposium, 2003. IEEE, Volume 3, 22-27 June 2003 Page(s):460 - 463 vol.3.

[11] Chun J.C., Shim J.R., Kim T.S., "Wideband cylindrical monopole antenna for multi-band wireless applications", Antennas and Propagation International Symposium, 2007 IEEE, 9-15 June 2007 Page(s):4749 – 4752.

[12] Telzhensky N., Leviatan Y., "Novel method of UWB antenna optimization for specified input signal forms by means of genetic algorithm" Antennas and Propagation, IEEE Transactions on, Volume 54, Issue 8, Aug. 2006 Page(s):2216 – 2225.

[13] Lee J.W., Choon Sik Cho, Jaeheung Kim, "A new vertical half disc-loaded ultra-wideband monopole antenna (VHDMA) with a horizontally top-loaded small disc", Antennas and Wireless Propagation Letters, IEEE, Volume 4, 2005 Page(s):198 – 201.

[14] Peyrot-Solis M. A., et al, "State of the Art in Ultra-Wideband Antennas", Electrical and Electronics Engineering, 2005 2nd International Conference on, 7-9 Sept. 2005 Page(s):101 – 105.

[15] Honda S., M. Ito, H. Sek, and Y. Jingo, "A disc monopole antenna with 1:8 impedance band width and omni directional radiation pattern," Antennas and Propagation, Proceedings of International Symposium on, Sapporo, Japan, 1992, page(s) 1145–1148.

[16] Liang J., Chiau C.C., Chen X., Parini C.G., "Analysis and design of UWB disc monopole antennas", Ultra Wideband Communications Technologies and System Design, 2004. IEE Seminar on, 8 July 2004, Page(s):103 – 106.

[17] Ooi B.L., Zhang Y.Q., Leong M.S., Shan X.C., Lu A., Sing C.H., "UWB Crossed Half Circle Disc Monopole Antenna", Personal, Indoor and Mobile Radio Communications, 2007. PIMRC 2007. IEEE 18th International Symposium on, 3-7 Sept. 2007, Page(s):1 – 5.

[18] Saou-Wen Su, Kin-Lu Wong, and Chia-Lun Tang, "Ultra-Wideband square planar monopole antenna for IEEE 802.16a operation in the 2–11-GHz band", Microwave and Optical Technology Letters, Jul 2004, Volume 42 Issue 6, Pages 463 - 46612 .

[19] Ammann M.J., "Improved pattern stability for monopole antennas with ultrawideband impedance characteristics", Antennas and Propagation Society International Symposium, 2003. IEEE, Volume 1, 22-27 June 2003 Page(s):818 – 821.

[20] Kiminanmi, K., et al, "Double-Sided Printed Bow-Tie Antenna for UWB Communications", IEEE Antennas and Wireless Propagation Letters, vol. 3, 2004.

[21] Schantz H.G., "Bottom fed planar elliptical UWB antennas", Ultra Wideband Systems and Technologies, 2003 IEEE Conference on, 16-19 Nov. 2003 Page(s):219 – 223.

[22] Eldek, A.A., Elsherbeni A.Z., Smith C.E., "Wideband printed lotus antenna for personal wireless communications", Wireless Communications and Applied

Computational Electromagnetics, 2005. IEEE/ACES International Conference on, 3-7 April 2005 Page(s):174 – 177.

[23] Yazdandoost K.Y., Kohno R., "Bow-tie antenna for UWB communication frequency", Antennas and Propagation Society International Symposium, 2004. IEEE Volume 3, 20-25 June 2004 Page(s): 2520 – 2523.

[24] Schantz H. G., et al., "The Diamond Dipole: A Gaussian Impulse Antenna", Antennas and Propagation Society International Symposium, 2001. IEEE,Volume 4, 8-13 July 2001 Page(s):100 – 103.

[25] Guofeng Lu, et al., "Diamond and Rounded Diamond antennas for Ultrawide-Band Communications" IEEE Antennas and Wireless Propagation Letters, Volume 3, 2004, Page(s):249 – 252.

[26] Smith L., Starkie T., Lang J., "Novel UWB antennas - theory and simulation" Ultra Wideband Systems, 2004. Joint with Conference on Ultrawideband Systems and Technologies. Joint UWBST & IWUWBS. 2004 International Workshop on, 18-21 May 2004, Page(s):299 – 303.

[27] Schantz H.G., "Planar elliptical element ultra-wideband dipole antennas", Antennas and Propagation Society International Symposium, 2002. IEEE, Volume 3, 16-21 June 2002, Page(s):44..

[28] Gueguen E., Thudor F., Chambelin P., "A low cost UWB printed dipole antenna with high performance", Ultra-Wideband, 2005. ICU 2005. 2005 IEEE International Conference on 5-8 Sept. 2005 Page(s):89 – 92.

[29] Zhang J.-P., Xu Y.-S., Wang W.-D., "Ultra-wideband microstrip-fed planar elliptical dipole antenna", Electronics Letters Volume 42, Issue 3, 2 Feb. 2006 Page(s):144 – 145.

[30] Chan Kenneth C. L., Huang Yi, "A novel CPS-fed balanced wideband dipole for ultra-wideband applications", Antennas and Propagation, 2006. EuCAP 2006. First European Conference on, 6-10 Nov. 2006 Page(s):1 – 4.

[31] Dubrovka F.F., Vasylenko D.O., "A Bell-Shaped Planar Dipole Antenna", Ultrawideband and Ultrashort Impulse Signals, The Third International Conference, Sept. 2006, Page(s):82 – 84.

[32] Cerny P., Mazanek M., "Optimized Ultra Wideband Dipole Antenna", Applied Electromagnetics and Communications, 2005. ICECom 2005. 18th International Conference on, 12-14 Oct. 2005, Page(s):1 – 4.

[33] Yin K., Xu J.P., "Compact ultra-wideband antenna with dual bandstop characteristic", Electronics Letters, Volume 44, Issue 7, March 27 2008 Page(s):453 – 454.

[34] Lule E., Babij T., Siwiak K., "Elliptical slot tuned planar teardrop ultra wideband dipole antenna", Antennas and Propagation Society International Symposium, 2005 IEEE, Volume 2A, 3-8 July 2005 Page(s):471 - 474.

[35] Seong-Youp Suh, Stutzman W., Davis W., Waltho A., Schiffer J., "A novel broadband antenna, the low profile dipole planar inverted cone antenna (LPdiPIC(A)", Antennas and Propagation Society International Symposium, 2004. IEEE, Volume 1, 20-25 June 2004 Page(s):775 – 778.

[36] Vasylenko D.O., Dubrovka O.F., Edenhofer P., "Contour optimization of a planar broadband dipole using genetic algorithms", Antenna Theory and Techniques, 2007 6th International Conference on, 17-21 Sept. 2007, Page(s):247 – 249.

[37] Lindenblad N.E., "Wide Band Antenna," U.S. Patent 2,239,724 (April 29, 1941).

[38] Ammann M.J., "A wideband monopole for reconfigurable multiband radio terminals", Antennas and Propagation Society International Symposium, 2001. IEEE, Volume 1, 8-13 July 2001 Page(s):170 - 173.

[39] Ammann M.J., Zhi Ning Chen, "A wide-band shorted planar monopole with bevel", Antennas and Propagation, IEEE Transactions on, Volume 51, Issue 4, April 2003 Page(s):901 – 903.

[40] Zhi Ning Chen, "Novel Bi-Arm Rolled Monopole for UWB Applications", Antennas and Propagation, IEEE Transactions on, vol. 53, no. 2, Feburary 2005.

[41] Valdares, D., et al, "Design of UWB Folded Plate – Monopole Antennas based on TLM", Antennas and Propagation, IEEE Transactions on, vol. 54, no. 6, June 2006.

[42] Matsuzaki K., Iwasaki H., "USB Memory Size Broadband Monopole Antenna for UWB", Personal, Indoor and Mobile Radio Communications, 2007. PIMRC 2007. IEEE 18th International Symposium on, 3-7 Sept. 2007, Page(s):1 – 4.

[43] Smith L. Starkie T. Lang J., "Measurements of Artimi's antenna designs", Ultra Wideband Systems, 2004. Joint with Conference on Ultrawideband Systems and Technologies. Joint UWBST & IWUWBS. 2004 International Workshop on, 18-21 May 2004, Page(s):304 – 306.

[44] Valdares, D., et al, "Design of UWB Folded Plate – Monopole Antennas based on TLM, Antennas and Propagation, IEEE Transactions on, vol. 54, no. 6, June 2006.

[45] Qiu X.N., Chiu H.M., Mohan A.S., "Techniques to improve ultra wide band performance of planar monopole antenna", Wireless Communications and Applied Computational Electromagnetics, 2005. IEEE/ACES International Conference on, 3-7 April 2005 Page(s):186 – 190.

[46] Kin-Lu Wong, Chih-Hsien Wu, Saou-Wen Su, "Ultrawide-band square planar metal-plate monopole antenna with a trident-shaped feeding strip", Antennas and Propagation, IEEE Transactions on, Volume 53, Issue 4, April 2005 Page(s):1262 – 1269.

[47] Antonino-Daviu E., Cabedo-Fabres M., Ferrando-Bataller M., Valero-Nogueira A., "Wideband double-fed planar monopole antennas", Electronics Letters, Volume 39, Issue 23, 13 Nov. 2003, Page(s):1635-6.

[48] Taeyoung Yang, Davis W.A., "Planar half-disk antenna structures for ultra-wideband communications", Antennas and Propagation Society International Symposium, 2004. IEEE, Volume 3, 20-25 June 2004 Page(s):2508 - 2511 Vol.3

[49] Chen X., Liang J., et al, "Planar UWB monopole antennas", Microwave Conference Proceedings, 2005. APMC 2005. Asia-Pacific Conference Proceedings, Volume 1, 4-7 Dec. 2005, Page(s):4 pp.

[50] Bo Tian, Cunqian Feng, Mingchun Deng, "Planar miniature elliptical monopole antenna for ultra wideband radios", Microwave and Millimeter Wave Technology, 2008. ICMMT 2008. International Conference on , Volume 3, 21-24 April 2008, Page(s):1240 – 1242.

[51] Liang X.-L., Zhong S.-S., Wang W., "Elliptical planar monopole antenna with extremely wide bandwidth", Electronics Letters, Volume 42, Issue 8, 13 April 2006, Page(s):441 – 442.

[53] Dissanayake T., Esselle K.P., "Design of slot loaded band-notched UWB antennas", Antennas and Propagation Society International Symposium, 2005 IEEE, Volume 1B, 2005, Page(s):545 - 548 vol. 1B.

[52] Yue Ping Zhan, Qiang Li, "Performance of UWB Impulse Radio With Planar Monopoles Over On-Human-Body Propagation Channel for Wireless Body Area Networks", Antennas and Propagation, IEEE Transactions on, Volume 55, Issue 10, Oct. 2007, Page(s):2907 – 2914.

[53] Curto S., John M., Ammann M.J., "Groundplane Dependent Performance of Printed Antenna for MB-OFDM-UWB", Vehicular Technology Conference, 2007. VTC2007-Spring. IEEE 65th, 22-25 April 2007, Page(s):352 – 356.

[54] Dissanayake T., Esselle K.P., "Design of slot loaded band-notched UWB antennas", Antennas and Propagation Society International Symposium, 2005 IEEE, Volume 1B, 2005, Page(s):545 – 548.

[55]Young Jun Cho, Ki Hak Kim, et al., "A miniature UWB planar monopole antenna with 5-GHz band-rejection filter and the time-domain characteristics", Antennas and Propagation, IEEE Transactions on, Volume 54, Issue 5, May 2006, Page(s):1453 – 1460.

[56] Radiom S., Aliakbarian H., Vandenbosch G., Gielen G., "A modified small-size tapered monopole antenna for UWB applications designed by genetic algorithm", Radio and Wireless Symposium, 2008 IEEE, 22-24 Jan. 2008, Page(s):323 – 326.

[57] Ki-Hak Kim, Seong-Ook Park, "Analysis of the small band-rejected antenna with the parasitic strip for UWB", Antennas and Propagation, IEEE Transactions on, Volume 54, Issue 6, June 2006, Page(s):1688 – 1692.

[58] Schantz, H.G. "UWB magnetic antennas", Antennas and Propagation Society International Symposium, 2003. IEEE, Volume 3, 22-27 June 2003, Page(s):604 – 607.

[59] Pengcheng Li, Jianxin Liang, Xiaodong Chen, "Study of printed elliptical/circular slot antennas for ultrawideband applications", Antennas and Propagation, IEEE Transactions on Volume 54, Issue 6, June 2006, Page(s):1670 – 1675.

[60] Lui, W. J., et al. "Frequency Notched Ultra-Wideband Microstrip Slot Antenna With Fractal Tuning Stub", Electronics Letters, 17th March 2005, vol. 41 No. 6.

[61] Abdallah A.S., Liu Yuan-an, Mohammed Y.E., "Wide-band wide-slot microstrip antenna", Asia-Pacific Radio Science Conference 2004, Proceedings of, 24-27 Aug. 2004, Page(s):27 – 30.

[62] Consoli F., et al., "Study of a CPW-fed Circular Slot Antenna for UWB Communications", Microwave and Optical Technology Letters, vol.48, no. 11, November 2006.

[63] Chair R., Kishk A.A., Lee, K.F., "Ultrawide-band coplanar waveguide-fed rectangular slot antenna", Antennas and Wireless Propagation Letters, Volume 3, Issue 1, 2004, Page(s):227 – 229.

[64] Marchais C., Leray G., Sharaiha A., "Stripline Slot Antenna for UWB Communications", Antennas and Wireless Propagation Letters, Volume 5, Issue 1, Dec. 2006, Page(s):319 – 322.

[65] Angelopoulos E. S., et al., "Circular and Elliptical CPW-Fed Slot and Microstrip-Fed Antennas for Ultrawideband Applications", IEEE Antennas and Wireless Propagation Letters, vol. 5, 2006.

[66] Saou-Wen Su, Kin-Lu Wong, Fa-Shian Chang, "Compact printed band-notched ultra-wideband slot antenna", 2005 IEEE Antennas and Propagation Society International Symposium, Volume 2B, 3-8 July 2005, Page(s):572 - 575.

[67] Jia-Yi Sze, Kin-Lu Wong, "Bandwidth enhancement of a microstrip-line-fed printed wide-slot antenna", Antennas and Propagation, IEEE Transactions on, Volume 49, Issue 7, July 2001, Page(s):1020 – 1024.

[68] Xianming Qing, Chia M.Y.W., Xuanhui Wu, "Wide-slot antenna for UWB applications", Antennas and Propagation Society International Symposium, 2003. IEEE, Volume 1, 22-27 June 2003, Page(s):834 - 837.

[69] Haeng-Lyul Lee, Hyun-Jin Lee, et al. "Broadband planar antenna having round corner rectangular wide slot", IEEE Antennas and Propagation Society International Symposium, 2002. Volume 2, 16-21 June 2002, Page(s):460 - 463.

[70] Yeo J., Mittra R., "Design of a wideband antenna package with a compact spatial notch filter for wireless applications", IEEE Antennas and Propagation Society International Symposium, 2002. Volume 2, 16-21 June 2002, Page(s):492 - 495.

[71] Tzyh-Ghuang Ma, Shyh-Kang Jeng, "Planar miniature tapered-slot-fed annular slot antennas for ultrawide-band radios", Antennas and Propagation, IEEE Transactions on, Volume 53, Issue 3, March 2005, Page(s):1194 – 1202.

[72] Gibson P.J., "The Vivaldi Aerial," Proc. 9th European, Microwave Conference, pp. 101-105, 1979.

[73] Sorgel W., Waldschmidt C., Wiesbeck W., "Transient responses of a Vivaldi antenna and a logarithmic periodic dipole array for ultra wideband communication", Antennas and Propagation Society International Symposium, 2003. IEEE, Volume 3, 22-27 June 2003, Page(s):592 - 595 vol.3.

[74] Gazit E., "Improved design of the Vivaldi antenna", Microwaves, Antennas and Propagation, IEE Proceedings H, Volume 135, Issue 2, Apr 1988, Page(s):89 – 92.

[75] Cerny P., Nevrly J., Mazanek M., "Optimization of tapered slot Vivaldi antenna for UWB application", Applied Electromagnetics and Communications, 2007. ICECom 2007. 19th International Conference on 24-26 Sept. 2007, Page(s):1 – 4.

[76] Langley J.D.S., Hall P.S., Newham P., "Novel ultrawide-bandwidth Vivaldi antenna with low crosspolarisation", Electronics Letters, Volume 29, Issue 23, 11 Nov. 1993, Page(s):2004 – 2005.

[77] Zhi Ning Chen, Ammann M.J., Xianming Qing, Xuan Hui Wu, See T.S.P., Cai A., "Planar antennas", Microwave Magazine, IEEE, Volume 7, Issue 6, Dec. 2006 Page(s):63 – 73.

[78] Hood, A.Z.; Karacolak, T.; Topsakal, E., "A Small Antipodal Vivaldi Antenna for Ultrawide-Band Applications," Antennas and Wireless Propagation Letters, IEEE , vol.7, 2008, pp.656-660.

[79] Xuan Hui Wu, Zhi Ning Chen, "Comparison of planar dipoles in UWB applications", Antennas and Propagation, IEEE Transactions on, Volume 53, Issue 6, June 2005 Page(s):1973 – 1983.

Chapter 4 A Wide-Slot Antenna for Breast Cancer Detection

4.1 Introduction

Breast Cancer is the most prevalent form of cancer in women (excluding skin cancers) [1], [2] however with early detection there is a high chance of successful treatment and long-term survival. The most common method in use for the detection of breast cancer is X-ray mammography and, while it has been an effective tool for detecting breast cancer it is recognised that the technique has a number of limitations including producing a significant number of false-negative and false-positive results [3], [4].

Microwave imaging has gained interest recently due to advances in both hardware and imaging software. The method is a potential alternative imaging technique that would be inexpensive, would provide more sensitive 3D imaging data, avoids using non-ionising radiation and would yield a system that is both quick and comfortable for the patient [5]. Microwave imaging technology relies on there being a detectable difference in the dielectric properties of a tumour and the surrounding breast tissue at microwave frequencies; such that when the breast is illuminated with microwave radiation there is a significant reflection from the tumour. Early work in this area was based on the premise that the breast structure is relatively electrically homogeneous and a contrast of approximately 5:1 exists between malignant and normal tissue [6], [7]. More recent studies [8] have shown that, while the contrast between malignant and normal adipose-dominated tissue could be as large as 1:10, the contrast in denser glandular tissue is much less at around 10%. This presents a significantly more challenging problem than was initially thought and serves to underline the need for an antenna design with the best possible performance in terms of bandwidth, size and pattern characteristics.

There are a number of techniques under investigation utilising microwave signals as a means of detection. One approach considers it as an inverse scattering problem (microwave tomography [9]), in which the breast is illuminated with microwave radiation and the scattered energy is received at a number of remote locations (Figure

4.1 (a)). From this information the permittivity distribution inside the breast may be estimated. However the data processing required when implementing this method is complex and it is not easy to see how information from many different frequencies may be included [10].

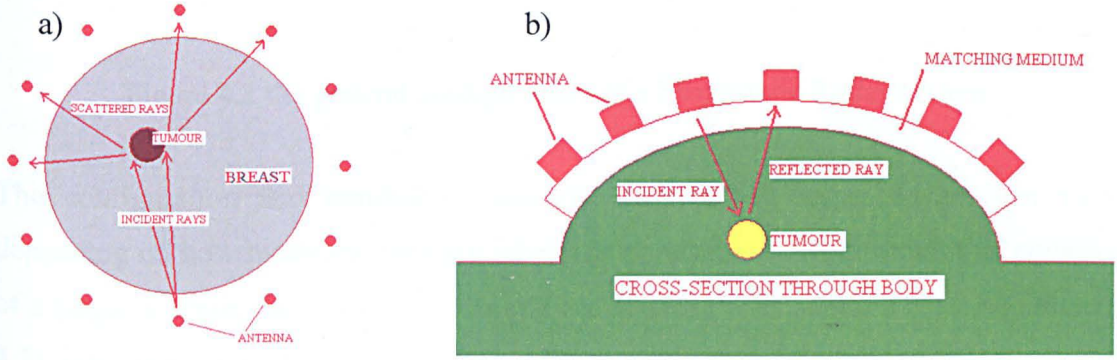

Figure 4.1 UWB Microwave detection of breast cancer using (a) tomography (b) radar

An alternative approach is to tackle the problem using a similar architecture to that of Ground Penetrating Radar (GPR) in an approach first introduced independently by Hagness et al. [11] and Benjamin [12], [13]. The detection of breast cancer using Ultra-Wideband (UWB) radar is a technique that is currently being developed by a number of research teams [11], [14], [15]. In these systems a short pulse, or a synthesised pulse constructed from a frequency sweep, is directed into the breast and the reflected signals are then detected by one or more receive antennas (see Figure 4.1(b)). The resulting set of received signals is then time or phase - shifted and added in order to enhance returns from high contrast objects and to reduce clutter. The wideband nature of the UWB signals means that such radar-based systems are capable of producing high resolution images, without the need for complicated reconstruction algorithms. With this approach there is a trade-off between simplicity of analysis and information, since material properties are not directly recovered [15].

4.1.1 Monostatic and Multi-Static Antenna Arrays

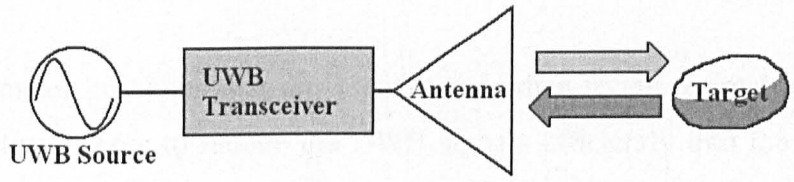

Figure 4.2 the general configuration of a Monostatic Radar system

The configuration and number of antennas in a UWB radar system can vary depending on how measurements are taken. A monostatic system is one that consists of a single antenna that both transmits and receives the microwave pulses (see Figure 4.2), effectively operating as reflectometer. Using this type of system either the target is scanned and the antenna is kept stationary or *visa versa* and an image is built up by repeated measurement.

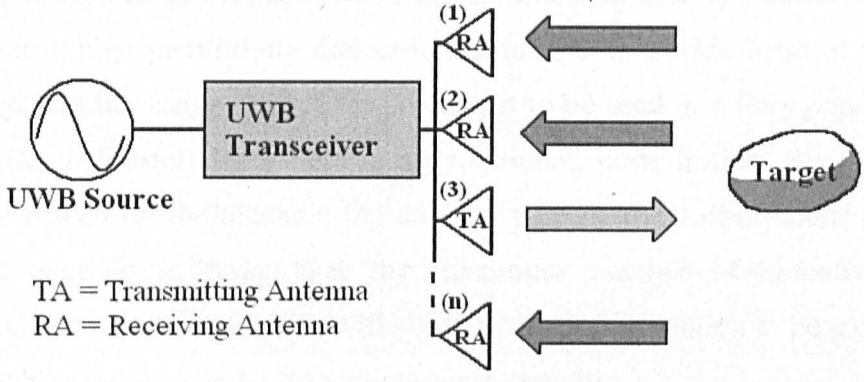

Figure 4.3 The general configuration of a Multistatic UWB Radar system

An alternative configuration is the bistatic radar system. This consists of two antennas; one transmitting and one receiving. The bistatic arrangement is a special case of the more general multistatic antenna configuration (see Figure 4.3). In a multistatic array there are multiple antennas in fixed positions. One antenna fires off a pulse and the reflections are picked up by the other antennas in the array. A multistatic system can be set up so that there are specialised antennas that solely

transmit or receive. Alternatively the antennas can do both, each antenna being fired off in turn.

One of the major problems that are encountered when trying to implement such an imaging system is how to radiate the UWB signals efficiently into the breast tissue without excessive reflection from the air/skin interface. One way that this problem has been solved is to immerse the antenna(s) in a matching medium that has similar dielectric properties to that of the tissue [16], [17]. An alternative method of preventing the returning signals being swamped by the skin response is to make use of the fact that signals reflected from a flat surface, like the skin, are co-polar whereas those reflecting from irregular objects such as tumours have a large cross-polar component [18], [19]. These cross-polar signals can be isolated using a transmit/receive combination of orthogonally polarised antenna.

A critical part of any UWB radar detection scheme is the antenna design. To obtain high resolution, accurate images the antennas must be able to radiate high fidelity signals into a high permittivity dielectric medium, over a wide band of frequencies and a large angular range [16]. If the antenna is to be used in a fully populated array aperture (as at Bristol) then there is an additional, quite critical, geometrical size constraint placed on the antenna; the antenna's geometrical dimensions must be as small as possible in order that the maximum number of antennas may be accommodated in the array. This will allow as much information to be gathered as is possible which, in turn, will reduce clutter in the results.

This chapter introduces a novel UWB wide-slot antenna intended for use in the next generation of the University of Bristol's UWB radar, breast cancer detection system. This chapter begins with a literature review of existing antenna designs, intended for use in UWB breast imaging systems. Next is a discussion on the process of developing the Wide-Slot antenna from an existing antenna design and the development of a compact cavity and feed for the antenna is considered. Finally a detailed study of the optimised antenna will be made, using measurement and simulation to characterise the antenna's performance. During this study the wide-slot

antenna will be compared to an existing stacked-patch design used in the previous generation of the University of Bristol's imaging system.

4.2 Wide Bandwidth Antennas for Microwave In-Body Imaging

This section presents a literature review of wide-band antenna designs that have been proposed for use in medical microwave imaging applications. Antennas intended for use in tomographic and UWB systems have been considered. While this review is not exhaustive it does cover the antennas developed by the major research groups in this area.

4.2.1 Monopoles and Dipoles

Monopoles and dipoles are commonly used in microwave detection systems. Their compact, simple linear or planar geometry makes them ideal candidates for use in arrays. Their simplicity also means that they can be easily modelled [15] making them especially attractive for tomographic imaging, as it reduces the complexity of solving the inverse scattering problem. These factors often outweigh the improved performance of other antenna designs e.g. the directive nature of horn antennas.

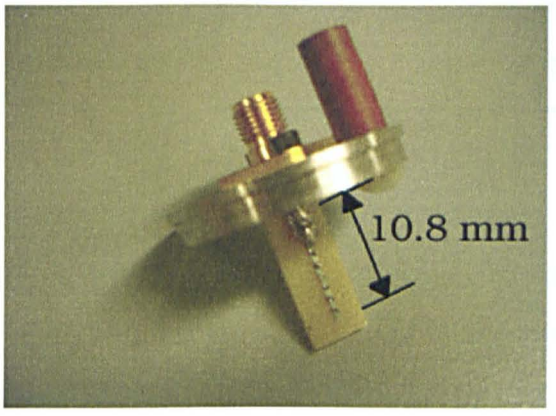

Figure 4.4 The Wu-King monopole investigated in [21]

One method that is commonly used to improve the wideband performance of such antenna is that of resistive loading. The University of Calgary have investigated both dipole [12] and monopole [20] antennas based on the Wu-King loading distribution [21] in a UWB radar imaging system. This type of antenna has reasonable UWB behaviour and is able to transmit pulses with a good level of fidelity, however the resistive loading results in low efficiency [15]. The monopole developed at Calgary can be seen in Figure 4.4. It is intended to operate in a medium with a dielectric constant of 3. To recreate the Wu-King loading distribution, the antenna is made from resistors placed end to end.

At the University of Dartmouth coaxial monopoles have been used in a tomographic system operating in the frequency band 300-1000 MHz [9]. These antennas are constructed by removing a length of the outer conductor from one end of a length of a solid coaxial cable. The antennas are immersed in a lossy medium which loads the antennas improving their radiation and S_{11} bandwidth and wide-band behaviour compared to the free-space case [22].

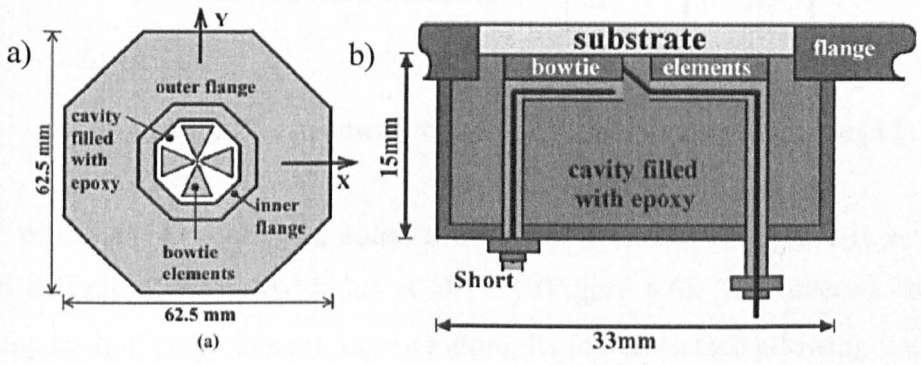

Figure 4.5 (a) a computer model of the cross bowtie antenna showing the antenna elements. (b) the cavity and feeding arrangement of the cross bowtie antenna

Bowtie antennas have also been investigated at the University of Calgary. An arrangement of two orthogonally polarized bowtie-type antennas has been investigated by Xing et al. [23] (Figure 4.5). The bowtie elements are arranged in a cross formation, mounted on a substrate ($\varepsilon_r = 3.05$) and are backed by an epoxy filled

cavity, to reduce back scatter. The system in which it is used exploits the fact that the cross-polarised reflections from axially asymmetric tumours can be distinguished from the co-polarised backscatter from skin and the chest wall.

The antenna uses the lower end of the UWB spectrum and has a -10dB impedance bandwidth of 2-4GHz. Simulated results have shown that it is feasible for the system to detect a 4 mm tumour at a distance of 70mm from the antennas while measured results in a phantom ($\varepsilon_r = 9.24$ $\sigma = 0.21$) indicated that a 15mm tumour phantom ($\varepsilon_r = 52.5$ $\sigma = 7$) maybe detected at a distance of 10mm from the antenna.

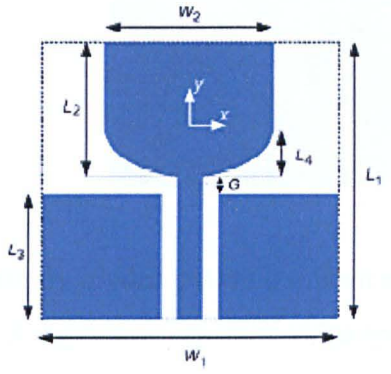

G	0.6 mm
W_1	30 mm
W_2	14 mm
L_1	26 mm
L_2	10.7 mm
L_3	14.7 mm
L_4	1.7 mm

Figure 4.6 The geometry of the CPW fed planar monopole [17]

A CPW fed planar monopole antenna has been investigated for use in a UWB radar based detection system by Jafari et al [17] (Figure 4.6). The antenna consists of a rectangular radiating element, tapered along its lower surface allowing the antenna to resonate across a wide range of frequencies. It is proposed that this antenna sit with the face seen in Figure 4.6 facing the body, with the whole antenna immersed in an imaging medium that has a dielectric constant similar to that of the tissues enclosed by the skin. As discussed previously this significantly reduces the reflections that would otherwise be present from the air/skin interface allowing the energy reflected from the tumour to be detected more easily. The monopole has been constructed on an FR4 substrate with a dielectric constant of 4.4. This value is similar to that of the dielectric constant of human fat tissue (ε_r=4.8) put forward in the paper concerned. In

the above configuration the antenna has a return loss of below -9.6dB from 3.4-9.9GHz and maintains reasonably stable near-field radiation patterns across this frequency range. It is proposed that this antenna work in a two antenna, co-polarised array with one antenna transmitting and the other receiving the reflected signals [24].

4.2.2 Horn Antennas

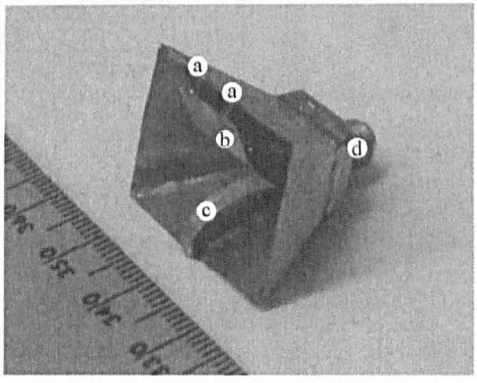

Figure 4.7 Resistively loaded pyramidal horn antenna where: (a) is the resistors, (b) is the launching plane, (c) is the ridge and (d) is the SMA coaxial feed.

The Ultra-wideband impedance bandwidth and frequency stable radiation patterns make horn antennas interesting candidates for UWB radar imaging. An example of a pyramidal horn antenna (see Figure 4.7) has been tested in a monostatic imaging system in work carried out by the University of Wisconsin [25], [26]. The antenna is based on a ridged design in which the wave guide section has been replaced with a direct coaxial feed. To make the antenna compact enough for use in an imaging system, the antenna has been resistively loaded by replacing one of the ridges with a curved metal launch plane, terminated with resistors.

The pyramidal horn antenna has a measured VSWR of below 1.5 for the entire 1 to 11 GHz operational bandwidth. FDTD simulations of the antenna have shown that it can transmit signals with fidelity greater than 92% across a 180° range centred on boresight [25]. In experiments using a breast phantom (ε_r=2.6, σ=0.05 at 6 GHz) the antenna was able to detect a 4mm simulated tumour at a depth of 20 mm below the

phantoms "skin" surface. The antenna and phantom were immersed in material with properties identical to that of the phantom to reduce reflections from the "skin" [26].

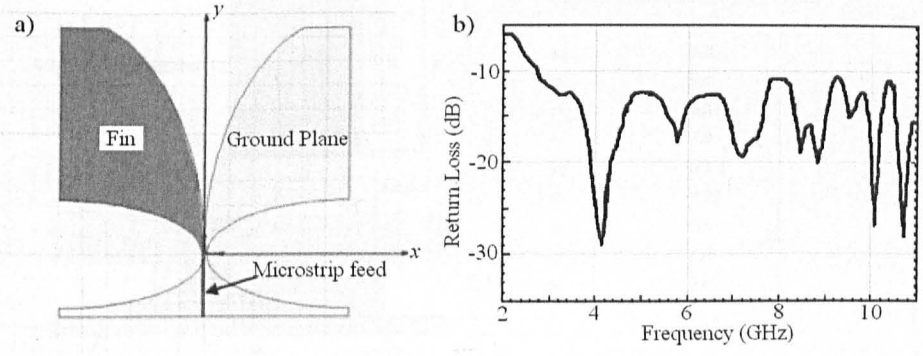

Figure 4.8 (a) Tapered-Slot antenna and (b) the S_{11} of the tapered slot antenna [27]

Khor et al. [27] has presented an Antipodal Vivaldi (Figure 4.8 (a)) as a candidate imaging antenna. This antenna is printed on 0.64mm thick, Rogers RT6010LM substrate that has a dielectric constant of 10.2 and the overall dimensions of the antenna in the x-y plane are 50 × 50 mm. The return loss of this antenna, which can be seen in Figure 4.8 (b), shows the antenna has an -10dB impedance bandwidth from 3 to in excess of 11GHz.

This antenna has been used in experimental trials of a monostatic radar system (see Figure 4.2). Located in free space, the antenna was mechanically scanned around the target to produce a number of 2D slices that are subsequently used to build up a three dimensional image. The target used in the trials was a small water-filled plastic container with a relative permittivity of 50. This was suspended inside a breast phantom made of a cylindrical plastic container filled with vegetable oil ($\varepsilon_r = 4$). The system allowed the detection of 5mm diameter targets by visual inspection of the resulting images.

4.2.3 Stacked Patch

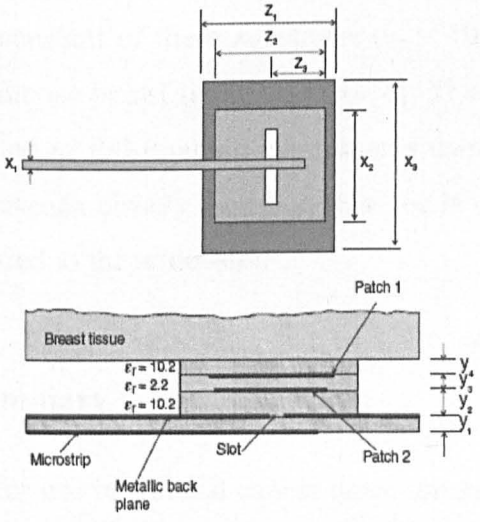

Parameter	Dimension, mm
x_1	0.66
x_2	6.0
x_3	9.0
y_1	0.64
y_2	1.9
y_3	0.8
y_4	1.27
z_1	6.5
z_2	6.0
z_3	3.0

Figure 4.9 Configuration of the stacked patch antenna

A PCB stacked patch antenna [28] has been proposed for use in the breast cancer detection system being developed at the University of Bristol [29], [14] (Figure 4.9). The antenna consists of a microstrip line feeding a slot, which in turn excites an arrangement of two stacked patches. The slot feed was used to eliminate the inductance associated with a probe feed. The size of the patches was chosen such that a lowest order resonance was achieved at either end of the desired spectrum. The dimensions were then manually optimised using an FDTD computer simulation [28].

This antenna has been designed to operate with the antenna face immersed in a matching medium with dielectric properties similar to that of human breast tissue. When in contact with such a matching medium the antenna has a -10dB return loss bandwidth of 4-9 GHz, with the exception of a slight mismatch between 6 and 7 GHz. The antenna produces stable radiation patterns across the required operational frequency range and is capable of transmitting short UWB pulses at angles of up to 45° away from the antenna's radiation pattern maximum with minimal distortion and ringing in the received signal.

A sandwich of different substrates is used in the construction of this antenna. The majority have high dielectric constants in order to minimise the antenna's size. The dielectric constant of these substrates (ε_r = 10.2) is similar to that suggested for the value of adipose breast tissue ($\varepsilon_r \approx 9$) [8]. The effectiveness of this antenna has been demonstrated in full imaging experiments using a 2D multistatic antenna array [28], [19]. An antenna closely based on this one is examined in greater detail in Section 0 and compared to the wide–slot.

4.2.4 Summary

Antennas for use in a breast cancer detection system need to be physically compatible with the problem. If they are to be used in a multi-antenna array the antennas must be as geometrically small as possible but still have a sufficiently large bandwidth to cope with the requirements of the imaging system. It is also desirable that antennas are easy to simulate so that accurate computer models of the system can be built. This has led to the use of resistively loaded antennas such as Wu-King monopoles that sacrifice efficiency for more desirable performance characteristics. The exception to this is the stacked patch antenna that uses substrates with high dielectric constants similar to those of breast tissue, to produce a reasonably compact antenna.

For those antennas that are intended for use in bistatic or monostatic imaging systems, the nature of the application means that geometrical size is not so much of an issue and the ability of the antenna to efficiently and effectively transmit UWB signals can be given greater priority. As a consequence, antennas presented for use in such systems tend to be more bulky and are not resistively loaded. Antennas proposed for use in this application include; bowtie, UWB monopole and Vivaldi antennas.

4.3 The Development of the Cavity-Backed Wide-Slot Antenna

This section presents the design process of a novel UWB antenna intended for use in the radar based, breast imaging system being developed at the University of Bristol. A

prototype of this array, populated with the Wide-Slot antenna presented in this chapter can be seen in Figure 4.10.

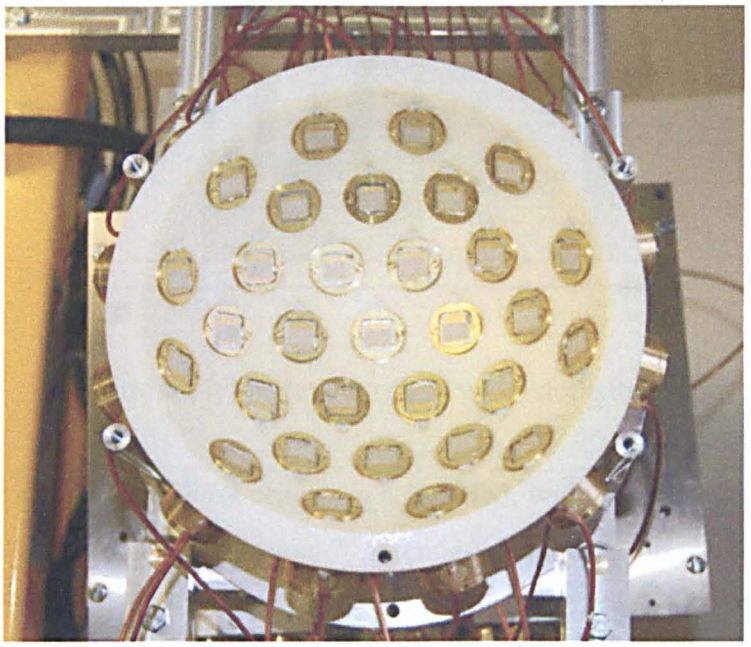

Figure 4.10 The prototype 31 antenna array being developed at the University of Bristol, populated with the wide slot antenna described in this chapter.

The design requirements of an antenna in such a system are that:

- It is as compact as possible so that the number that can be fitted into the array can be maximised.
- The antenna is as simple as possible making it easy to manufacture and simulate.
- The antenna is required to be as efficient as possible while its UWB performance should be comparable or superior to existing designs.
- In order to reduce back-radiation and cross-coupling of the antennas it is desirable for the antenna to be cavity backed or directional.

The antenna must be optimised to transmit signals into the matching medium that has been developed for the system [30] which has a dielectric constant of approximately 9 across the UWB range.

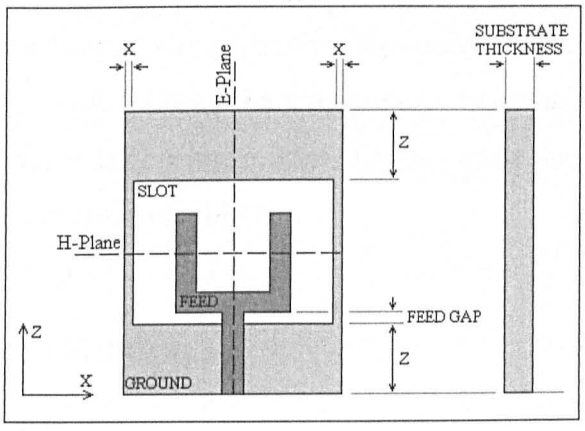

Figure 4.11 The layout of the wide-slot antenna

The design chosen to fulfil these criteria is a fork-fed, wide-slot antenna whose layout can be seen in Figure 4.11. This type of antenna was chosen due to its simplicity in terms of manufacture and simulation, its promising UWB characteristics and the fact that this antenna type lends itself to be easily cavity backed. This design potentially offers a compact simple directional antenna that is physically compatible with the multi-static radar system at the University of Bristol.

This antenna is based on that described in [31] but has been heavily modified and optimised to work efficiently when the slot is in contact with a matching medium with relative permittivity of approximately 10. The optimisation was a manual iterative procedure performed using FDTD simulations, that included the resizing and rescaling of the slot, fork feed and ground plane and the introduction of a high permittivity substrate.

The simulations used in the optimisation process were run using FDTD software developed at the University of Bristol. In the simulation the slot side of the antenna radiates into a 50mm-thick block of dielectric (σ=0 ε_r=9) with an air gap behind the antenna. The meshes used in the optimisation process have cells of sizes varying from 1 to 0.1mm, while number of cells in the mesh varied from 178×51×186 to 203×134×210 cells depending on the stage of the optimization. The workspace was

terminated by Mur 1st order absorbing boundary conditions. A planar current source connected between the ground and microstrip, was used to excite the feed line with a raised cosine pulse of width 112ps. The transmission line was terminated inside the workspace using a vertical 50Ω resistive load. The S_{11} was calculated by sampling the field at a mesh node in the microstripline.

4.3.1 Initial Model Verification

The original antenna design presented in [31] is a 53.7mm square, wide-slot antenna with a dual fork-shaped, 50Ω microstrip feed built on a substrate with relative permittivity of 4.4. The antenna in its original form is designed for UWB communications and so the antenna is intended to radiate into free-space. To characterise this antenna and prove the validity of the simulation, its S_{11} was found both experimentally and by simulation.

To obtain measured results, the antenna in [31] was built and can be seen in Figure 4.12 (a). The antenna was manufactured on FR4 ($\varepsilon_r = 4.4$), the same substrate used in the paper and was fed using a female SMA jack. The S_{11} measurements were made using an Anritsu 37397c VNA. The same antenna was simulated using FDTD, the layout of this model can be seen in Figure 4.12 (b).

A comparison of the simulated and measured S_{11} of This antenna (found by the author) can be seen in Figure 4.13. This shows a good agreement between the two sets of data, both plots have the same -10dB bandwidth of 4.5GHz from 2 – 6.5GHz, approximately the same return levels and resonances at similar frequencies of around 2 and 6 GHz. This verifies the computer model and gives confidence in its use in the development of the new antenna.

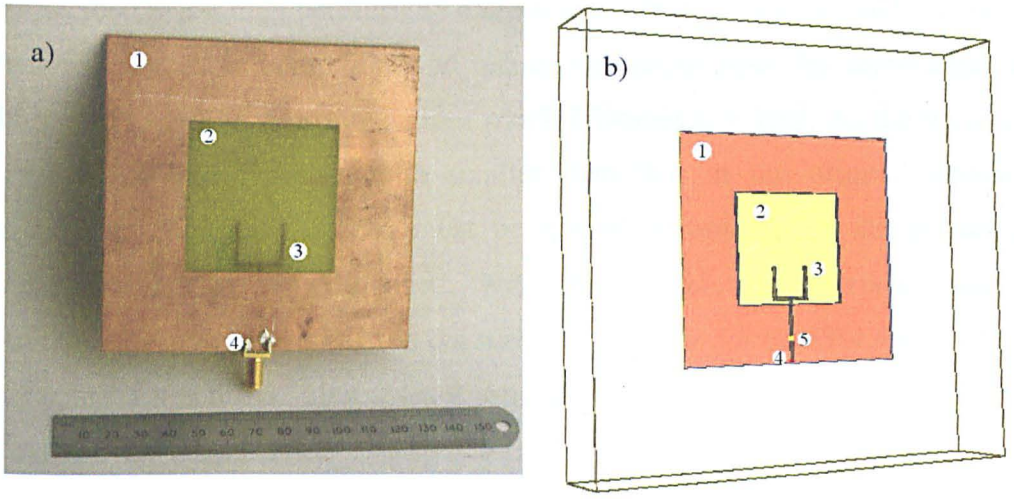

Figure 4.12 (a) The original wide slot antenna from [31] and (b) the FDTD model of this antenna where (1) is the ground plane (2) is the square slot (3) is the fork-feed (4) is the feed point (5) is the field probe in the FDTD model .

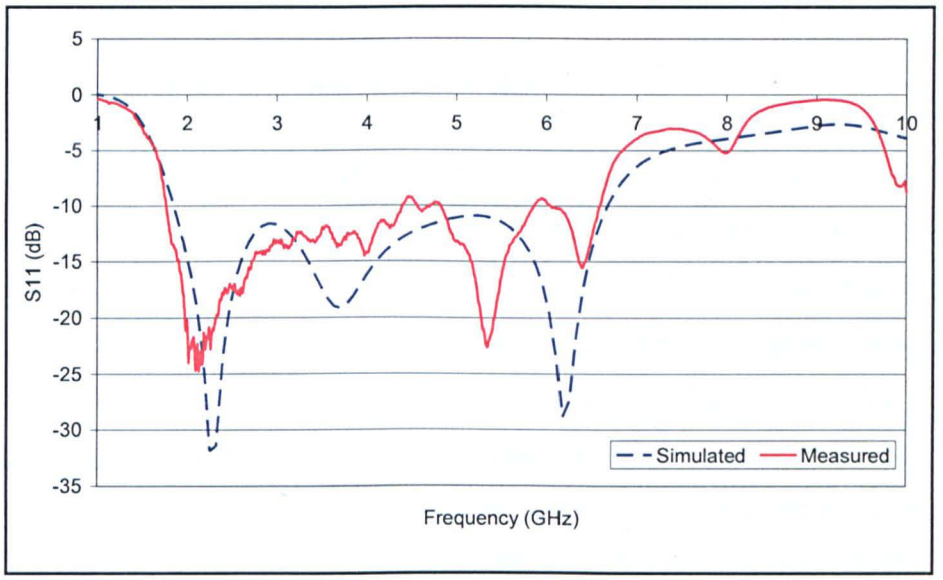

Figure 4.13 Comparison of measured and simulated S_{11} magnitude for the wide original microstrip fed slot antenna.

4.3.2 High Value Permittivity Substrate

It was decided that a high permittivity dielectric substrate would be used to make the antenna as compact as possible and to reduce reflections from the antenna/matching medium interface. The substrate chosen was RT/Duroid $\varepsilon_r = 10.2$. As the wavelength (λ) in the RT/Duroid substrate is smaller than that in the original design the dimensions of the slot and feed must be altered accordingly if the performance characteristics are to be maintained. With the air/dielectric interface taken into account the effective permittivity, at the surface of the slot for the FR4 and RT/Duroid antennas are 3.8 and 8.6. This gives a ratio between the original antenna geometry (G_1) and the new (G_2) is [32]:

$$\frac{G_2}{G_1} = \frac{\lambda_2}{\lambda_1} = \sqrt{\frac{\varepsilon_{r1}}{\varepsilon_{r2}}} \approx \sqrt{\frac{3.8}{8.6}} = 0.66 \qquad (4.1)$$

Using the RT/Duroid substrate allows the size of the slot and feed fork to be reduced by a factor of 1/3 while maintaining roughly the same performance. The width of the microstrip fork feed was recalculated for the new substrate permittivity.

4.3.3 Accounting for the matching medium

It is intended that the antenna is able to transmit pulses into a phantom with a relative permittivity of approximately 9. To take this into account the antenna model was changed to include a block of dielectric material that filled the workspace from the boundary to the "slot side" of the antenna. As this dielectric material is replacing air the size of the slot maybe reduced further due to the higher effective dielectric constant. On the opposite side of the substrate the feed remains unaffected by the medium since the dielectric/air interface is still present. It should be noted that while the real life-phantom has frequency dependent loss the dielectric block used in the simulation is lossless.

Applying the above changes to the substrate and including the matching medium allows the size of the antenna to be reduced without significantly altering its bandwidth. This is illustrated by comparing the S_{11} of the original antenna (Figure 4.13) and the antenna with these changes in place and the slot dimensions reduced by a factor of 3 to 17mm × 17mm (Figure 4.14 labelled "Square"). Despite the significant difference in geometrical size between the altered and original antenna, the lower -10dB bandwidth cut-off frequency of the altered antenna is shifted upwards by only 0.5GHz, while the impedance response is improved between 6 and 10GHz.

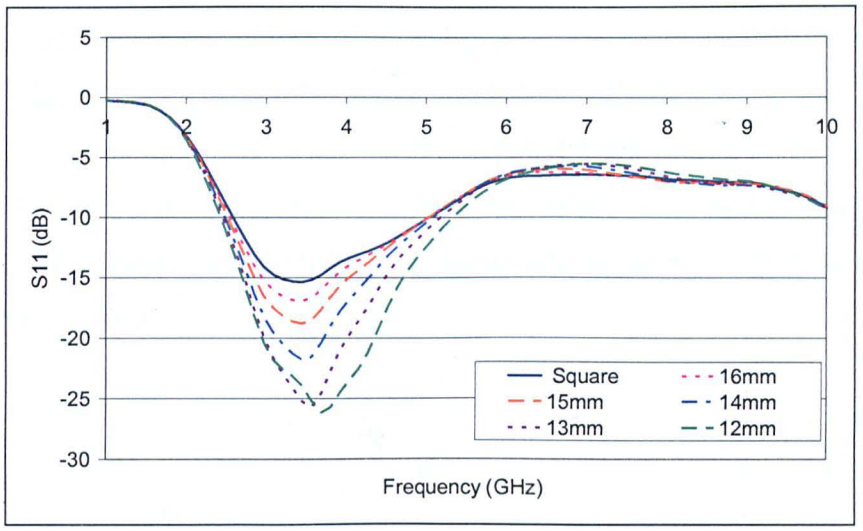

Figure 4.14 Simulated S_{11} magnitude for Slots with 17mm x-dimension and varying z-dimension.

4.3.4 Effect of the Slot Dimensions

It is desirable that the new antenna be as compact as possible. As a result the possibility of reducing the size of the slot is a major consideration. To reduce the size of the slot any further we must determine how this will affect the performance of the antenna. From Figure 4.14 it is clear that altering the z-dimension of the slot has little effect on the -10dB bandwidth of the antenna, while reducing this parameter improves the response by around 10dB at the 3.5GHz resonance. This allows the z-dimension of the slot to be reduced to 12mm without any negative effect on the input performance

of the antenna. It was found that the slot x-dimension was almost directly related to the antenna's lower bandwidth cut-off point. This is agreement with results found for similar slot antennas [33].

4.3.5 Effect of the Ground Plane Geometry

The ground plane is one of the major contributing factors to the size of the antenna. But altering it will inevitably change the antenna's input and radiation characteristics [32]. The effect of changing z (the size of the ground plane above and below the slot see Figure 4.11) on the return loss of the reduced size slot seen in Section 4.3.10, can be seen in Figure 4.15. The ground above and below the slot is set at the same value so as to try to maintain the symmetry in the radiated field. Figure 4.15 shows that as the size of the z-ground is increased, the return loss in the major null is improved from -15dB to -25dB. The overall -10dB bandwidth is reduced from 2-5.5GHz (3.5GHz) to 3-5.25GHz (2.25GHz).

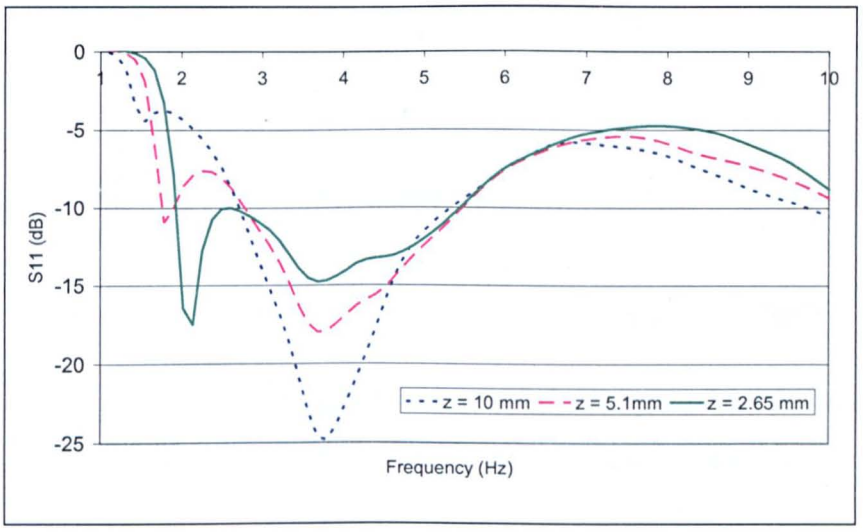

Figure 4.15 The simulated S_{11} magnitude for a 17 × 12 mm slot with varying the ground plane in the z-direction.

Figure 4.16 shows the boresight free-space transfer function of the antennas seen in Figure 4.15. These plots show that regardless of the ground geometry the bore sight

transfer function varies less than 10dB in the worst case (1×10mm ground) and 6dB in the best case (1×5mm ground). The relative "flatness" of the transfer function across the frequency range of interest means that any signal transmitted by the antenna is likely to have low levels distortion [34]. At angles away from bore sight the flattest transfer function is seen with the 5.1mm ground above and below the slot.

Varying x, the extent of the ground in the x-direction either side of the slot, has only a small effect on the antenna S_{11}. The general trend is that there is a slight improvement in the antennas performance when x is reduced. This suggests that x can be made as small as required, allowing a significant reduction in antenna size. In summary the most appropriate values of x and z are 1 and 5mm respectively.

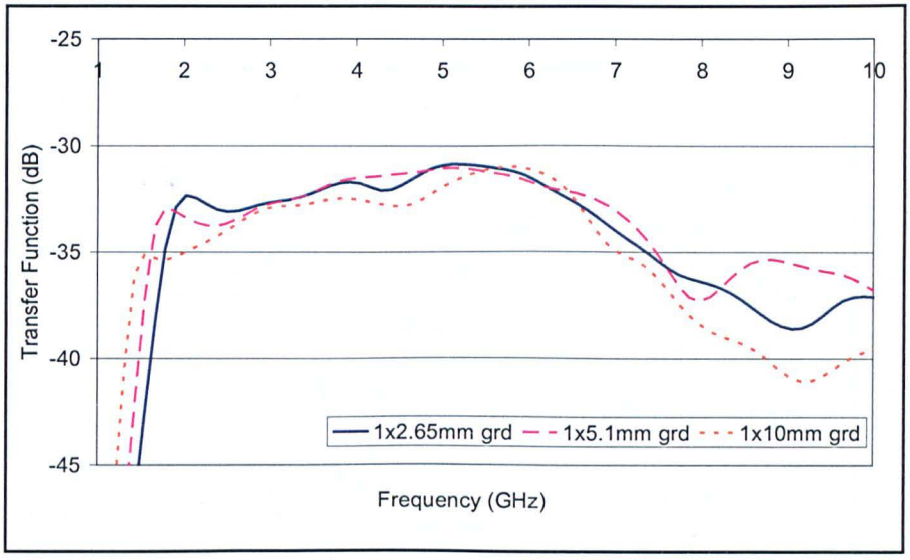

Figure 4.16 The simulated bore sight transfer function magnitudes at 35mm into the phantom for the antenna configurations seen in Figure 4.15.

4.3.6 Effect of Changing the Feed Gap Between the Bottom of the Fork Feed and the Slot Edge

The 'feed gap', or the gap between the lower edge of the slot and the fork feed, is one of the most critical factors when tuning the antenna. Figure 4.17 shows the variation in S_{11} with the size of the feed gap, for the optimised antenna configuration seen in

Section 4.3.5 (17×12mm slot with a 1×5.1mm ground). This shows that as the gap increases in size from 0.5mm to 2.0mm there is an improvement in the -10dB bandwidth from 2GHz (3-5GHz) to 5.5GHz (1.5-7GHz). Above this value there is no significant increase in bandwidth but the response rises above -10dB in the 2.5GHz-0.5GHz frequency range.

The transmission characteristics show a general improvement with increasing feed gap, especially at higher frequencies. Taking both this and the S_{11} results into consideration, the most appropriate feed gap dimension is 2mm. These results also highlight the sensitivity of the antenna's performance to even a small change in this parameter. As such, care must be taken when manufacturing the antenna and the associated tolerances must be taken into account when analysing the measured results.

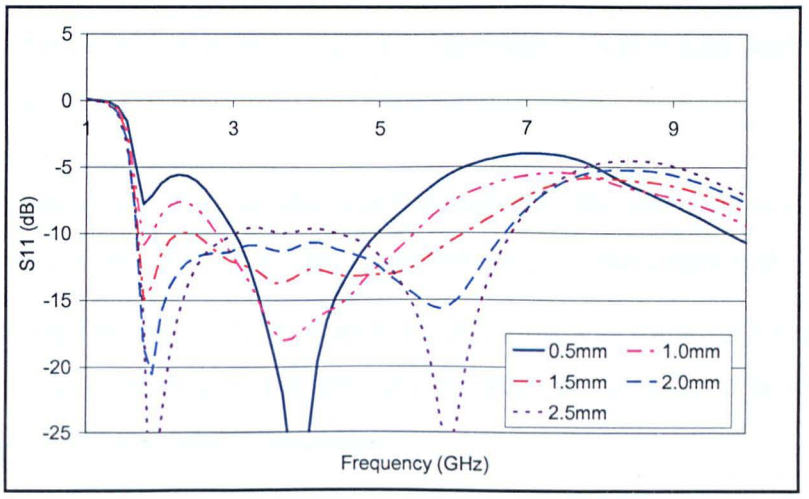

Figure 4.17 The simulated S_{11} magnitude for antennas with a 17x12mm slot, 1x5mm ground plane and various feed gaps.

4.3.7 Effect of Changing Substrate Thickness

The operational bandwidth of the breast imaging system is around 4-10GHz. The lower S_{11} cut off frequency of the antenna is shifted to this value by halving the dimensions of the ground plane (x = 0.5, z = 2.5), feed and slot (8.5×6mm). This antenna was simulated with two substrate thicknesses of 1.27 and 0.8mm that were

being considered for the antenna's manufacture. The input performance of the antenna in each case can be seen in Figure 4.18. It can be seen that while the substrate doesn't affect the bandwidth of the antenna and has little effect at lower frequencies, at higher frequencies the response is significantly improved if the 1.27mm substrate is used. Using the thicker substrate also results in a slight improvement in transmission properties (see Figure 4.19). The boresight transfer function is increased by approximately 3dB across the entire frequency range. The thicker substrate is therefore the preferable option.

4.3.8 Summary of Results

The effect of parameters on the wide-band performance of the Wide-Slot antenna has been quantified using an FDTD simulation. The antenna has been progressively optimised in terms of its geometrical size, impedance bandwidth and transmission properties. The points of note from this investigation were:

1. The most sensitive parameter was the feed-gap. By varying this dimension the antenna can be "tuned" and the impedance bandwidth optimised.
2. Reducing the size of the slot in the *z*-direction was found to have little effect on the performance of the antenna whereas the *x*-dimension was found to dictate the lower cut-off frequency.
3. The size of the *z*-ground has a large effect on the S_{11} of the antenna; the smaller the ground the better the bandwidth however the boresight transfer function shows that a ground that that is either too large or small can have a detrimental effect on the performance.
4. It was found that the thicker substrate improved both the input and radiation characteristics of the antenna.

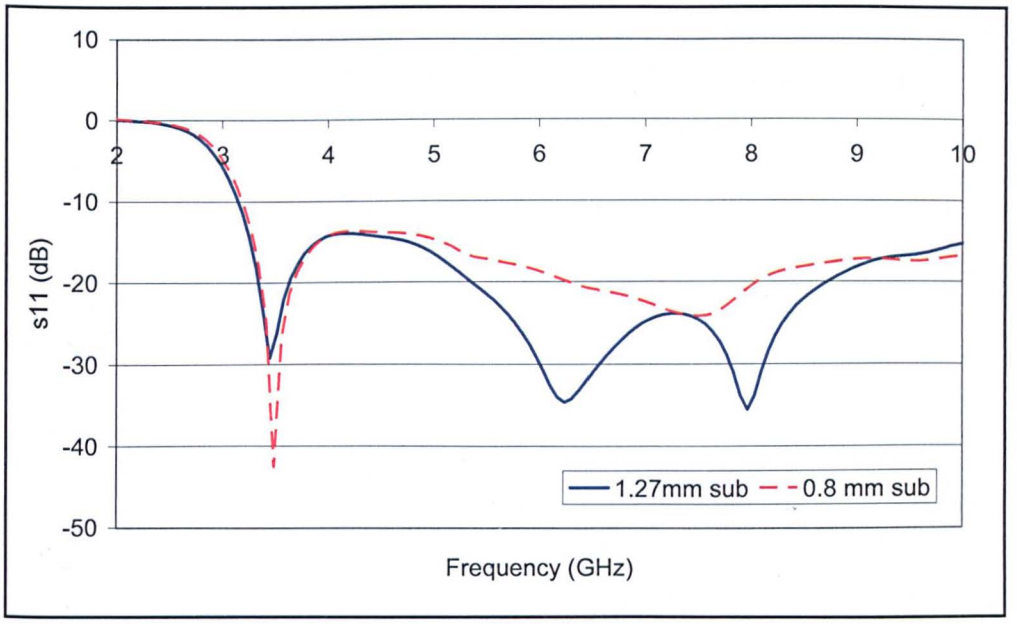

Figure 4.18 Comparison of the S_{11} magnitude for 8.5x6mm slot antenna with a 1mm feed gap on 1.27mm and 0.8mm substrate.

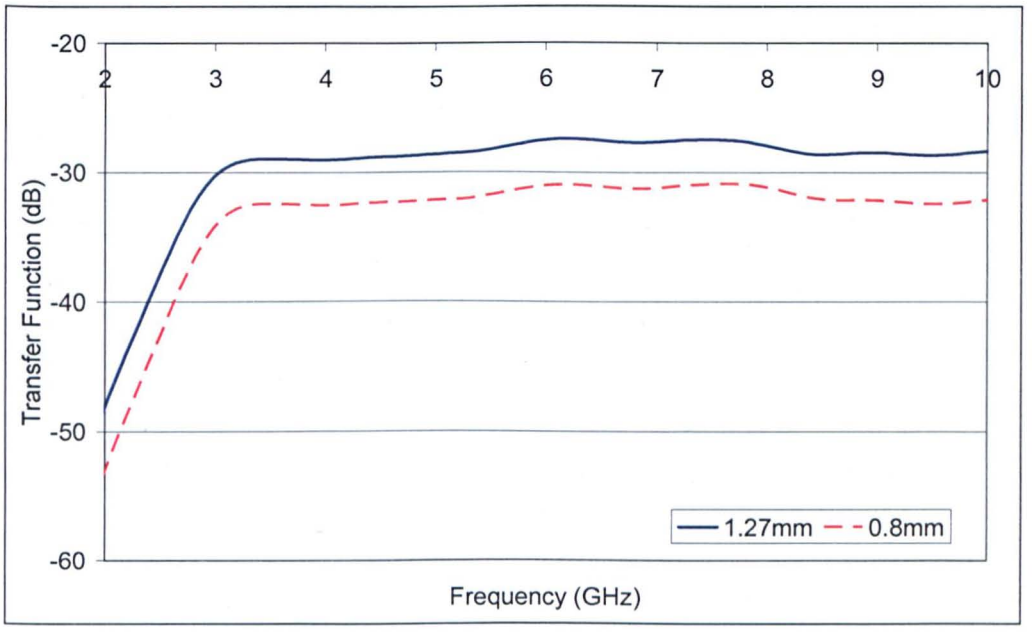

Figure 4.19 The simulated bore sight transfer function magnitudes at 35mm into the phantom for substrate thickness of 0.8 and 1.27mm.

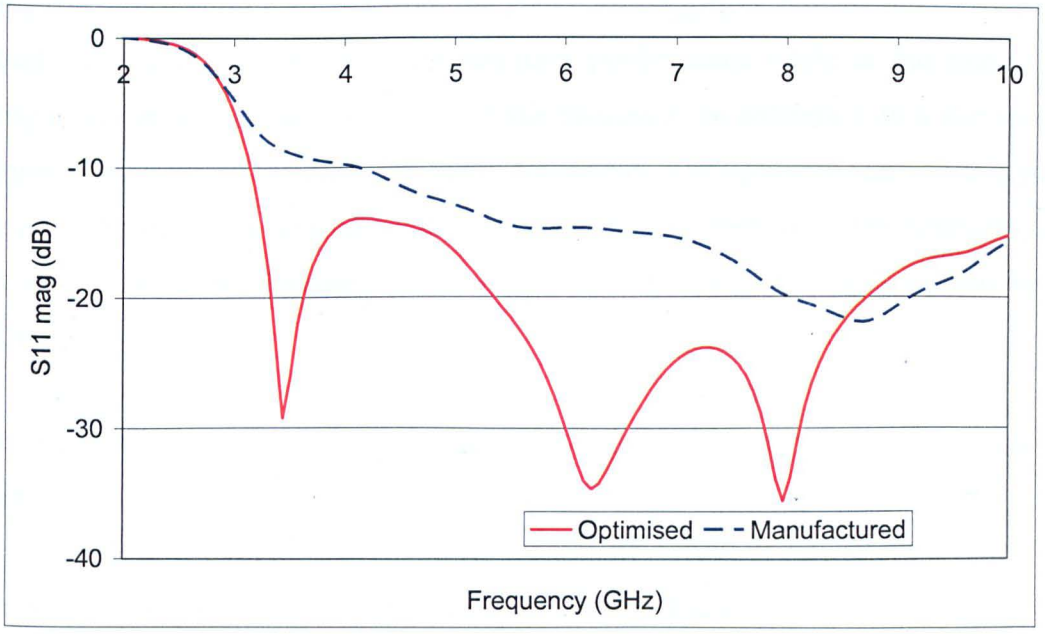

Figure 4.20 the S_{11} magnitude for the optimised and manufactured antennas

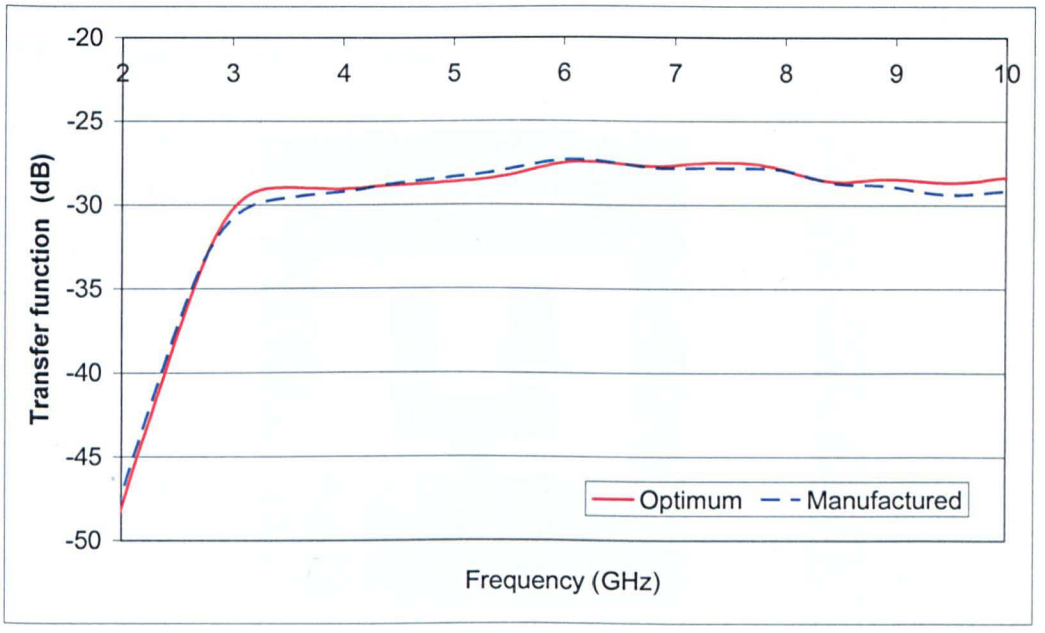

Figure 4.21 The simulated bore sight transfer function magnitudes at 35mm into the phantom for the optimised and manufactured designs.

4.3.9 The Optimised Antenna

Using the information gathered from the above investigation, the antenna design was optimised in terms of its input and radiation performance while at the same time trying to minimise its size. The result of this process is an antenna with a slot size of 8.5mm in the *x*-direction and 6 mm in the *z*-direction. The optimum size of the ground plane is 2.5 mm above and below the slot and 0.5mm either side. The optimum feed gap was 1 mm on a substrate with a relative permittivity of 10.2 and a thickness of 1.27mm.

The simulated return loss of this antenna can be seen in Figure 4.18 under the label; optimised. This shows the antenna has a -10dB impedance bandwidth of better than 1:3.3 from 3 to above10+ GHz, with resonances occurring at 3.5, 6 and 8 GHz. The transmission response of this antenna can be seen in Figure 4.21. This illustrates the fact that the free space transfer function varies by less than 2 dB across the frequency range of 3-10 GHz.

4.3.10 Antenna for Manufacture

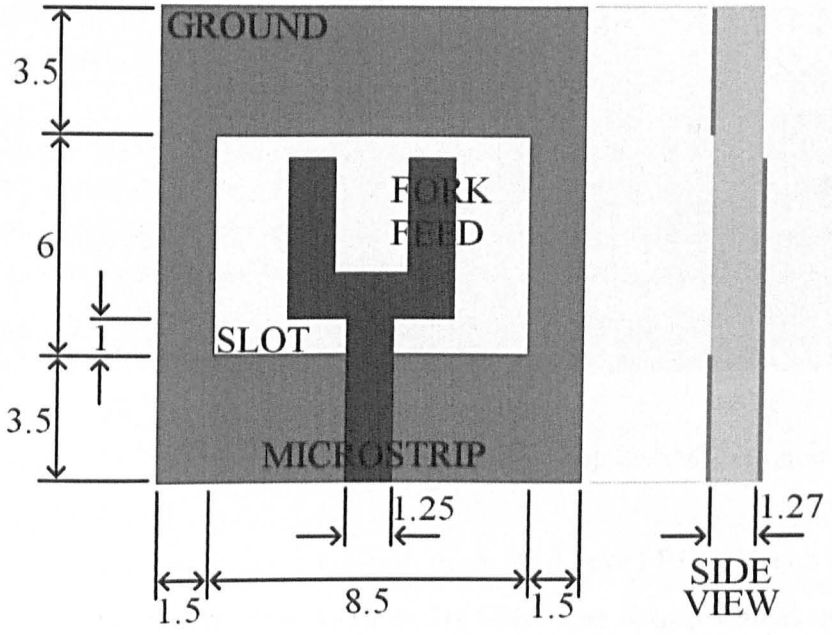

Figure 4.22 The antenna intended for manufacture (all dimensions in mm)

For reasons of manufacture, namely ease of construction and handling, the ground plane of the antenna was increased in size by 1mm on either side and above and below the slot. This finalised antenna design can be seen in Figure 4.22 and a comparison of the S_{11} of this antenna to that of the optimised antenna can be seen in Figure 4.20. With the changes to the ground plane the lower cut off frequency of the -10dB impedance bandwidth is increased by 1GHz to 4GHz while the magnitude of the return loss is increased across the entire frequency range. However when the boresight transfer function is observed (Figure 4.21) it can be seen that the transmission properties of the antenna are largely unaffected by the change. The only noticeable differences between the performances of the two antennas are a drop of about 1dB in the transfer function of the finalised antenna between 3 - 4 GHz and 9 – 10 GHz when compared to the optimised antenna. This gives a maximum variation of 3 dB across the frequency range 3-10 GHz.

4.3.11 The Measured Antenna Performance and Refinement of the FDTD Model

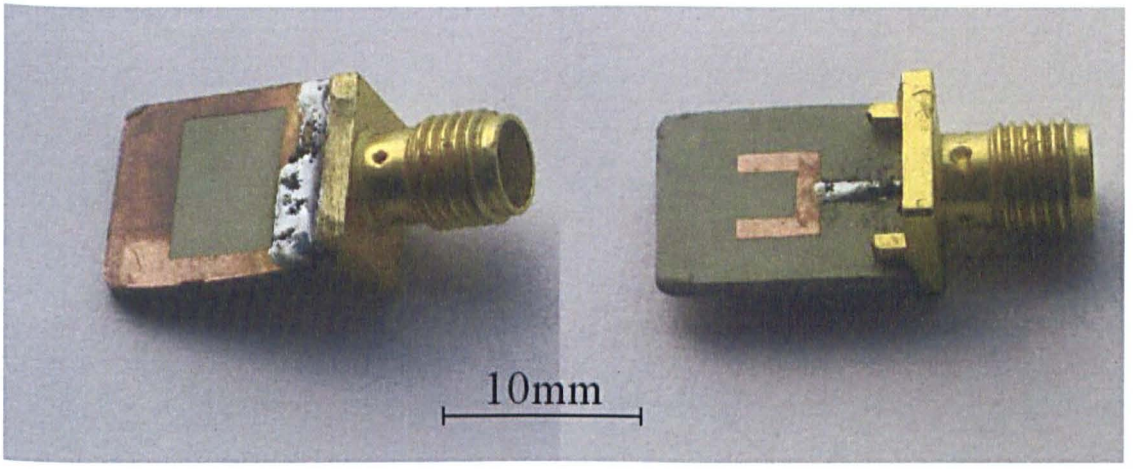

Figure 4.23 The manufactured antenna fed using an SMA connector

The antenna was manufactured on 1.27mm thick RT/Duroid RO3010 substrate which has a dielectric constant of 10.2 ± 0.3 at 10 GHz. The manufactured antenna, fed using a female SMA jack, can be seen in Figure 4.23. To measure the antenna S_{11}, it

was suspended above a large volume of the matching medium developed at the University of Bristol [30] with the slot surface in contact with the medium. The input characteristics were measured using an Anritsu 37397c VNA. These results can be seen in Figure 4.24, which also shows the simulated result for comparison. This indicates that the antenna's measured -10dB impedance bandwidth is in reality smaller than that found for the simulated antenna extending from 4.5-9GHz. The magnitude of the measured return loss is also greater across the entire frequency range the simulation showing the worst agreement at high frequencies.

The fact that the comparison between measured and simulated results showed the greatest difference at high frequencies tends to suggest that it is the feed region of the antenna that is inaccurate as it is usually dictates the high frequency performance of UWB antennas [35]. This idea is reinforced when the SMA feed of the antenna is examined (Figure 4.23); the metal plate on which the jack is mounted visually dominates the antenna. To take this into account and improve the accuracy of the model a "feed plate", of the same dimensions as the plate of the SMA, was added to the model (Figure 4.25). The return loss for this arrangement can also be seen in Figure 4.24.

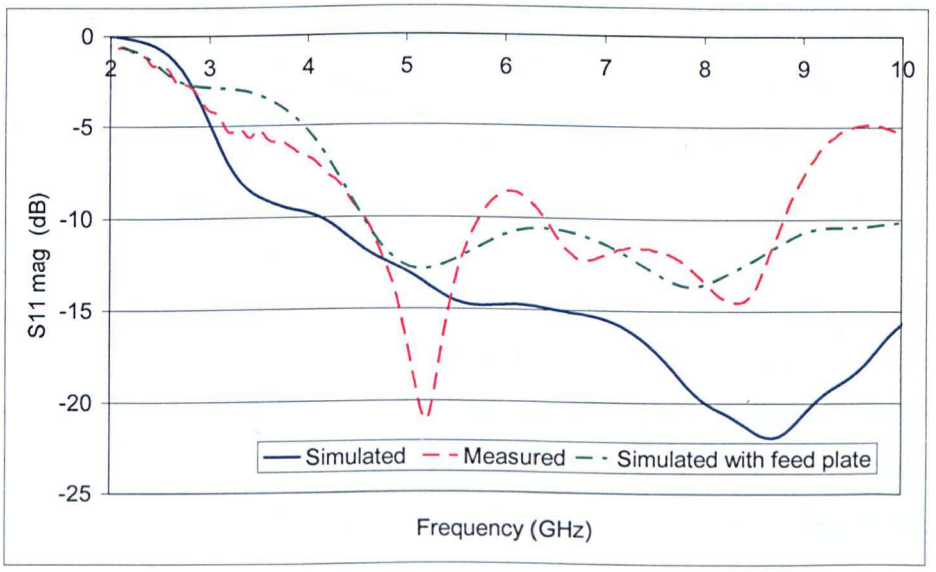

Figure 4.24 The simulated and measured S_{11} magnitude for the manufactured Wide-Slot antenna

The new FDTD model shows a much better level of agreement with the measured results. Both responses have an S_{11} lower cut off frequency of 4.5GHz. Differences between the two plots are probably due to manufacturing errors which inevitably occur at this prototype stage. The effect that just a small difference can have on the antennas performance was highlighted in the development process of this antenna.

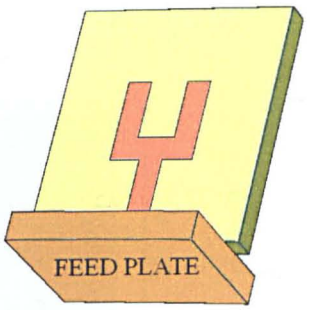

Figure 4.25 The feed plate added to the FDTD simulation

4.4 The Development of the Cavity and Feed

In order to reduce back radiation and coupling between antennas the antenna will be cavity backed. As with the design of the antenna, the geometrical size of the cavity in the x-z plane should be kept to a minimum. The geometrical size of the cavity in the y-direction is primarily dictated by keeping it as practical as possible while minimising its effect on the antenna.

The cavity has been designed by manufacturing a number of different examples and measuring the S_{11} of the antenna using the same method as was used to measure the antenna's performance in Section 4.3.11. The cavities were constructed from 0.25mm copper sheet and lined with 1mm thick Eccosorb FGM40, a material that will absorb any emission from the rear of the antenna. To avoid absorption losses in the feed a 3mm gap was left between the lower extent of the absorber and the rear face of the antenna and the microstrip feed.

Two different cavities were investigated, both which can be seen in Figure 4.26. The smaller of these cavities is a quarter of a wavelength long at 6GHz while the larger cavity is quarter of a wavelength at 3.3GHz. The measured S_{11} of the wide-slot with and without these cavities can be seen in Figure 4.28 and Figure 4.29. It should be noted that the input responses of the two antennas without the cavities are not the same due to differences arising in the manufacturing process.

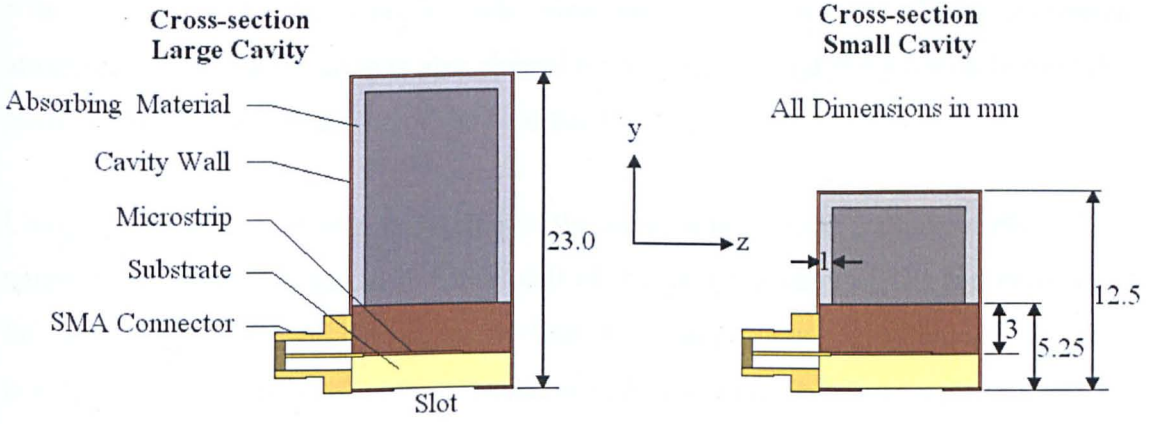

Figure 4.26 Schematics of the constructed cavities

Examining the effect of the small cavity, it can be seen that the -10 dB impedance bandwidth is reduced by approximately 0.5 GHz to 4 GHz. At the same time the lower cut-off frequency shifts from 4.5 GHz to 5 GHz. The response of the antenna above 5.5 GHz is largely unchanged. The effect of the larger cavity is less pronounced. The S_{11} of the antenna is largely unaffected at frequencies above 4 GHz and the -10dB bandwidth is the same as without the cavity. The only significant change is the further degradation in performance between 5.5 GHz - 6.5 GHz. In summary the results suggest that the cavities start to affect the S_{11} of the antenna at frequencies where the y-dimension of the cavity is close to or less than a quarter of a wavelength. As a result the S_{11} of the antenna is largely unaffected by the addition the larger cavity.

4.4.1 The Bent Coaxial Feed

The feed is one of the main contributing factors to the overall geometrical size of the antenna. If a conventional SMA feed is used as in Figure 4.23, the SMA connector is almost as large again as the antenna itself. With the addition of a coaxial cable and male connector, the assembly is at least twice as large as the antenna. In order to address this problem a new feed has been developed that directly feeds the antenna with a section of RG405 coaxial cable, eliminating the need for an SMA connector altogether. The coaxial cable is also shaped in such a way, that it curves up behind the cavity reducing the dimension of the feed still further.

Using this feed the antenna is excited in the same way as with a conventional SMA connector. A hole is made in the side wall of the cavity level with the top surface of the antenna substrate and the microstrip line. The outer conductor of the coaxial cable is soldered to the edges of the hole which is just large enough for the inner conductor and dielectric insulator to pass through. Inside the cavity the dielectric stops at the edge of the antenna substrate and the inner conductor is soldered to the top surface of the microstrip line.

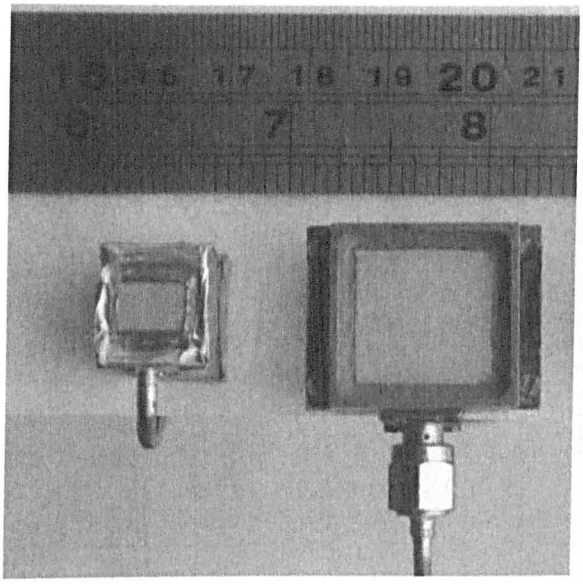

Figure 4.27 The large cavity backed, wide slot antenna with bent coax feed (left). The stacked patch antenna with a standard SMA feed (right)

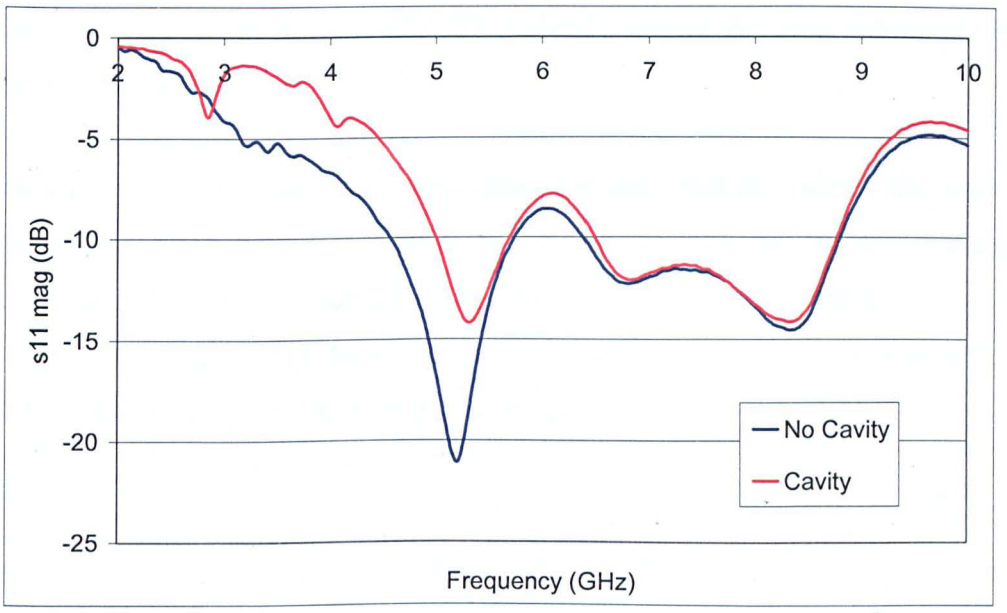

Figure 4.28 The measured S_{11} magnitude of the Wide-Slot antenna with and without the small cavity

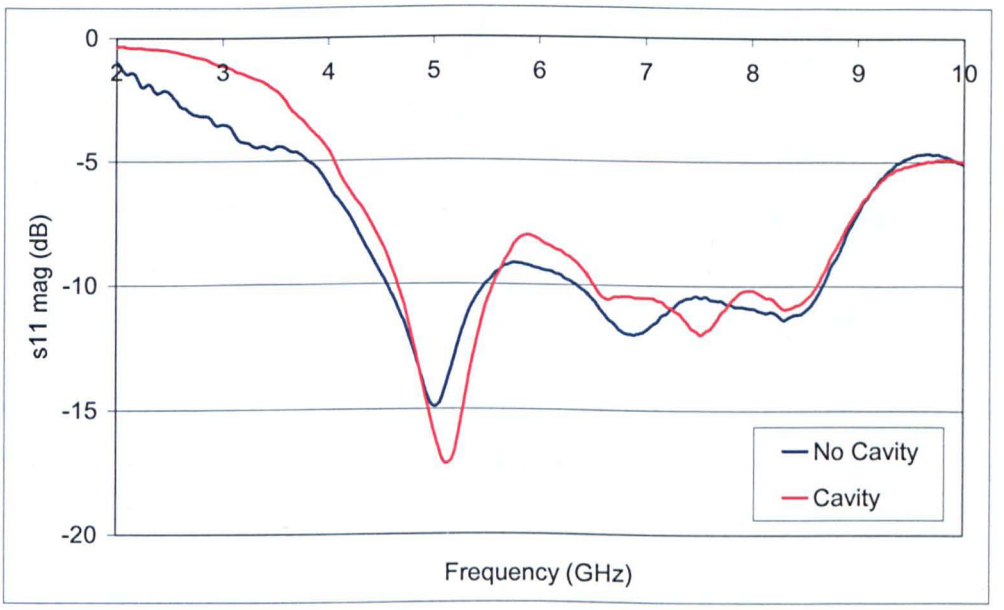

Figure 4.29 The measured S_{11} magnitude of the Wide-Slot antenna with and without the large cavity.

A comparison of the bent coax fed, large cavity backed, wide-slot antenna and the SMA fed stacked patch antenna, with which it will be compared with later in this chapter, can be seen in Figure 4.27. This clearly shows the size reduction that is achieved with the bent feed.

In order to ensure that the bent feed does not detrimentally affect the wide-slot antenna's performance, the measured S_{11} of an antenna fed in this manner is compared to an SMA-fed antenna Figure 4.30. This shows that the bent feed has little effect on the S_{11}, the differences in the two responses can be accounted for by differences that result from the manufacturing process.

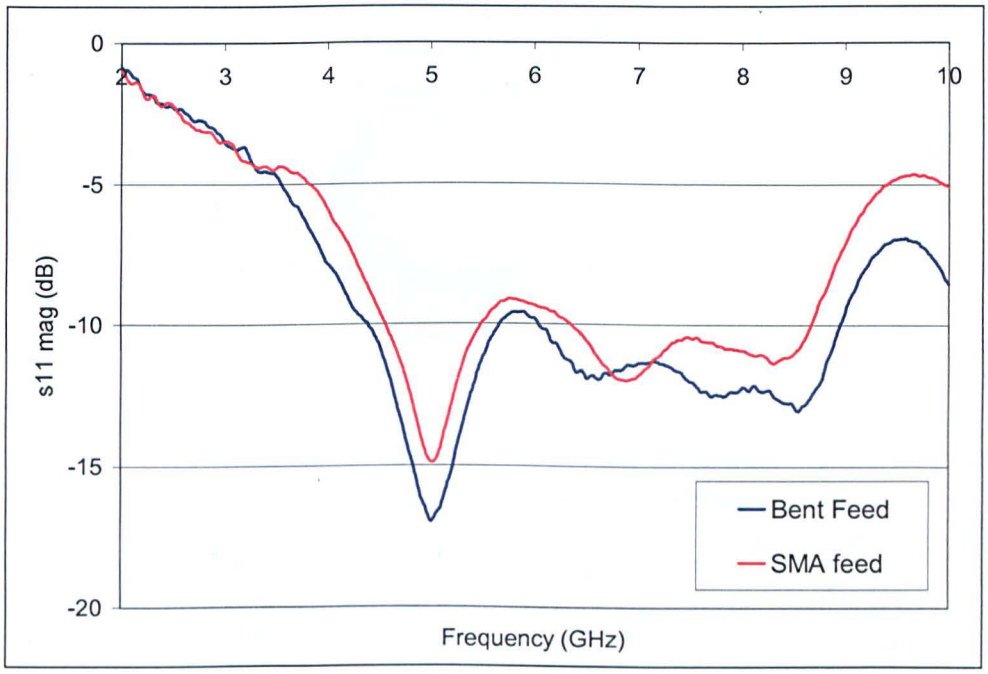

Figure 4.30 Comparison of the measured S_{11} of the Wide-Slot antenna with an SMA and bent feeds.

4.4.2 FDTD Simulation of the Antenna with the Cavity

To allow further investigation into the effects the large cavity, the FDTD model was updated to include it (Figure 4.31). A comparison of the measured and simulated S_{11} of this arrangement can be seen in Figure 4.32. The simulated results show a

reasonable level agreement with the measured response up to approximately 7.5 GHz. Both plots have similar -10dB lower cut off frequencies at 5.2 and 4.5 GHz, the first resonances are at 5 and 5.7 GHz and both plateau after this point. Above 7.5 GHz the two plots diverge, the simulation predicting significantly better performance than was measured. The fact that this occurs at higher frequency suggests that this may be due to differences between the simulated and measured antenna geometries. As the frequency increases the electrical size of the variations and so their effect on the response becomes more significant.

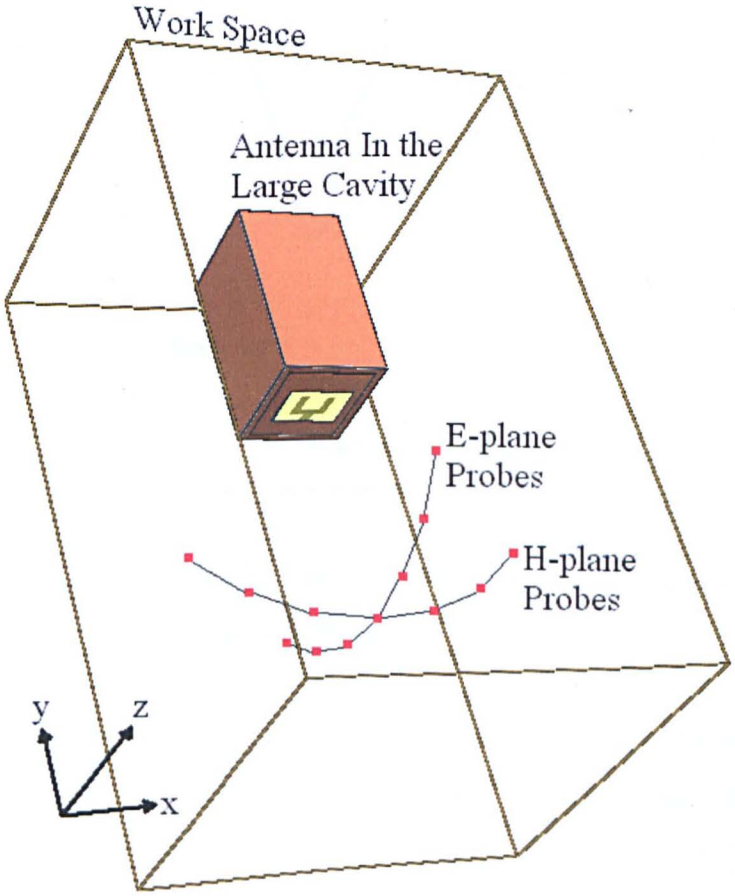

Figure 4.31 The configuration of the FDTD simulation of the large cavity backed slot (Dielectric phantom not shown for clarity).

An important requirement in this application, is that the antenna fields remain as constant as possible with regards to angle from boresight and frequency, ensuring that the radiated microwave signals maintain their fidelity (see Section 2.5.3) regardless of

illumination angle. To investigate the performance in this respect, the near field of the antenna is measured at 14 points across two circular arcs in the E and H – planes (see Figure 4.31). The radius of both arcs is 30mm, centred on the middle of the slot. The angular spacing of the measurement points is 15° giving an angular range of ± 45° in each plane with 0° at boresight.

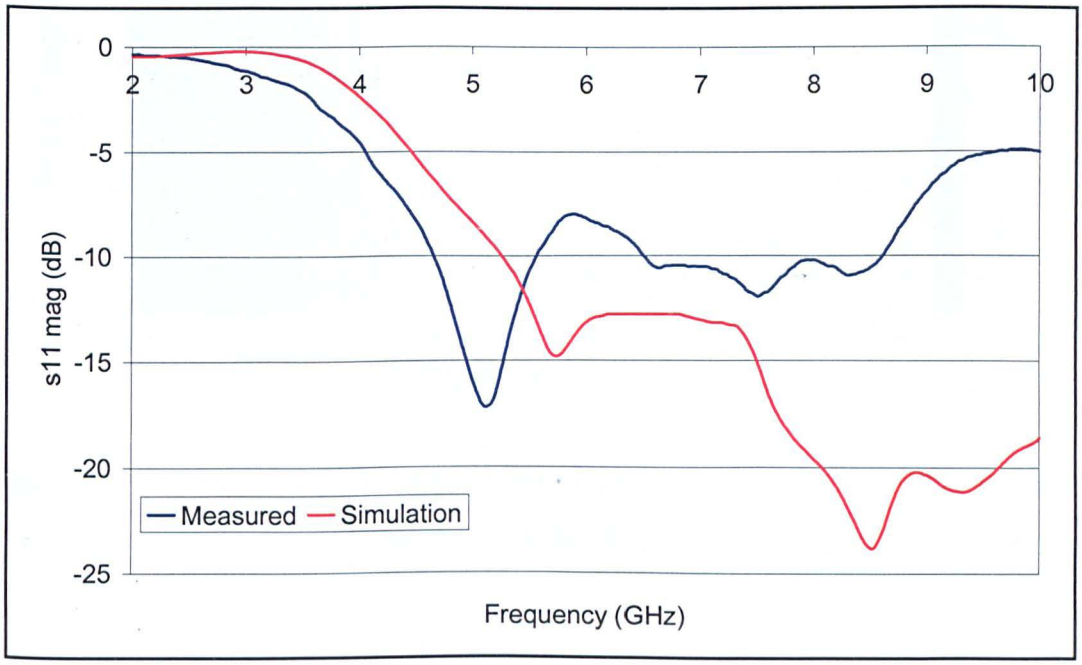

Figure 4.32 Comparison of the simulated and measured s_{11} for the wide-slot antenna backed with the large cavity.

The information from these field measurements was processed in the same manner as for the trident monopole in Section 3.4, providing a way of examining the near field transfer function in terms of frequency and angle from boresight. The H-plane plot in Figure 4.33 shows that from 0Hz to 4GHz the transfer function increases uniformly from -100dB to -30dB across the angular range. The peak in the response corresponds to the point where the return loss also starts to improve rapidly. Between 4 and 8 GHz the antenna shows a reasonably flat response across the angular and frequency ranges. Above 8GHz the response starts to degrade slightly at angles away from boresight. In summary the antenna has frequency stable beam at boresight that narrows slightly at higher frequencies. It should also be noted that the response of this antenna is

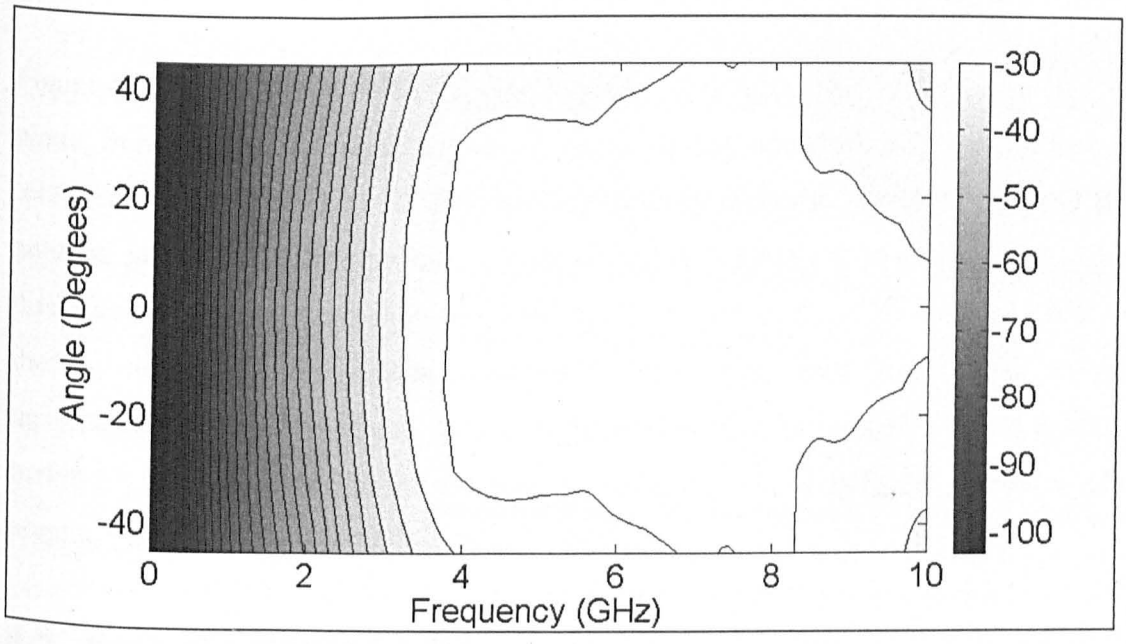

Figure 4.33 Contour plot (level step = 3dB) of the H-plane near-field versus frequency for the wide slot antenna

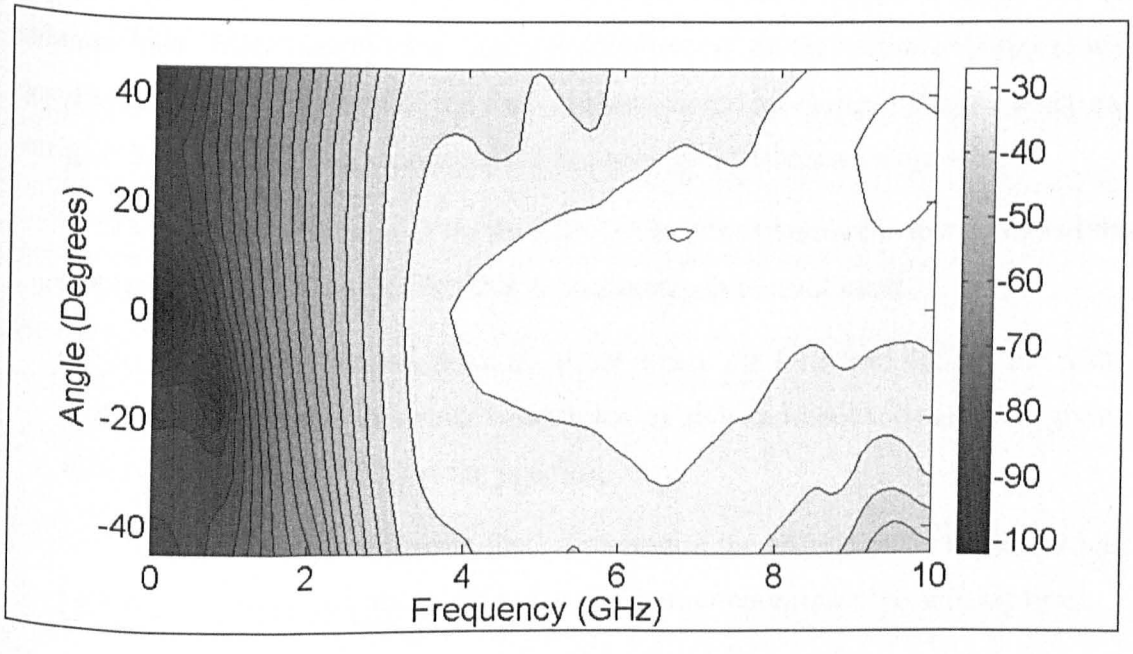

Figure 4.34 Contour plot (level step = 3dB) E-plane near-field versus frequency for the wide slot antenna

symmetrical about boresight due to the symmetrical nature of the antenna's geometry in this plane.

Figure 4.34 shows the same data for the E-plane. This figure shows that as for the H-plane, from 4 to 7 GHz the antenna has a response that, while not quite as uniform, is relatively stable. From 7 to 10 GHz, as the frequency increases, the main beam of the antenna gradually shifts upwards. At 10 GHz the "squint" is at it's greatest. The direction of maximum radiation is shifted by 30° resulting in a difference of 15dB in the S_{21} magnitude the angular extremes (+/-45°). This behaviour is due to the unsymmetrical way in which the antenna is fed in this plane. This frequency instability is undesirable as it will lead to distortion of the radiated signals at the angular extremes.

4.5 Revised Antenna Design

In the last section it was found that the main beam of the antenna showed a "squint" in the E-plane at higher frequencies because of the unsymmetrical nature of the antenna feed. After consultation with other members of the research group it was decided that the arrangement of the feed and slot should be changed slightly to try and mitigate these effects. The changes made to the original antenna design were:

- The horizontal section of the fork feed was moved below the lower edge of the slot in an attempt to reduce the lack of symmetry in the slot itself.
- To minimise reflections from the point where the fork feed divides the width of the fork feed above this point was altered to give an impedance of 100Ω giving an input impedance of 50Ω at the junction.
- The slot itself was shifted in the z direction in the ground plane to make room for the new feed arrangement and to try and further counteract the shifting beam.

The revised antenna design can be seen in Figure 4.35. From this point on the revised antenna will be referred to as version 2 and the previous antenna will be referred to as version 1.

The simulated and measured S_{11} for version 2 can be seen in Figure 4.36. It can be seen that there is a pleasing level of agreement between the two data sets; both have a -10dB bandwidth of more than 5.5GHz with a lower cut-off frequency 4 GHz (4.5GHz in the simulated case) and a higher cut-off in excess of 10GHz. This is larger than the measured S_{11} of version 1. At around 6 GHz there are some points in the measured data where the return loss rises above -10dB. This frequency region will be examined later to assess the impact of this increased level of reflection, on the transmission response. Both simulated and measured results show that there are two major nulls in the response at 4.75 GHz and 7.5 GHz and are in good agreement to their location and magnitude.

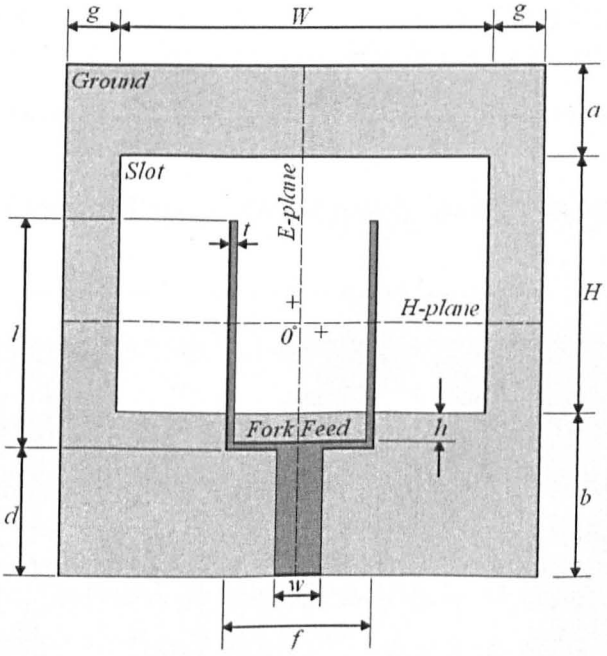

Parameter	H	W	a	b	d	f
Dimension	7	10	2.5	4.5	3.5	4

Parameter	g	h	l	w	Overall
Dimension	1.5	1.8	6.5	1.25	13×15

Figure 4.35 The revised antenna design (all dimensions in mm)

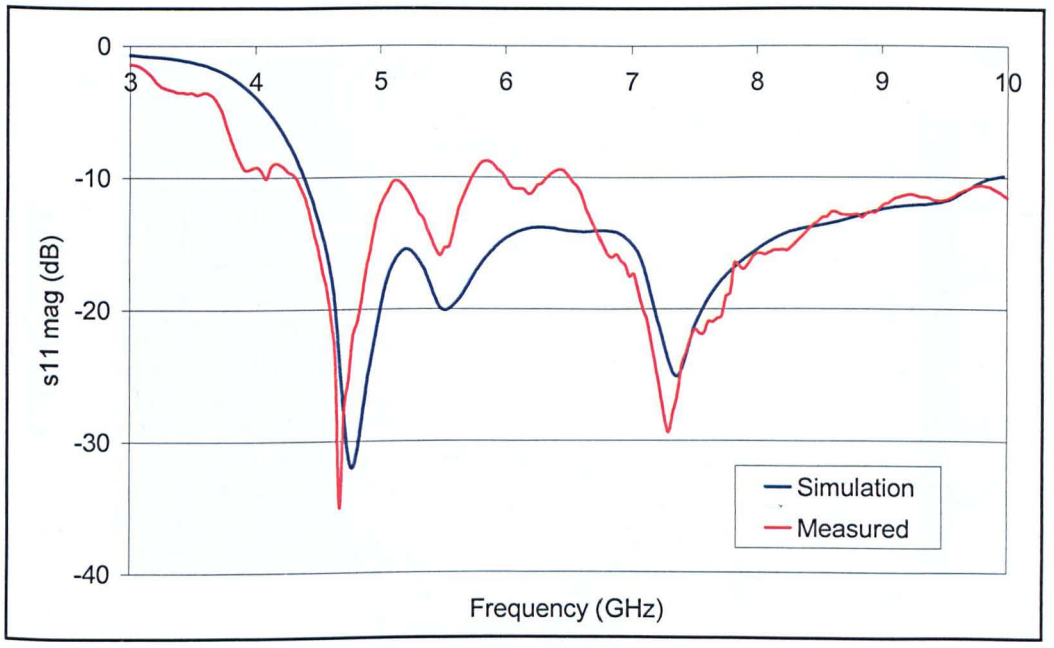

Figure 4.36 Simulated and measured S_{11} of the revised antenna

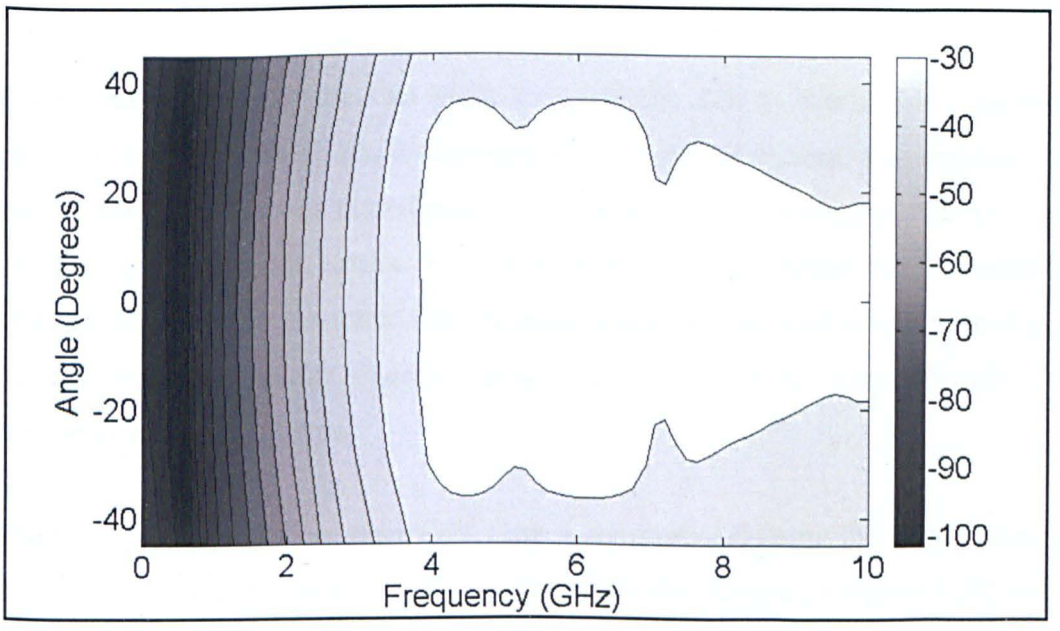

Figure 4.37 A contour plot (level step = 3dB) of the H-plane near-field in terms of frequency and angle from boresight for the version 2 antenna

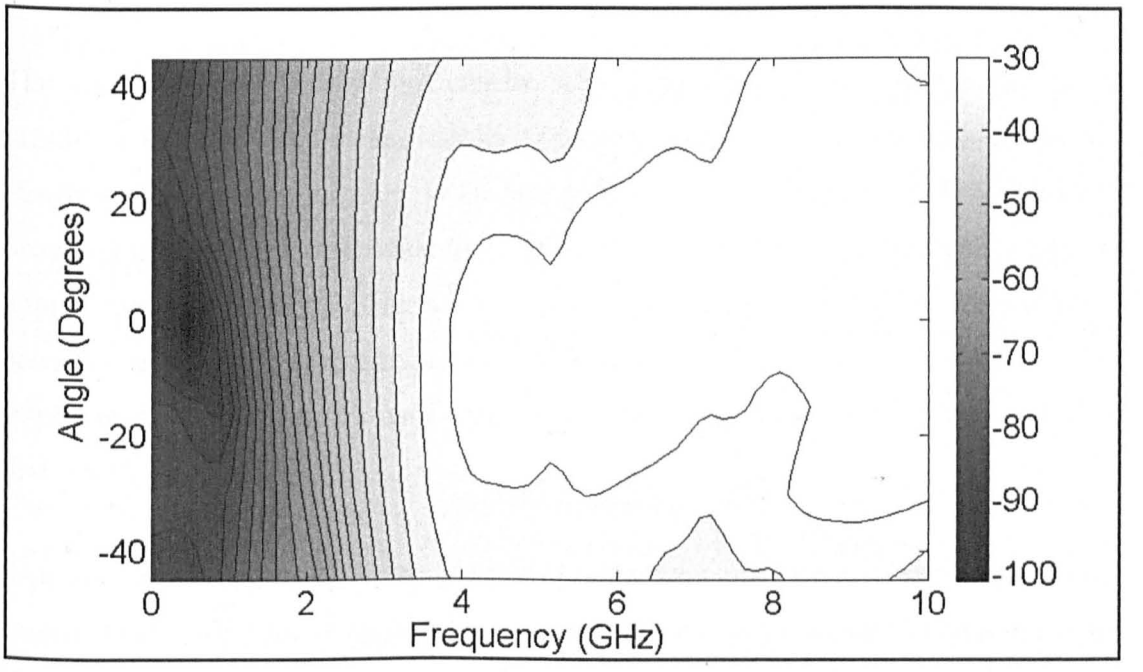

Figure 4.38 A contour plot (level step = 3dB) of the E-plane near-field in terms of frequency and angle from boresight for the version 2 antenna

The differences between the two plots are probably due to fabrication tolerances, particularly the feed, which has dimensions of the order of 0.2mm. The antenna used in these measurements was manufactured with much higher tolerances than that used to produce the results for version 1. This is the most likely reason for the improved agreement between the simulated and measured results. This level of agreement gives confidence that other results obtained using the FDTD model will correctly reflect the true properties of the antenna.

Using the FDTD simulation, near-field plots were produced using the same technique as for version 1. The H-plane, transfer function data for version 2 (Figure 4.37) shows that the main beam of this antenna is broad and relatively frequency independent. The magnitude of the antenna's transfer function varies by less than 6dB from 4-10 GHz across the entire angular range. The beam is symmetrical about boresight and from 8-

10 GHz, narrows with increasing frequency. Overall the beam is slightly narrower than that seen for version 1 most notably between 6 and 8 GHz.

The corresponding E-plane plot can be seen in Figure 4.38 and shows that as for version 1 the near-field beam has an upward squint that increases with frequency. However, in this case the shift is far less pronounced and from 8-10 GHz the beam broadens out giving a difference in magnitude between the two angular extremes of approximately 3dB at 10 GHz, a significant improvement over the 15 dB difference seen for version 1. As a consequence the beam is broader and more frequency stable implying that the antenna will radiate UWB pulses more effectively with less distortion.

The above investigation of the version 2 antenna's performance shows a marked improvement over that of version 1. The changes made to the design seem to have had the desired effect, the impedance bandwidth of the antenna has been maintained while the squint present in the E-plane near field has been reduced.

4.5.1 Effect of the Cavity

The cavity has been included to reduce the backscatter radiation produced by the Wide-Slot antenna. The effect of the cavity can be judged by examining the fields around the antenna. This has been done using the FDTD model already used to model the antenna (see Figure 4.31). The time-domain fields in the H-plane of the antenna have been sampled at 10 degree intervals, at a radial distance of 30mm from the face of the antenna. Performing a Fourier transform on the resultant time-domain signals the antenna fields have been extracted at 3, 6 and 9 GHz. This data is displayed in polar form in Figure 4.39. In each case the plots have been normalised so the magnitude of the field in the direction of maximum radiation is set to 0dB. In these plots 0° corresponds to the direction normal to the slot side of the antenna.

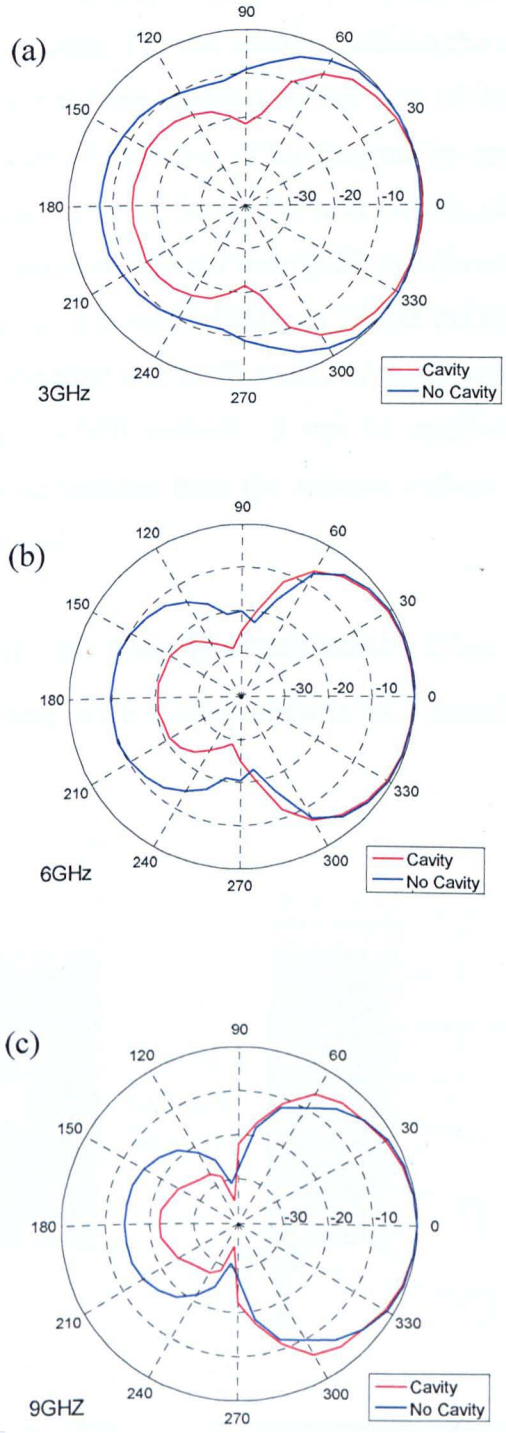

Figure 4.39 The Simulated H-plane antenna fields of the Wide-Slot antenna with and without the cavity at (a) 3GHz (b) 6 GHz (c) 9 GHz. The radial scale of the plots is the normalised field magnitude in dB.

These plots show that both with and without the cavity the radiation occurs is greater from the slot side of the antenna. For the antenna without the cavity this is primarily due to the presence of the matching medium on this side of the slot. The presence of the cavity reduces the backward radiation of the antenna by approximately 8-10dB at all three frequencies while the main boresight lobe of the antenna remains largely unaffected. Subsequently the front-to-back ratio (FBR) of the cavity backed antenna is significantly better than when it is unshielded: At 3 GHz the FBR is 14.6dB with and 7.2dB without, at 6 GHz the FBR is 20.6dB with and 9.7dB without and at 9 GHz the FBR is 22.3dB with and 14.3dB without. It can be concluded that the cavity is significantly reducing the backscatter from the antenna without significantly affecting the boresight radiation pattern.

4.6 An Investigation of the Transmission Characteristics of the Wide-Slot Antenna with Comparison to a Stacked Patch.

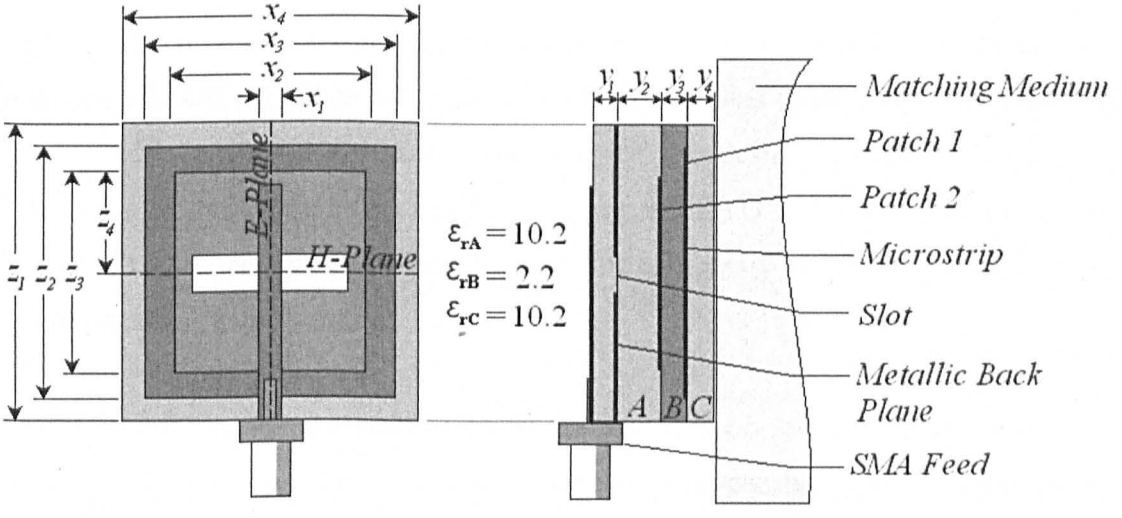

Parameter	x_1	x_2	x_3	x_4	y_1	y_2
Dimension	0.66	6.0	9.0	18.0	0.64	1.9

Parameter	y_3	y_4	z_1	z_2	z_3	z_4
Dimension	0.8	1.27	18.0	6.5	6.0	3.0

Figure 4.40 The stacked patch comparison antenna (all dimensions in mm)

In this section the radiation performance of version 2 of the Wide-Slot antenna will be measured and compared with that of a slot-fed, stacked patch antenna that was previously designed for the same application and closely based on that seen in [28] (see Section 4.2.3). The experimental setup used in the transmission measurements will be discussed. The input and transmission response of the stacked patch will be compared to the wide-slot. Finally the results of a simple radar experiment will be presented and discussed.

4.6.1 The Stacked Patch

Figure 4.40 shows the stacked patch antenna that will be compared to the wide-slot. It should be noted that this figure shows the antenna without the cavity used to back the antenna while taking measurements. The antenna consists of a microstrip line feeding a slot, which in turn excites an arrangement of stacked patches. The slot feed was used in order to eliminate the inductance associated with a probe feed. The patches sandwich a lower permittivity substrate and their size was chosen such that a lowest order resonance was achieved at either end of the desired frequency band. The dimensions were then manually optimised using an FDTD computer simulation [28]. Figure 4.27 shows this antenna mounted in the cavity used for the following measurements.

The measured S_{11} for the stacked patch antenna can be seen in Figure 4.41, also included in this figure is the S_{11} for the Wide-Slot. Comparing the performance of the two antennas it can be seen that both show similar performance, with similar -10dB bandwidths; the patch demonstrating a 5.5GHz -10dB bandwidth between 4.25 and 9.75GHz. As with the Wide-Slot, the patch antenna data also shows a drop in performance across the frequency range of interest between 7.3 and 8.3 GHz where the s_{11} rises to -8dB at it's maximum. This discrepancy will be examined in the measured transmission response.

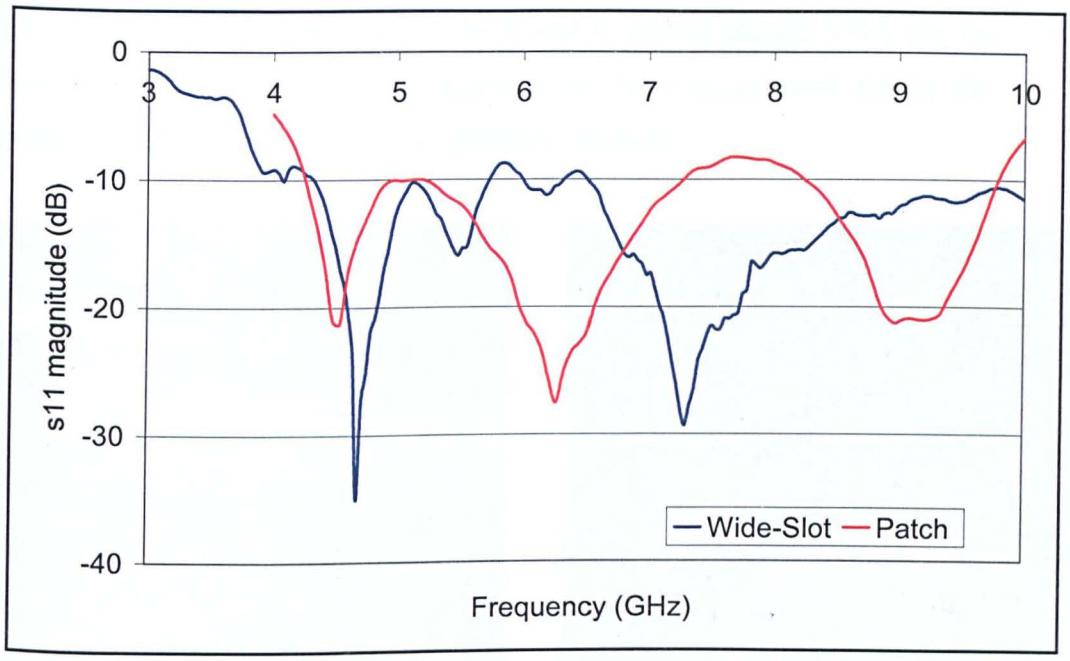

Figure 4.41 Measured S_{11} for the Wide-Slot and patch antennas.

4.6.2 Experimental Arrangement

In order to fully characterise the antennas the radiation characteristics must be determined. As these results are required with the antennas radiating into a breast phantom, obtaining measurements, especially the radiation data, is quite a challenge. Since it is the transmission performance between two of the antennas that is the critical factor in the imaging application and due to a lack of suitable reference antenna, the radiation characteristics of the antenna under test were found by measuring the transmission between two identical antennas of that type.

The experimental setup used to take measurements can be seen in Figure 4.42. In this arrangement both receiving and transmitting antennas are immersed in a large tank of the matching medium/phantom (1). The transmitting antenna (2) is fixed close to the tank wall in a stationary position facing out into the medium. The receiving antenna (3) is mounted on a rig (4) that describes an arc of radius 100mm around a central point at which is the centre of the face of the first antenna. The manner in which the second rig follows the arc results in the second antenna always directly facing the

first. Measurements were taken in the E and H planes using a VNA (5), the chosen plane selected by attaching the antennas to the measurement rig in the correct orientation before immersion in the phantom medium.

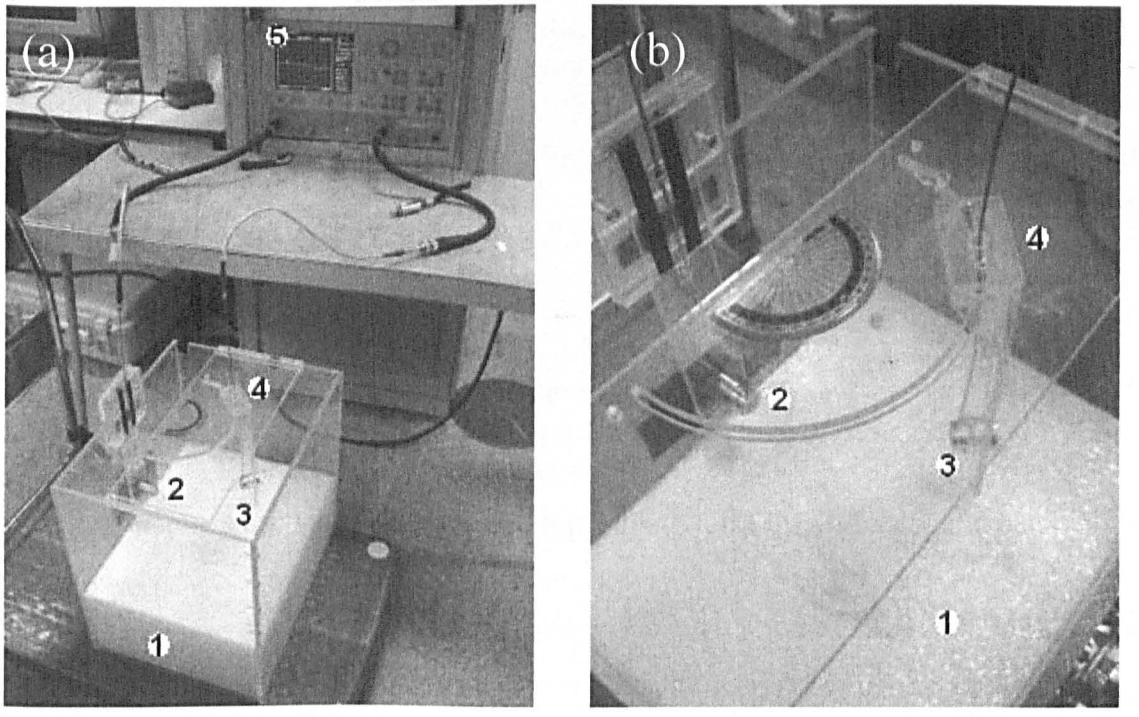

Figure 4.42 (a) Experimental arrangement (b) close-up of positioning apparatus.

4.6.3 Transmission Response

As has already been discussed, for an antenna to radiate UWB signals with minimal distortion, the magnitude of the antenna transfer function must be as flat as possible across the required frequency range [36]. Examining the measured bore-sight S_{21} in Figure 4.43 (bore-sight being normal to the plane of the antennas – see Figure 4.35 and Figure 4.40) shows that both antennas have approximately the same performance; both having a maximum magnitude around 4GHz which then drops steadily with frequency.

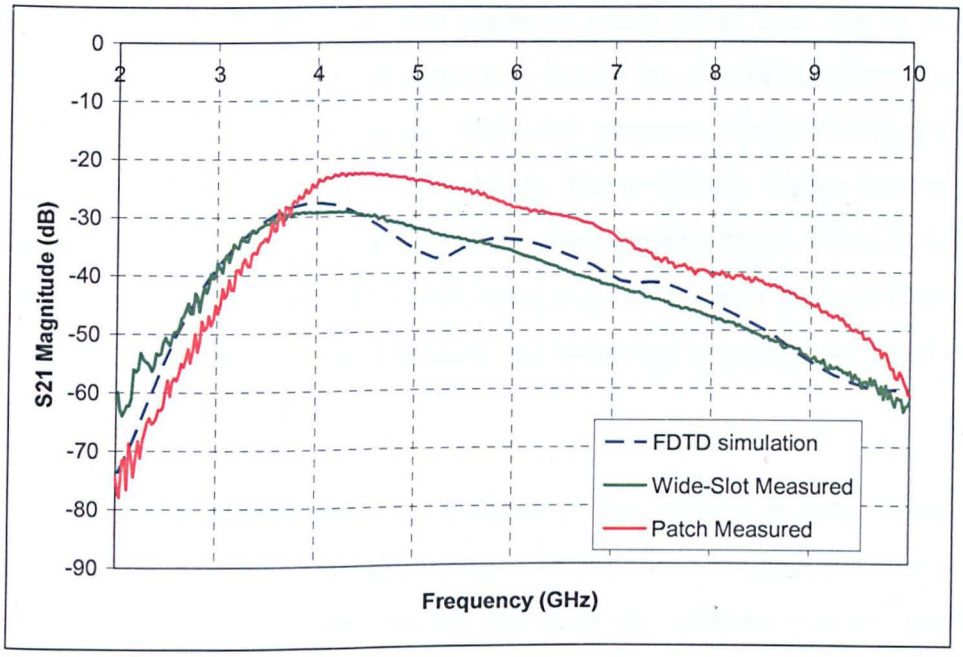

Figure 4.43 Simulated and measured boresight S_{21} for the wide-slot and patch antennas

The major difference is that between 4 to 9 GHz the magnitude of the stacked patch transfer function is consistently 7dB higher. This is because (as will be shown later) the main beam of the patch antenna is narrower than that of the wide-slot, concentrating the radiated energy at bore-sight. In other words, the patch has a higher gain due to its larger aperture. This can be illustrated by finding the directivity of both antennas at bore-sight [D_0], using an approximation based on the main beam-widths at a single frequency. Assuming that each antenna only has one main lobe the directivity in dBs is given by equation 2.26. In this case θ_{1r} and θ_{2r} are the 3dB beam widths in degrees for the E and H – planes. Substituting the beam width values for the patch and slot at 4.5GHz gives;

$$D_{0slot} = 10\log\left[\frac{41253}{74^\circ \times 78^\circ}\right] = 8.5\text{dB}, \quad D_{0patch} = 10\log\left[\frac{41253}{54^\circ \times 64^\circ}\right] = 10.8\text{dB}$$

Hence the gain would be approximately 2.3 dB less for the wide-slot antenna than for the patch. The transfer functions in Figure 4.43 are measured using two antennas,

therefore for one antenna the wide-slot's gain is 3.5dB lower than that of the patch. Comparing this value to the 2.3 dB difference due to the change in aperture it can be seen that the lower directivity of the wide-slot accounts for the majority of this difference; the remaining 1.2dB is most likely due to slightly higher back-radiation from the slot or to measurement errors. The wider antenna beam (hence lower gain) seen in the results for the slot is desirable, since it gives the most uniform illumination of the breast by the antenna array elements, the reduction in bore-sight gain is simply an unavoidable consequence of this.

The main reason for the shape of the slope of the graphs in both cases is the attenuation in the matching medium, which increases with frequency. This is borne out in the fact that the simulated S_{21} for the wide slot antenna was practically flat before losses in the phantom were taken into account. With their inclusion (post simulation using a frequency dependent model) the simulated results show a good level of agreement with the measured data.

Referring back to the issues with the S_{11} data raised in Sections 4.3.10 and 4.6.1. The transmission performance of the wide-slot antenna seems unaffected by the slight mismatch in the 6 GHz region. However, the stacked patch transfer function does show a slight dip at around 7-8 GHz indicating that in this case the mismatch may be having an effect. Neither of these effects is very significant.

Examining only the bore-sight gain gives a limited view of the antennas' performance. To get a better understanding of the radiated field, the E and H-Plane transfer functions have been measured between 2 and 11 GHz. Measurements were made with an angular resolution of 15°, over the range +60° to -60° away from bore-sight. This information has been processed in the same way as in Section 3.5.4.1 to produce plots of the field in terms of angle and frequency. These can be seen in Figure 4.44 - Figure 4.47 (in these figures an angle of 0° corresponds to boresight).

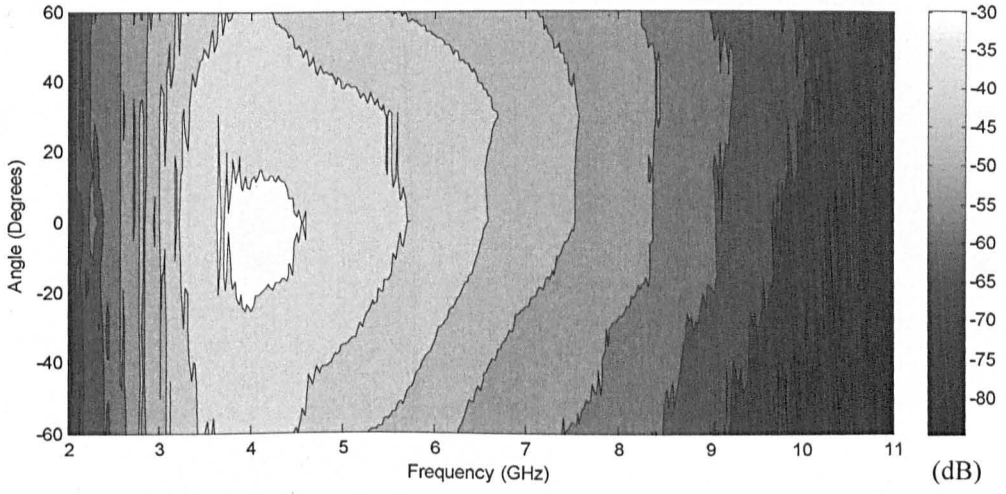

Figure 4.44 Measured S_{21} E-plane data for the wide slot antenna

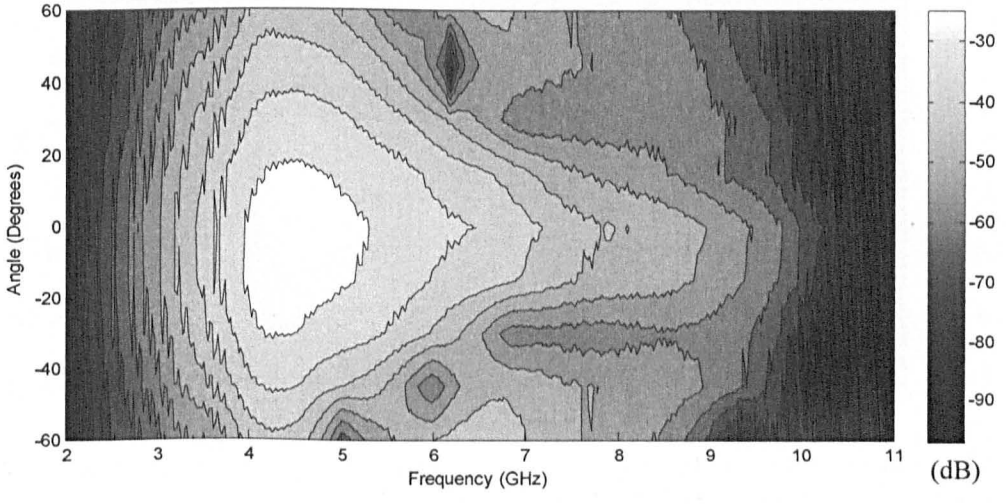

Figure 4.45 Measured S_{21} E-plane data for the patch

Examining the E-plane transfer function data shows that the wide slot antenna (Figure 4.44) maintains its signal strength across the angular range examined. The antenna has maximum field strength at 0° but never drops below 10dB of this value. The variation in the magnitude with frequency is similar at all angles. As was seen for the simulated results there seems to be a slight squint in the positive direction, at higher frequencies that is probably a result of the lack of symmetry in this plane. This squint is minimal, manifesting itself as a 3-5dB difference between values at the angular extremes.

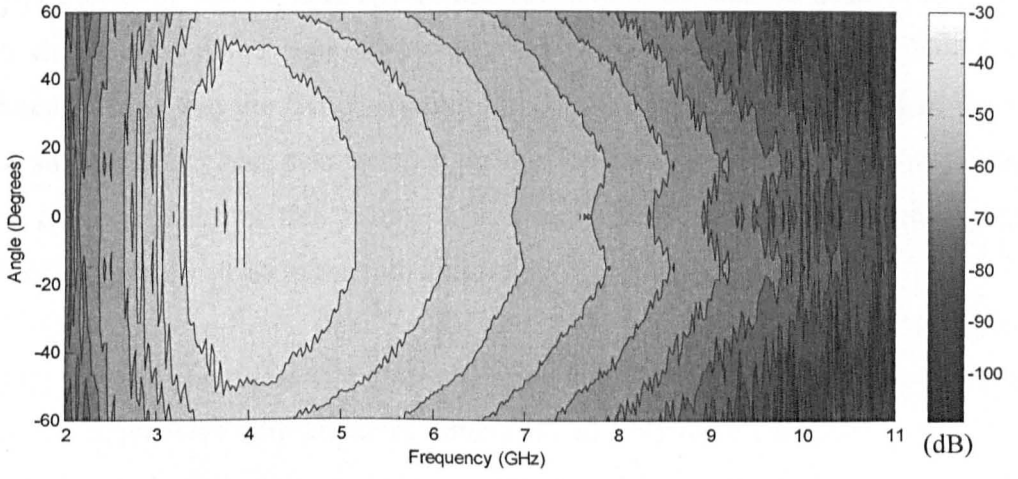

Figure 4.46 Measured S_{21} H-plane data for the wide slot antenna

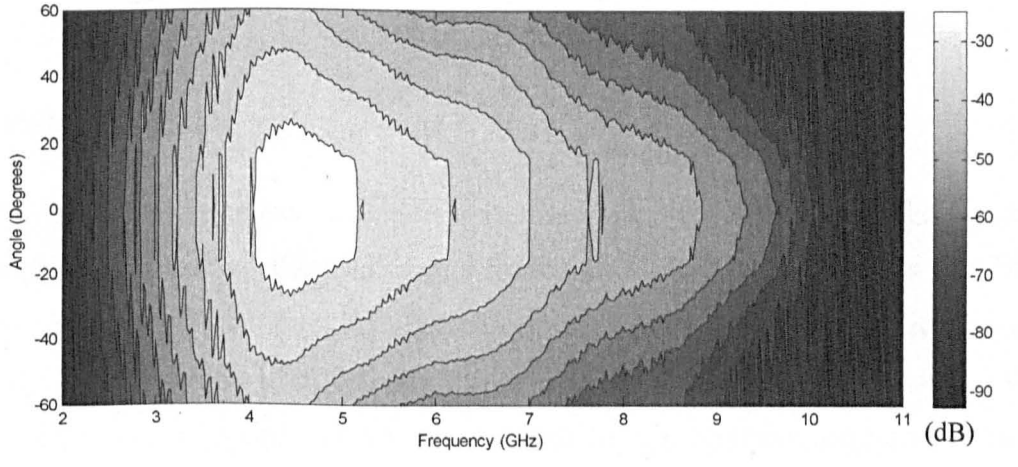

Figure 4.47 Measured S_{21} H-plane data for the patch

Figure 4.45 shows the equivalent results for the patch. This shows that the main beam of the patch antenna is narrow and much less consistent in comparison and above 7 GHz splits into a number of lobes which vary by up to 25dB between the nulls and peaks in only 30°. The drop off of signal magnitude at higher frequencies noted in the bore-sight transfer functions (Figure 4.43) is again highlighted between 9 and 10 GHz, with the addition that at more extreme angles this occurs at lower frequencies.

The asymmetries in the E-plane S_{21} of the patch (and as will be seen later, pulse duration data) are related and likely due to the feed. The microstrip/slot feed arrangement means that the fields exciting the patches are not symmetrical in the E-plane (a similar effect can also be seen in the form of the squint in the wide-slot radiation characteristics in this plane). These asymmetries in the field feeding the patches lead to asymmetries in the radiated fields.

Examining the equivalent H-plane results (Figure 4.46 and Figure 4.47) it can be seen that at most frequencies both antennas have a broad, relatively consistent beams that are symmetrical about bore-sight. The symmetry in these plots arises because the antennas are also symmetrical in this plane. It should be noted that, as in the E-plane, the wide-slot antenna shows a flatter response across frequency and angular ranges, the beam width of the patch becoming narrower at higher frequencies.

4.6.4 Pulse Duration

For radar-based breast cancer detection it is important that pulses produced by the antenna (or in this case synthesised from a frequency sweep) are as short as possible with minimal late-time ringing [11]. Therefore pulse duration is a good indication of the ability of the antenna to effectively transmit UWB signals into the medium. To test this, the measured frequency domain S_{21} data for the transmission between two antenna elements was obtained. Pulses were then synthesised by applying the pulse template to this transfer function. Some examples of received pulses can be seen in Figure 4.48 while a detailed description of the time and frequency domain responses of the template pulse can be seen in [37].

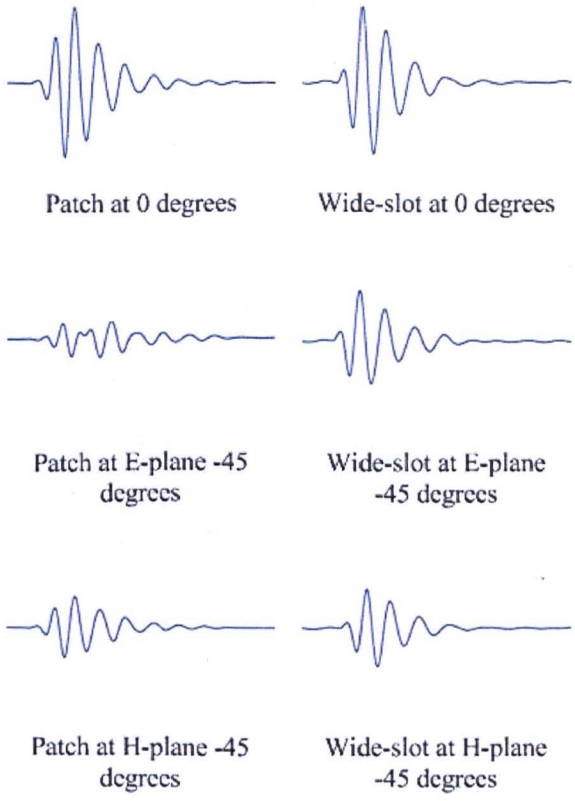

Figure 4.48 Examples of Pulses Synthesised from Measured Transfer-Functions Normalised to the Maximum Field Strength at 0°. Each pulse is displayed in a 2 ns time window.

The time taken for 99% of the energy of these pulses to be received was then calculated. This process was carried out in the E and H-planes at an angular resolution of 15° from +60° to -60°. Pulse durations for the E-plane (Figure 4.49) show that, as in the S_{21} plots, there is an asymmetry present for both antennas. The performance of the wide slot shows in general that the pulses produced by this antenna are shorter and there is far less variation with angle (0.8-0.9ns) than those produced by the patch (0.75 – 1.45 ns). This can be seen in the example pulses (Figure 4.48) where there is little difference between the pulses produced by both at bore-sight but significantly more late-time ringing at -45° in the pulse produced by the patch.

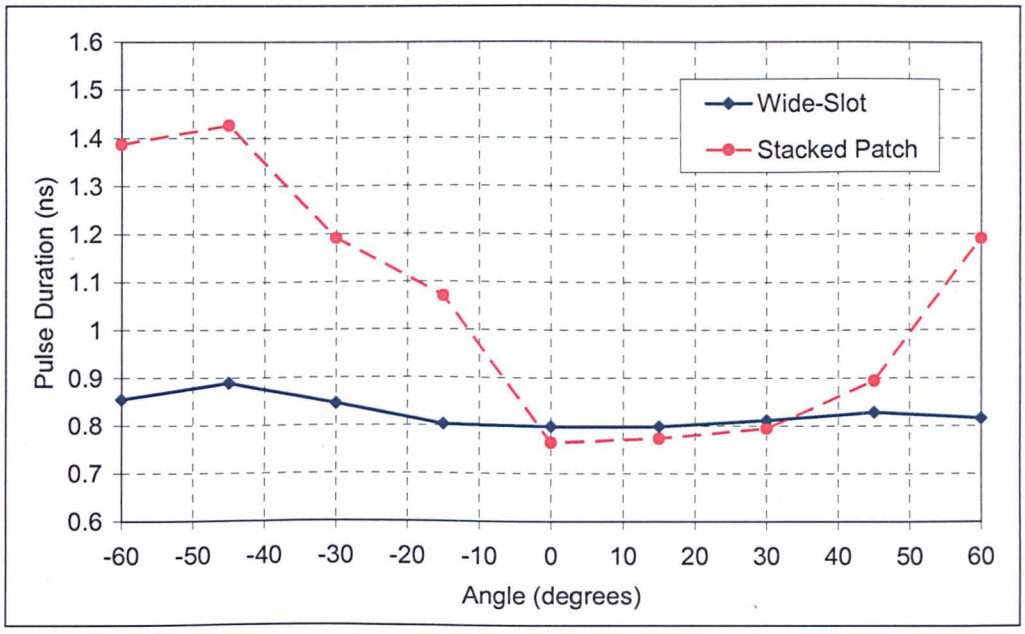

Figure 4.49 Comparison of measured pulses' duration (99% of pulse energy) in the E-plane

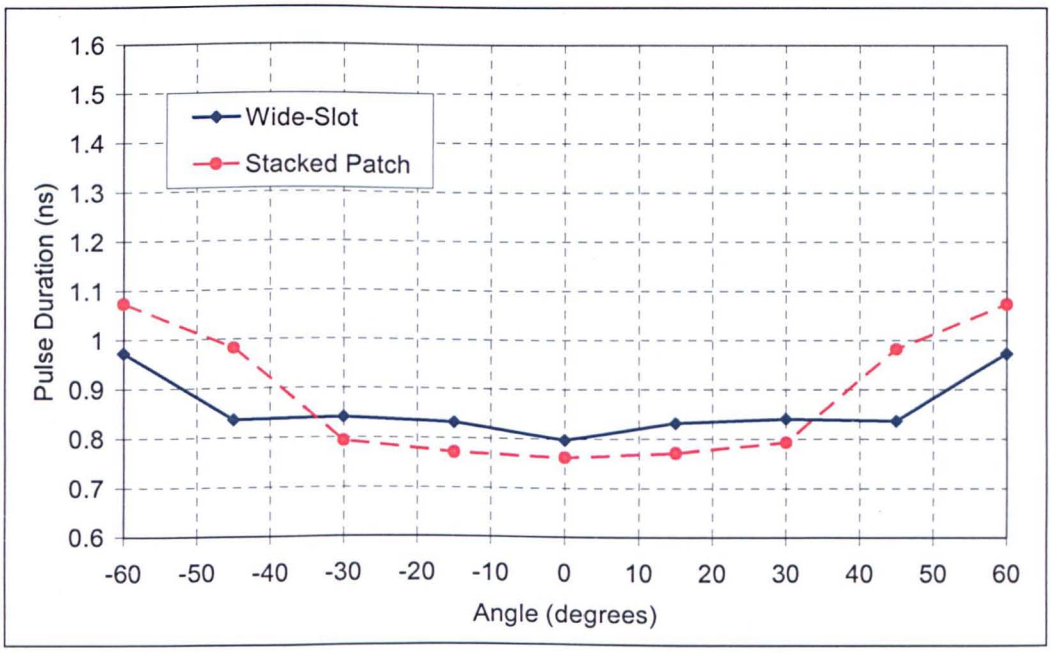

Figure 4.50 Comparison of measured pulses' duration (99% of pulse energy) in the H-plane

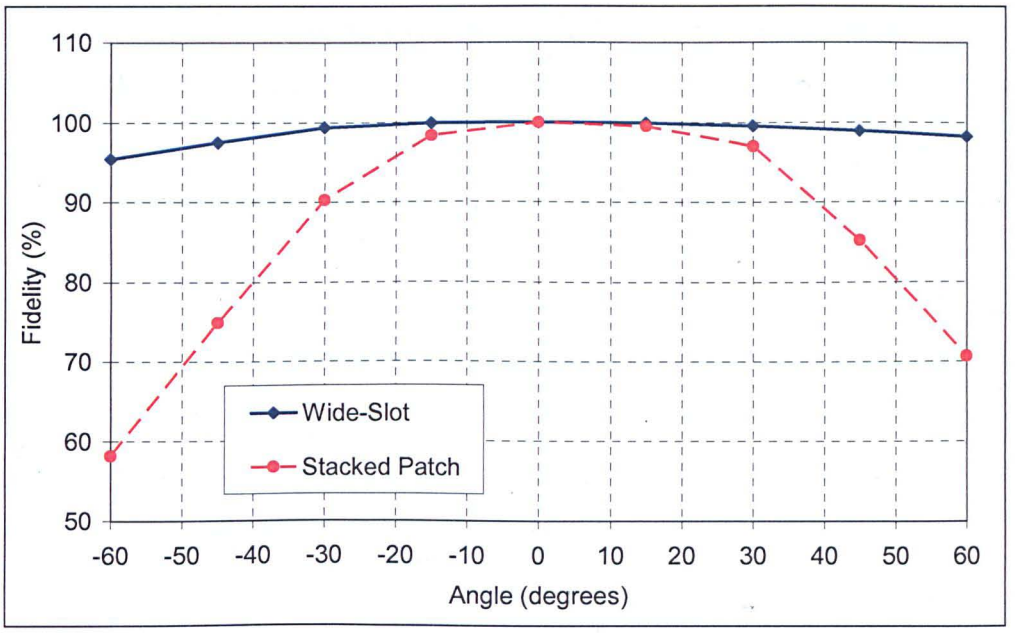

Figure 4.51 Comparison of measured fidelities in the E-plane

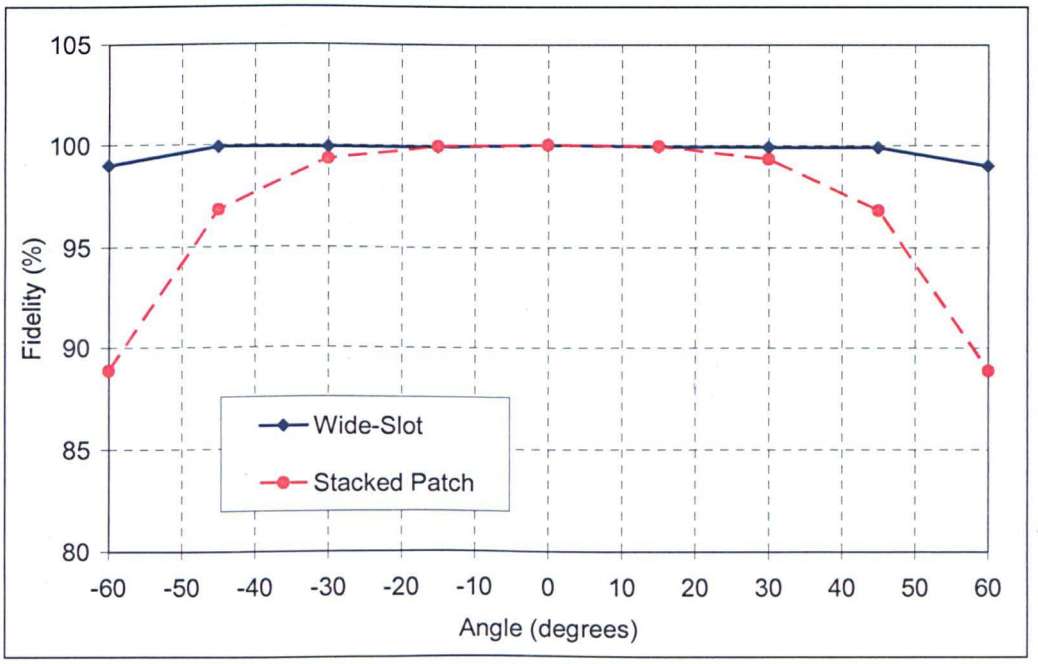

Figure 4.52 Comparison of measured fidelities in the H-plane

Examining the equivalent H-plane data (Figure 4.50) shows that the wide slot antenna maintains a pulse width of just above 0.8ns in the range of +/-45°, this rises to a value of 0.97ns at the angular extremes. The patch antenna shows a marginally better

performance than the wide-slot between the angles +/-30°, with a pulse duration of just below 0.8ns. Beyond these angles the length of the pulses increases to 0.98ns at +/-45° and 1.07ns at +/-45°. As with the E-plane this difference is illustrated in Figure 4.48 where, although not as marked as in the E-plane there is still evidence of late-time ringing.

The difference in the performance of the two antennas is the result of the poorer transmission properties of the patch antenna at high angular values (Figure 4.45) when compared to the equivalent transmission characteristics for the wide-slot (Figure 4.44), which are much more similar to those at bore-sight.

4.6.5 Fidelity

In order to study the level of distortion in the radiated pulses the fidelity (see Section 2.5.3) of the signals was computed at the same points for which pulse duration was found. In this case the reference signal (E(t)) was the pulse received at boresight. The calculated fidelity for the antennas in the E-plane can be seen in Figure 4.51. The asymmetry noted previously can again be seen in both sets of results. The fidelity of the signals transmitted by the wide-slot antenna is excellent and fidelity remains above 95% for the entire angular range. Near bore-sight the performance of the patch is good, however beyond angles of +/-20° the fidelity drops dramatically. This distortion is due to the irregularities seen in the transfer function data and borne out in the pulse duration measurements. When the pulses at -45° are compared the distortion at larger angles can be seen (Figure 4.48). The wide-slot antenna reproduces the signal at bore-sight with reasonable accuracy at this angle whereas the pulse produced by the patch shows significant distortion.

For the H-plane (Figure 4.52) both antennas perform well, with the fidelity remaining above 90% for almost the entire angular range; the fidelity of signals radiated from the wide-slot never dropping below 98%. Once again the stacked patch performance degrades at high angles. This drop in performance can also be related back to the transfer function data: and is most likely due to the rapid drop off seen in the signal

content at higher frequencies, subsequent ringing (seen in the lengthening pulse duration) and signal distortion that occurs at these higher angles.

4.6.6 Radar Detection Experiment

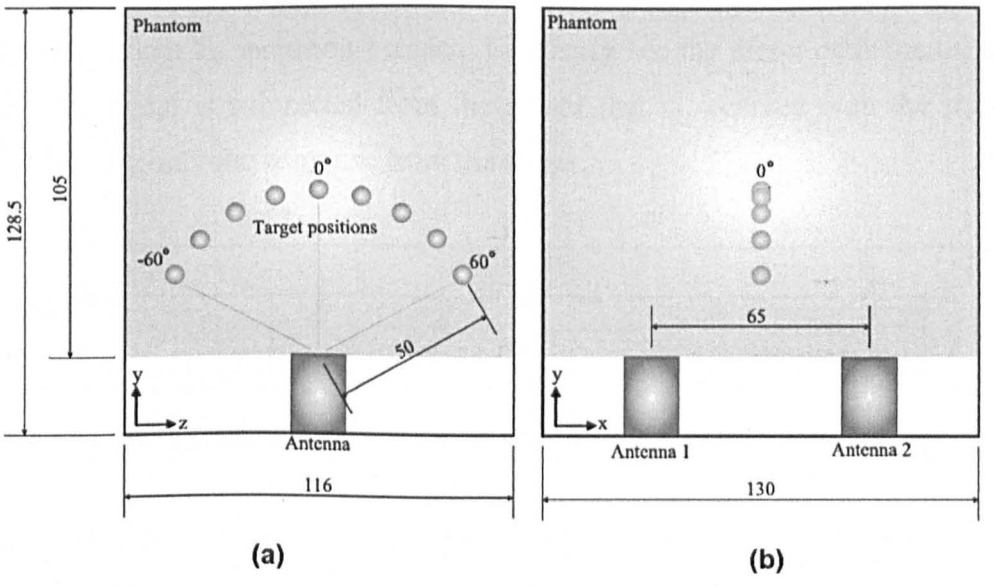

Figure 4.53 Schematic of the (a) y-z plane and (b) the y-x plane of the FDTD model used in the radar detection experiments (all dimensions in mm)

A numerical experiment has been conducted to demonstrate the suitability of the wide-slot antenna for the radar imaging application. The experiment consists of transmitting a UWB pulse into a numerical breast phantom to locate a tumour-like inclusion. The FDTD experimental setup uses the same excitation arrangement, boundary conditions and is based on the same mesh structure as the simulations used to obtain the antenna's S-parameters. Two antennas are spaced 65mm apart. Antenna 1 radiates a pulse into a phantom which is received by antenna 2. The dielectric properties of the phantom ($\varepsilon_r = 9$, $\sigma = 0.2$ S/m) closely resemble that of human breast fat. A 5mm diameter spherical inclusion is positioned in the phantom. The relative permittivity of the inclusion is set at 50 giving a contrast of 5:1 with the phantom medium, similar to the contrast that might be seen between a tumour and adipose breast tissue [8]. The position of the inclusion is varied between +/- 60°, at 10°

intervals, along an arc located mid-way between the two antennas as shown in Figure 4.53.

As the signal received at antenna 2 contains clutter, reflections and coupling between the antennas, as well as the response from the inclusion, a calibration is performed to remove these unwanted signals. The calibration signal is obtained by running simulation without an inclusion present. To clearly see the effect of the antenna this background signal is subtracted from the signal that is received with the inclusion present, leaving only the response from the target.

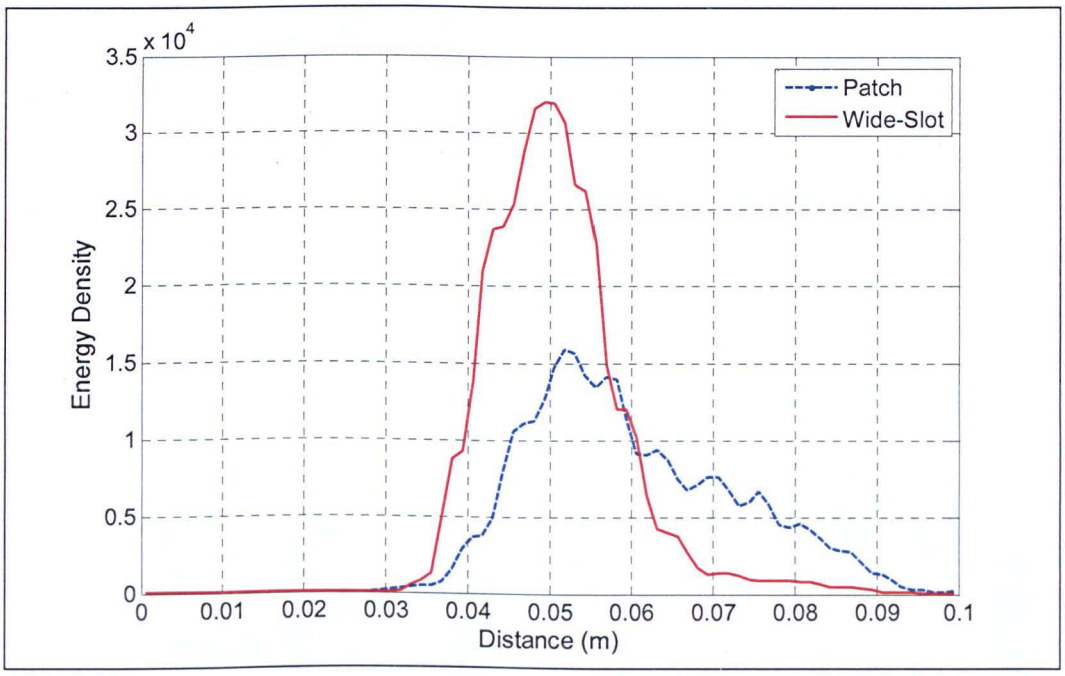

Figure 4.54 Integrated spatial energy on a radial path outwards from the centre of the arc on which the inclusions are positioned

As the path length is the same for each inclusion, waveforms from the different inclusion positions, normalised to their maximum value, can be added coherently to produce an aggregate pulse that summarises the antenna performance over the entire angular range. Squaring and then integrating this pulse over a sliding window corresponding to the transmit pulse width yields an energy curve that can be

calibrated to show the radial distance of the inclusion from the centre of the arc (Figure 4.53). The curve should peak at the true position of 5cm.

The results of this analysis (Figure 4.54) show that the energy distribution for the wide-slot response has a single peak exactly centred at the radial location of the inclusion. The peak has a width-at-half-height of just over 15.6mm, allowing the position of the inclusion to be easily identified. In comparison the energy distribution produced by the patch response is much more diffuse with a lower, less well-defined peak and a width-at-half-height of 2.63mm, nearly twice that of the slot antenna. This is a result of the increased distortion and dispersion of pulses produced by the stacked patch at angles away from boresight. From these results it can be concluded that the performance of the wide-slot would make it a good candidate for use in a radar-based breast imaging system.

4.6.7 Experimental Breast Phantom Imaging Results.

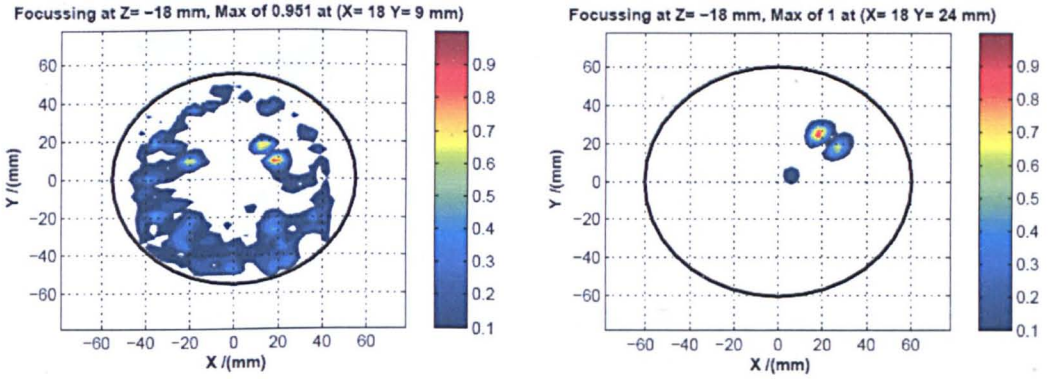

(a) (b)

Figure 4.55 A comparison of 2D imaging plots, imaging a tumour located at x=20mm, y=20mm, z=20mm using (a) the 16 element Stacked-Patch array and (b) the 31 element Wide-Slot array.

Experiments have been carried out to illustrate the improvement in imaging performance gained when using the new 31-element Wide-Slot imaging array (see Figure 4.10) compared to the 16-element Stacked Patch array. Measurements were carried out to image a breast phantom with a tumour like inclusion. The phantom consists of a hemispherical volume of the matching medium introduced in Section 4.5 ($\varepsilon_r \approx 9$, attenuation = 16 dB/cm at 6 GHz) enclosed in a 2mm skin layer ($\varepsilon_r \approx 9$, attenuation = 16 dB/cm at 6 GHz). The tumour phantom ($\varepsilon_r \approx 50$, conductivity = 7 at 6 GHz) is located at P(x = 20mm, y = 20mm, z=20mm), giving a contrast with the background medium of 5:1. For a more detailed description of the phantom see [38] and for a more information about the imaging experiment see [39].

Both antenna arrays were used to image the above phantom. 2D plots of the results from these imaging experiments can be seen in

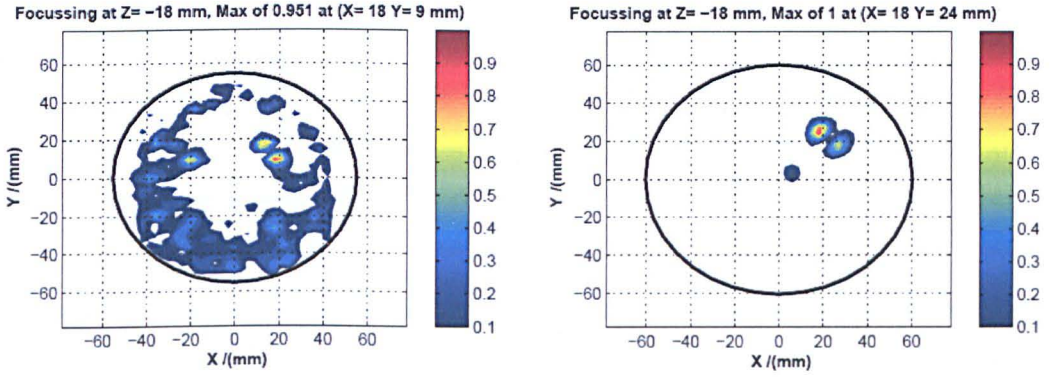

(a) (b)

Figure 4.55. Comparing the plots it can be seen that there is a much higher level of clutter in (a) and while the target is identified it is far less distinct than the clearly defined response in (b). While some of the improvement in image quality is down to the increased number of antennas in the Wide-Slot array the key difference is the superior performance of the Wide-Slot antenna [39].

4.7 Conclusions

This chapter presented the development of a cavity-backed, wide-slot antenna for use in the University of Bristol's UWB multi-static antenna array for breast cancer

detection. It had been identified that in order to obtain as much information as possible and so reduce clutter in results from the University of Bristol's system, the number of antenna in the array should be maximised. As a result there was a requirement for an efficient, simple, compact antenna with the appropriate UWB impedance and radiation performance. A literature review of existing antennas intended for microwave detection of breast cancer showed that these designs were too bulky, complex or compromised efficiency for better UWB performance and so a novel design was required.

The Wide-Slot antenna designed to fulfil this criteria was based on an existing UWB antenna, but has been developed and optimised to operate in a breast cancer detection scenario using a combination of the University of Bristol's in house FDTD program and measurement. The results of the development process have been presented, the effects of various parameters on the antenna quantified and from this an optimised antenna design has been produced. In order to reduce backscatter and coupling between antennas in the array, a cavity has been developed along with a curved coaxial feed which eliminated the need for SMA connectors ensuring the overall design was compact as possible.

The simulated and measured return loss of the antenna showed good agreement. The -10 dB bandwidth was found to be in excess of 6 GHz from 4 to 10+ GHz while simulated near-field data showed that the antenna had a beam that was stable across the frequency range at angles up to 60° from boresight.

In order to investigate this antenna further the radiation properties of the antenna were measured along with those of a stacked patch antenna previously designed for the same application. The stacked patch intended as a means of providing data for direct comparison. On examination of the transmission properties it was found that, while the stacked patch performed well at angles close to bore-sight, at wider angles of illumination (which are very important in this application) the transfer function showed significant degradation which manifested itself as significant late-time ringing and distortion of transmitted signals. This was especially notable in the E-plane.

The wide-slot antenna performed well over the entire angular/frequency range and faithfully radiated pulses at angles up to 60° away from bore-sight. These results suggest that, along with the fact that the antenna is approximately half the size of existing antenna designs; the wide slot antenna is an excellent candidate for use in the University of Bristol's UWB breast cancer detection system.

References

[1] B. C. Cancer agency, http://www.buccancer.bc.ca.

[2] Ferlay J., Bray F., Pisani P., Parkin D., "Globocan 2000: Cancer Incidence, Mortality and Prevalence Worldwide." IARC CancerBase, Version 1.0(5), 2001.

[3] Elmore J. G., Barton M. B., et al, "Ten Year Risk of False Positive Screening Mammograms and Clinical Examinations", The New England Journal of Medicine, Vol 338, number 16, pgs. 1089 – 1096.

[4] Huynh P. T., Jarolimek A.M., "The False-negative Mammogram", Radiograph, vol 18, no. 5, 1998, pp. 1137-1154,.

[5] Fear E., Hagness S. C., Meaney P., Okoniewski M., Stuchly M., "Enhancing breast tumor detection with near-field imaging," IEEE Microwave Magazine, vol. 3, no. 1, March 2002, pp. 48-56.

[6] Surowiec A.J., Stuchly S.S., Barr J.R., Swarup A., "Dielectric properties of breast carcinoma and the surrounding tissues," Biomedical Engineering, IEEE Transactions on , vol.35, no.4, April 1988, pp.257-263.

[7] Joines W. T., Yang Zhang, Chenxing Li, Jirtle R. L., "The measured electrical properties of normal and malignant human tissues from 50 to 900 MHz", Med. Phys. 21, 1994, page 547.

[8] Lazebnik M., et al, "A large-scale study of the ultrawideband microwave dielectric properties of normal, benign and malignant breast tissues obtained from cancer surgeries" 2007 Physics in Medicine and Biology. 52.

[9] Meaney P.M., Fanning M.W., Dun Li, Poplack S.P., Paulsen K.D., "A clinical prototype for active microwave imaging of the breast", Microwave Theory and Techniques, IEEE Transactions on, Volume 48, Issue 11, Part 1, Nov. 2000, Page(s):1841 – 1853.

[10] Qianqian Fang, Meaney P.M., Paulsen K.D., "Microwave image reconstruction of tissue property dispersion characteristics utilizing multiple-frequency information", Microwave Theory and Techniques, IEEE Transactions on, Volume 52, Issue 8, Part 2, Aug. 2004, Page(s):1866 – 1875.

[11] Hagness S.C., Taflove A., Bridges J.E., Two-dimensional FDTD analysis of a pulsed microwave confocal system for breast cancer detection: fixed-focus and antenna-array sensors, Biomedical Engineering, IEEE Transactions on, Volume 45, Issue 12, Dec. 1998, Page(s):1470 – 1479.

[12] Benjamin R., "Detecting reflective object in reflective medium", UK patent GB2313969, Publication date: 1997-12-10.

[13] Benjamin R., "Synthetic, post-reception focusing in near-field radar", EUREL International Conference (Conf. Publ. No. 431) The Detection of Abandoned Land Mines: A Humanitarian Imperative Seeking a Technical Solution, 7-9 Oct. 1996, Page(s):133 – 137.

[14] Craddock I.J., Nilavalan R., Leendertz J., Preece A., Benjamin R., "Experimental investigation of real aperture synthetically organised radar for breast cancer detection", Antennas and Propagation Society International Symposium, 2005 IEEE Volume 1B, 2005, Page(s):179 – 182.

[15] Fear, E.C., Stuchly, M.A., "Microwave detection of breast cancer" Microwave Theory and Techniques, IEEE Transactions on, Volume 48, Issue 11, Part 1, Nov. 2000 Page(s):1854 – 1863.

[16] Shannon C.J., Fear E.C., Okoniewski M., "Dielectric-filled slotline bowtie antenna for breast cancer detection" Electronics Letters, Volume 41, Issue 7, 31 March 2005 Page(s):388 – 390.

[17] Jafari H. M., et al., "A Study of Ultrawideband Antennas for Near-Field Imaging", Antennas and Propagation, IEEE Transactions on, Volume 55, Issue 4, April 2007, Page(s):1184 – 1188.

[18] Hagness S.C., Taflove A., Bridges J.E., "Three-dimensional FDTD analysis of a pulsed microwave confocal system for breast cancer detection: design of and antenna array element", Biomedical Engineering, IEEE Transactions on, Volume 45, Issue 12, Dec. 1998 Page(s):1470 – 1479.

[19] Jingjing Zhang, Fear E.C., Johnston R.H., "Preliminary Investigation of Breast Tumor Detection Using Cross-Vivaldi Antenna", IEEE-EMBS 27th Annual International Conference of the Engineering in Medicine and Biology Society, 2005, Page(s):6691 – 6694.

[20] Sill J.M., Fear E.C., "Tissue sensing adaptive radar for breast cancer detection: preliminary experimental results", Microwave Symposium Digest, 2005 IEEE MTT-S International, 12-17 June 2005, Page(s):4 pp.

[21] Wu T., King R., "The cylindrical antenna with nonreflecting resistive loading", Antennas and Propagation, IEEE Transactions on, Volume 13, Issue 3, May 1965, Page(s):369 – 373.

[22] Meaney P.M., Paulsen K.D., Hartov A., Crane R.K., "An active microwave imaging system for reconstruction of 2-D electrical property distributions", Biomedical Engineering, IEEE Transactions on, volume 42, Issue 10, Oct. 1995, Page(s):1017 – 1026.

[23] Xing Yun, Fear E.C., Johnston R.H., "Compact Antenna for Radar-Based Breast Cancer Detection", Antennas and Propagation, IEEE Transactions on, Volume 53, Issue 8, Part 1, Aug. 2005 Page(s):2374 – 2380.

[24] Liu W., Jafari H.M. Hranilovic, S. Deen M.J., "Time Domain Analysis of UWB Breast Cancer Detection Communications ", 2006 23rd Biennial Symposium on, May 29 - June 1, 2006 Page(s):336 – 339.

[25] Xu Li, Hagness S.C., Choi M.K., Van Der Weide D.W., "Numerical and experimental investigation of an ultrawideband ridged pyramidal horn antenna with curved launching plane for pulse radiation", Antennas and Wireless Propagation Letters, IEEE, Volume 2, Issue 1, 2003, Page(s):259 – 262.

[26] Xu Li, Bond E.J., Van Veen B.D., Hagness S.C., "An overview of ultra-wideband microwave imaging via space-time beamforming for early-stage breast-cancer detection", Antennas and Propagation Magazine, IEEE Volume 47, Issue 1, Feb 2005, Page(s):19 – 34.

[27] Khor W. E. et al. "An Ultra Wideband Microwave Imaging System for Breast Cancer Detection", IEICE Trans. Commun., vol. E90-B, no. 9, sept. 2007, pgs. 2376-2381.

[28] Nilavalan R., Craddock I.J., Preece A., Leendertz J., Benjamin R. "Wideband microstrip patch antenna design for breast cancer tumour detection" Microwaves, Antennas & Propagation, IET, Volume 1, Issue 2, April 2007, Page(s):277 – 281.

[29] Nilavalan R., Leendertz J., Craddock I.J., Preece A., Benjamin R., "Numerical analysis of microwave detection of breast tumours using synthetic focussing techniques" Antennas and Propagation Society International Symposium, 2004. IEEE Volume 3, 20-25 June 2004, Page(s):2440 – 2443.

[30] Leendertz, J., Preece, A., Nilavalan, R., Craddock, I.J., and Benjamin, R.: 'A liquid phantom medium for microwave breast imaging'. 6th Int. Congress of the European Bioelectromagnetics Association, Budapest, Hungary, November 2003.

[31] Jia-Yi Sze, and Kin-Lu Wong, "Bandwidth enhancement of a microstrip-line-fed printed wide-slot antenna," Antennas and Propagation, IEEE Transactions on, Volume 49, July 2001, pp: 1020 – 1024.

[32] Kraus, John D. and Marhefka, Ronald J. "Antennas For all Applications", 3rd Edition, McGraw Hill, New York, 2002.

[33] Yangfen Liu, et al, "Microstrip-Fed Wide Slot Antenna with Wide Operating Bandwidth", IEEE Antennas and Propagation Society International Symposium. Volume 3, 20-25 June 2004 pp:2285 - 2288 Vol.3.

[34] Tzyh-Ghuang Ma, et al, "Planar Miniature Tapered-Slot-Fed Annular Slot Antennas for Ultrawide-Band Radios" Antennas and Propagation, IEEE Transactions on, Vol. 53, No. 3, March 2005, pp. 1194-1202,

[35] Schantz H. "The art and science of ultrawideband antennas", Artech House, Norwood, MA, 2005.

[36] Lamensdorf D., Susman, L., "Baseband-pulse-antenna techniques", Antennas and Propagation Magazine, IEEE, Volume 36, Issue 1, Feb. 1994, Page(s):20 – 30.

[37] Klemm, M., I. J. Craddock, A. Preece, J. Leendertz, and R. Benjamin, "Evaluation of a hemi-spherical wideband antenna array for breast cancer imaging", Radio Sci., vol 43, 2008.

[38] Klemm Klemm, M., I. J. Craddock, A. Preece, J. Leendertz, and R. Benjamin, "Radar-Based Breast Cancer Detection Using a Hemispherical Antenna Array—Experimental Results," Antennas and Propagation, IEEE Transactions on , vol.57, no.6, pp.1692-1704, June 2009.

[39] Klemm M., Leendertz J., Gibbins D., Craddock I.J., Preece A., Benjamin R, "Microwave Radar-based Breast Cancer Detection: Imaging in Inhomogeneous Breast Phantoms", IEEE Antennas and Wireless Propagation Letters, Awaiting publication.

PAGE NUMBERING AS ORIGINAL

Chapter 5 FDTD Simulation Using an Orthogonal Hybrid Mesh

5.1 Introduction

Conventional Cartesian FDTD is an excellent tool for simulating antennas, but the technique becomes inefficient when considering complex geometries that have curved or oblique surfaces [1], [2]. To model this type of structure the FDTD algorithm uses a "staircase" approximation, illustrated in Figure 5.1 [3]. To represent these surfaces accurately a very fine mesh must be used leading to excessive computation times. In addition, it has been shown that even when a fine mesh is used this approximation still causes numerical errors [2]. As a result a number of techniques have been developed to cope with complex geometries without resorting to staircasing.

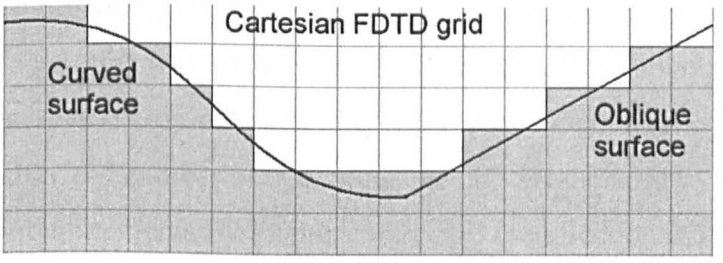

Figure 5.1 The representation of curved and oblique surfaces on a Cartesian grid using the staircase approximation.

Some problems may be accurately described using alternative orthogonal co-ordinate systems. The advantage of such schemes is that the FDTD algorithm may be formulated to run just as efficiently as with the standard code [4], [5]. Cartesian meshes are the most commonly used orthogonal co-ordinate system, others include spherical [6], [7], [8] and cylindrical co-ordinate schemes [9] [10]. The usefulness of these meshes is limited because the inflexible structure of these meshes restricts the geometries that can be modelled.

Contour Path FDTD (CPFDTD) [11], [12], [13], [14] addresses the problem of complex geometries by locally distorting the cells of a standard Cartesian mesh so that their edges correspond to the edges of the complex structure. Based on the integral form of Maxwell's equations, this technique requires that the standard FDTD

formulas be rewritten, to accommodate the deformed cells. CPFDTD has proved to be successful for modelling perfectly electrically conducting (PEC) boundaries [11] and has been used in various scattering problems such as Radar Cross Section (RCS) calculations for double spheres [12]. However, this method cannot be directly applied to dielectric boundaries because, unlike the PEC case, the tangential E-field is nonzero. Additional equations are required to deal with this and the extra difficulties that arise are such that the method becomes impracticable [13]. And so while other problems with late time stability and mesh generation have been addressed [13], [14] this limits the usefulness of CPFDTD.

Alternatively the FDTD code can be rewritten to operate with conformal, non-orthogonal (NO) meshes that can be built to follow exactly the contours of an object [1], [15], [4], [16]. In this way the surface can be modelled accurately while avoiding an overly dense mesh. Unfortunately NO FDTD is much less efficient than the Cartesian algorithm; the number of operations per cell is increased by a factor of three and the memory requirements by a factor of six [4] (see Section 5.3). So modelling large scale geometries in this way can lead to prolonged run times.

NO/Cartesian Hybrid meshes [16] address some of the issues associated with, large purely NO curvilinear grids and the inflexibility of orthogonal-based co-ordinate systems. This strategy involves limiting the use of NO mesh to the regions of the model that contain curved or oblique surfaces and descritizing the majority of the computational domain with conventional Cartesian mesh. This ensures that any complex surfaces are accurately modelled, while at the same time, the number of computationally intensive NO mesh cells, and as a result the computational costs, are kept to a minimum.

An alternative take on this idea is to produce a hybrid mesh in which orthogonal grids with different orientations, co-ordinate systems [17] or even different EM solvers [18], [19], are linked together to model a geometry that can not be dealt with by one of the meshes on their own. The main issue with these schemes is how to link the different regions of mesh in a way that will not distort fields that cross it and so avoid

introducing errors into the simulation. One way in which this problem has been tackled is to overlap the mesh regions and transfer the field values from the nodes of one mesh to the other. Obviously the nodes of the two different meshes will not align with each other and so an interpolation scheme is employed [17]. Inevitably this method is computationally complex and in the case of the overlapping mesh, the approximation resulting from the interpolation will lead to errors.

Motivated by the promise of short run times and low memory requirements a number of techniques have been developed to construct conformal orthogonal meshes in 2D [20], [21], [22], [23], and 3D applications [24] [25] [26] [27] [28]. Running the FDTD algorithm with a mesh that is both orthogonal and flexible has obvious advantages and solves many of the problems associated with NO schemes. On the other hand, orthogonal grids have limitations when modelling sharp, non-smooth features and boundaries because of difficulties when constructing the mesh [28].

This chapter presents an alternative method for modelling three dimensional complex structures, based on an orthogonal, hybrid, FDTD mesh. As already noted one of the most critical parts of a hybrid mesh is the transition between the different regions. In this case it is proposed that a section of 3D, Orthogonal Curvilinear (OC) mesh be used to link mesh-regions that are based on different orthogonal co-ordinate systems. This will result in a mesh that is both computationally simple and efficient to simulate, while at the same time the OC mesh will provide a smooth, continuous transition between the different regions.

The novelty of this hybrid meshing technique is the construction method of, and way in which the rest of the mesh relates to, the OC section. The construction of the OC mesh takes advantage of the orthogonal nature of field lines and isopotentials in a potential field. Using the Laplace equation, the potential field is solved for in a volume with the same shape as the OC mesh region, whose boundary conditions have been carefully chosen to create a field that mimics the desired structure of the mesh. Field lines are traced through this volume from set points on its boundary. A 3D orthogonal mesh is created by saving nodes at specific points along the length of these

field lines corresponding to predetermined potentials. The OC mesh is then used as a template to construct the rest of the hybrid mesh.

This study focuses on producing a mesh to model a section of the multi-static array used in the breast imaging system being developed at the University of Bristol (see Section 4.3). It is desirable to have a numerical model of the array so that, among other factors, the position and number of antenna elements can be optimised without resorting to physically building the array. As seen in the previous chapter this array has a hemispherical structure (see figure 4.10) that conforms to the shape of the breast being imaged. Using this geometry means that the breast is illuminated with as much energy as possible, but also that it is difficult to accurately and efficiently simulate using existing strategies.

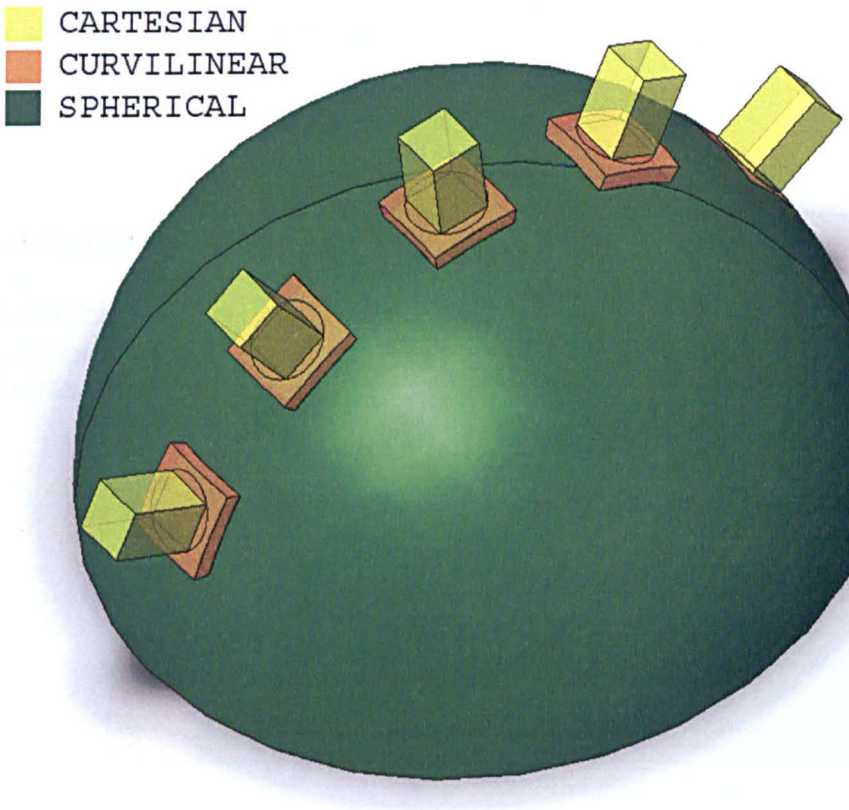

Figure 5.2 A 3D view of the mesh regions used to model the array

5.2 The Problem Geometry and General Structure of the Orthogonal Mesh

The large scale curved geometry of the University of Bristol imaging array, combined with the planar, right angled nature of the antennas means that the structure cannot easily be modelled. To simplify the problem only one row of antennas will be considered, however this still presents a considerable challenge (Figure 5.2). The approach taken in this work is based on a hybrid mesh that uses a number of different orthogonal mesh types to model specific regions of the array. The antenna is modelled using a conventional Cartesian mesh, while the large hemispherical structure of the breast is represented by a spherical based mesh with an overall radius of 100mm as can be seen in Figure 5.2 and Figure 5.3.

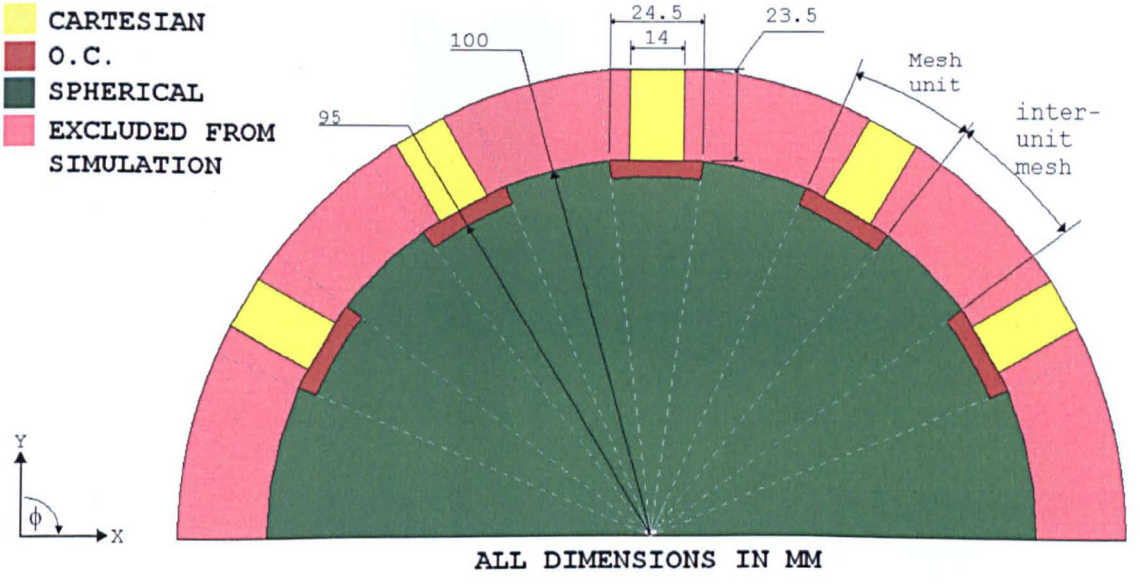

Figure 5.3 Cross section through the mesh (see Figure 5.2).

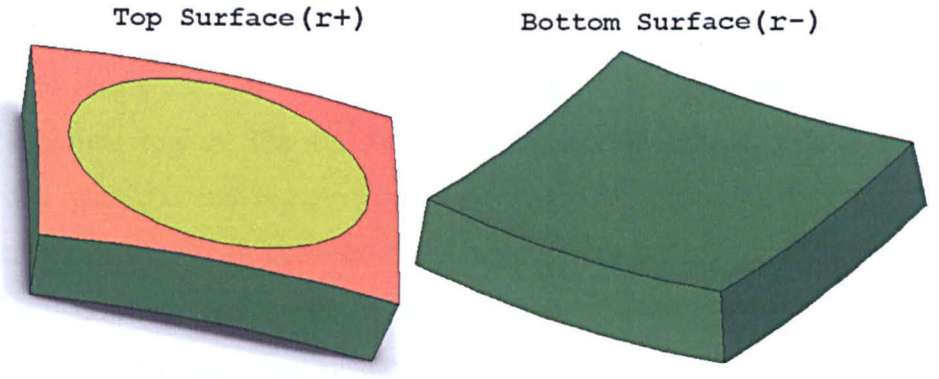

Figure 5.4 The top and bottom surfaces of the OC block of mesh. Areas that interface with the spherical mesh coloured green, the flattened surface that interfaces with the Cartesian mesh coloured yellow and the boundary with the excluded mesh coloured orange.

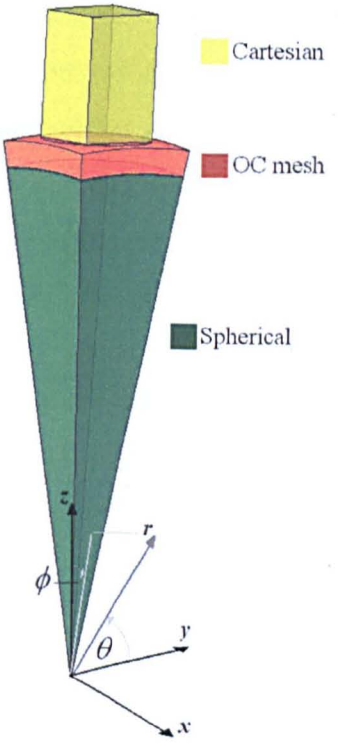

Figure 5.5 A "mesh-unit", the first stage of mesh construction (The excluded mesh has been removed for clarity). Note the unconventional spherical co-ordinate system.

As previously discussed the main challenge with this type of meshing scheme, is trying to produce a link between the different mesh regions. The solution in this instance is to locate the Cartesian mesh on a block of OC mesh that blends smoothly into the spherical region. The OC block, which can be seen in Figure 5.4 and in location in Figure 5.2 and Figure 5.3, consists of a 3D solid angle of the spherical region that spans 14.07 ° in both the θ and φ directions and has a radial thickness of 5mm at its maximum. The Cartesian mesh integrates with the upper surface of this block, which is flattened to produce a circular surface, 20.5mm in diameter. The lower and side planes of the OC block are constructed so that they integrate seamlessly with a spherically based mesh. For a detailed description of how the OC mesh is built see Section 5.4.

5.2.1 Mesh Construction

The rest of the mesh is built using the OC block as a reference. To illustrate this process take the example of a cube of Cartesian mesh. A new section of Cartesian mesh is to be added to this cube added in the $X+$ direction. The section of new mesh is constructed using the z and y co-ordinates of the nodes on the $X+$ surface of the cube. New planes of mesh are added in the x-direction by selecting appropriate x-coordinates for each new plane.

Based on this technique, a wedge of spherical mesh is added to the $r-$ surface of the OC block that extends to the centre of the spherical region. The φ and θ coordinates of the new mesh are referenced from nodes on the $r-$ surface of the OC block and new planes are created in the $r-$ direction (Figure 5.4). The Cartesian mesh, used to model the antenna, is created in a similar manner using the x and y coordinates on the, $r+$ surface of the OC block and creating new planes in the $Z+$ direction. Once this process is complete the result is a "mesh-unit" that can be used as a template to construct the rest of the mesh (Figure 5.5).

5.2.2 The Inter Unit Mesh

The mesh that is used to discretise the inter-unit regions is constructed in a similar way to that already described. The r and φ co-ordinates of the surfaces either side of the unit are used as reference planes to produce new mesh by varying the θ-values. Once all the mesh-units have been joined, the same technique can be used to extend the mesh in the in the φ-direction, to model as much of the spherical phantom as is required (Figure 5.1).

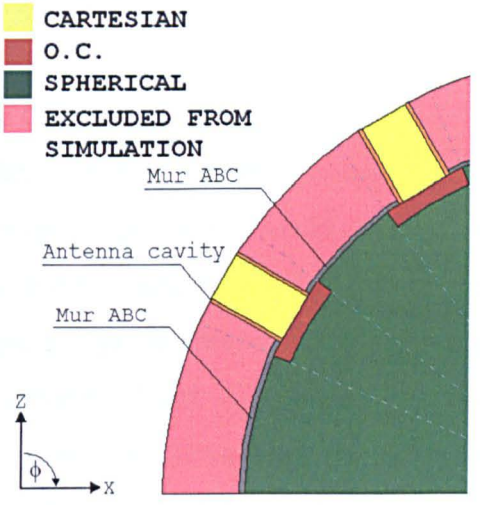

Figure 5.6 Illustration of how the excluded mesh is isolated from the other regions.

By meshing the volume in this way it is obvious that the properties of the mesh, as a whole, depend directly on those of the OC block. The orthogonality of the block is critical as any distortions will be reflected in the rest of the mesh. Another consequence of constructing the mesh in this way is that it will leave discontinuities in the area of mesh either side of the Cartesian regions. This occurs where the spherical, inter-unit mesh interfaces with the Cartesian grid. To deal with this problem these regions will be excluded from the simulation (see Figure 5.6). The Cartesian sections of mesh are isolated from the excluded regions by the metal cavity used to back the antennas. The curved boundary between the excluded mesh and the spherical mesh (including the top surface of the OC block that does not interface with the Cartesian

section) is dealt with using a 1st order Mur ABC (referred to as the interior Mur boundary) that acts as an absorber completely cutting off the mesh above it from the rest of the simulation. As the region behind the interior Mur boundary would be treated as free space anyway this is a valid model. Holes are left in absorbing Mur boundary through which, the front face of the antennas protrudes into the breast phantom. For an in depth description of the implementation of the interior Mur boundary, see Section 5.5.3.

5.3 Non-Orthogonal FDTD

The volume that links the Cartesian mesh used to model the antenna and the spherical mesh used to model the breast region will be discretised using a section of curvilinear mesh. Applying meshes with generalized co-ordinates to FDTD was first investigated by Holland [1] in 1983 and developed further by Fusco [15] and Lee et al. [3] in the early nineties. The magnetic and electrical field components in such meshes are represented using two different, local co-ordinate systems. In this section these generalized co-ordinate systems are introduced and their application to the FDTD technique is discussed for orthogonal and non-orthogonal meshes.

5.3.1 Generalized co-ordinate Systems

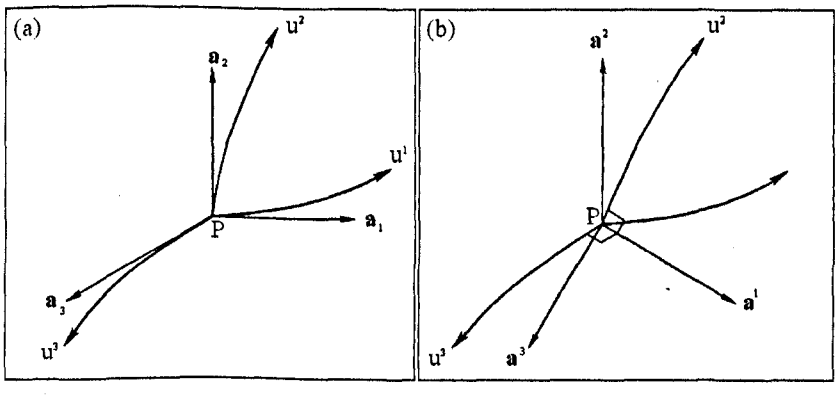

Figure 5.7 (a) Unitary covariant vectors for a non-orthogonal co-ordinate system and (b) contravariant unitary vectors for the same co-ordinate system [1]

At a point P, a curvilinear co-ordinate system (u^1, u^2, u^3) may be characterised by its covariant vectors $\mathbf{a}_i$ (see Figure 5.7 (a)) orientated along the tangent to the co-ordinate system at point P. Equivalently it may be characterised by its contravariant vectors $\mathbf{a}^i$ (see Figure 5.7 (b)), which are normals to surfaces of constant u^i.

These co-ordinate systems can be applied to a curvilinear FDTD mesh by setting the covariant vectors along the cell edges and setting the lengths of these vectors to the dimensions of the cell. This results in a set of in a set of normal basis vectors $\mathbf{A}_i$ (i = 1, 2, 3 for the 3D case). The equivalent contravariant basis vectors $\mathbf{A}^i$ are defined by the relationship;

$$\mathbf{A}^i = \frac{\mathbf{A}_j \times \mathbf{A}_k}{\sqrt{g}} \quad (i, j, k = 1, 2, 3) \tag{5.1}$$

Where g is the determinant of the metric tensor $g_{ij} = \mathbf{A}_i \cdot \mathbf{A}_j$ and $\sqrt{g}$ is the volume of the mesh cell spanned by $\mathbf{A}_i$, $\mathbf{A}_j$ and $\mathbf{A}_k$. The covariant ($\mathbf{A}_i$) and contravariant component ($\mathbf{A}^j$) are related by the metric tensor g_{ij};

$$\mathbf{A}_i = g_{ij}\mathbf{A}^j \tag{5.2}$$

In addition it should be noted that the dual bases $\mathbf{A}^i$ and the original bases $\mathbf{A}_i$ satisfy the reciprocal relationship:

$$\mathbf{A}^i \cdot \mathbf{A}_j = \delta_{ij} \tag{5.3}$$

Where δ_{ij} is the Krondecker delta. Using these local coordinates the total electric field vector $\mathbf{E}$ can be expressed in terms of either of the two bases as:

$$\begin{aligned} \mathbf{E} &= \sum_i E^i \mathbf{A}_i \\ \mathbf{E} &= \sum_i \mathbf{A}^i E_i \end{aligned} \tag{5.4}$$

where E_i and E^i are the co- and contravariant electric field components of **E**. The same principle may be applied to the magnetic field vector **H**, as well as the electric and magnetic flux density **D** and **B**.

5.3.2 The Staggered Mesh

As in the original FDTD scheme developed by Yee [29] the electric and magnetic fluxes in non-orthogonal FDTD are discretized over staggered computational grids formed by a primary grid and its dual grid. These staggered meshes are made polyhedrons, which can be seen in Figure 5.8. The dual mesh is formed by connecting the centres of adjacent cells in the original mesh to form the edges of the new cells. In this way the corners of the new dual grid cells are located at the centre of the primary cells [30].

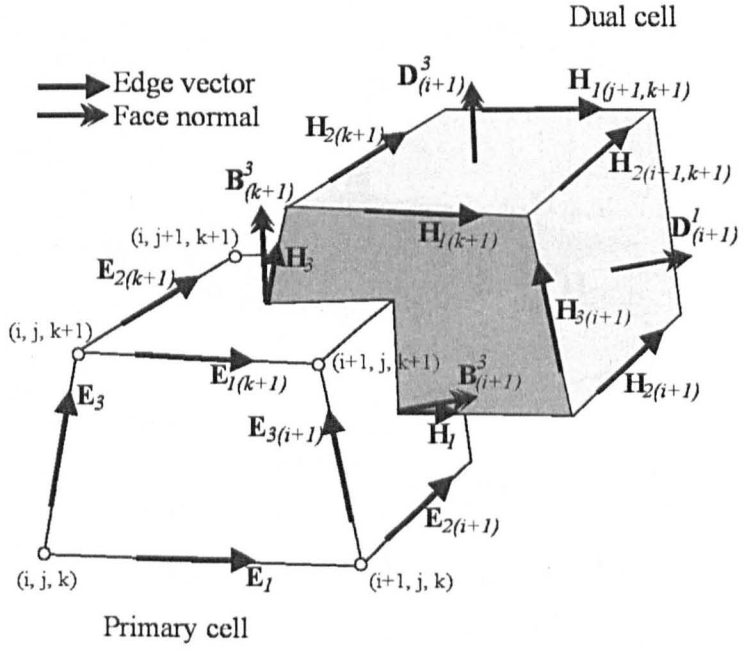

Figure 5.8 The discrete electric and magnetic field components on generalized non-orthogonal FDTD cells [30]

Figure 5.8 shows the location of the various $\mathbf{E}_i$, $\mathbf{H}_i$, $\mathbf{D}^i$ and $\mathbf{B}^i$ field components in relation cells of the staggered mesh. The position of the field components is given using logical co-ordinates. This system indicates the location of the $\mathbf{E}_i$ and $\mathbf{B}^i$ field components relative to the base node (i, j, k) of the primary cell. For example the electric field component $\mathbf{E}_{3(i+1)}$ is associated with the node shifted by one coordinate in the logical *i*-direction, relative to the $\mathbf{E}_3$ field component. If there is no shift, no logical subscript is included. The $\mathbf{H}_i$ and $\mathbf{D}^i$ components are labelled in a similar manner, but relative to the base node of the dual cell.

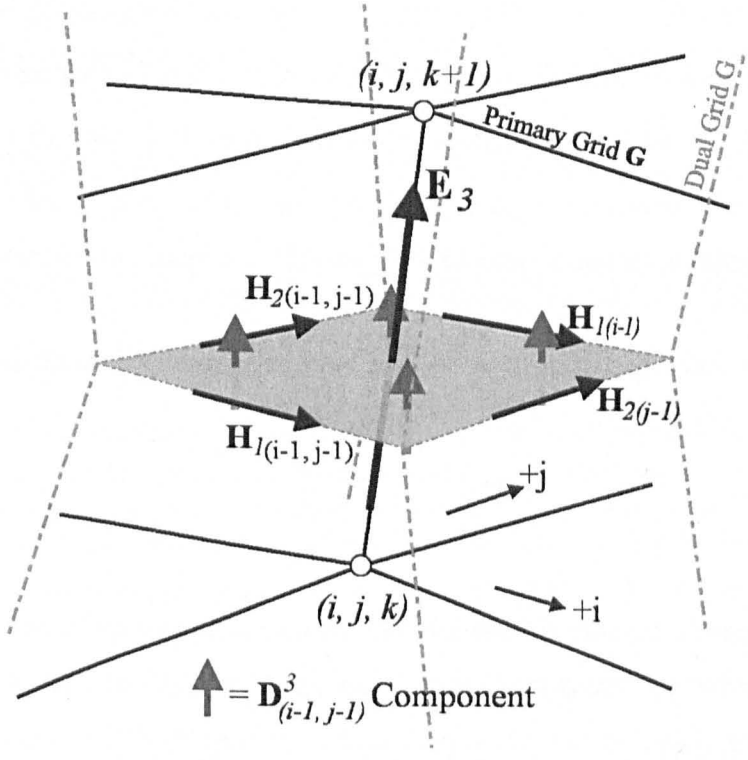

Figure 5.9 The 3D staggered grid and field components associated with the calculation of $\mathbf{E}_3$ from the adjacent covariant $\mathbf{H}_i$ values. This figure uses the field notation introduced in Figure 5.8

Physically the covariant $\mathbf{E}_i$ field components in Figure 5.8 can be interpreted as the flow of electric field along the edges of the primary cell, whereas the contravariant components $\mathbf{D}^i$, which are normal to the faces of the dual cell, represent the electric flux through that face. Similarly the $\mathbf{H}_i$ components represent the magnetic fields along the edges of dual cell and the $\mathbf{B}^i$ components, the magnetic flux through the faces of the primary cell [5].

5.3.3 Maxwell's Curl Equations

Figure 5.9 focuses in on the area of Figure 5.8 around $\mathbf{E}_3$. Let us examine this covariant field component more closely and derive its associated FDTD update equations. The surface Ω is the face of a dual grid cells located half way up the $\mathbf{E}_3$ component, the Electric flux through Ω is the contravariant field component $\mathbf{D}^3_{(i-1,j-1)}$. Around the border of the surface are the four covariant magnetic field components that together describe the magnetic fields on the closed boundary around Ω.

The source-free Integral form of Amperes law, for isotropic media is;

$$\frac{\partial}{\partial t}\int_{\Omega}\mathbf{D}\cdot dA = \oint_{\partial\Omega}\mathbf{H}\cdot dl \tag{5.5}$$

The left hand side of this equation represents the rate of change of electric flux with time through a surface Ω. The right hand side represents the circulation of the magnetic fields around the boundary edge ($\partial\Omega$) of Ω. Let us apply this equation to the descretized fields in Figure 5.9.

Because the area of Ω is arbitrarily small the right side of equation 5.5 reduces to $\partial\mathbf{D}/\partial t$ or the change of the electric flux with time, which in terms of the descretized field components can be written as;

$$\frac{\partial}{\partial t}\int_{\Omega}\mathbf{D}\cdot dA \Rightarrow \frac{\mathbf{D}^3_{(i-1,j-1)}\Big|^{(n+1)} - \mathbf{D}^3_{(i-1,j-1)}\Big|^{(n)}}{\Delta t} \tag{5.6}$$

Where n and $n+1$ indicate the electric flux values before and after the discrete time interval Δt. The rotation of the magnetic field around the boundary of Ω can be found by summing the magnetic field components with clockwise as the negative direction (the right hand rule);

$$\oint_{\partial\Omega}\mathbf{H}\cdot dl \Rightarrow \mathbf{H}_{1(i-1,j-1)}\Big|^{(n)} - \mathbf{H}_{1(j-1)}\Big|^{(n)} + \mathbf{H}_{2(i-1,j-1)}\Big|^{(n)} - \mathbf{H}_{2(i-1)}\Big|^{(n)} \tag{5.7}$$

Setting equations 5.6 and 5.7 equal and rearranging gives the FDTD update equation for the $\mathbf{D}^3_{(i-1,j-1)}\Big|^{(n+1)}$ field component;

$$\begin{aligned}\mathbf{D}^3_{(i-1,j-1)}\Big|^{(n+1)} = \mathbf{D}^3_{(i-1,j-1)}\Big|^{(n)} + \Delta t\cdot[&\mathbf{H}_{1(i-1,j-1)}\Big|^{(n)} \\ &- \mathbf{H}_{1(j-1)}\Big|^{(n)} + \mathbf{H}_{2(i-1,j-1)}\Big|^{(n)} - \mathbf{H}_{2(i-1)}\Big|^{(n)}]\end{aligned} \tag{5.8}$$

A similar update equation can be derived for the contravariant magnetic flux field component $\mathbf{B}^3_{(k+1)}\Big|^{(n+1)}$;

$$\begin{aligned}\mathbf{B}^3_{(k+1)}\Big|^{(n+1)} = \mathbf{B}^3_{(k+1)}\Big|^{(n+1)} + \Delta t\cdot[&\mathbf{E}_{1(k+1)}\Big|^{(n)} \\ &- \mathbf{E}_{1(j+1,k+1)}\Big|^{(n)} + \mathbf{E}_{2(k+1)}\Big|^{(n)} - \mathbf{E}_{2(i+1,k+1)}\Big|^{(n)}]\end{aligned} \tag{5.9}$$

These update equations are very similar to those for conventional FDTD [29]. The main difference being that the now covariant $\mathbf{E}_i$, $\mathbf{H}_i$ components are transformed into the contravariant field flux quantities $\mathbf{D}^i$ and $\mathbf{B}^i$. Summarising for all field components, in matrix form the above equations become [30];

$$-\frac{1}{\Delta t}\mathbf{b} = \mathbf{C}\mathbf{e} \quad \text{and} \quad \frac{1}{\Delta t}\mathbf{d} = \tilde{\mathbf{C}}\mathbf{h} \tag{5.10}$$

where the vectors $\mathbf{e} = (\mathbf{E}_i), \mathbf{h} = (\mathbf{E}_i), \mathbf{b} = (\mathbf{B}^i)$ and $\mathbf{d} = (\mathbf{D}^i)$ are built from covariant and contravariant field components. If N is the number of vertices in the NO mesh then the length of these vectors is equal to $3N$. The vectors $\mathbf{C}$ and $\tilde{\mathbf{C}}$, are known as the 'topological curl matrices' of the primary and dual grids and contain the sign factors of the right hand sides of equations 5.8 and 5.9.

5.3.4 The Material Equations

To complete the system of update equations an additional step is required to convert the contravariant field flux vectors into the corresponding covariant voltage vectors and to include the effect of the cell material properties. This process will be illustrated once again by examining the $\mathbf{E}_3$ field component in Figure 5.9.

5.3.4.1 Orthogonal Meshes

If the mesh is orthogonal then the two vectors will be collinear and the conversion can be done on a one to one basis. As already noted, the contravariant electric component $\mathbf{D}^3_{(i-1,j-1)}$ represents the electric flux through the face of the dual mesh cell (Ω). From Maxwell the electric field and flux are related by the permittivity ($D = \varepsilon E$) while the area of Ω is proportional to $\sqrt{g}\mathbf{A}^3$. Thus the relationship between the **contravariant** electric field component $\mathbf{E}^3$ and electric flux is given by [4], [5];

$$\begin{aligned} \mathbf{D}^3_{(i-1,j-1)} &= (\varepsilon E) \cdot (\sqrt{g}\mathbf{A}^3) \\ &= \sqrt{g}\varepsilon\, \mathbf{E}^3 \end{aligned} \tag{5.11}$$

From equation 5.2 we know that $\mathbf{E}^3$ and $\mathbf{E}_3$ are related by the metric tensor g_{33}. Combining this relationship with equation 5.2 and rearranging to make $\mathbf{E}^3$ the subject gives the material update equation for $\mathbf{E}_3$;

$$\mathbf{E}^3 = \frac{g_{33}\mathbf{D}^3_{(i-1,j-1)}}{\sqrt{g}\varepsilon} \tag{5.12}$$

Once again similar equations can be derived for the other covariant field components resulting in a set of material equations that in general matrix form can be written as;

$$\mathbf{e} = \mathbf{M}_\varepsilon \mathbf{d} \quad \text{and} \quad \mathbf{h} = \mathbf{M}_\mu \mathbf{b} \tag{5.13}$$

where the '**M**' terms are N by N dimensioned diagonal matrices, their terms having the form $g_{ii}/\sqrt{g}\varepsilon$ [5]. In combination, the computational memory and time costs required to perform the two steps in equations 5.10 and 5.13 are similar to those for the update equations in standard FDTD. This means that orthogonal FDTD formulated in generalized co-ordinates is just as computationally efficient as standard FDTD, albeit with slightly extended initialisation times.

5.3.4.2 Non-Orthogonal Meshes

In the case of a non-orthogonal mesh, $\mathbf{E}^3$ and $\mathbf{E}_3$ are not collinear and so contributions from all three contravariant fields must be considered. As the $\mathbf{E}^2$ and $\mathbf{E}^1$ contravariant components are not available at the same location in the grid as the $\mathbf{E}^3$ and $\mathbf{E}_3$ vectors an interpolation scheme must be employed. Holland [1] developed a simple scheme that averages neighbouring field components, however this approach has been found to cause numerical stability problems [5]. Schuman et al developed an alternative, more complex interpolation scheme in which the $\mathbf{E}_3$ field component is calculated as;

$$\begin{aligned}\mathbf{E}^3 = {} & \frac{\mathbf{A}_3\cdot\mathbf{A}_3}{\sqrt{g}\varepsilon}\mathbf{D}^3_{(i-1,j-1)} + \left\{\frac{\mathbf{A}_3\cdot\mathbf{A}_1}{\sqrt{g}\varepsilon}\mathbf{D}^1_{(j-1,k-1)} + \frac{\mathbf{A}_3\cdot\mathbf{A}_{1(k+1)}}{\sqrt{g}\varepsilon}\mathbf{D}^1_{(j-1)}\right. \\ & + \frac{\mathbf{A}_3\cdot\mathbf{A}_{1(i-1,k+1)}}{\sqrt{g}\varepsilon}\mathbf{D}^1_{(i-1,j-1)} + \frac{\mathbf{A}_3\cdot\mathbf{A}_{1(i-1)}}{\sqrt{g}\varepsilon}\mathbf{D}^1_{(i-1,j-1,k-1)} + \frac{\mathbf{A}_3\cdot\mathbf{A}_2}{\sqrt{g}\varepsilon}\mathbf{D}^2_{(i-1,k-1)} \\ & \left. + \frac{\mathbf{A}_3\cdot\mathbf{A}_{2(k+1)}}{\sqrt{g}\varepsilon}\mathbf{D}^2_{(i-1)} + \frac{\mathbf{A}_3\cdot\mathbf{A}_{2(j-1,k+1)}}{\sqrt{g}\varepsilon}\mathbf{D}^2_{(i-1,j-1)} + \frac{\mathbf{A}_3\cdot\mathbf{A}_{2(j-1)}}{\sqrt{g}\varepsilon}\mathbf{D}^2_{(i-1,j-1,k-1)}\right\}\end{aligned} \tag{5.14}$$

where $\sqrt{g}$ must be calculated from using the local unit vector associated with that component i.e. in

$$\frac{\mathbf{A}_3 \cdot \mathbf{A}_{2(j-1,k+1)}}{\sqrt{g}\varepsilon} \mathbf{D}^2_{(i-1,j-1)} \tag{5.15}$$

g must be calculated using $\mathbf{A}_3$ and $\mathbf{A}_{2(j-1,k+1)}$. In this way, similar material equations may be derived for the other covariant field components to produce a material matrix with the same dimensions as that for the orthogonal case, but with eight off-diagonal components. Storing these extra terms and performing the extra calculations in equation 5.14 is the cause of the increased computer complexity associated with NO FDTD.

5.3.5 Mesh Angles

The angles that the $\mathbf{A}_i$ vectors make with the surface over which the associated $\mathbf{D}^i$ components are calculated (in the case of Figure 5.9 the angle $\mathbf{E}_3$ makes with Ω) are a good measure of the orthogonality of a mesh. As such it will be used to assess the quality of the meshes presented later in this chapter.

5.4 3D Orthogonal Mesh Generation

The method used in the construction of the 3D orthogonal mesh is based on finding specific "field-lines" or paths of steepest descent/ascent in a three dimensional potential field. Potential fields are useful in investigating physical problems and are important in many applications, notably electromagnetism, astronomy, and fluid dynamics. The static electrical field between two differently charged metal plates being a good example.

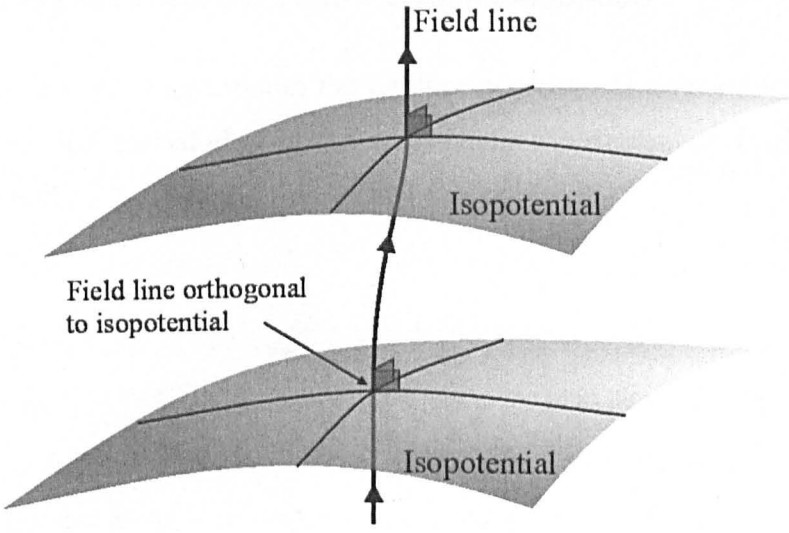

Figure 5.10 The isopotentials and field lines in a potential field

This technique produces an OC grid by exploiting the fact that the iso-potentials and field-lines of a potential field are orthogonal (Figure 5.10). To do this, a potential field is found whose form is representative of the desired mesh. The structure of the field is defined by applying an appropriate set of boundary conditions within a Laplace solver. The starting locations for streamlines are on one of the boundaries of the potential field, their positions defined by a pre-determined 2D "reference-mesh" which in turn is based on the section of mesh that interfaces with the boundary. From these starting locations the field-lines are followed through the field.

The mesh is created by positioning nodes along the length of the streamline corresponding to certain potentials. The selection of these potentials dictates the spacing between the nodes and so the planes in the mesh. Assuming that the reference-mesh is orthogonal, the nature of the potential field will ensure the orthogonality of the resulting curvilinear mesh.

5.4.1 Defining the Potential Field – Laplace Equation

A potential field is one that satisfies the Laplace equation. The equation states that the sum of the second partial derivatives (the Laplace operator, or Laplacian) of an unknown potential ξ is zero [31];

$$\frac{\partial^2 \xi}{\partial x^2} + \frac{\partial^2 \xi}{\partial y^2} + \frac{\partial^2 \xi}{\partial z^2} = 0 \tag{5.16}$$

It can apply to functions of two or three variables, and can be written in terms of a differential operator as $\Delta\xi = 0$, where Δ is known as the Laplace operator. In order to solve Laplace's equation and so define the potential distribution, we must find the unique function who's derivatives satisfy $\Delta\xi = 0$, and simultaneously satisfy the boundary conditions that define the physical problem. There are many elegant analytical solutions to Laplace's equation in special geometries but generally real problems are solved numerically. There are two common approaches to finding a numerical solution:

5.4.1.1 Finite Element Methods

Finite element methods divide the problem of interest into a mesh of geometric shapes called finite elements. The potential within an element is described by a function that depends on its values at the cell corners and parameters defining the state of the element. A problem is solved by assembling a number of cells together such that they represent the volume to be solved. A total energy associated with the mesh configuration is found as part of the calculation and this is minimised by adjusting the parameters specifying the elements. The solution can be refined by subdividing the regions of the mesh that contribute most to the total "energy" of the solution. General purpose programmes to perform these calculations are fairly complicated.

5.4.1.2 Finite Difference Methods

Finite-difference methods are used to solve Laplace's equation by superimposing a regular grid on the region of interest and approximating Laplace's equation at each grid-point. The resulting system of equations is solved by iteration. The method is extremely easy to program. Let us start by considering a three-dimensional grid of points each separated by a distance h from its six nearest neighbours and the potential at a position (x,y,z) is $\xi(x,y,z)$. Then the potential at the positions either side of this location along the x direction are given by:

$$\xi(x+h,y,z)=\xi(x,y,z)+h\frac{\partial\xi}{\partial x}+\tfrac{1}{2}h^2\frac{\partial^2\xi}{\partial x^2}+\tfrac{1}{6}h^3\frac{\partial^3\xi}{\partial x^3}+O(h^4) \tag{5.17}$$

$$\xi(x-h,y,z)=\xi(x,y,z)-h\frac{\partial\xi}{\partial x}+\tfrac{1}{2}h^2\frac{\partial^2\xi}{\partial x^2}-\tfrac{1}{6}h^3\frac{\partial^3\xi}{\partial x^3}+O(h^4) \tag{5.18}$$

Adding these potentials together eliminates the 1st and 3rd order terms to give;

$$\xi(x-h,y,z)+\xi(x+h,y,z)=\xi(x,y,z)+h^2\frac{\partial^2\xi}{\partial x^2}+O(h^4) \tag{5.19}$$

Adding this result to the equivalent equations in the y and z directions and neglecting any terms that are 4th order or above gives;

$$\begin{aligned}\xi(x,y,z)=\tfrac{1}{6}\{&\xi(x-h,y,z)+\xi(x+h,y,z)+\xi(x,y-h,z)+\xi(x,y+h,z)\\&+\xi(x,y,z-h)+\xi(x,y,z+h)\}\end{aligned} \tag{5.20}$$

Where the second order terms have been eliminated as the addition of these terms results in zero due to Laplace's equation (equation 5.16).From this relationship it can be seen that the potential at a grid point is simply the average potential of its nearest neighbours. To find the solution, the node values at the boundaries must be fixed according to the boundary conditions of the problem and the potentials are iterated

until the potentials at successive iterations agree to within a set limit. This method is easy to program and as such will be implemented here [32] [31].

5.4.2 Implementation of the Numerical Laplace Solver

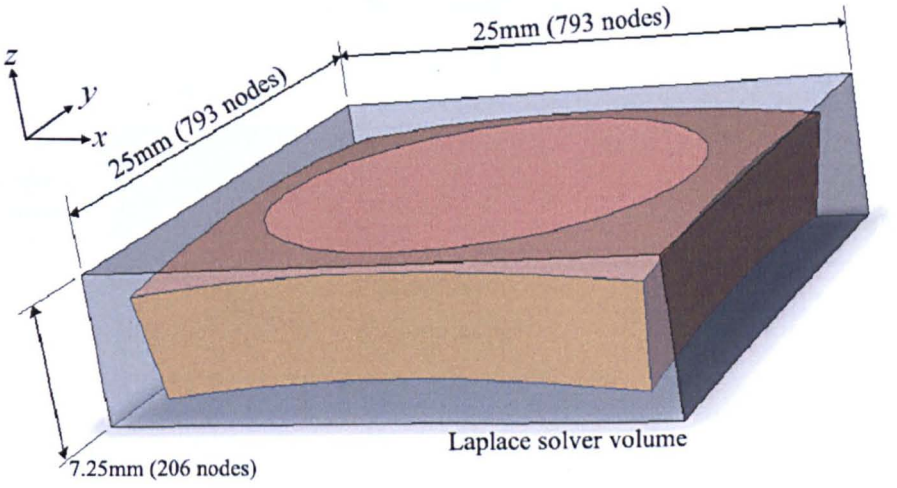

Figure 5.11 The Laplace solver domain and the position of the mesh volume within it. The no of nodes per dimension corresponds to a node spacing of 0.35mm.

To construct the OC mesh a descritized domain is defined on which the Laplace solver will operate (Figure 5.11). This has the form of a regularly spaced grid with dimensions of 25×25×7.25mm. The OC volume is defined within this volume using an appropriate set of boundary conditions. The size of the Laplace volume has been chosen to be only slightly larger than the OC mesh minimising the number of nodes and so runtime of the Laplace solver.

5.4.2.1 Defining the Boundary Conditions for the Mesh Volume

The potential field found using the Laplace solver is defined by the boundary conditions enforced within the solution volume. The field-lines will trace a path through space that links regions with different potentials, so for example, if one boundary is set to have a potential of 1 and another zero, the field lines will traverse

between them. In the problem in question an OC mesh is required that links the known Cartesian mesh of the antenna to the arbitrary but spherical mesh of the phantom. The Cartesian mesh interfaces with the OC mesh on the $z+$ boundary while the spherical mesh interfaces on the $z-$ boundary (see Figure 5.3 and Figure 5.5).

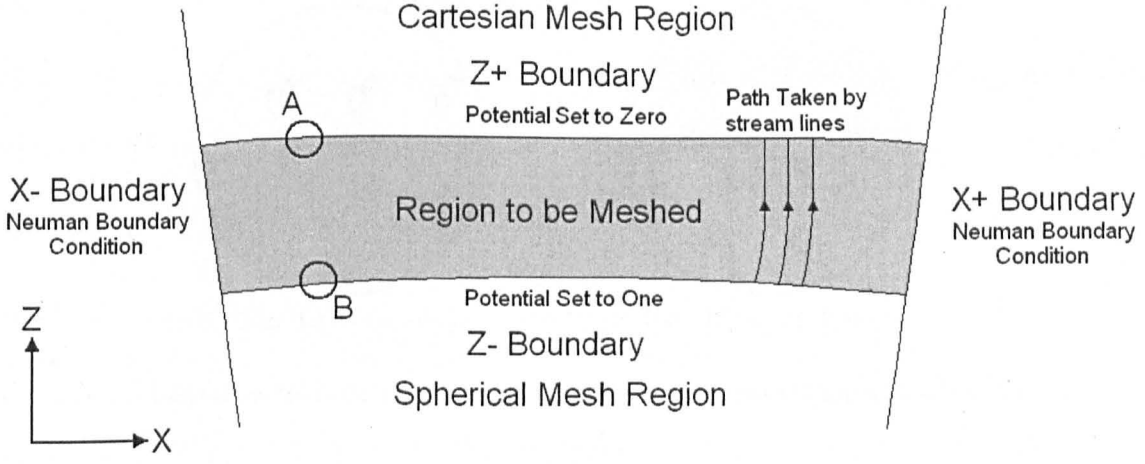

Figure 5.12 The boundary conditions for the Laplace solver volume in the X-Z plane using the Cartesian coordinate system of the antenna mesh as a reference.

The $z-$ boundary of the volume to be meshed, is part of the surface of a sphere 95mm in radius, that has angular dimensions of 14.07° in both the φ and θ directions. It is this curved surface that will allow the OC mesh to interface with the spherical mesh below. The $z+$ boundary has the same angular dimensions but part of a sphere that has a diameter of 100mm the central region of which has been flattened to create a circular surface 20.5mm in diameter (see Figure 5.4 and Figure 5.5). The flattened region allows the OC mesh to interface with the Cartesian mesh of the antenna. The x and y boundaries are flat angled surfaces that join the z boundaries. These interface with the spherical mesh in the φ and θ directions. The x and y boundaries will be discussed in the next section.

The starting location of the field-lines will be on the $z+$ boundary, as the structure of the Cartesian mesh, that interfaces with this boundary, is dictated by the geometry of the antenna. To produce a practicable mesh the field lines must be forced to traverse

between this and the z- boundary. This is affected by forcing all the nodes below the z- boundary to a constant potential of 1 while those above the z+ boundary are set to zero (see Figure 5.13).

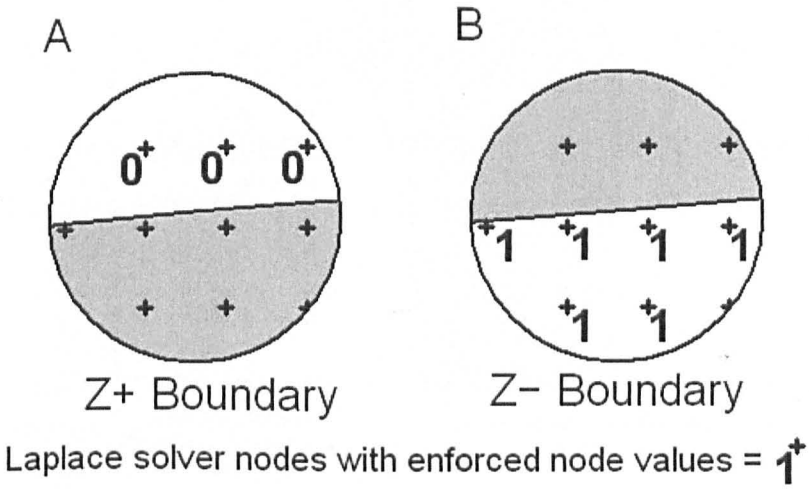

Figure 5.13 The enforced boundary conditions at A) the Z+ boundary above which all nodes are set to zero and B) the Z- boundary below which all nodes are set to one. These diagrams are enlarged regions of Figure 5.12.

5.4.2.2 Neumann Boundary Condition

On the x and y boundaries a Neumann condition is imposed. The Neumann (or second type) boundary condition is named after Carl Neumann [31]. When imposed on an ordinary or a partial differential equation, it specifies the value that the derivative of a solution is to take across the boundary where it is applied [32]. In this case a condition is chosen that forces the gradient across the boundary to zero by forcing nodes adjacent to, and outside the boundary to have the same value as those on the inside. This ensures that a field line started at the top of the boundary will follow the radial path of the boundary, allowing the mesh at the x and y boundaries of OC region to be integrated with the spherical mesh that surrounds it.

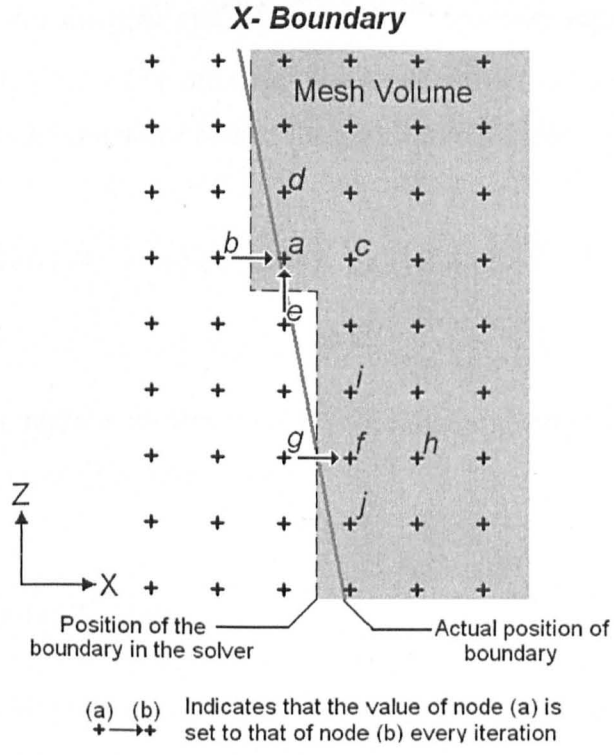

Figure 5.14 The Neumann boundary condition applied to the X-, X+, Y- and Y+ boundaries, exemplified at the X- boundary.

Figure 5.14 shows the X- Neumann boundary passing through a 2D region of mesh with. It can be seen that rather than following the exact path, the boundary takes a stepped route through the Laplace mesh. Figure 5.14 shows the two possible situations that can occur when calculating the update for nodes along this boundary, assuming that the y-direction nodes are not on the outside of either of the y boundaries. Examining first node f, in this case the node is adjacent to a vertical section of boundary. The value of node g is forced to be that of node f in the previous iteration and the calculation of the potential for iteration n becomes;

$$\xi(x,y,z)^n = \tfrac{1}{6}\{\xi(x,y,z)^{n-1} + \xi(x+h,y,z)^{n-1} + \xi(x,y-h,z)^{n-1} + \xi(x,y+h,z)^{n-1} + \xi(x,y,z-h)^{n-1} + \xi(x,y,z+h)^{n-1}\} \quad (5.21)$$

Note that the value for the potential $\xi(x+h,y,z)^{n-1}$ has been replaced by $\xi(x,y,z)^{n-1}$ compared to equation 5.20. For the case of node a situated on a step in the boundary both nodes b and e take the value of a at the previous iteration;

$$\xi(x,y,z)^n = \tfrac{1}{6}\{2\xi(x,y,z)^{n-1} + \xi(x+h,y,z)^{n-1} + \xi(x,y-h,z)^{n-1} + \xi(x,y+h,z)^{n-1} + \xi(x,y,z+h)^{n-1}\} \quad (5.22)$$

For cases where the node is located next to more than one boundary a combination of the above two cases would be implemented.

5.4.2.3 Convergence Criteria

Once the Laplace solver has run for a sufficiently long time, the change of potential per iteration for each node will become negligible and the solution will have converged to the final solution. To identify when this occurs the change in average potential value over a number of iterations is calculated. Rather than averaging over the entire mesh volume, two planes in the centre of the volume are selected, one in the x-z orientation and the other in the y-z orientation. For a plane of $N_a \times N_b$ nodes, the average percentage potential change per node $\Delta\bar{\xi}$ at the nth iteration is calculated using;

$$\Delta\bar{\xi}^n = 100 \times \left(\sum_{i=1}^{N_a}\sum_{j=1}^{N_b}\xi_{i,j}\right)^n \Big/ \left(\sum_{i=1}^{N_a}\sum_{j=1}^{N_b}\xi_{i,j}\right)^{n-4} N_a N_b \quad (5.23)$$

If the value of $\Delta\bar{\xi}$ is below a certain threshold, for both planes the solver has converged and the iteration is stopped. The threshold is identified by running the solver and both visually checking for convergence and producing simple meshes and examining their angular composition.

5.4.2.4 Implementation of the Solver

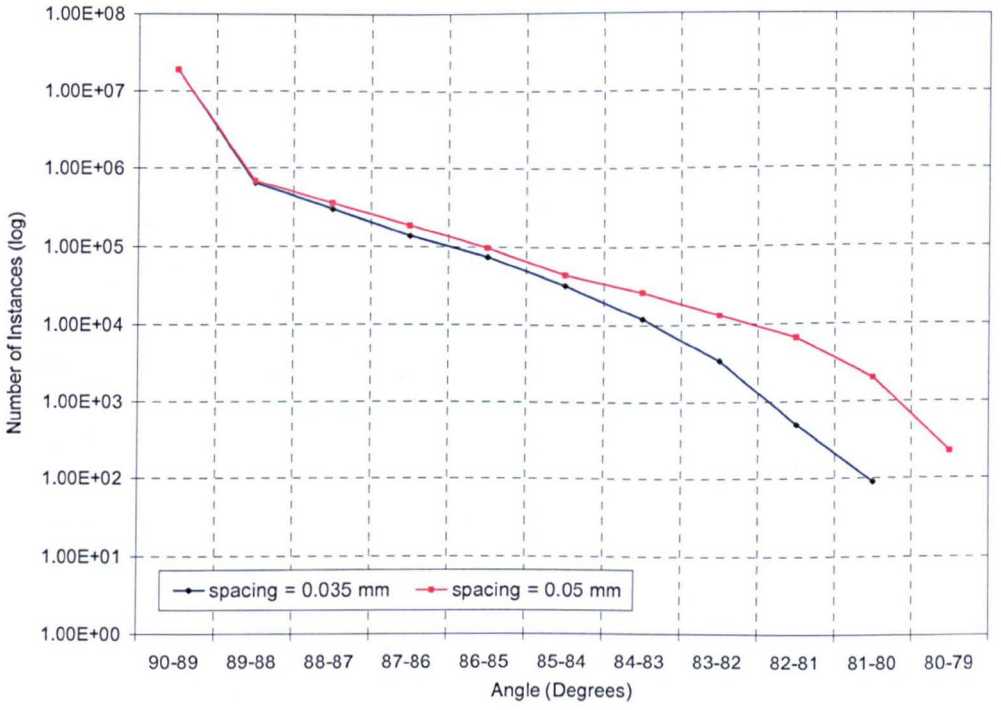

Figure 5.15 The angles between nodes in orthogonal curvilinear meshes with different mesh spacing.

A finite difference based solver has been developed and programmed in Delphi. A flow chart of the main procedures carried out in the solver can be seen in Figure 5.16.

The spacing of the nodes in the Laplace solver mesh is one of the most important factors when considering its implementation. On the one hand it is desirable that the number of nodes be kept to a minimum, ensuring the computational costs of running the Laplace solver are kept as small as possible. On the other, the spacing of the nodes must be small enough to ensure that the potential distribution is sufficiently described for the curvilinear mesh to be accurately constructed.

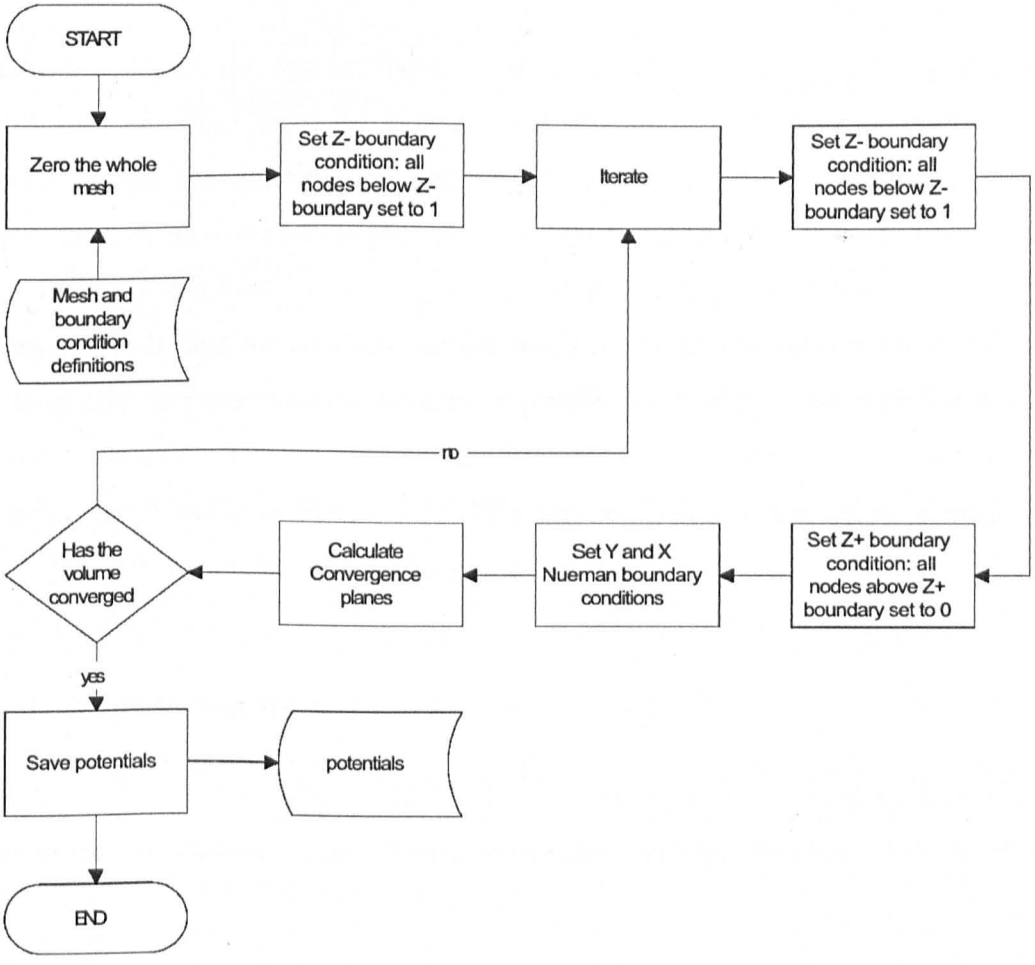

Figure 5.16 Flow chart for the Laplace solver

The Laplace solver was run with different node spacings to find the appropriate value. Curvilinear meshes were then constructed, with structures and cell sizes representative of those that are required to simulate the antenna. The meshes were analysed and the angular composition of the meshes found (see Section 5.3.5). In an ideal case the mesh will be orthogonal and all angles will be 90°, the amount by which the angles in the mesh deviate from this ideal is a measure of the "orthogonality" of the mesh.

Figure 5.15 shows the angular make up of two meshes, constructed using spacings of 0.035 mm and 0.05 mm. As expected the smaller spacing size produces a better quality mesh; the number of nodes with angles of 79° - 83° is reduced by approximately an order of magnitude when compared to the case with larger spacing. The memory required to store the solved potentials was 1.53GB and 0.85GB respectively. In fact the memory requirements of running the solver were such that a spacing of 0.035 mm was the smallest possible that could be run with the computer facilities available. The solution domain used to produce the OC mesh, with this node spacing, can be seen in Figure 5.11. The solver mesh is made up of is made up of 793×793×206 or 129,542,894 nodes in total.

5.4.3 Mesh Generation

Figure 5.18 shows a flow chart of the computer program used to construct the orthogonal curvilinear mesh. These processes can be grouped into three main categories;

1. Finding the starting positions of the field lines on the $z+$ boundary of the mesh volume based on the Cartesian mesh used to model the antenna.
2. Calculation of the gradient of the potential field at a point in the mesh volume and using this to follow the field-lines.
3. Calculating the potentials at which the nodes need to be positioned in order to get the required spacing in the z-direction and using this information to position of the nodes.

5.4.3.1 Field-Line Starting Positions

The first step in building the mesh is the construction of a single 3D plane of reference points that maps the starting locations of the field-lines onto the *z*+ boundary of the mesh volume. The surface that makes up this boundary is complex and takes the form of a solid angle of a sphere with a circular flattened region in its centre, as illustrated in Figure 5.17. This shape allows the geometric integration of the flat Cartesian mesh with the overall spherical structure of the problem, but means that production of the reference mesh is a non-trivial task.

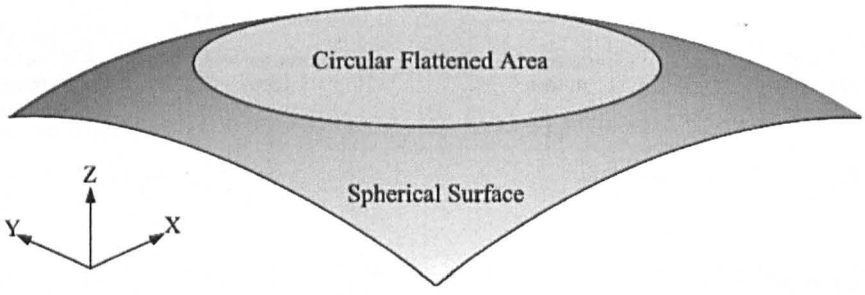

Figure 5.17 The 3D surface that makes up the Z+ boundary of the mesh volume (not to scale – Z axis has been stretched to emphasise the shape)

The degree of orthogonallity of the reference mesh is critical, as it will dictate the quality of the OC mesh. In the flattened section of the surface, the placement of the reference points is simply dictated by the positions of the nodes in the Cartesian antenna mesh. The difficulty arises when trying to integrate this with the mesh on the spherical surface. There is no way to do this perfectly so some degree of non-orthogonallity must be accepted.

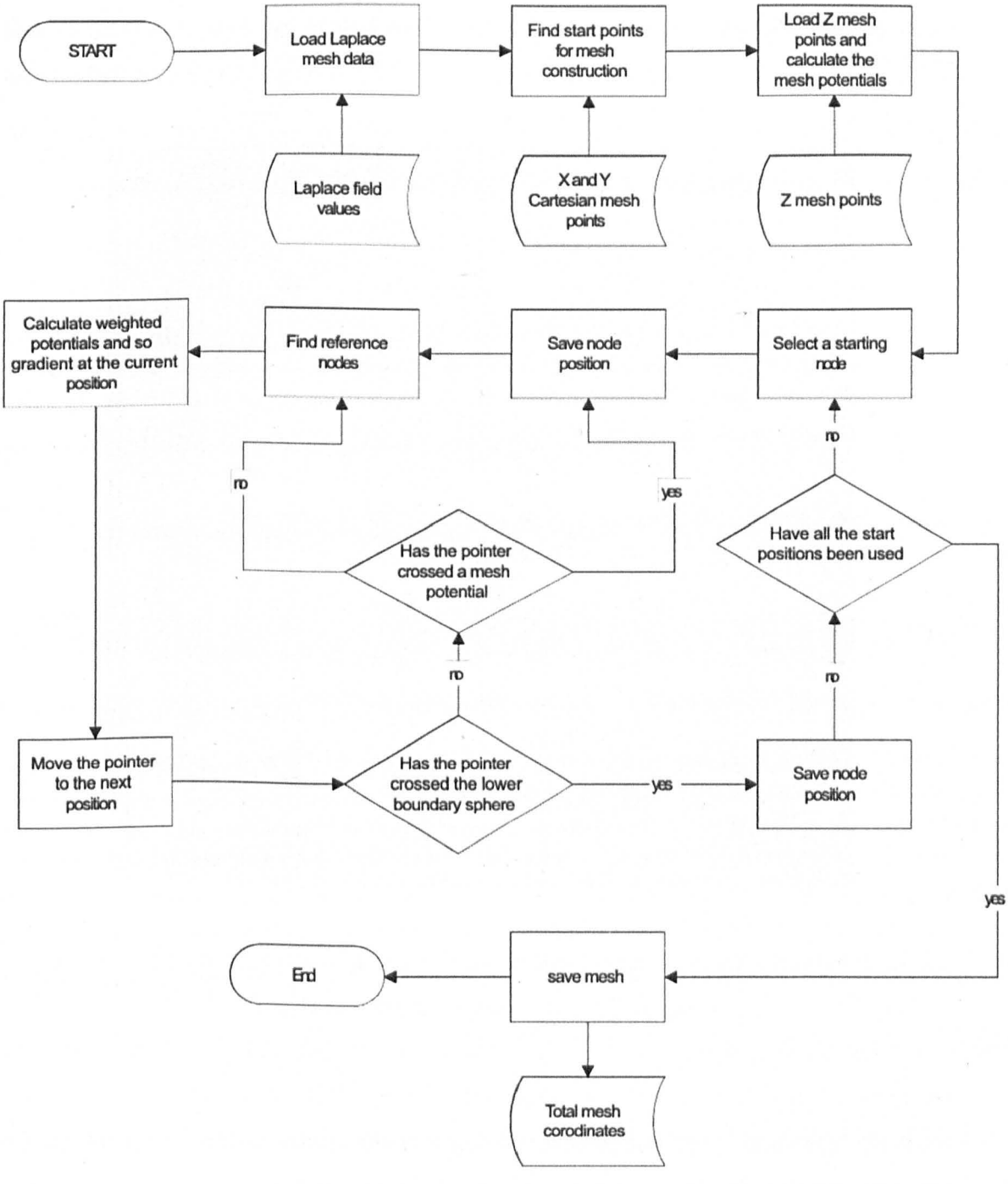

Figure 5.18 Flow chart of the processes involved in the construction of the orthogonal mesh.

The method used to produce the reference-mesh assumes that there will only be a slight deformation of the grid at the interface between the flattened and spherical surfaces, as the size of the flattened section is so much smaller than the sphere on which it is located. In addition any distortions in the curvilinear mesh that result from this discontinuity will be located away from the face antenna and the intense fields around the slot.

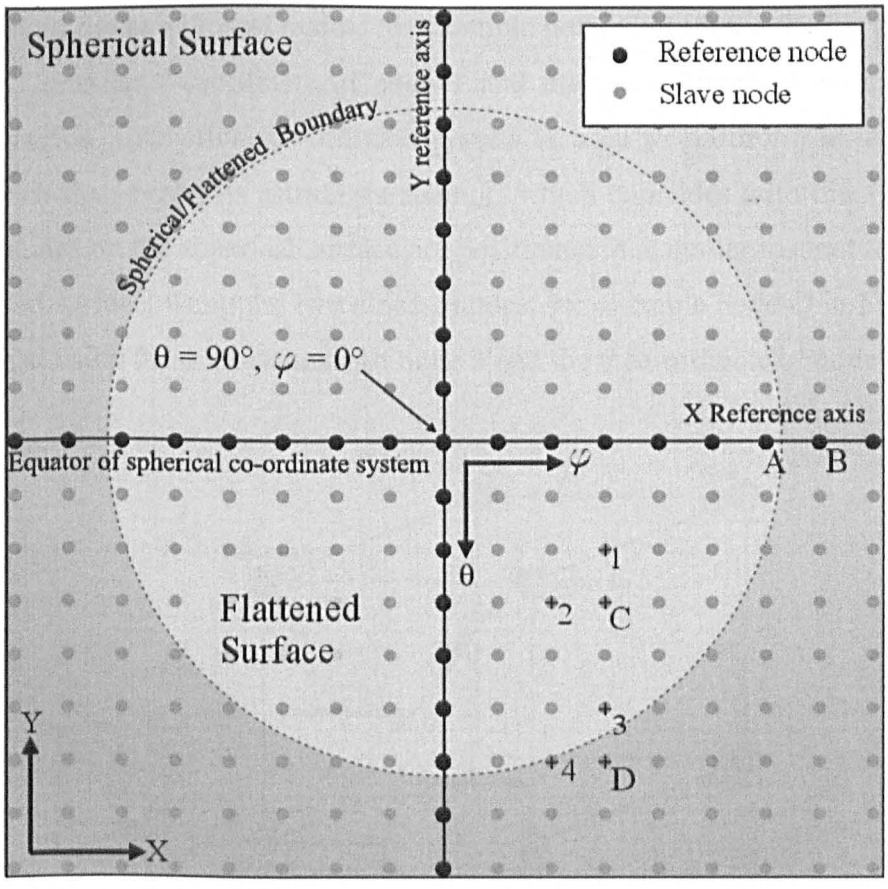

Figure 5.19 Positioning nodes in the reference mesh (view of the Z+ boundary of the mesh volume from above the XY plane)

To construct the mesh, two lines of reference nodes are built outwards from the centre of the flattened surface, one in the x (logical i) and one in the y (logical j) direction (see Figure 5.19). The lines are constructed in a step by step fashion similar to that described in Section 5.2.1. Each node's position is based on that of the previous node, while their spacing is the same as in the x-y planes of the Cartesian antenna mesh. The

transition from the flattened to the spherical surface; e.g. positioning node *B* based on the position of node *A* (Figure 5.19), is handled by translating the Cartesian spacing to an angular shift that results in the same spacing between nodes, across the curved surface of the spherical section.

Based on the position of the reference nodes, the rest of the nodes are positioned from the centre out. Nodes on the flattened surface are placed using the Cartesian coordinates of the two closest nodes; for example node *C* in Figure 5.19 is positioned using the Cartesian *x*-coordinate of node 1 and the y-coordinate of node 2. In the spherical region a spherical co-ordinate system is used to position the nodes. It is orientated so that mesh sits astride its equator, which coincides with the *x*-reference line. The nodes on the spherical surface are positioned in a similar manner to those on the flattened surface, using the two closest nodes; for example node *D* in Figure 5.19 is positioned using the φ co-ordinate of node 3 and the θ co-ordinate of node 4.

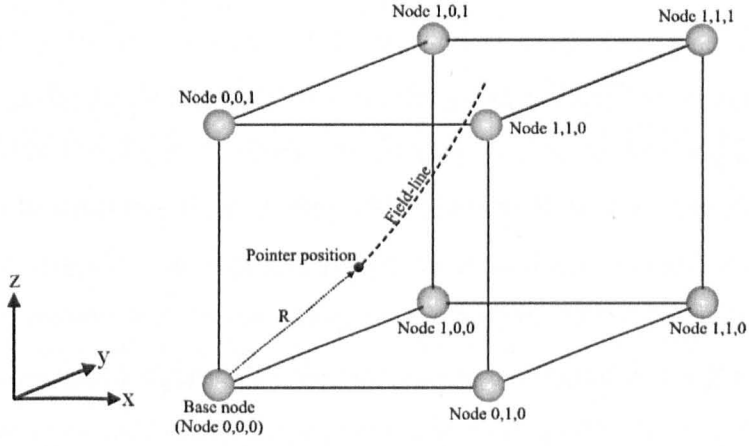

Figure 5.20 Pointer located within 8 closest nodes in the Laplace mesh.

It should be noted that the position of the surface astride the equator of the spherical coordinate system has been chosen specifically to make the construction of the mesh possible. The positioning of the equator along the *x*-reference line means that the *y*-orientated mesh lines enter and exit the flattened region at positions with the same *y* and φ – coordinates either side of the equator. This means that the Cartesian and

spherical co-ordinate systems coincide at the boundary of the two regions allowing the integration of the meshes with minimal distortion.

5.4.3.2 Finding the Gradients and Following the Field Lines

Once the reference mesh has been constructed, the field-lines can be found. To follow them through the volume a 'pointer' is located at one of the start points dictated by the reference mesh. The gradient is calculated at that point and a small step is taken through the volume based on that gradient. The gradients $\dot{\xi}$ of the field in the x, y and z directions at the logical node position (i, j, k) are simply calculated by:

$$\begin{aligned}
\dot{\xi}_x(i,j,k) &= \xi(i+1,j,k) - \xi(i-1,j,k) \\
\dot{\xi}_y(i,j,k) &= \xi(i,j+1,k) - \xi(i,j-1,k) \\
\dot{\xi}_z(i,j,k) &= \xi(i,j,k+1) - \xi(i,j,k-1)
\end{aligned} \tag{5.24}$$

As it is unlikely that the pointer will be located directly on a node, the gradient must be found using the gradients at the surrounding nodes. First we must identify the eight nodes that form the cube in which the pointer is located (see Figure 5.20). This is done by identifying and then finding the distance R to the "base node" (the node closest to the origin). T he distance to the other nodes in the cube can be calculated based on the value of R. Normalised to the length of the side of the cube, these distances are used as weighting factors to calculate the gradient at the pointer position. The x-direction gradient at the location of the pointer ($\dot{\xi}_x^{POINTER}$) is calculated by;

$$\dot{\xi}_x^{POINTER} = \frac{\sum_{n=1}^{N} \dot{\xi}_x^n \times w^n}{\sum_{n=1}^{N} w^n} \tag{5.25}$$

where N is the number of nodes (in the case seen in Figure 5.20 $N = 8$) and w^n is the weighting factor associated with node n which is calculated by;

$$w^n = \left(\frac{R^{MAX} - R^n}{R^{MAX}} \right)^2 \tag{5.26}$$

where R^{MAX} is the maximum possible distance from a node to the pointer, normalised to the length of the cubes sides. For the case of the eight nodes seen in Figure 5.20 $R^{MAX}=\sqrt{2}$. R^n is the normalised distance from the pointer position to node n. The gradients in the y and z directions are calculated in a similar fashion.

Once the gradients are calculated the movement of the pointer in the x, y, and z directions is found by multiplying each of the gradients by a pre-determined factor that is a fraction of the size of one of the Laplace cells. The pointer is then moved and the process repeated.

5.4.3.3 Optimising the Number of Nodes used in the Gradient Calculation

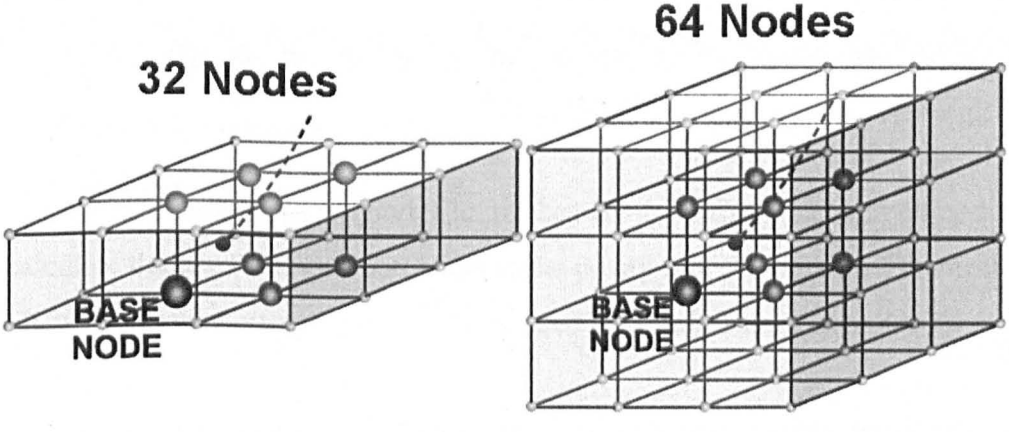

Figure 5.21 formations of Laplace mesh nodes used to calculate the gradients at the pointer position.

To identify the optimum number and layout of nodes used in the calculation of the gradients, three different arrangements were used. The first contains 8 nodes and can be seen in Figure 5.20. The second arrangement contains 32 nodes and can be seen in

Figure 5.21. This arrangement uses two planes of 16 nodes located above and below the location of the pointer. The third arrangement consists of a cube containing 64 nodes with the original 8 located at the centre. The location of the original 8 nodes in the both these lattices can be seen in Figure 5.21.

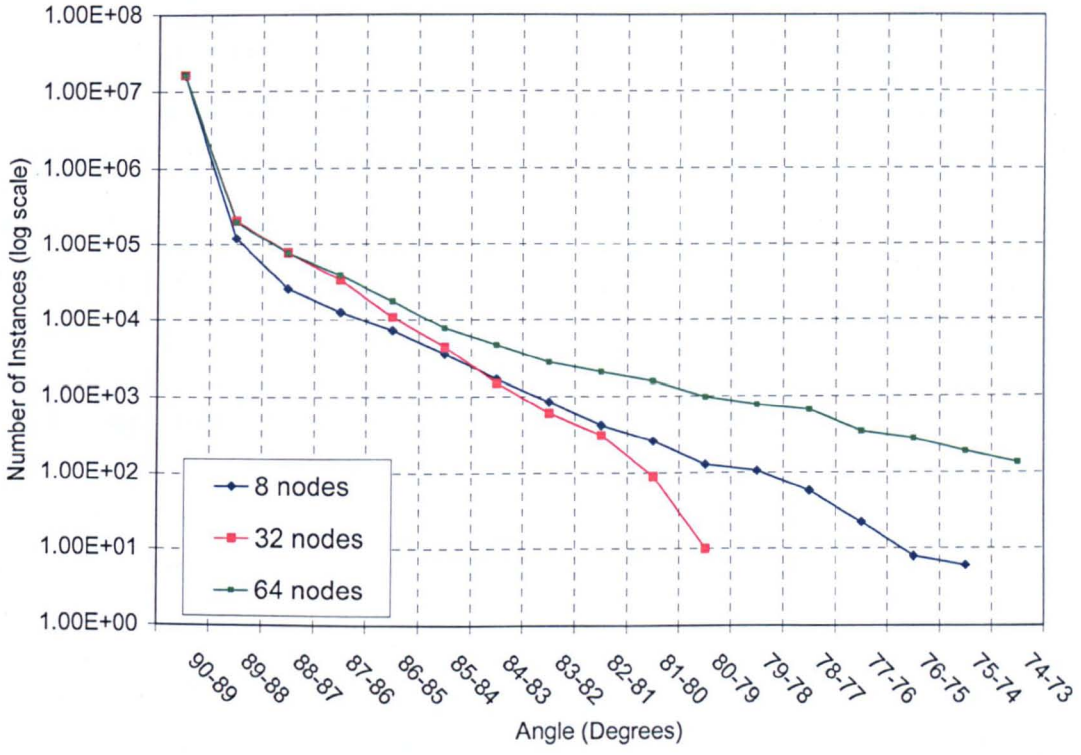

Figure 5.22 Angles between nodes in meshes created using 8, 32 and 64 nodes to calculate the gradients and potentials at the position of the pointer. The meshes created were typical of those used to simulate the antenna.

To find which arrangement of nodes produced the best quality mesh, curvilinear meshes were constructed based on those that will be used to model the antenna. The interior angles were calculated for each mesh (in the same way as for Figure 5.15) and can be seen in Figure 5.22. This data shows that the best quality mesh is produced using the 32 node scheme. The maximum deviation from the orthogonal in this is only 10 degrees while deviations of up to 15 and 16 degrees are present in the meshes produced using the 8 and 64 node schemes.

5.4.3.4 Positioning Nodes and Calculating Node Potentials

Nodes are positioned in the logical '*k*' direction by locating them at predetermined potentials along the field-lines. These are calculated based on the required location and spacing of the *i,j* planes. To find the node potentials, a line is drawn between the *z*+ and *z*- boundaries, in the middle of the mesh volume. The required *k*-direction node spacings are worked out along this line and converted to potential values by directly mapping the geometrical positions to the corresponding potentials. As a result the first node, which will be located on the Z+ boundary, will have a potential of zero, a node at the centre of the line will have a potential of 0.5 and the node at the bottom, on the Z- boundary, will be located at a potential value of one.

5.4.4 Summary: The Optimised Laplace 3D Mesh Generator

A Laplace based, orthogonal mesh generator has been presented and optimised to produce an orthogonal mesh that can potentially be used as the basis of a mesh to model a section of the wide-slot antenna array (Figure 5.2). The Laplace solver and the mesh generation algorithm have been "tuned" to produce a mesh that is as orthogonal as possible. The Laplace solver was found to produce the highest quality mesh when a node spacing of 0.035 was used, while the mesh generation algorithm performed best when the potential gradient was calculated when referencing 32 nodes from the Laplace mesh. Using these parameters the mesh generator will be used to create a mesh to model part of the imaging array.

5.5 Simulation of Two Antennas at 45°

The following section presents a number of meshes that have been produced by referencing an OC block, constructed using the Laplace mesh generator described above. To build the OC grid the 2D, logical *i-j,* reference grid and spacing of mesh planes in the in the *k*-direction are based on the Cartesian mesh used to model the wide-slot antenna in Section 4.3. Using the technique outlined in Section 5.2.1, this

mesh will be used as a template and extended to produce a mesh-unit. The spacing of the planes in the mesh-unit is, once again, referenced from the Cartesian model of the wide-slot.

Further expansion of the mesh is used to connect two mesh-units together to create a model capable of simulating two antennas angled at 45 degrees to one-another. Using this mesh a number of numerical experiments have been conducted. The resulting S-parameters, antenna near field and response from a dielectric target located in the phantom, will be used to gauge the quality of the mesh and ultimately its ability to accurately model the array. The performance of the curvilinear simulation will be compared to measured results and equivalent simulations run using Cartesian based FDTD.

5.5.1 The OC Mesh

The manufactured OC mesh can be seen in Figure 5.23 and Figure 5.24. The mesh is made up of 62 × 55 × 10 ($i \times j \times k$) nodes (34100 in total). The largest cell size in the grid is 1mm while the smallest is 0.095mm. On visual inspection of the mesh there seems to be no obvious signs of distortion. The angular composition of the mesh can be seen in Figure 5.21 (labelled 32 nodes). This figure shows that the number of non-orthogonal cells is very low, approximately 98% of the angles in the mesh lying between 90° and 89° and 99.9% above 86°. In the worst case there are around 10 angles that fall between 89°-90°. The worst deformation of the mesh occurs in the lower k planes of the mesh and is probably due to the accumulation of errors as the field lines trace down through the Laplace volume. The magnitude of these errors is the same for all the cells regardless of their size. As a result it is inevitable that the smallest cells will show the greatest deviation from orthogonal.

The mesh-unit produced using the OC grid can be seen in Figure 5.25. The logical dimensions of this mesh are 62 × 55 × 83 nodes (283030 in total). Comparing this to the mesh shown in Figure 5.5, it can be seen that this mesh does not extend down to

the centre of the spherical co-ordinate system. Instead the radial dimension of the spherical mesh has been limited to between 50 and 100mm. The reason for this is to keep the mesh as small and efficient as possible, avoid complications associated with the singularity at the centre of the spherical co-ordinate system and to avoid very small cell sizes that would affect an impracticably small time step.

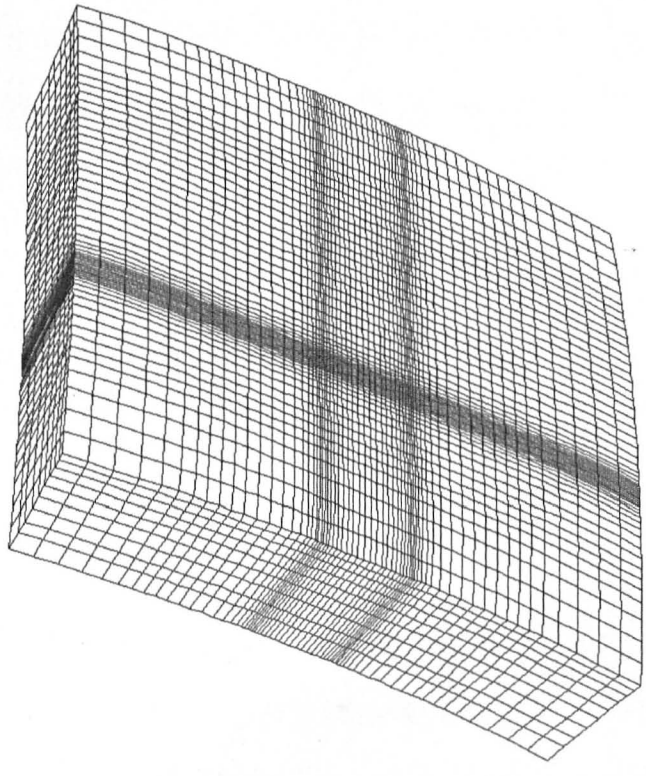

Figure 5.23 A three-dimensional projection showing the top ($z+$) surface of the OC mesh.

The angular composition of the mesh-unit can be seen in Figure 5.26. As the orthogonallity of the Cartesian mesh region can be guaranteed, this figure only includes the mesh contained in the OC block and spherical mesh. The quality of the mesh-unit is slightly poorer than the OC block. Though, the number of non-orthogonal cells is still low; approximately 94% of the angles in the mesh lying between 90° and 89° and 99.4% above 86°. The reason for this slight increase in the variation of mesh angles, is most likely due to the spherical mesh section referencing

the z- surface of the OC grid. As already noted it is this region of the mesh that is least orthogonal and so these errors are reproduced in the k-planes of the spherical mesh.

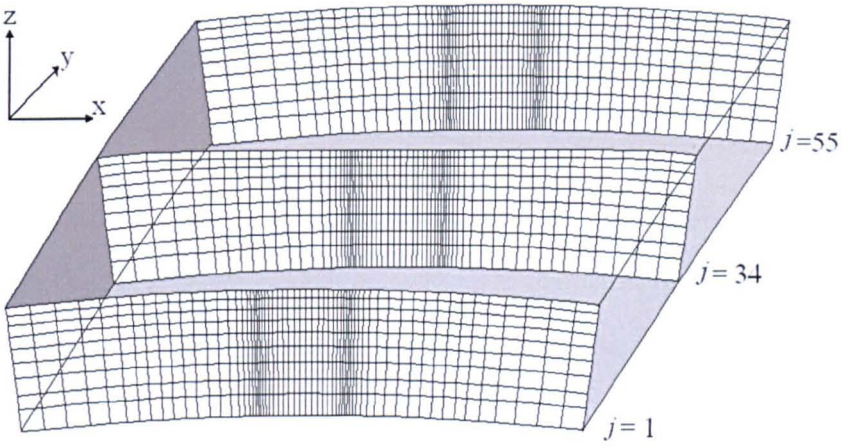

Figure 5.24 Three i-k sections through the OC mesh at j = 1, 34 and 55

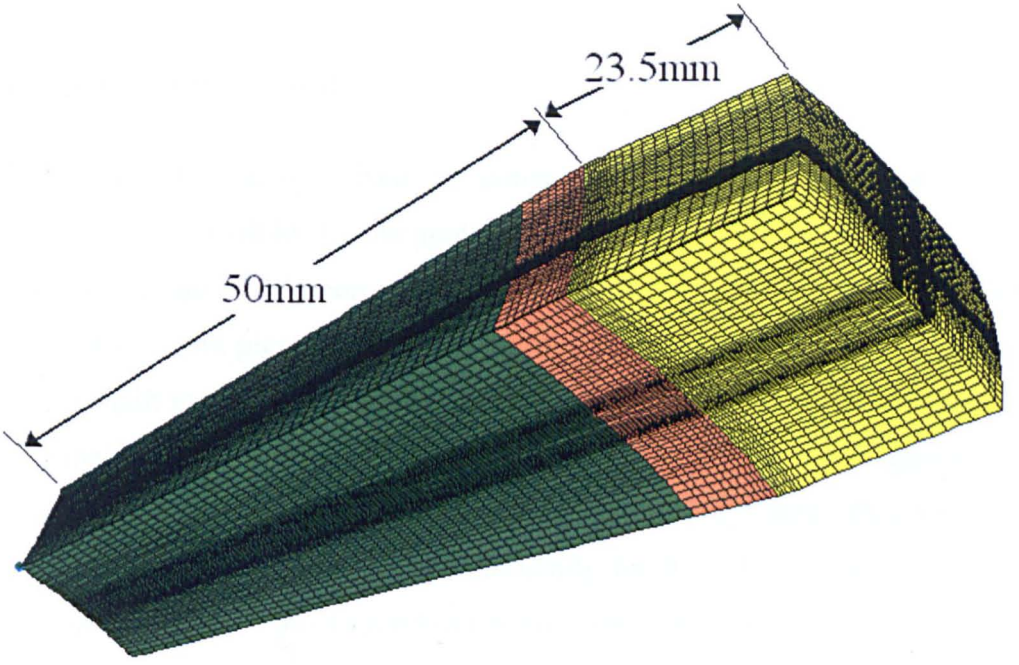

Figure 5.25 A three dimensional projection of the mesh-unit with the spherical (green), OC (orange) and Cartesian/excluded (yellow) mesh regions highlighted.

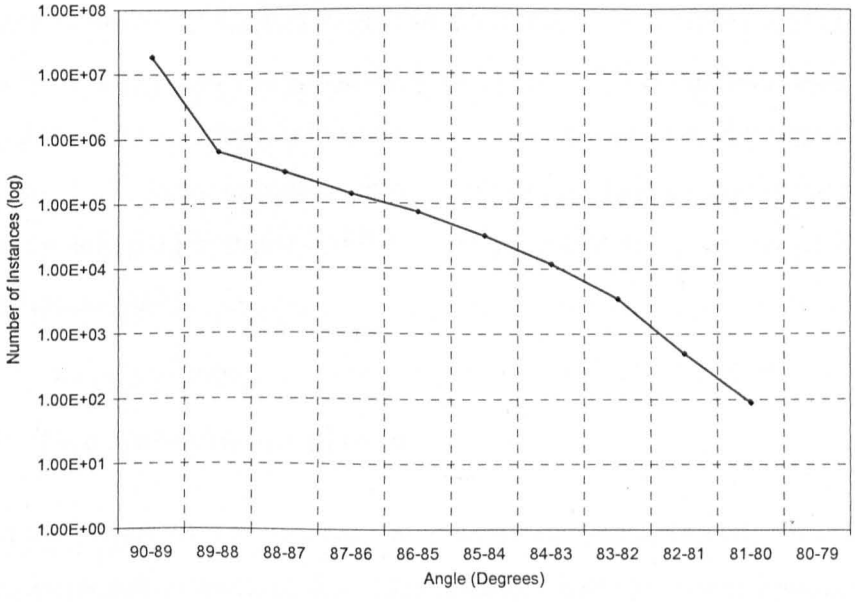

Figure 5.26 The angular composition of the mesh unit.

5.5.2 Two Antenna Mesh

The mesh-unit is used as a basis to construct a grid that models two wide-slot antennas at an angle of 45° to one another (Figure 5.27). The two mesh-units used in its construction have been connected by a region of spherical mesh that covers an angle of 30.93°, with planes spaced 0.57° in the φ-direction. The r and θ co-ordinates of this inter-unit region are referenced from the j-k plane on the φ+ boundary of mesh-unit 1. Finally the two antenna mesh has been extended by 5 cells in the +/- θ and φ directions, using the same angular spacing as the inter-unit grid. This was done to ensure the θ and φ boundaries were sufficiently far from the antennas. The logical dimensions of this mesh are 183×65×84 nodes (999180 in total). Figure 5.27 shows a cross-section through this mesh highlighting various regions and showing the location of the mesh-units.

Figure 5.27 also shows the mesh discontinuity alluded to in Section 5.2.2. This deformity is a result of the mesh-plane geometry, referenced in the construction of the inter-unit grid. This grid can be accurately constructed up to the r+ boundary of the

OC mesh, because the nodes of the reference plane are part of a spherical based mesh. Above this point the Cartesian grid of the antenna is sampled, producing a mesh that doesn't correspond to the spherical grid below. This manifests itself most obviously as the defect at the interface between the inter-unit grid and the second mesh-unit seen in Figure 5.27. More significantly it results in a plane of non-orthogonal cells at the Cartesian/spherical boundary of the inter-unit mesh that must be isolated from the rest of the simulation.

5.5.3 Two Antenna Simulation

The basic setup of the orthogonal curvilinear simulation is the same as for the Cartesian model in Section 4.3. The antennas have the same structure and the same numerical phantom is used (ε_r=9). The main difference is in the application of the Mur ABC. While the +/- φ and θ boundaries are flat, on the +/- r boundaries the Mur ABC is implemented on a curved surface reducing its effectiveness. From experience it was found that the r+ boundary performed sufficiently well, probably because it's radius of curvature is large and the antennas are not radiating directly toward it. On the r- boundary the radius of curvature is twice as great reducing the ABC's effectiveness to the extent that reflections from the boundary were affecting results. This problem was overcome by inserting a 20 cell thick, absorbing, lossy layer along the r- boundary. This was designed in an iterative manner, optimally made up of 4 layers of dielectric, each 5 cells thick with conductivities of 1.6 S/m closest to the boundary, 0.8, 0.4 and 0.2 S/m in the final outer layer.

The r+, or Interior absorber, also has the function of isolating the non-orthogonal grid and the mesh deformity (Figure 5.27) from the rest of the workspace. To avoid numerical instability the edges of the Mur ABC must be terminated with another orthogonal Mur ABC or an orthogonal metal surface extending more than two cells beyond the Mur boundary. For this reason, to correctly terminate the Mur boundary at the antenna holes, the cavities of the antenna protrude through the interior boundary by 0.5mm (2 cells).

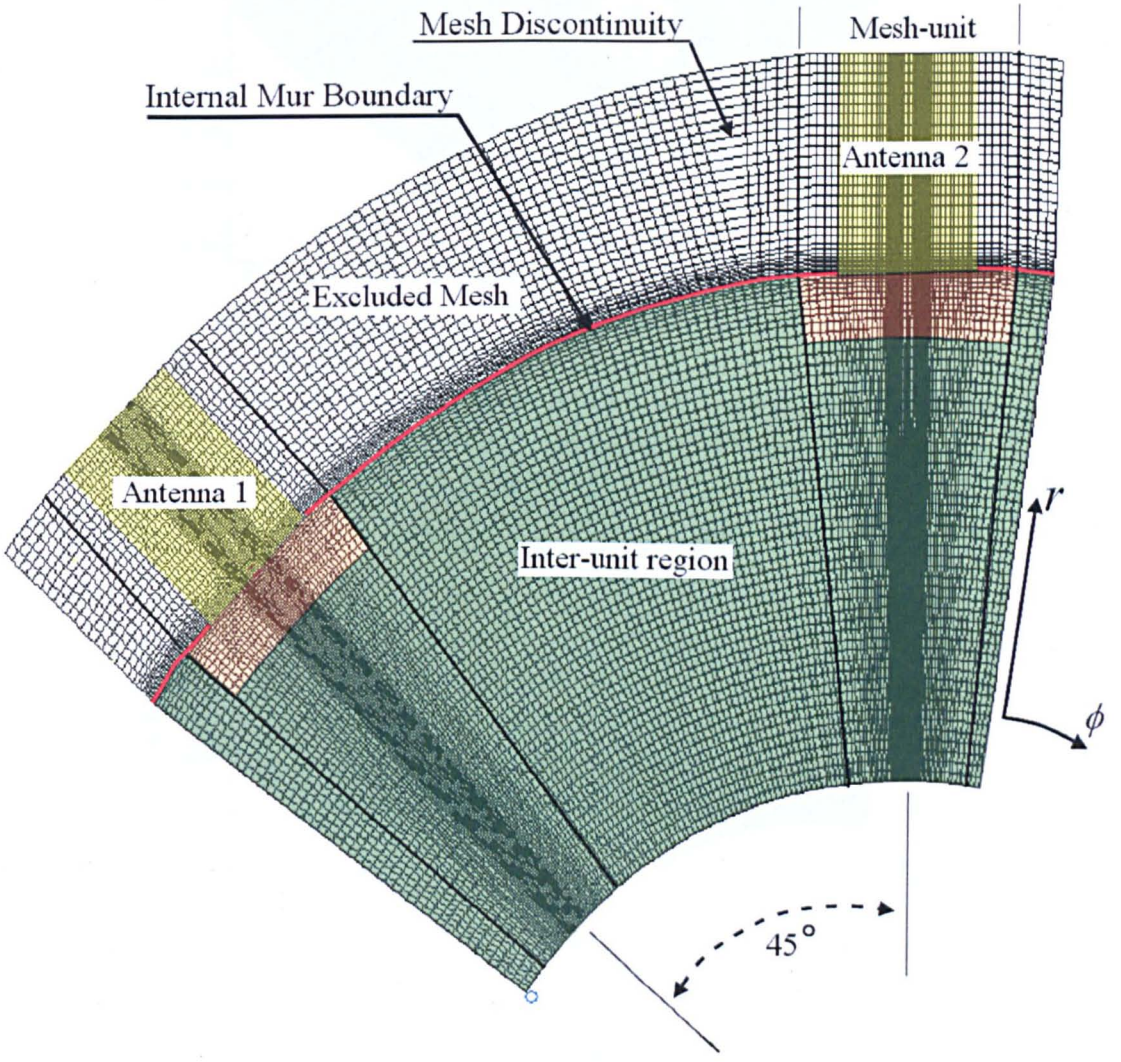

Figure 5.27 The *i-k* plane of the two-antenna mesh at $j = 30$ with the spherical (green), OC (orange) and Cartesian/excluded (yellow) mesh regions highlighted. The uncoloured regions represent the mesh excluded from the simulation.

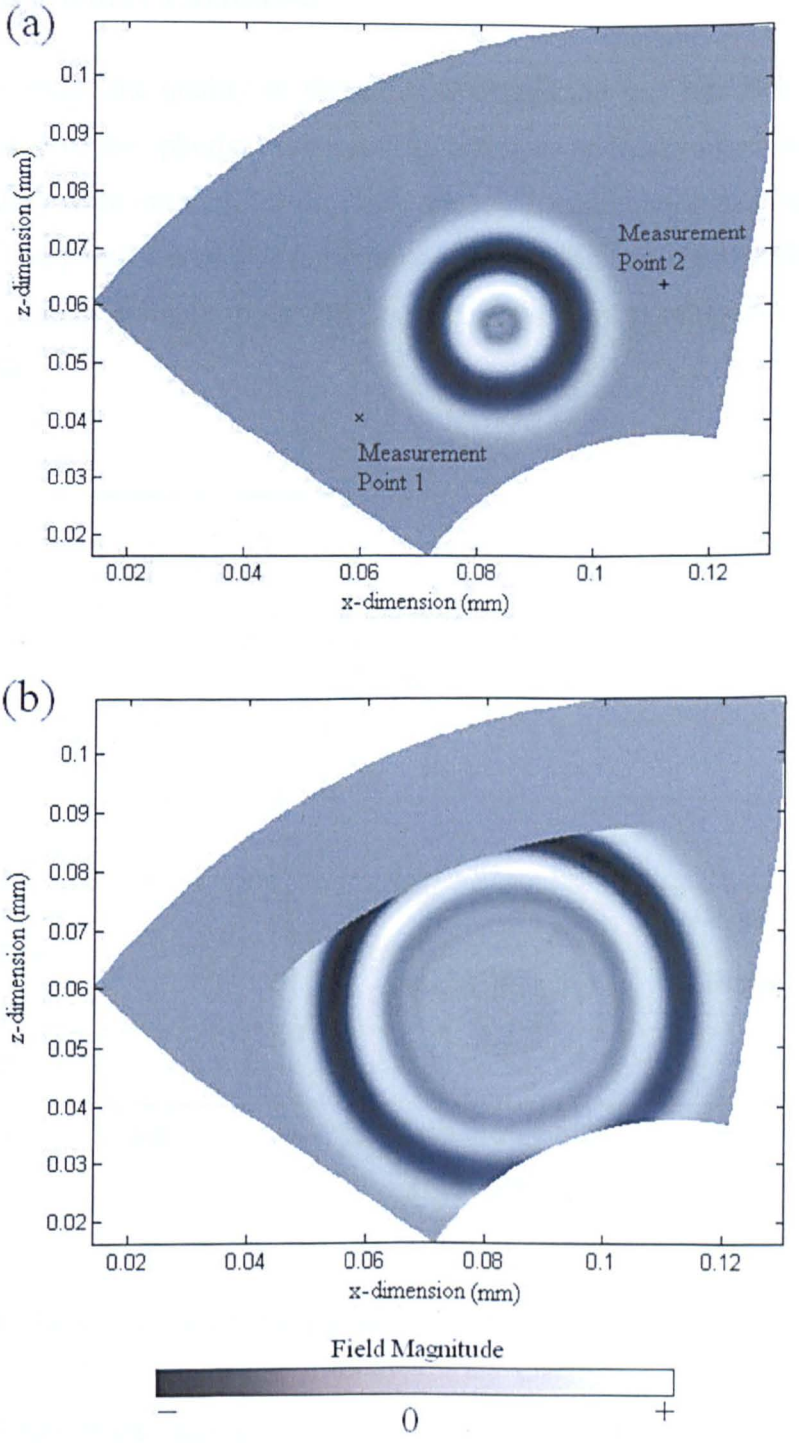

Figure 5.28 The *y*-direction electric field radiating from a virtual "point-source" after (a) 226 ps (2000 iterations) and (b) 452 ps (4000 iterations). Data shown from the *i*-*k* plane at $j = 38$ (mid-plane of the simulation). Figure (a) shows the two measurement points used in Figure 5.29

5.5.4 Point Source Excitation

To visually judge the quality of the mesh, a simulation was run with a virtual point source located in the spherical section. The antennas and their associated holes in the Mur boundary were omitted, leaving only the mesh and boundary conditions to affect the fields. The point source was implemented by exciting an electric field along the *y*-orientated edge of a single mesh cell, located at the logical midpoint of the spherical mesh region.

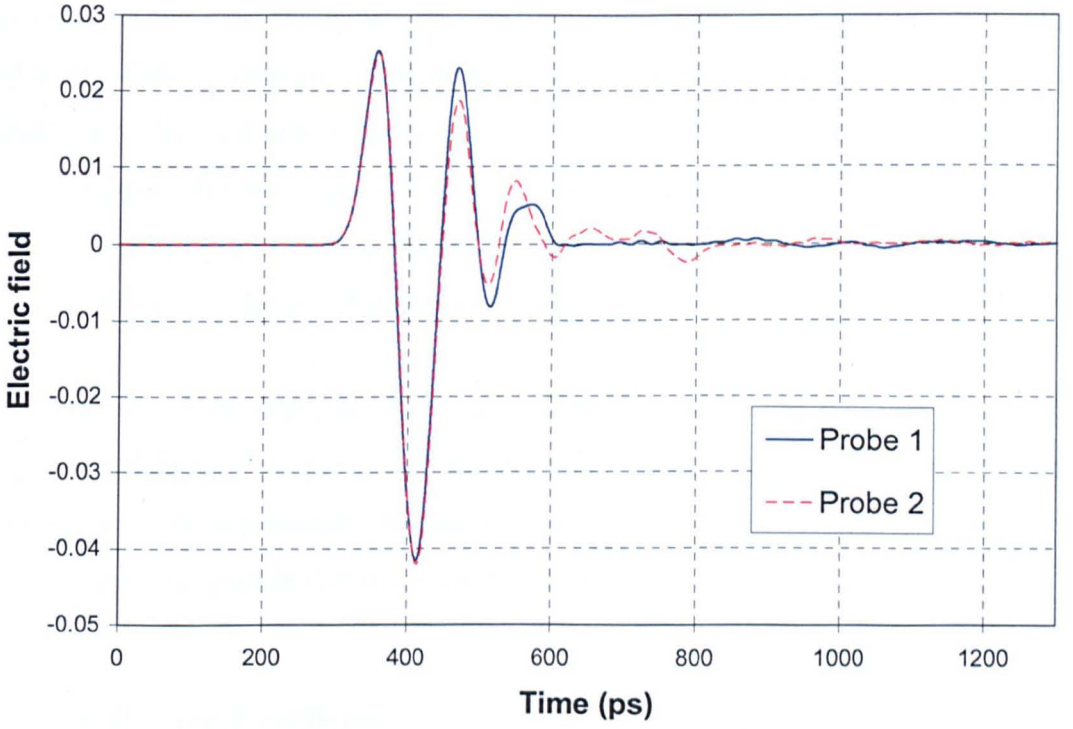

Figure 5.29 The y-direction E-field at the measurement points indicated in Figure 5.28

Figure 5.28 shows the resulting *y*-direction field component after 226 and 452 ps. In both cases the propagation through the volume is regular and undistorted. After 226 ps the excitation pulse is concentrated in the inter unit-mesh and hasn't yet reached the boundaries so up to this point the mesh is the only thing that has acted on the fields. As there are no obvious problems we can conclude that, in this region, the model is able to accurately propagate the radiated fields. At 452ps the field has begun

to interact with the ABCs and the position of the interior Mur boundary can be clearly seen. As there are no significant reflections or distortion of the fields it can be concluded that the boundary conditions are relatively effective. It should be noted that towards the *r*- boundary the intensity of the field drops off. This is because the field is attenuated by the conductive absorbing layer.

Figure 5.29 shows the *y*-direction E-field at two points in the simulation workspace. The points are equidistant from the source and so the radiated pulses should arrive simultaneously (see Figure 5.28 for their position). The plots show that the pulse reaches both points at the same time and both pulses have the same form. Towards the end of the pulses there are slight differences as spurious reflections interact with the signals, most likely due to reflections from the boundaries. As the points are located at what would be the boresight of the antennas, the radiated waves must pass through some of the most non-orthogonal mesh to reach them. So, the level of similarity between the plots indicates that the mesh and simulation are working reasonably well.

These results show that the mesh is able to propagate the radiated signals to a reasonable degree of accuracy and the boundary conditions are operating reasonably effectively. This experiment also shows that there are no major sources of numerical noise or spurious signals that result from the mesh.

5.5.5 Reflection Coefficient

Figure 5.30 shows the S_{11} for the antennas in the curvilinear simulation (the response of both antennas was identical) and the same response from a Cartesian simulation with a similar sized mesh and the same number of nodes. The -10dB bandwidths are in close agreement at 4.2 (4.3 - 8.5GHz) and 4.55 GHz (4.2 - 8.75GHz) respectively. In terms of their shape the responses have approximately the same form with no significant variation between the two plots above -13dB. The main differences between the plots are the three, well defined resonances at 4.6, 5.4 and 7.3GHz in the standard response. While these may be visually significant, numerically they represent

maximum differences of only 4% of the maximum reflected signal. The cause of these variations is likely down to the implementation of the resistor terminating the microstrip feed being slightly different in the curvilinear code, but could also be due to differences in mesh near the antenna.

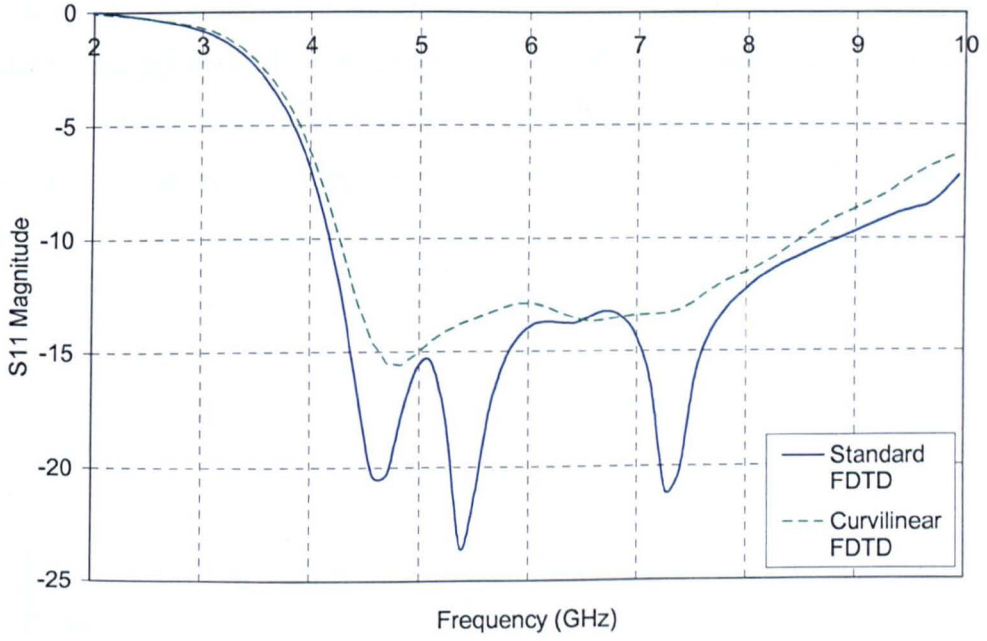

Figure 5.30 The S_{11} of the antenna as found using the University of Bristol in-house Cartesian FDTD and the Curvilinear FDTD simulation.

5.5.6 Transmission Between the Two Antennas

The transmission response between the two antennas can be seen in Figure 5.31, with the equivalent measured results shown for comparison. The measurement was made using the same experimental arrangement and phantom as in Section 4.6 but with the antennas positioned in the middle of the of the measurement tank in the same geometrical arrangement as in the simulation. The simulated results were produced using a lossless numerical phantom ($\varepsilon_r = 9$). The frequency dependent attenuation in the medium was accounted for post simulation in the same way as in Section 4.6 using the measured properties of the matching medium.

These results show that the curvilinear simulation is able to reproduce the measured result reasonably accurately. Overall, the shape and magnitude of the simulated response is similar to the measured results and the two plots do not differ by my more than 10 dB, except at the extreme high end of the frequency range. Differences between the responses are most likely caused by measurement errors, such as differences in the physical/theoretical phantom properties and manufacturing tolerances, and errors in the simulation such as reflections from the boundaries of the simulation domain or distortion of the radiated fields by non-orthogonal cells in the mesh. As the variations are reasonably small it can be assumed that none of these factors is significant compared to the overall fields in the simulation domain.

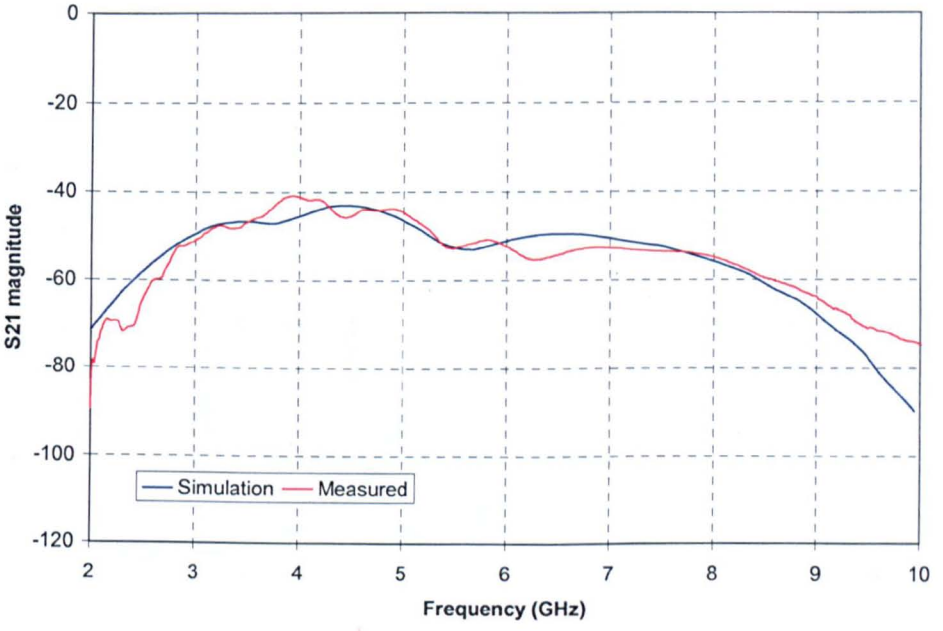

Figure 5.31 The measured and simulated S_{21} between two antennas at 45°

5.5.7 Response from a Scatterer

The intended purpose of this mesh is to simulate a radar imaging array, so it is crucial that it is able to accurately model the response from a dielectric scatterer located in the phantom. To test this, a small inclusion is placed in the phantom, directly between the

two antennas at a distance of 30mm from the interior Mur boundary (Figure 5.32(a)). The scatterer occupies one mesh cell of dimensions 0.7×0.7×1mm and has a relative permittivity of 50. This gives a contrast of 5:1 with the background medium, a ratio typical of that between a tumour and adipose breast tissue [32]. Setup in this way the illumination angle of the scatterer is 37.9° from bore-sight in the antenna H-plane.

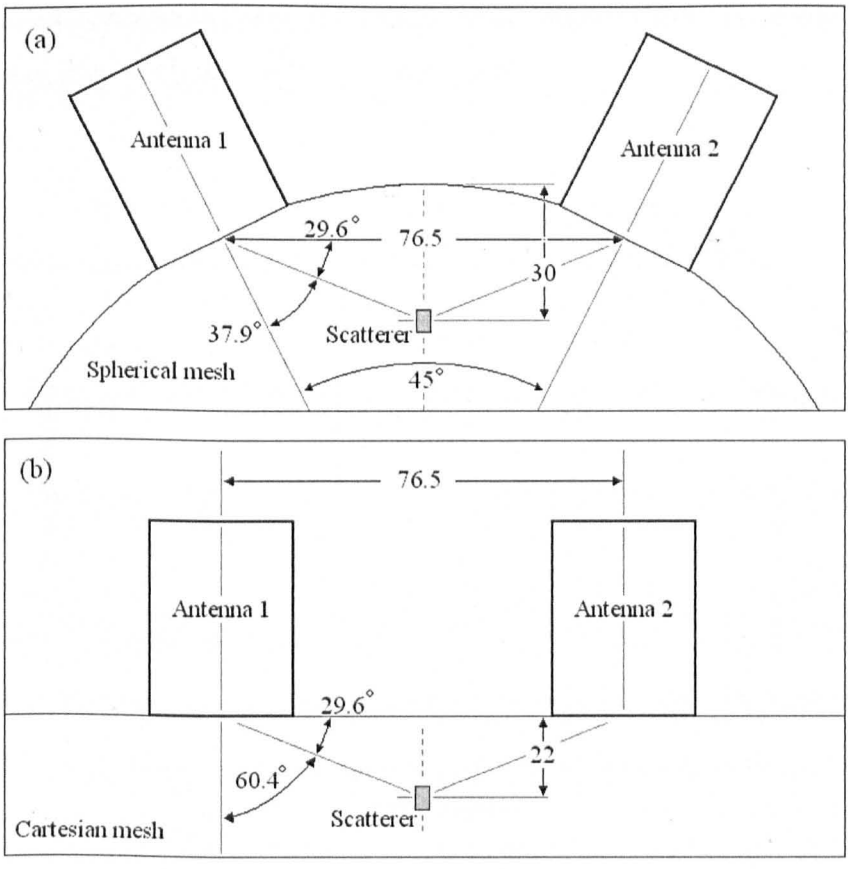

Figure 5.32 The location of the scatterer in the (a) the curvilinear and (b) the Cartesian simulations. These diagrams are not to scale, all dimensions are in mm.

To provide a comparison, the same scatterer is also placed in a Cartesian simulation with a similar geometry (Figure 5.32(b)). This model consists of two antennas position so that the distance between the central points of the antenna faces is the same as in the curvilinear geometry. Otherwise the simulation setup is identical. The scatterer is positioned so that the distance to the central points is the same as the

curvilinear mesh. In this location the illumination angle of the scatterer is different (60.4°) but the path length (Antenna1 – scatterer – Antenna 2) is the same in both cases.

Single cell scatterers were chosen because it would have been difficult to produce two identical, large scale scatterers using the spherical and Cartesian basis of the two meshes. Any differences between the single celled targets should be negated by virtue of the fact that they are both electrically very small.

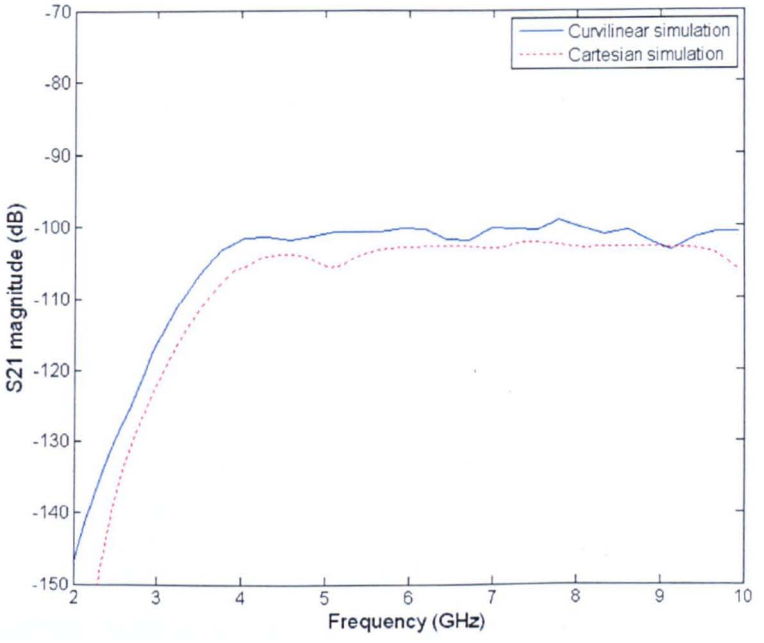

Figure 5.33 The frequency domain response (S_{21} magnitude) of the scatterer at antenna 2 with antenna 1 transmitting.

The response from the scatterer is found in the same way as in Section 4.6.6, with a calibration signal subtracted from the response at Antenna 2. This removes any 1st order reflections from the boundaries leaving only the effects of the mesh. As a result this experiment will allow a direct judgement of the mesh quality.

The magnitude of the frequency domain response from the scatterer can be seen in Figure 5.33. To compare the responses we must refer to the measured S_{21} data for the wide-slot, shown in Figure 4.45. From these transfer functions we find that the difference between the radiation intensity at 37.9° and 60.4° is between 4.5 and 5dB in the frequency range 3-8GHz (above 8GHz the transfer function at 60° is below the noise floor and so a sensible comparison cannot be made). Although the frequency dependent losses were not included in these simulations the difference in radiation intensity at different angles should still be the same. Examining the responses in Figure 5.33 shows that the difference between the simulated responses has a pleasing level of agreement with the measured value. Although the spacing of the two plots varies between 0 and 7dB, for the majority of frequencies the spacing is approximately 3-5dB in close agreement with the expected figure of 4.5-5 dB. The errors in the responses are probably due to the curvilinear mesh 2nd order reflections from the scatterers that cannot be removed by the calibration process.

5.5.8 Computational costs

The computational costs of running an FDTD simulation using this hybrid meshing technique are comparable to running a problem with the standard Cartesian FDTD algorithm with the same number of cells. This is illustrated by examining the computer resources required to run the two simulations in the previous section (Figure 5.32), each of which contain 183×65×84 nodes. Running the simulations for 32000 iterations on a 3.2 GHz Pentium desktop PC took 6 hours 45 minutes for the hybrid and 5hrs 25min for the cartesian mesh.

The memory requirements for the meshes were 896 MB for the hybrid and 607 MB for the Cartesian mesh. The difference between these values is due to the way the coefficients are stored in each case. In the hybrid simulation, due to the nature of the mesh, the majority of cells are different sizes; their update coefficients are different and so have to be stored individually. In the cartesian simulation there are a larger number of identical cells whose coefficients are instead stored in a catalogue fashion

with identical cells assigned a reference. This means that for complex cases such as this where there are many different cell sizes in the Cartesian mesh, the memory requirements are comparable, for simpler problems however, the difference in memory requirements maybe greater.

5.5.9 The Antenna Fields

Figure 5.34 shows the relative values of the H-plane electric field of the wide-slot antenna, found using the curvilinear mesh and a standard Cartesian based solver. In both cases the patterns were found by sampling the *j*-direction E-field at 10° intervals between 0° and 80° from bore sight, at a distance of 30mm from the antenna. The transfer functions were then calculated and the resulting data set examined at 3, 6 and 10GHz. Field values at 90° have not been included as the curve of the interior Mur boundary, in the curvilinear mesh, precludes their measurement.

To reduce unwanted reflections only antenna 1 was included in these simulations. In the curvilinear setup this meant removing antenna 2, and the associated hole in the interior Mur boundary. The Cartesian simulation setup was based on that used to model the antenna in Section 4.3. In this case a lossy numerical phantom (ε_r=9, σ = 0.2) is used that has a considerably larger volume (115×115×100 mm) than that employed in the curvilinear model. Consequently any reflections from the boundaries are significantly attenuated and are negligible compared to fields directly radiated by the antenna.

The plots from the Cartesian simulation have been normalised to their maximum value, while the plots from the curvilinear simulation have been normalised to give the best fit with the Cartesian data. All three graphs show that in general the fields in the curvilinear simulation are similar to those of the standard FDTD model. At 3GHz the two plots vary by less than 2dB between +/- 70°. The main deviation within this angular range is at +/-20° where the curvilinear plot peaks. This could be due to reflections from the conductive absorber, however the location of the measurement is

also directly below the smallest cells of the OC mesh, which could also be distorting the radiated field. The other major deviation from the Cartesian plot occurs at the angular extremes. This is probably due to the close proximity of the interior Mur boundary at this location.

Close to bore sight, the fields at 6 and 10GHz show the same irregularities as at 3GHz. For the rest of the 6GHz plot the agreement is very good, the maximum difference being 2dB across the entire angular range. At 10GHz the agreement is slightly worse, the curvilinear plot offset by around 2-3dB across the entire frequency range and 7 dB at the angular extremes. The overall shape of the plots is also different suggesting that errors in the mesh and/or reflections from the boundaries are more significant at higher frequencies.

In summary these results imply that the curvilinear mesh models the antenna and spherical phantom to a reasonable degree of accuracy. And though errors in the simulation have a noticeable effect, these are small compared to the direct antenna fields. When they do occur, these problems seem to manifest themselves more prominently at higher frequencies. With discrepancies of no more than 2-3dB between +/- 70° the effects seen in Figure 5.34 are still relatively minor.

5.6 Extension of the Mesh and Other Modelling Considerations

The results presented in the last section show that this meshing technique provides a viable method for modelling a section of the University of Bristol imaging array. The technique provides a relatively flexible way of producing orthogonal meshes that can used in conjunction with an efficient FDTD algorithm. To produce a mesh capable of simulating the portion of the array in Figure 5.2, the mesh units modelling the various antennas would be positioned in a circular pattern along the θ direction and linked using the inter-unit meshing technique described above. This would produce a wedge of mesh that could then be extended in the +/- φ direction to simulate as much of the spherical phantom as required.

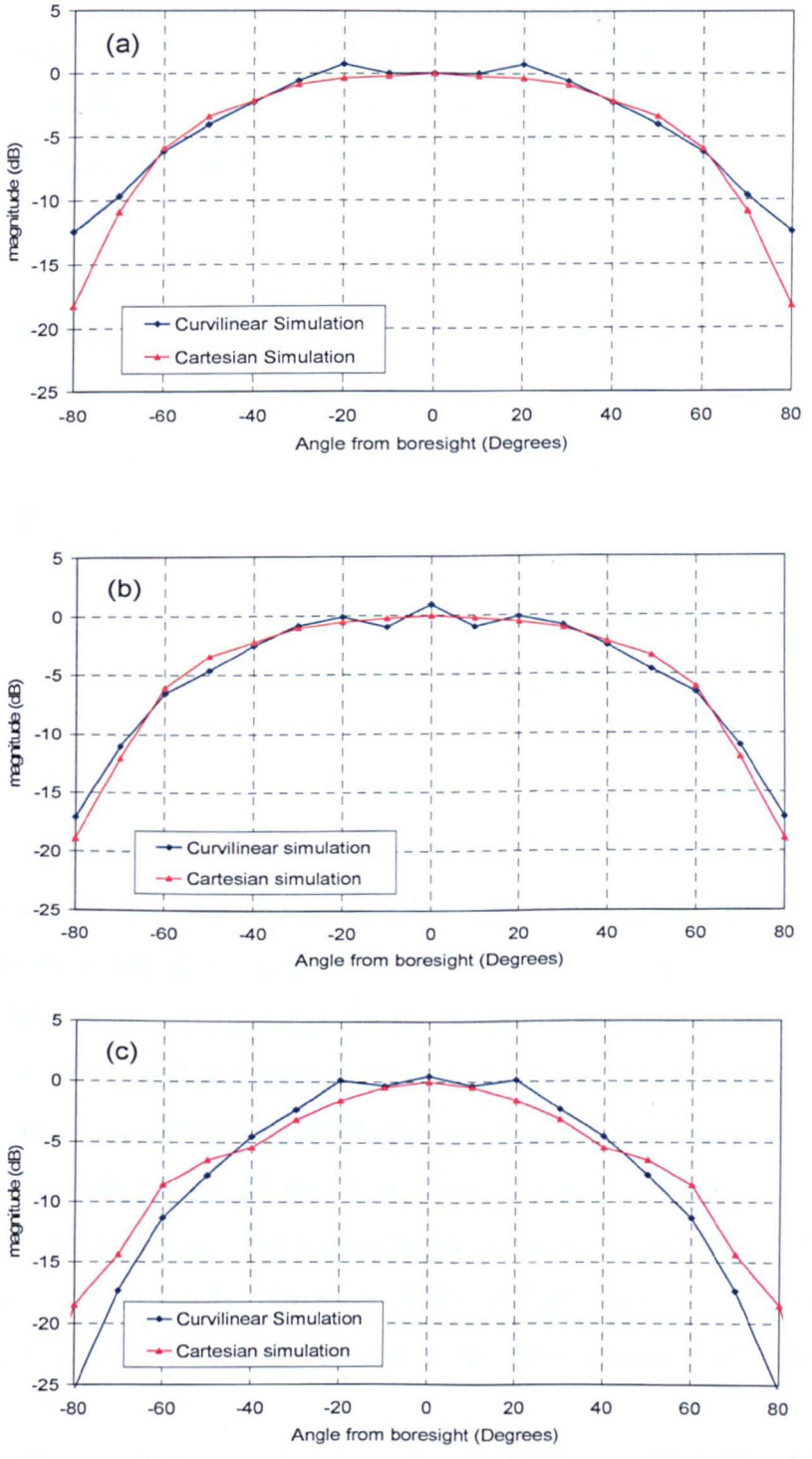

Figure 5.34 The E-plane electric field at (a) 3GHz, (b) 6Ghz and (c) 10GHz found at a radial distance of 30mm from the antenna.

Unfortunately using the method outlined here it would be very difficult to produce a mesh capable of simulating the entire array. This is because of the way in which the 2D reference mesh, used to build the OC block, is positioned either side of the equator of the spherical co-ordinate system. Although this allows the integration of the resulting OC block with the spherical mesh of the phantom, it precludes the positioning of other antennas away from this position without significant deformation of the mesh.

5.7 Conclusion

This chapter presents a novel method of producing hybrid, orthogonal curvilinear meshes. The meshing procedure involves producing a volume of OC mesh that allows Cartesian and spherical based meshes to be linked. The resulting orthogonal, hybrid lattice can be simulated using a curvilinear-coordinate based FDTD program, with the same efficiency as a standard Cartesian based simulation with the same number of nodes.

The OC section of mesh is constructed using a method that exploits the orthogonal nature of field lines and isopotentials in a potential field. A field with the same form as the OC mesh is found, using a finite-difference based Laplace-solver. The field structure is defined by applying appropriate boundary conditions within the Laplace solver volume. Field lines are then followed through the field from suitable starting points on its boundary, defined by a 2D reference mesh. The nodes of the OC grid are positioned along the length of the field lines at potentials corresponding to the required mesh plane spacing. The hybrid mesh is completed using the OC mesh as a reference. Mesh-planes on the boundary of the OC-grid are sampled and replicated using different co-ordinate systems to build up the spherical and Cartesian meshes.

This technique has been used to produce a mesh capable of simulating a section of the UWB radar imaging array, being developed at the University of Bristol. Initially a mesh-unit is produced capable of simulating a single wide-slot antenna and a segment

of the spherical phantom. A number of mesh units are then joined by further regions of spherical mesh to produce the curved array. The reference mesh used in the construction of this unit is based on the Cartesian grid used to model the wide-slot antenna in Section 4.3. The orthogonallity of the mesh in the unit was assessed by analysing its angular composition. This showed that the vast majority of the angles in the grid were very close to ninety degrees, verifying the construction technique.

Results are presented from a model containing two antennas spaced by 45°. With the antennas removed, the transmission of a pulse from a point source located in the middle of the spherical section, shows that the mesh is able to propagate fields without significant distortion. With the antennas included, they have a similar S_{11} response to an equivalent Cartesian simulation, verifying the antenna model and excitation. The coupling between the two antennas is shown to compare favourably with measured results. In conjunction with the point source excitation experiment, this suggests that the simulation is able to replicate the radiated fields with a reasonable degree of accuracy. This point is confirmed with the near field measurement that also shows that the effects of the mesh and reflections from the boundaries are minor compared to the direct fields radiated by the antenna

To examine the performance of the model in a scattering scenario, an experiment was run to find the response from a small dielectric scatterer with a contrast of 5:1 with the background medium. Simulations were run using both curvilinear and Cartesian meshes. The resulting transfer functions were compared by relating both data sets to the measured field intensity found in Chapter 4. Because this test removes the majority of effects from the boundaries, it allows the validity of the curvilinear mesh to be assessed directly. The pleasing level of agreement in the analysis suggests that the curvilinear simulation is able to replicate the effect of dielectric objects in the spherical mesh. This confirms that the mesh is capable of modelling the intended segment of array to a reasonable degree of accuracy and suggests, in conjunction with the other results presented in this chapter, that this may be a useful tool in numerical radar experiments.

Unfortunately fundamental changes are needed for this technique to be capable of producing a mesh that can model the entire array. At present this goal is impracticable due to the way that the OC mesh unit is constructed at the spherical co-ordinate system equator. However the Laplace/potential field technique of building OC mesh could still provide a basis for a revised method.

References

[1] Holland, Richard, "Finite-Difference Solution of Maxwell's Equations in Generalized Non-orthogonal Coordinates," Nuclear Science, IEEE Transactions on, vol.30, no.6, Dec. 1983, pp.4589-4591.

[2] Cangellaris A.C., Wright, D.B., "Analysis of the numerical error caused by the stair-stepped approximation of a conducting boundary in FDTD simulations of electromagnetic phenomena," Antennas and Propagation, IEEE Transactions on, vol.39, no.10, Oct 1991, pp.1518-1525.

[3] Taflove A., Brodwin, M.E., "Numerical Solution of Steady-State Electromagnetic Scattering Problems Using the Time-Dependent Maxwell's Equations," Microwave Theory and Techniques, IEEE Transactions on , vol.23, no.8, Aug 1975, pp 623-630.

[4] Jin-fa-Lee, Palandech R., Mittra R., "Modeling three-dimensional discontinuities in waveguides using nonorthogonal FDTD algorithm," Microwave Theory and Techniques, IEEE Transactions on , vol.40, no.2, Feb 1992, pp.346-352.

[5] Schuhmann R., Weiland T., "Stability of the FDTD algorithm on nonorthogonal grids related to the spatial interpolation scheme," Magnetics, IEEE Transactions on , vol.34, no.5, Sept 1998, pp.2751-2754.

[6] Holland R., "THREDS: A Finite-Difference Time-Domain EMP Code in 3d Spherical Coordinates," Nuclear Science, IEEE Transactions on, vol.30, no.6, Dec 1983, pp.4592-4595.

[7] Holland R., Hill J. Roger, "Self-Consistent Atmospheric EMP Coupling in Three Dimensions," Nuclear Science, IEEE Transactions on, vol.23, no.3, June 1976, pp.1283-1293.

[8] Franek O., Pedesen G.F., Andersen J.B., "Numerical modelling of a spherical array of monopoles using FDTD method", Antennas and Propagation, IEEE Transactions on, vol 54, Jul 2006, pp.1952-1963.

[9] Yinchao Chen, Mittra R., Harms P., "Finite-difference time-domain algorithm for solving Maxwell's equations in rotationally symmetric geometries," Microwave Theory and Techniques, IEEE Transactions on, vol.44, no.6, June 1996 pp.832-839.

[10] Chen Q., Fusco V.F., "Three dimensional cylindrical coordinate finite-difference time-domain analysis of curved slotline," Computation in Electromagnetics, 1994. Second International Conference on, 12-14 Apr 1994, pp.323-326.

[11] Jurgens T.G., Taflove A., Umashankar K., Moore T.G., "Finite-difference time-domain modeling of curved surfaces [EM scattering]," Antennas and Propagation, IEEE Transactions on , vol.40, no.4, Apr 1992, pp.357-366.

[12] Jurgens T.G., Taflove A., "Three-dimensional contour FDTD modelling of scattering from and multiple bodies", Antennas and Propagation, IEEE Transactions on, vol.41, Apr 1993, pp.1703-1708.

[13] Railton C.J., Cradock I. J., Schneider J.B., "Improved locally distorted CPFDTD algorithm with proven stability", Electronic letters, vol. 31, no. 18, Aug 1995.

[14] Railton C.J., Cradock I. J., "A modified CPFDTD algorithm for the analysis of arbitrary 3D PEC structures", Proc. Inst. Elec. Eng., pt. H, vol. 143, Oct 1996, pages 367-372.

[15] Fusco, M., "FDTD algorithm in curvilinear coordinates [EM scattering]," Antennas and Propagation, IEEE Transactions on, vol.38, no.1, Jan 1990, pp.76-89.

[16] Yang Hao, Railton C.J., "Analyzing electromagnetic structures with curved boundaries on Cartesian FDTD meshes," Microwave Theory and Techniques, IEEE Transactions on , vol.46, no.1, Jan 1998, pp.82-88.

[17] Yee K.S., Chen J.S., Chang A.H., "Conformal finite difference time domain (FDTD) with overlapping grids," Antennas and Propagation Society International Symposium, 1992. AP-S. 1992 Digest. Held in Conjuction with: URSI Radio Science Meeting and Nuclear EMP Meeting., IEEE, vol. 4, 18-25 July 1992, pp.1949-1952.

[18] Yee K. S., Chen J. S., "Conformal Finite Difference Time Domain and Finite Volume Time Domain", Antennas and Propagation, IEEE Transactions on, vol 42, Oct 1994, pp.1450-1455.

[19] Mrozowski M., Okoniewski M., Stuchly M.A., "Hybrid PEE-FDTD method for efficient field modelling in cylindrical co-ordinates," Electronics Letters , vol.32, no.3, 1 Feb 1996, pp.194-195.

[20] Abrahamsson L., "Orthogonal grid generation for two-dimensional ducts", Journal of Computational and Applied Mathematics, v.34 n.3, Apr 26 1991, p.305-314.

[21] Allievi A, Calisal S. M., "Application of Bubnov-Galerkin formulation to orthogonal grid generation", Journal of Computational Physics, v.98 n.1, Jan 1992, p.163-173.

[22] Duraiswami R., Prosperetti A., "Orthogonal mapping in two dimensions", Journal of Computational Physics, v.98 n.2, Feb 1992, p.254-268.

[23] Tamamidis P., Assanis D. N., "Generation of orthogonal grids with control of spacing", Journal of Computational Physics, v.94 n.2, May 1991, p.437-453.

[24] Knupp P., Steinberg S., "Fundamentals of Grid Generation", CRC Press, Boca Raton, FL, 1993.

[25] Thompson J. F., Warsi Z. U. A., Mastin C. W., "Numerical grid generation: foundations and applications", Elsevier North-Holland, Inc., New York, NY, 1985

[26] Warsi Z. U. A., Thompson J. F., A noniterative method for the generation of orthogonal coordinates in doubly-connected regions, Math. Comput.38, 501 (1982).

[27] Meliani H., Djebbar J. A., de Cogan D., "Generation of orthogonal curvilinear meshes in three dimensions", International journal of numerical modelling: electronic networks, devices and fields, 2003, vol. 16, pp. 401-415.

[28] Zhongqiang Xie, Chi-Hou, Bo Zhang, "An explicit fourth-order orthogonal curvilinear staggered-grid FDTD method for maxwell's equations", Journal of Computational Physics, 2002, vol. 175, pp. 739-736.

[29] Kane Yee, "Numerical solution of inital boundary value problems involving maxwell's equations in isotropic media," Antennas and Propagation, IEEE Transactions on , vol.14, no.3, May 1996, pp. 302-307.

[30] Lui J., Brio M.,"Overlapping Yee FDTD Method on Non-orthogonal Grids" Journal of Scientific computing, issue 39, 2009, pages 129-143.

[31] Cheng A. H.-D., Cheng D.T., "Heritage and early history of the boundary element method, Engineering Analysis with Boundary Elements", Volume 29, Issue 3, March 2005, Pages 268-302.

[32] Lazebnik M., et al, "A large-scale study of the ultrawideband microwave dielectric properties of normal, benign and malignant breast tissues obtained from cancer surgeries" 2007 Physics in Medicine and Biology. 52.

PAGE NUMBERING AS ORIGINAL

Chapter 6 Conclusions

The University of Bristol is currently developing a UWB radar imaging system with the aim of detecting early stage breast cancer. The technology is similar to that used in existing GPR schemes. In both these scenarios the antenna used to illuminate the target is one of the most critical elements. To ensure that the target is illuminated with as much energy as possible the Bristol imaging system uses a hemispherical, multistatic array that completely surrounds the breast. The greater the numbers of antennas in this array the more measurements can be taken ultimately leading to less clutter and better imaging results. For this reason it is desirable that the antenna is as small as possible so the maximum number can be fitted into the array. The transmission performance of the antenna is also a determining factor of the image quality. Signals radiated with distortion and frequency dispersion will cause clutter in resulting images. Ideally the antenna should be able to radiate short, high fidelity UWB pulses over a large angular range. This thesis focuses on producing an antenna that fulfils these criteria and then goes on to examine a novel technique for modelling this antenna in the hemispherical array.

The vast majority of existing UWB antennas have been designed to operate in communication systems and are optimised to operate in free space (see the literature review Chapter 3). Chapter 3 presents a trident-fed, square monopole fit for this purpose. This antenna was optimised to operate over the entire UWB frequency band. It has a -10dB bandwidth of 6:1 from 1.8GHz -11GHz and maintains frequency stable radiation patterns in the same frequency range. This performance was achieved by means of the trident which stabilises the current distribution on the antenna forcing it to resonate in a single mode across the majority of the UWB band. These attributes make this antenna a good candidate for use in CDMA modulation schemes, which require antennas that are capable of transmitting high fidelity UWB signals over a wide angular range. These characteristics mean the many different types of antenna designed for use in such schemes also have potential in a radar imaging system.

6.1 The Wide-Slot Antenna

The chosen antenna design is based on that presented by Jia-Yi Sze *et al.* in [1]. This consists of a wide-slot, excited by a microstrip fork-feed, which enhances the UWB performance of the slot in a similar way to the trident feed of the square monopole. This antenna was chosen because of its simplicity in terms of manufacture and simulation and its promising UWB characteristics. The planar 2D structure of the antenna lends itself to this application and also means it can be backed with a cavity to prevent back radiation.

Chapter 3 presents the development process in which the wide slot is optimised to radiate into a high permittivity matching medium with similar electrical properties to human adipose breast tissue. This manual iterative procedure is performed by FDTD simulation and includes the resizing and rescaling of the slot, fork feed and ground plane and the introduction of a high permittivity substrate. The result is a physically compact antenna consisting of slot with dimensions of 7×10mm, located off-centre in a 14×15mm ground plane.

To prevent unwanted radiation from the rear of the antenna the wide-slot is backed with an absorber lined cavity, designed to leave the performance of the antenna largely unaffected. Integrated with the cavity is a curved coax feed that eliminates the need for an SMA connector. With the feed and cavity the maximum dimension of this antenna is around half that of the SMA fed, stacked patch antenna previously designed for the array.

The UWB characteristics of this antenna also show considerable promise. The measured and simulated input response of the cavity backed antenna radiating into the matching medium, show it has a -10dB bandwidth in excess of 6GHz with a lower cut off frequency of 4GHz (measured). To examine the transmission performance of the antenna the transfer function was found at 15° intervals, between +/- 60° from boresight in the E and H-planes. Using this data contour plots were constructed showing the variation of

relative antenna gain with angle and frequency. These show that the antenna fields are stable with angle and vary from the value at bore sight by less than 10dB at all frequencies. The variation of the field with frequency has been shown to be due to the effects of frequency dependent losses in the matching medium. A slight squint was identified in the E-plane field that probably arises because the antenna is not symmetrical in this plane. Locating the slot off centre and alterations to the fork feed ensure the differences that result at angular extremes are kept to below 3dB.

The stable transmission properties of this antenna are reflected in its ability to radiate UWB signals. Within the measured angular range it is able to radiate pulses with a fidelity of >95% with regards to boresight. There is also little evidence of late time ringing resulting in short pulse durations of between 0.97 and 0.8 ns. In this regard, at boresight the performance of the wide-slot is slightly inferior to a stacked patch antenna previously designed for this application. Away from boresight the superiority of the slot was marked, highlighting the importance of examing the performance of the antenna over a range of angles. These results suggest that the wide-slot is a good candidate for use in a radar imaging system, a fact confirmed in a simple radar detection experiment.

6.2 Modelling the Wide-Slot Antenna in a Hemispherical Array

The complex geometry of the University of Bristol imaging array makes it difficult to simulate using conventional, Cartesian FDTD. Other simulation techniques such as NO-FDTD and CPFDTD are either limited in what they can simulate or introduce computational costs and/or complexity that make full scale simulation of the array impracticable. Chapter 5 presents an alternative method of simulating the array that uses a novel, orthogonal hybrid mesh capable of simulating part of the array.

The new meshing technique breaks down the problem geometry into regions that can be descretized using orthogonal coordinate systems. The different regions are joined using a

section of purpose built OC mesh. This provides a smooth transition between the different regions that requires no interpolation or individual deformation of the mesh cells. In addition because the whole mesh is orthogonal, the FDTD algorithm will run with the same efficiency as an equivalent Cartesian FDTD simulation with the same number of nodes.

The hybrid mesh is built by first constructing the OC grid and then using this as a reference to produce the rest of the lattice. For this reason, the orthogonallity of the OC section is critical as it will determine the overall quality of the hybrid mesh and so the accuracy of the simulation. The technique used to construct the OC mesh takes advantage of the orthogonal nature of the field lines and iso-potentials in a potential field. Using a finite-difference Laplace solver, a potential field is produced that has the same structure as the OC mesh. The composition of the field is determined by the choice of appropriate boundary conditions in the solver. Field lines are traced through the field from pre-selected points on its boundary. Nodes are saved at appropriate potentials to form the final OC mesh. The rest of the hybrid mesh is built up using orthogonal coordinate systems that reference the mesh planes on the boundary of the OC lattice.

In the case of the University of Bristol array the antenna is modelled using a Cartesian mesh based on that used to simulate the wide-slot in Chapter 4. Positioned in various orientations in the hemispherical array, the Cartesian mesh regions sit atop blocks of OC mesh that interface with an arbitrary, but orthogonal, spherical based mesh that represents the volume inside the array.

The validity of this method has been tested by modelling two of the wide-slot antennas angled at 45° to one another, radiating into a high dielectric numerical phantom. The simulated antenna S_{11} obtained via this model is very similar to the same results produced by an equivalent Cartesian simulation. The simulated coupling between the antennas also shows a good level of agreement with the measured response, once the frequency

dependent losses of the physical phantom have been accounted for. The quality of the mesh has been examined directly by analysing its angular composition. This indicates that above 99.4% of the angles in the mesh were greater than 84°. Confirmation of this was found by examining the field propagation from a point source located in the centre of the spherical region. No major distortion of the radiated fields was identified although this did highlight the presence of reflections in the mesh probably caused by the inadequate boundary conditions. Despite this, a direct measurement of the antenna near field in the curvilinear simulation compared favourably with the same results obtained from a Cartesian simulation with a much larger workspace.

Simulating the response from a dielectric scatterer located in the spherical mesh allows the majority of the boundary effects to be removed. To examine the performance of the model in a scattering scenario, the response was found from a small dielectric target with a contrast of 5:1 with the background medium. This was compared to the response from a similar target in a cartesian simulation by relating both data sets to the measured field intensity found in Chapter 4. The pleasing level of agreement found by this experiment, along with the results from the previous tests, confirm that the mesh is capable of modelling the segment of array to a reasonable degree of accuracy.

The first novel contribution of this work is the design of the wide-slot antenna and the hybrid-meshing technique. Based on an existing design, this antenna was heavily modified and optimised to operate in the imaging system. The cavity and bent feed were also designed specifically for this application. The second major novel contribution is the technique developed to construct the curvilinear, orthogonal mesh in Chapter 5 and the way in which this mesh is then used as a basis to construct the rest of the hybrid mesh.

6.3 Future Work

The antenna presented in Chapter 4 is a good candidate for use in a radar imaging system, however the initial brief, laying down the requirements for this antenna intrinsically implies that more can be done to improve the antenna design. Further reduction in the size of the antenna and feed would mean even more elements could be included in the array. These reductions could be affected by optimizing the antenna to work at higher frequencies. The size of the feed could be reduced by developing a method to excite the microstrip line with a vertically orientated coaxial cable, leaving only the antenna and cavity to dictate the overall dimensions.

Simulations have shown that when radiating into a lossless high permittivity medium the antenna has a very flat transmission response. Unfortunately in reality the frequency dependent losses of the matching medium distort the radiated pulses resulting in the sloped transfer function seen in Section 4.6.3. To compensate, the transmission response of the antenna could be altered to have a gradient that is the inverse of the "loss slope".

The work presented in Chapter 5 takes the first steps in the development of a technique that could potentially be used to model the imaging array and needs a lot more work before it can be practicably applied. First the two antenna simulation should be extended to model more antennas and eventually an entire row of antennas in the array. In its present state, the structure of the mesh restricts its use to simulating only a linear section. To enable its application to the entire array the basic structure of the mesh must be redefined or a method developed to allow a number of array "wedges" to be linked together. This latter strategy could be realised using a large intermediate section of OC mesh between the wedges, though constructing this would be quite a challenge.

One of the most significant procedures in terms of computer resources is the time taken solving the Laplace equations when finding the potential field. For the case of the OC-

mesh produced in this chapter, these calculations push a conventional 32-bit desktop machine to its limits. Currently the Laplace solver used is relatively crude and could be refined, potentially giving significant time and memory savings.

The fundamental principles of the OC mesh construction are valid and could prove useful in other problems, where large sections of the geometry can be accurately modelled using different orthogonal coordinate systems. The method used to construct the OC mesh could also prove useful in efficiently simulating curved microwave structures or resonators. The author also recognises that the degree of non-orthogonallity in the OC mesh and so hybrid mesh as a whole, is probably too high and further work must be carried out to reduce these errors still further. This could be accomplished by developing a finer Laplace solver mesh and further refinement of the field-line tracing algorithm.

For the technique to be useful, further work should be done towards benchmarking the method. Simulations should be carried out to validate the orthogonal meshing algorithm and explore its limitations. These should include how cell size and mesh curvature affects the quality of the mesh.

The technique could be generalised and an automatic meshing procedure developed to make the method more "user-friendly" and accessible. Ideally an algorithm would be found that decides the optimum orthogonal co-ordinate system for a given geometry and how best to link the resultant mesh volumes with the OC sections.

References

[1] Jia-Yi Sze, and Kin-Lu Wong, "Bandwidth enhancement of a microstrip-line-fed printed wide-slot antenna," Antennas and Propagation, IEEE Transactions on, Volume 49, July 2001 pp: 1020 – 1024.